BRNO UNIVERSITY OF TECHNOLOGY
VYSOKÉ UČENÍ TECHNICKÉ V BRNĚ

FACULTY OF MECHANICAL ENGINEERING
FAKULTA STROJNÍHO INŽENÝRSTVÍ

INSTITUTE OF AUTOMOTIVE ENGINEERING
ÚSTAV AUTOMOBILNÍHO A DOPRAVNÍHO INŽENÝRSTVÍ

MODELING THE IMPACT OF PISTON RINGS ON OIL CONSUMPTION OF INTERNAL COMBUSTION ENGINES

MODELOVÁNÍ VLIVU PÍSTNÍCH KROUŽKŮ NA SPOTŘEBU OLEJE SPALOVACÍCH MOTORŮ

DOCTORAL THESIS
DIZERTAČNÍ PRÁCE

AUTHOR AUTOR PRÁCE	Ing. Peter Raffai
SUPERVISOR ŠKOLITEL	doc. Ing. Pavel Novotný, Ph.D.

BRNO 2017

MODELING THE IMPACT OF PISTON RINGS ON OIL CONSUMPTION OF INTERNAL COMBUSTION ENGINES

by

Peter Raffai

Submitted to the Faculty of Mechanical Engineering on May 5, 2017
in Partial Fulfillment of the Requirements
for the Degree of Doctor of Philosophy

ABSTRACT

Within the frame of the present work a complex simulation tool was developed, built on strong physical and chemical foundations, supplemented with the appropriate mathematical approaches. The resulting software is capable of determining the performance of a piston ring pack by addressing all key mechanisms and their mutual influence during standard operating conditions of a piston ring. The outputs of the simulation were designed in accordance with industrial interest, like the volumetric gas flow through the piston assembly, the friction power losses and the lubricant oil consumption from the sources, which are affected by the piston ring pack.

Besides the development of the simulation model, experiments were conducted with the intention of input data obtainment and results validation on an inline three-cylinder engine. Sample results were shown by applying the model to the parameters of the experimental engine. Possible industrial application of the source code is demonstrated with parameter studies.

The work carried out within the frame of this doctoral dissertation was intended to fill the gap in the research area of combined simulation tools, able to support the needs of piston ring manufacturers and engine research centers, to calculate the impact of design parameter changes on friction losses and lubricant oil consumption simultaneously.

Thesis supervisor:
Pavel Novotný
Associate Professor, Institute of Automotive Engineering

KEYWORDS

Internal Combustion Engines, Piston Rings, Computer Simulation, Friction Loss, Lubricant Oil Consumption, Experimental Validation

DECLARATION OF AUTHORSHIP

I, Peter Raffai, hereby declare that this thesis – “Modeling the Impact of Piston Rings on Oil Consumption of Internal Combustion Engines” – is my own work based on my own original survey, and all the sources have been quoted and acknowledged by means of a complete list of references in this document.

Brno, May 5, 2017

....

Signature of Author

ACKNOWLEDGEMENTS

First of all, I would thank my supervisor, Assoc. Prof. Pavel Novotný, not only for his advice and guidance during the development of the simulation model but also for the opportunities to attend international conferences and internships. I would like to thank Prof. Václav Píštěk, for the consultations and assurance of the technical experiments. Furthermore, I wish to express my luck and happiness for the great collective and the permanent positive work atmosphere at the Institute, thanks to my colleagues. Special thanks to Dr. Ondřej Maršálek for his collegiality, valuable help and cooperation, to Lubomír Drápal for the unconditional sharing of his deep technical knowledge, to Dr. Veronika Vencúrik-Pituková for the irreplaceable language review, to Jiří Knotek for the endless amount of constructive ideas, to Dr. David Svída and Martin Beran for the lab assistance, and every colleague, who somehow contributed to the formation of this dissertation.

I also would like to acknowledge the cooperation of industrial partners, who contributed to the conduction of the technical experiments. Namely, Dr. Michal Pavlov from Škoda Auto, and Jan Havlík from Buzuluk. Special thanks to Dr. Kent Froelund from Da Vinci Emissions Services for his mentoring and kind hospitality during my internship in San Antonio.

Cardinal thank belongs to my parents for their constant and unlimited love, support and belief in me, not only during my university studies. Unique thank goes to Judit for standing by my side even in the most difficult times, continuously inspiring and motivating me towards reaching the final goal. Without their help and patience, it would not have been possible to complete this doctoral thesis.

TABLE OF CONTENTS

Abstract ... iii
Declaration of Authorship ... v
Acknowledgements ... vii
Table of Contents ... ix
List of Figures ... xii
List of Tables ... xvi
Introduction ... 1
1 Initial Problem Definition ... 3
2 State-of-the-Art ... 5
3 Doctoral Thesis Goals ... 7
4 Simulation Model ... 8
  4.1 Main Body of the Software ... 8
  4.2 Data Initialization ... 8
  4.3 Piston Rings Primary Motion ... 9
  4.4 Gas Flow Through the Piston Ring Pack ... 10
    4.4.1 Gas Flow Through the Piston Ring Gap ... 11
    4.4.2 Gas Flow Through the Ring-Groove Clearance ... 14
    4.4.3 Numerical Solution ... 14
  4.5 Equilibrium State Calculation ... 16
    4.5.1 Axial Motion ... 16
    4.5.2 Radial Motion ... 17
    4.5.3 Numerical Solution ... 17
  4.6 Ring Profile Generator ... 18
  4.7 Ring Pretension ... 19
  4.8 Gas Pressure Forces ... 21
  4.9 Lubrication Regimes ... 22
    4.9.1 Hydrodynamic Lubrication ... 22
    4.9.2 Partial (Mixed) Lubrication ... 25
    4.9.3 Boundary Lubrication ... 28
    4.9.4 Numerical Solution ... 30
  4.10 Oil Transport Mechanism ... 31

4.10.1 Flow Balance at the Leading Edge ... 31
4.10.2 Flow Balance at the Trailing Edge ... 33
4.11 Lubricating Oil Consumption ... 36
4.11.1 Oil Evaporation ... 37
4.11.2 Oil Throw-Off ... 42
4.11.3 Oil Flow Due to Gas Blow-Back ... 44
4.12 Data Handling ... 45
5 Experimental Setups ... 46
5.1 Fired Engine Measurement ... 46
5.2 Real Surface Structure ... 52
6 Sample Results and Discussion ... 62
6.1 Piston Rings Primary Motion ... 62
6.2 Interring Gas Pressures ... 63
6.3 Ring Profiles ... 68
6.4 Force Equilibrium ... 70
6.4.1 Minimum Oil Film Thickness ... 70
6.4.2 Wetted Area ... 72
6.4.3 Gas Force ... 74
6.4.4 Hydrodynamic Force ... 76
6.4.5 Contact Force ... 81
6.5 Oil Film Thickness on the Cylinder Liner ... 83
6.6 Oil Consumption ... 85
6.6.1 Evaporation Induced LOC ... 85
6.6.2 Blow-Back Induced LOC ... 90
6.6.3 Throw-Off Induced LOC ... 90
6.6.4 Total Lubricant Oil Consumption ... 91
7 Parameter Studies ... 93
7.1 Viscosity Influence on Friction ... 93
7.2 Surface Structure Influence on Friction and LOC ... 101
7.2.1 Impact on Hydrodynamic Lubrication ... 101
7.2.2 Impact on Asperity Contact ... 103
7.2.3 Total Impact on Friction ... 103

7.2.4 Impact on LOC 106
8 Future Work 108
8.1 Improvements of the Simulation Model 108
8.2 Input Parameter Obtainment and Experimental Validation 108
9 Summary 110
10 References 111
11 List of Abbreviations 118
12 List of Symbols 119
Appendix A 124
Appendix B 128
Appendix C 131
Appendix D 132
Appendix E 133
Appendix F 136
Appendix G 139
Appendix H 140
Appendix I 142

LIST OF FIGURES

Figure 1 Compression ignition passenger car engine emission standards in the EU 1

Figure 2 Annual CO_2 emission reduction in the EU [89] 2

Figure 3 Energy distribution in a fired internal combustion engine [71] 3

Figure 4 Screenshot of the data input window of RingSIM GUI 9

Figure 5 Schematics of the crank mechanism 10

Figure 6 Scheme of the gas labyrinth model for blow-by calculation [60] 11

Figure 7 Ring gap area nomenclature 12

Figure 8 Nusselt flow function in dependency on pressure ratio [20] 13

Figure 9 Graphical representation of the RK4 method derivation points [17] 15

Figure 10 Screenshot of the data displaying window of RingSIM GUI 15

Figure 11 Forces acting on a piston ring segment 16

Figure 12 Drawbacks of the CNR; left: local extremum; right: nonconvergent loop [17] 18

Figure 13 Graphical interpretation of the worn piston ring profile [54] 19

Figure 14 Piston ring design nomenclature [4] 19

Figure 15 Different contact pressure shapes due to ring pretension [4] 20

Figure 16 Nomenclature of ring pretension contact pressure and tangential force [4] 20

Figure 17 Interpretation of gas force calculation of a ring segment 21

Figure 18 Lubrication regimes of piston rings – Stribeck curve 22

Figure 19 Hydrodynamic pressure profile with Reynolds exit condition [22] 24

Figure 20 Rough contact interpretation [64] 26

Figure 21 Surface roughness orientations [64] 27

Figure 22 Comparison of linear and polynomial interpolation of the statistical function 29

Figure 23 Oil flow components at the leading edge 32

Figure 24 Oil flow components at the trailing edge 34

Figure 25 Oil consumption sources in an IC engine [27] 36

Figure 26 Character of gas flow above a liquid layer [25] 37

Figure 27 Nomenclature of oil evaporation mechanism from the cylinder liner [50] 38

Figure 28 Nomenclature of the heat transfer mechanism [50] 42

Figure 29 Nomenclature of the oil throw-off mechanism 43

Figure 30 Nomenclature of the oil entrainment mechanism 44

Figure 31 Tested steady state engine operating conditions – graph 47

Figure 32 Measurement principle of the blow-by flow [85] 48

Figure 33 Blow-by measurement configuration scheme [23] 48

Figure 34 Measured results of volumetric gas flow through the piston assembly – graph 49

Figure 35 Measured combustion chamber pressures at 2500 rpm 50

Figure 36 Intake manifold pressures at measured operating conditions 50

Figure 37 Calculated temperature distribution along the cylinder liner at 2500 rpm 51

Figure 38 In-cylinder temperature variation 52

Figure 39 Surface topography of a worn cylinder liner 54

Figure 40 Surface topography of an unworn cylinder liner 54

Figure 41 Areal autocorrelation function of the worn cylinder liner surface 55

Figure 42 Areal autocorrelation function of the unworn cylinder liner surface 55

Figure 43 Surface topography of the worn compression ring 57

Figure 44 Areal autocorrelation function of the worn compression ring surface 57

Figure 45 Surface topography of the nitrided compression ring 59

Figure 46 Areal autocorrelation function of the nitrided compression ring surface 59

Figure 47 Surface topography of the PVD CrN coated compression ring 60

Figure 48 Areal autocorrelation function of the PVD CrN coated compression ring 60

Figure 49 Surface topography of the PVD DLC coated compression ring 61

Figure 50 Areal autocorrelation function of the PVD DLC coated compression ring 61

Figure 51 Axial position, velocity and acceleration of the piston at 2500 and 5000 rpm 62

Figure 52 Interring volume and flow type nomenclature 63

Figure 53 Temperature distribution and deformation of the piston at 2500 rpm WOT 63

Figure 54 Interring gas pressures at 2500 rpm WOT 64

Figure 55 Blow-back mass flow at 2500 and 5000 rpm WOT 65

Figure 56 Blow-by mass flow at 2500 and 5000 rpm WOT 65

Figure 57 Measured and calculated blow-by flows at WOT 67

Figure 58 Compression ring profile 68

Figure 59 Scraper ring profile 69

Figure 60 Oil control ring profile 69

Figure 61 Minimum oil film thickness of the compression ring at 2500 and 5000 rpm WOT 70

Figure 62 Minimum oil film thickness of the scraper ring at 2500 and 5000 rpm WOT 71

Figure 63 Minimum oil film thickness of the oil control ring at 2500 and 5000 rpm WOT 71

Figure 64 Wetted profile of the compression ring at 2500 rpm WOT 72

Figure 65 Wetted profile of the compression ring at 5000 rpm WOT 72

Figure 66 Wetted profile of the scraper ring at 2500 rpm WOT 73

Figure 67 Wetted profile of the oil control ring blade at 2500 rpm WOT 73

Figure 68 Gas pressure forces acting on the compression ring 74

Figure 69 Gas pressure forces acting on the scraper ring 75

Figure 70 Gas pressure forces acting on the oil control ring 75

Figure 71 Values of dynamic viscosity under the ring profiles at 2500 and 5000 rpm WOT .. 76

Figure 72 Flow factors of the worn cylinder liner and worn piston ring surface pair 77

Figure 73 Hydrodynamic pressure profile of the compression ring 78

Figure 74 Hydrodynamic pressure profile of the scraper ring 78

Figure 75 Hydrodynamic pressure profile of the oil control ring 79

Figure 76 Hydrodynamic forces acting on the compression ring profile 79

Figure 77 Hydrodynamic forces acting on the scraper ring profile 80

Figure 78 Hydrodynamic forces acting on the oil control ring profile 80

Figure 79 Asperity contact forces acting on the compression ring profile 82

Figure 80 Asperity contact forces acting on the scraper ring profile 82

Figure 81 Asperity contact forces acting on the oil control ring profile 83

Figure 82 Oil film thickness left on the cylinder liner after the downward piston strokes 84

Figure 83 Oil film thickness left on the cylinder liner after the upward piston strokes 84

Figure 84 Partial pressure of the n-Pentacosane vapor 88

Figure 85 Oil evaporation rate from cylinder liner surface 89

Figure 86 Oil consumption rate due to gas blow-back 90

Figure 87 Oil consumption rate due to throw-off 91

Figure 88 Total amount of lubricant oil consumption at WOT condition 92

Figure 89 Comparison of dynamic viscosities under the CR profile at 2500 rpm WOT 93

Figure 90 Comparison of the CR MOFT for different viscosities at 2500 rpm WOT 94

Figure 91 p-V diagram of the Škoda EA111 engine for 2500 rpm WOT 95

Figure 92 Mean effective pressures and mechanical efficiency at WOT 96

Figure 93 Friction mean effective pressure share of the rings with 5W40 oil at WOT 97

Figure 94 Total friction mean effective pressures of the piston ring pack at WOT 98

Figure 95 Friction mean effective pressures due to viscous friction at WOT 99

Figure 96 Friction mean effective pressures due to asperity contact friction at WOT 100

Figure 97 Flow factors of the unworn cylinder liner – nitrided piston ring 101

Figure 98 Flow factors of the unworn cylinder liner – chromium nitrided piston ring 102

Figure 99 Flow factors of the unworn cylinder liner – diamond-like carbon piston ring 102

Figure 100 Comparison of fmep of compression rings with different coatings at WOT 104

Figure 101 Viscous friction mean effective pressures at WOT 105

Figure 102 Asperity contact friction mean effective pressures at WOT 105

LIST OF TABLES

Table 1 Values of the statistical function for asperity contact calculation 28

Table 2 Coefficients of the polynomial 29

Table 3 Test engine parameters 46

Table 4 Tested steady state engine operating conditions – values 47

Table 5 Measured results of volumetric gas flow through the piston assembly – values 48

Table 6 Worn cylinder liner surface parameters 56

Table 7 Unworn cylinder liner surface parameters 56

Table 8 Worn compression ring surface parameters 58

Table 9 Surface parameters of the nitrided compression ring 59

Table 10 Surface parameters of the PVD CrN coated compression ring 60

Table 11 Surface parameters of the PVD DLC coated compression ring 61

Table 12 Piston land diameters of the thermally loaded piston 64

Table 13 Parameters of the t-tests 67

Table 14 Design parameters of the baseline ring pack 68

Table 15 Parameters of the Vogel equation for engine oil viscosity grade 5W40 76

Table 16 Surface parameters of the worn cylinder liner and ring pack 81

Table 17 Combined input parameters for the G&T calculation 81

Table 18 Lubricating oil base stock composition 85

Table 19 Variables of the diffusion coefficient calculation 86

Table 20 Sutherland constants for air viscosity 87

Table 21 Antoine equation parameters for n-Pentacosane 88

Table 22 Isobaric specific heat capacity 89

Table 23 Total lubricant oil consumption for WOT running condition 91

Table 24 Vogel parameters of the compared engine oils 94

Table 25 Mean effective pressures and mechanical efficiency at WOT 96

Table 26 Friction mean effective pressures of the ring pack with 5W40 oil at WOT 97

Table 27 Friction mean effective pressures of the ring pack with 0W30 oil at WOT 97

Table 28 Friction mean effective pressures of the ring pack with 0W20 oil at WOT 98

Table 29 Hydrodynamic friction mean effective pressures at WOT 99

Table 30 Asperity contact friction mean effective pressures at WOT 99

Table 31 Surface parameters of the unworn cylinder liner and compression rings 103

Table 32 Combined surface parameters for the G&T calculation 103

Table 33 Friction mean effective pressures of the nitrided ring at WOT 104

Table 34 Friction mean effective pressures of the chromium nitrided ring at WOT 104

Table 35 Friction mean effective pressures of the diamond-like carbon ring at WOT 104

Table 36 Lubricant oil consumption with the nitrided ring at WOT 106

Table 37 Lubricant oil consumption with the chromium nitrided ring at WOT 107

Table 38 Lubricant oil consumption with the diamond-like carbon ring at WOT 107

INTRODUCTION

In the early 70s of the 20th century, the Council and the Parliament of the European Union agreed on the limitation of exhaust gas emissions for new light-duty vehicles and passenger cars, while heavy-duty vehicles are regulated since 1988. From then on various new, stricter directives and regulations have been introduced, where the limits vary depending on fuel type and vehicle size. This is meant to ensure sustainable emissions for the future with the growing number of produced vehicles. Among the restricted components, we find the amount of particulate matter (PM), hydrocarbon compounds (HC), nitrogen oxide compounds (NOx), or carbon oxide compounds (CO). As seen in Figure 1, the marginal values for these emissions in the last 24 years have decreased by as much as 97.5%. Values are obtained from EU directives [79], [80], [81], [82], [83], and regulation [84].

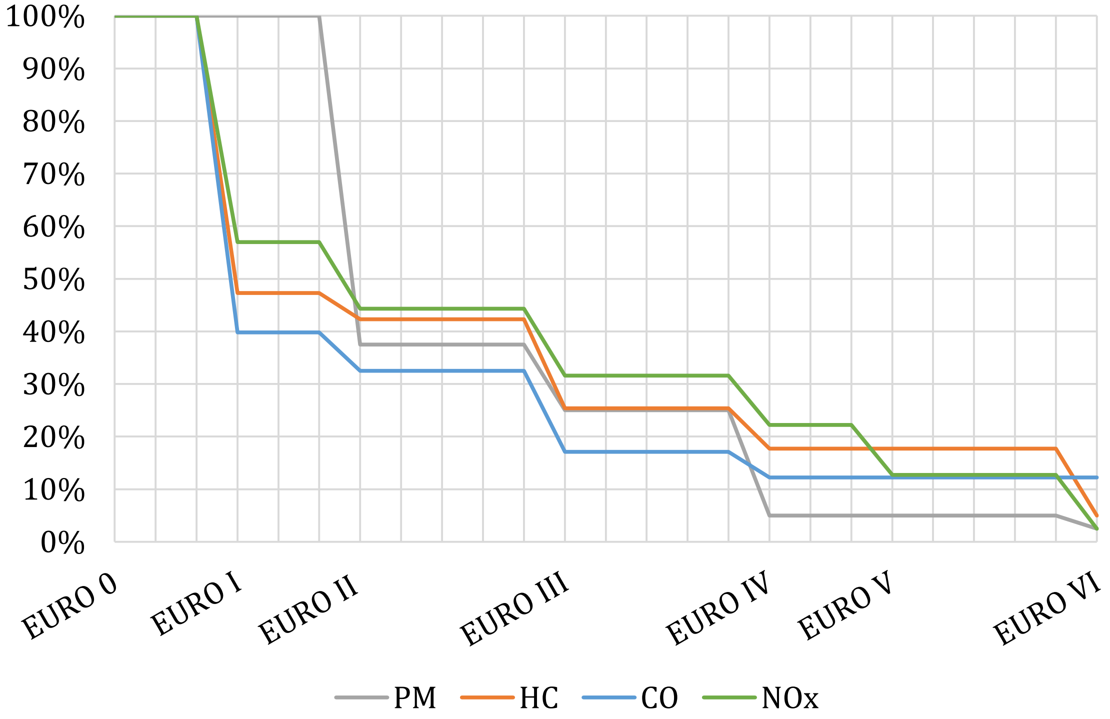

Figure 1 Compression ignition passenger car engine emission standards in the EU

Out of the limited components of the exhaust gases the most widely monitored for passenger cars is the amount of CO_2 emission, the main greenhouse gas, as internal combustion (IC) engines of vehicles could be accounted for around 12% of the total CO_2 emission of the EU [88]. This value is in direct connection with the consumed fuel by a given IC engine and is limited for the whole fleet of a given manufacturer, where exceeding the marginal value results in a penalty payment after each registered vehicle of the penalized manufacturer. The marginal values for passenger cars are shown in Figure 2.

Figure 2 Annual CO_2 emission reduction in the EU [89]

As seen in the above two graphs, after each period new, stricter limits were set, which became more and more difficult to meet by the manufacturers. Especially these continuous restrictions have led to the need for research and optimization of every segment of IC engines. There are several available tools for achieving the set goals, but undoubtedly one of them is the approach via increasing the mechanical efficiency of the powertrains, where our solution further focuses on lowering the mechanical losses of IC engines.

While in the case of passenger cars and light-duty vehicles the most important goal is to lower the CO_2 component of the emissions, in the case of heavy-duty vehicles the focus is put on restricting the amount of PM. This component of the outdoor air pollution is classified by the World Health Organization’s specialized cancer agency, the International Agency for Research on Cancer as carcinogenic to human beings [92], therefore its limitation is a high priority.

One of the main sources for PM formation during the combustion process is the undesired leakage of excess lubricant oil into the combustion chamber and its unwanted burning due to high temperatures. Resulting from the chemical-mechanical properties of lubricant oils this combustion is imperfect, which leads to the creation of hard coke carbon particles. Besides the aforementioned air pollution, this process also negatively affects the mechanical parts of the engine, e.g. the coke deposits on the surface of the piston, which reduces its heat exchange capability resulting in a raised risk of piston cracking.

1 INITIAL PROBLEM DEFINITION

As stated in the previous chapter, one of the approaches to meet the EU legislation for exhaust gas CO_2 emission is via lowering the mechanical losses of IC engines. In the earlier times, when IC engines were not as sophisticated as they are nowadays, more emphasis was put on the research and development of those parts of the engine which held a greater potential of gain per the input effort. As time has passed and the emission limits have further decreased the development of the mainstream engine parts was not enough to fulfill the requirements, so researchers turned their focus to previously neglected parts.

By taking a closer look at the distribution of the total energy in a fired diesel engine in Figure 3 it is visible, that between 4 and 15 percent [71] is lost due to the friction of mechanical parts of an engine. Moreover, approximately half of the mechanical friction is caused by the piston assembly and the connecting rods, out of which, depending on the engine load, approximately for one-third, the piston ring pack could be accounted. This non-negligible part of the total friction loss, which further rises due to other trends in the construction of modern IC engines, like downsizing and turbocharging, make the research of the piston ring pack important in the present and in the future of IC engine development.

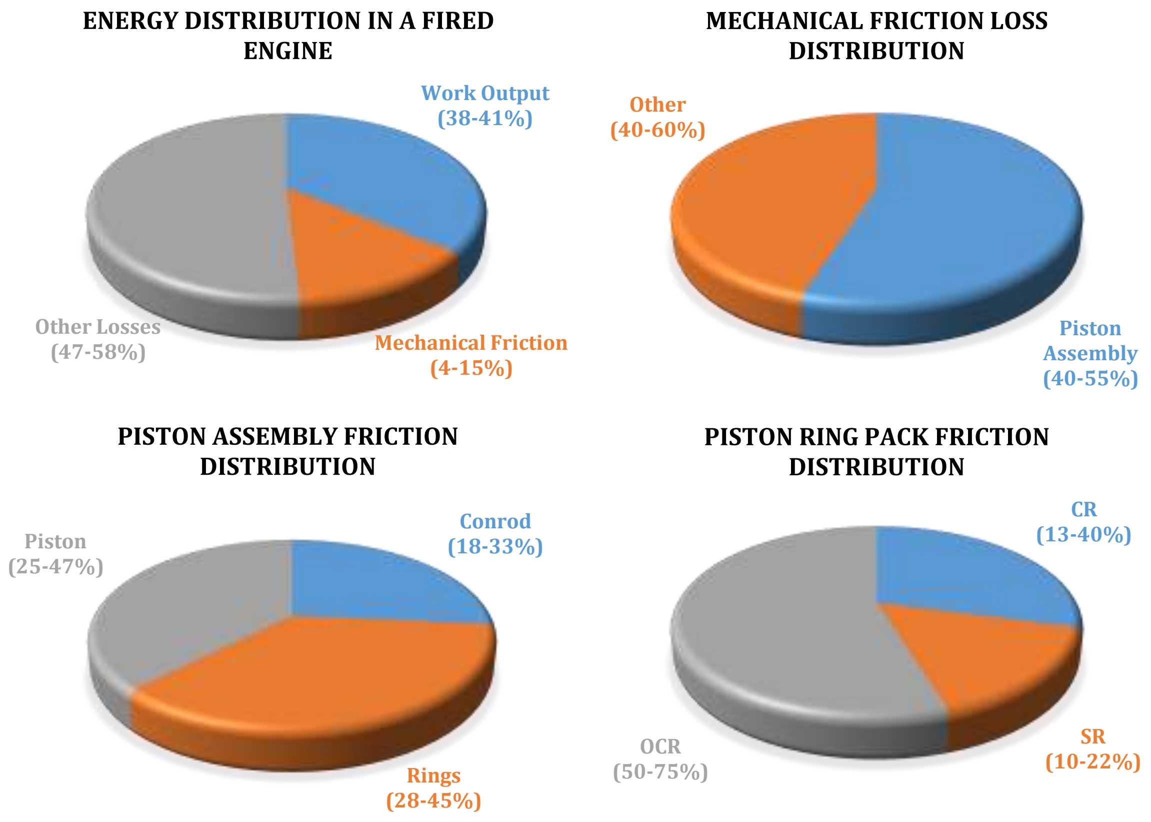

ENERGY DISTRIBUTION IN A FIRED ENGINE

MECHANICAL FRICTION LOSS DISTRIBUTION

PISTON ASSEMBLY FRICTION DISTRIBUTION

PISTON RING PACK FRICTION DISTRIBUTION

Figure 3 Energy distribution in a fired internal combustion engine [71]

Besides acting as an undesired source of friction loss, the role of the piston ring pack is complex, therefore its correct function is very important. Its key functions are:

- combustion chamber sealing,
- lubricant film height control,
- heat transfer and
- piston secondary motion support.

To be able to ensure the above-listed functions, the following requirements have to be met:

- high effectivity – low friction but high oil scraping ability,
- reliable operation – high resistance ability but high conformability and
- low cost production.

These contradictory requirements result in the need for a complex approach for the purpose of the creation of a progressive method for the solving of the piston ring pack problem.

2 STATE-OF-THE-ART

Over the last two decades, the number of complex numerical approaches for the simulation of the piston ring pack published worldwide has risen significantly. Each of them is unique in a specific way, but they all can be divided into 2 main groups according to the utilized software tool:

- commercial software tools combined with specialized subroutines and
- standalone user-written programs.

The approach through commercial software tools in combination with some specialized subroutines for the resolution of specific areas of the research of the piston ring pack carries the potential to give highly accurate results. This approach is presented by Ortjohann et al. [62] and Reipert and Voigt [69], whose solution is based on finite element method (FEM) software. Another approach based on a commercial software tool is presented by Ragot and Rebbert [68], who utilized a multi-body system (MBS) software for his simulations. Common drawbacks of these approaches are lengthy computational times due to a high number of elements of the model, therefore high degree of freedom throughout the calculation. On the other hand, the complexity of these approaches makes them suitable to consider various phenomena simultaneously, e.g. the force interactions between the segments of the piston rings, or to include the modal characteristics of the interacting parts.

Standalone user-written subroutines are suitable for detailed calculation of some specific theoretical phenomena, which many times have not yet been incorporated into the commercial software. They also give more freedom of altering various parameters and inputs for their creator. After optimizing the source code of these user-written programs they usually perform a lot faster than commercial software, but since it is hard to consider complex force interactions in 3D solutions, they represent a compromise between precision and speed. They are suitable mainly for targeted computations of a certain area of the piston ring pack research, where carefully chosen simplifications do not distort the obtained results. The majority of the published approaches share the same proven governing equations, mainly concerning the calculation of hydrodynamics, asperity contact, and crevice pressures. User-written subroutines for complex simulation of the piston ring pack were published by e.g. Wannatong [77], Gulwadi [49], Arcoumanis [1], Novotný [61], and Raffai [65], while other researchers focused on a certain area of study in more detail, like the phenomenon of blow-by through the piston ring pack presented by e.g. Ejakov [39], Furuhama [46],[47], and Kuo et al. [56], or the investigation of elasto-hydrodynamic lubrication of the piston rings by e.g. Dowson et al. [35], Hwu and Weng [53], and Hu et al. [52].

One of the most complex and comprehensive research work in the field of piston ring study is being carried out at the Massachusetts Institute of Technology and its technical R&D center, Sloan Automotive Laboratory. The fundamentals of their simulation model has been created by Tian [24], followed by detailed studies and developments of its sub-modules, e.g. implementing a 3D approach for the inclusion of the non-axisymmetric characteristics of cylinder bore by Liu [11], or the detailed theoretical and experimental study of surface parameters affecting the resulting friction of a twin land oil control ring by Liao [9]. Extensive research work has been carried out also in the field of lubricant oil consumption study, where e.g. Yilmaz [27] experimentally determined the main oil consumption sources and validated the simulation model on a production engine, while Thirouard [23] further analyzed the oil transport mechanism in the piston ring pack with respect to total engine oil consumption. Recently Baelden [2] refined the simulation tool by developing a multi-scale modeling approach for simultaneous consideration of oil transport mechanisms. Besides the above-mentioned dissertations the study of piston rings has been extensively supported by many master's theses and research publications as well.

All of the aforementioned researchers, their papers and approaches share at least one thing in common – the effort to use the latest available information technology to develop advanced simulation algorithms. These algorithms are intended to support the research and development of, not only, modern internal combustion engines and their parts to achieve higher effectiveness, lower losses encountered, better fuel economy and a more sustainable general exhaust gas emission, in order to help make the Earth a better place to live.

3 DOCTORAL THESIS GOALS

Simulation tools play an important role in the R&D process of modern internal combustion engines in the last few decades. Therefore, creating a calculation algorithm for the simulation of the piston – ring – liner system could be important and beneficial for the automotive industry. The focus of this particular thesis is put on the topic of lubricating oil transport through the piston ring pack and also its consumption modeling.

The main goals of the dissertation thesis can be divided into two main parts:

1. Development of a complex simulation tool suitable for the determination of lubricating oil consumption from certain sources in an internal combustion engine.
2. Validation of the simulation tool throughout suitably proposed experiments.

The main aim of this thesis was to propose a specialized software tool which incorporates all the latest theoretical approaches for the simultaneous calculation of the dynamics, the lubrication regimes and some lubricating oil consumption mechanism present in an engine, at the same time utilizing the potential of modern information technology. The main focus of the work was further put on the detailed determination of the lubrication oil film height due to various phenomena, like the mutual interaction between the rings due to their scraping ability, or the oil transport mechanism through the wetted profile of the rings affected by temperature and pressure influences resulting from the combustion process. The lubrication oil consumption module includes the determination of the amount of consumed oil from the major sources of oil loss in IC engines. The obtained computational results were partially validated throughout technical experiments, as well as some input data were obtained from measurements described within the frame of this thesis.

The simulation tool was intended to address all the mechanisms of the piston – ring – liner system which directly or indirectly affect the lubricating oil consumption. These sub-modules include e.g.:

- piston and ring pack dynamics,
- lubrication regimes in the ring-liner tribopair,
- gas flow through the piston assembly,
- oil transport mechanism,
- oil consumption due to evaporation, gas blow-back and throw-off.

Besides being complex and accurate, another requirement for the simulation algorithm was speed. Therefore, suitably chosen numerical solutions were implemented to solve mathematical problems, e.g. the iterative solution of force equilibrium on a ring segment; the solution of non-linear differential equations; relaxation methods, etc.

The following chapters describe in detail the theoretical background of the outlined simulation tool, the experimental setups and show the capabilities of the created model via sample results.

4 SIMULATION MODEL

The most important outcome of this dissertation thesis, the simulation model has been developed in Matlab programming environment. The main reason why Matlab has been preferred to others is its user-friendly graphical user interface (GUI), fast and easy options for analyzing and plotting the calculated results and the extensive amount of built-in functions, which aid the coding process.

The created simulation tool has been named as RingSIM, the final version of the source code has over 2.800 lines and had been divided into 19 separate functions and 1 script grouped together on the basis of the carried out calculations. This chapter is dedicated to the description of these sub-modules, and to the flow of the computation process. The individual functions are lined up based on the order of their utilization in the algorithm, not according to their complexity.

4.1 MAIN BODY OF THE SOFTWARE

For running the software RingSIM a script named MAIN has to be called. This script executes general data initialization, incremental force and oil transport equilibrium state calculation for the given number of rings, and checks for the fulfillment of the termination criteria for the whole calculation cycle. The variables between the consequential functions are handed over via both as global or local workspace variables. For static values mostly global variables are used, while the recurrently changing ones are updated in each calculation step in the local workspace.

4.2 DATA INITIALIZATION

To input, read and convert the necessary parameters used during the calculation two separate functions have been created. The INPUTDATA function enables the user to enter the values of various parameters, which are grouped together based on their origin, e.g. engine parameters, ring parameters, lube oil parameters, etc. Since INPUTDATA requires the user to enter the parameters in SI derived units, in some cases it is beneficial to transform these values into different units to achieve a higher measure of numerical stability throughout the calculations; moreover, the use of some auxiliary variables are also desirable. These transformations and declarations are carried out by the second function, called INITIALIZE. All variables declared in these two function are stored in structural global variables.

To ease up the defining of some key parameters a GUI has been created in addition to the INPUTDATA function. The user can therefore, enter the values of some variables into input fields, while the distinguishing of the required dimensions is aided by demonstrative sketches. Furthermore, four push buttons can be used to either save the entered values into a data file, load a previously saved configuration, commence calculation or open another GUI for displaying results. More information about the results displaying GUI is given at the description of the blow-by calculation in chapter 4.4. A screenshot of the GUI is showcased in Figure 4.

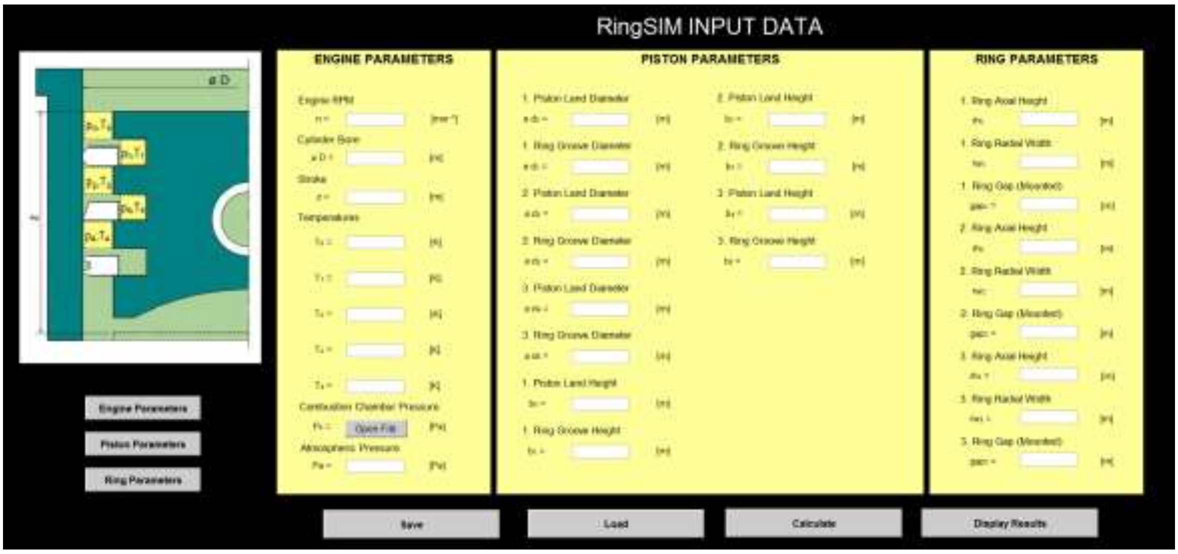

Figure 4 Screenshot of the data input window of RingSIM GUI

4.3 PISTON RINGS PRIMARY MOTION

After the data initialization process, the solver part begins. This section gathers all the functions, which take part in the calculation. The calculation steps refer to values of rotational angles of the crankshaft. The starting angle and angular step are user defined variables.

The first function utilized in the solver section is the calculation of the instantaneous values of the piston dynamics since the primary motion of the piston rings is considered to be identical with the reciprocating primary motion of the piston, on which the rings are mounted. The velocity and acceleration of this translational motion are resulting from the motion of the crank mechanism and their instantaneous values serve as one of the basic input parameters in the determination of the friction and lubrication parameters of the rings. Figure 5 shows the scheme of the crank mechanism.

Instantaneous piston displacement from TDC:

$$s(\varphi) = r\left[1 - \cos\varphi + \frac{1}{\lambda}\left(1 - \sqrt{1 - \lambda^2 \sin^2\varphi}\right)\right]. \tag{1}$$

Instantaneous piston velocity:

$$v(\varphi) = r\omega\left(\sin\varphi + \frac{\lambda}{2}\sin 2\varphi\right). \tag{2}$$

Instantaneous piston acceleration:

$$a(\varphi) = r\omega^2\left(\cos\varphi + \lambda\cos 2\varphi\right). \tag{3}$$

The above equations are formulated for crank mechanisms without piston eccentricity.

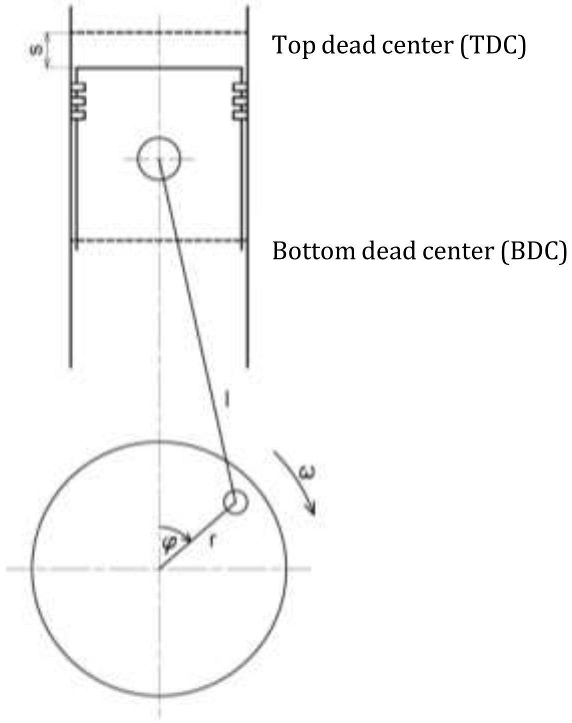

l – conrod length, [m]
r – crankshaft radius, [m]
s – piston position, [m]
φ – crank angle, [rad]
ω – angular velocity, [rad s^{-1}]
λ – r to l ratio, [-]

Figure 5 Schematics of the crank mechanism

4.4 GAS FLOW THROUGH THE PISTON RING PACK

The second utilized function in the solver section of the computation model is the calculation of the interring gas pressures, called BLOWBY.

The undesired gas flow through the piston assembly not only lowers the efficiency of IC engines due to pressure decrease in the working cylinder, but, besides others, also contributes to the lubrication oil consumption of the engine. Whereas the gas stream transports molecules of lubricant either towards the crankcase (blow-by) or towards the combustion chamber (blow-back). In both cases, the particles of lubricant get into the exhaust stream which negatively affects the emissions as described in the Introduction chapter.

For the correct determination of gas flow through the piston ring pack a labyrinth flow model is utilized, based on the suggestion of Furuhama and Tada [46], which divides the piston-rings-liner system into *N-1* stagnation volumes, where *N* is the number of rings on the piston. The volumes are connected via a narrow gap bounded by the ring gap, piston groove, and cylinder liner. This theory was further enhanced by Namazian and Heywood [60], who considered also the mass flow rate between the ring side and the piston groove, defining more crevice volumes. The created labyrinth gas flow model is shown in Figure 6. Experimentally validated flow models [47] and [60] showed that the leaking gas temperature is almost identical to the piston surface temperature. The pressure of piston crown crevice (volume 1) is assumed to be identical to combustion chamber pressure, while the oil control ring shows very poor pressure sealing ability, thus crankcase pressure is assumed to act below volume 5. The pressure within each region is uniform.

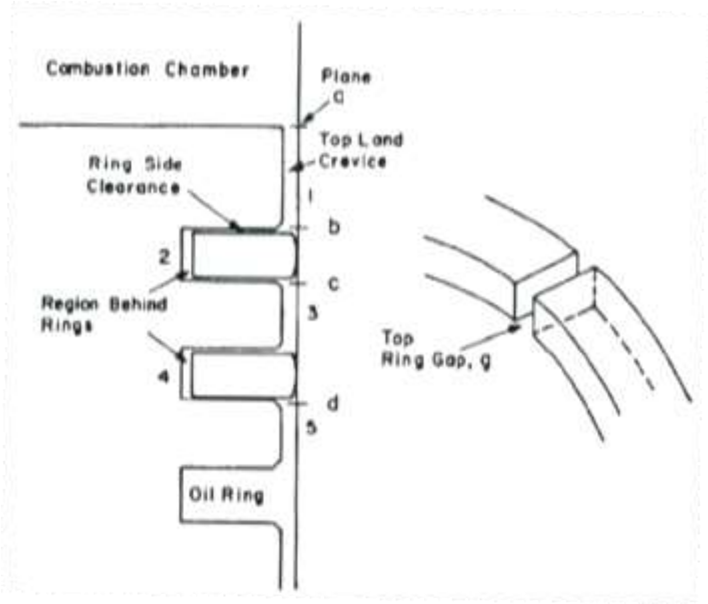

Figure 6 Scheme of the gas labyrinth model for blow-by calculation [60]

By taking the assumptions from above into consideration, the continuity equations for the calculated regions are as follows:

$$\frac{m_{o_2}}{P_{o_2}}\frac{dP_2}{dt}=\dot{m}_{12}-\dot{m}_{23}, \tag{4}$$

$$\frac{m_{o_3}}{P_{o_3}}\frac{dP_3}{dt}=\dot{m}_{13}+\dot{m}_{23}-\dot{m}_{34}-\dot{m}_{35}, \tag{5}$$

$$\frac{m_{o_4}}{P_{o_4}}\frac{dP_4}{dt}=\dot{m}_{34}-\dot{m}_{45}, \tag{6}$$

where P_{o_i} are the initial pressures of volumes 2 – 4, m_{o_i} are the initial masses in volumes 2 – 4 and $\dot{m}_{ij}$ are the mass flows between volumes *i* and *j*.

4.4.1 GAS FLOW THROUGH THE PISTON RING GAP

The mass flow rates through the piston ring gaps are calculated as an isentropic orifice flow [20]:

$$\dot{m}_{gap}=C_d\ A_g\ f_m\sqrt{2\frac{p_u}{v_u}}, \tag{7}$$

where C_d is the discharge coefficient, A_g is the gap area, f_m is the compressibility factor, p_u is the upstream pressure, and v_u is the specific volume of upstream gas.

However, based on the equation of state for ideal gases:

$$p\,v = R\,T\,, \tag{8}$$

equation (7) can also be written as:

$$\dot{m}_{gap} = C_d\ A_g\ p_u\ f_m\ \sqrt{\frac{2}{R_u\ T_u}}\,, \tag{9}$$

where R_u is the universal gas constant and T_u is the temperature of the upstream gas.

The relation for the determination of the discharge coefficient is obtained by fitting experimentally obtained values [19]:

$$C_d = 0.85 - 0.25\left(\frac{p_d}{p_u}\right)^2\,. \tag{10}$$

The gap area is the tiny opening circumscribed by ring gap, the cylinder liner, and the piston land surfaces. For its calculation the piston is considered to be centered in the cylinder, graphically interpreted in Figure 7.

$$A_g = gap\,\frac{D-d}{2}\,, \tag{11}$$

where gap is the piston ring gap width in mounted state, D is the cylinder bore and d is the piston land diameter.

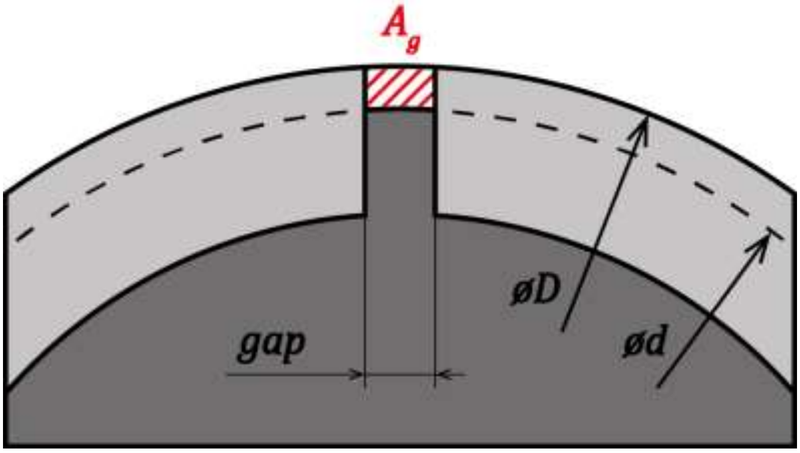

Figure 7 Ring gap area nomenclature

The calculation of the compressibility factor is governed by the Nusselt flow function, graphically shown in Figure 8:

$$f_m = \sqrt{\frac{\kappa}{\kappa-1}\left[\left(\frac{p_d}{p_u}\right)^{\frac{2}{\kappa}} - \left(\frac{p_d}{p_u}\right)^{\frac{\kappa+1}{\kappa}}\right]}\,, \tag{12}$$

where κ is the specific heat ratio (isentropic expansion factor) of the gas:

$$\kappa = \frac{c_p}{c_v}. \tag{13}$$

defined as the ratio of the isobaric heat capacity c_p to the isochoric heat capacity c_v.

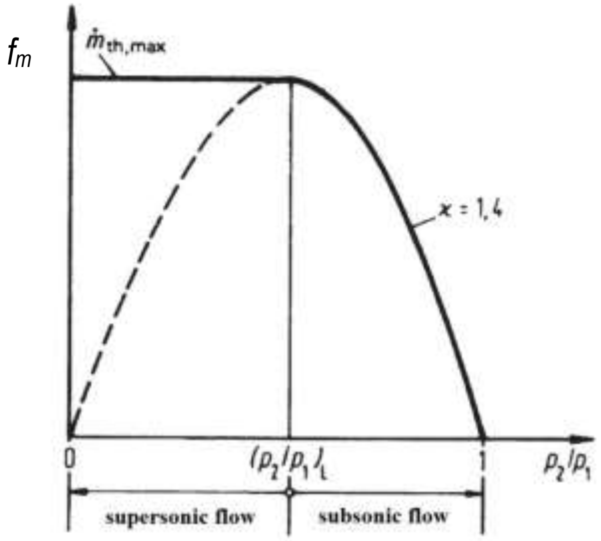

Figure 8 Nusselt flow function in dependency on pressure ratio [20]

From the parabolic course of the Nusselt flow function is evident that by lowering the downstream pressure the flow rate increases (subsonic flow) until it reaches its maximum at the critical pressure ratio $\left(\frac{p_d}{p_u}\right)_{cr}$. This ratio is also referred to as Laval pressure ratio, which is characteristic for every gas and can be calculated as [20]:

$$\left(\frac{p_d}{p_u}\right)_L = \left(\frac{2}{\kappa+1}\right)^{\frac{\kappa}{\kappa-1}}. \tag{14}$$

After reaching the Laval pressure ratio, by further decreasing of the downstream pressure, the compressibility factor, and therefore the theoretical mass flow rate as well, remains constant at its maximum value (supersonic flow) [20]:

$$f_{m,\max} = \left(\frac{2}{\kappa+1}\right)^{\frac{1}{\kappa-1}} \sqrt{\frac{\kappa}{\kappa+1}}. \tag{15}$$

4.4.2 GAS FLOW THROUGH THE RING-GROOVE CLEARANCE

Since the gas flow through the clearance between the ring side and the opposing surface of the piston groove has low Reynolds number (below 2000), it is considered a fully-developed, quasi-steady, and locally parallel flow (Poiseuille flow) [24] of an isothermal compressible fluid, where the mass flow rate per unit length along the circumferential direction can be expressed as [19], [24]:

$$\dot{m}_{clea} = \frac{\left(p_u{}^2 - p_d{}^2\right)}{24\eta_{gas} RT \int\limits_{x_a}^{x_b} \frac{dx}{h^3}}, \tag{16}$$

where R is the gas constant, T is the temperature of the piston groove, h is the height of the clearance, and η_{gas} is the viscosity of the gas, which can be calculated as [60]:

$$\eta_{gas} = 3.3\times10^{-7} T^{0.7}. \tag{17}$$

4.4.3 NUMERICAL SOLUTION

For the solution of ordinary differential equations (ODE), like the ones used for gas flow calculation different methods can be used. The utilized method in RingSIM is the 4th order Runge-Kutta (RK4) approach, which is based on the Euler method; however is derived to eliminate the unsymmetrical behavior of the base formula due to the use of a single derivative for the determination of the next step value. The RK4 method is based on four evaluations of the derivative per one step, which makes the calculation more time-demanding, but increases the accuracy of the obtained result for the given step size. The method is graphically shown in Figure 9, which shows the four derivative evaluations, first at the initial point (y_n), two at trial midpoints and the last one at the trial endpoint, from which the next step functional value is determined (y_{n+1}). The RK4 method solves the ODE using the following system of equations [17]:

$$y_{n+1} = y_n + \frac{1}{6}k_1 + \frac{1}{3}k_2 + \frac{1}{3}k_3 + \frac{1}{6}k_4 + O\left(h^5\right), \tag{18}$$

Steps k_1, k_2, k_3 and k_4 can be calculated as follows:

$$\begin{aligned} k_1 &= h\ f\left(x_n, y_n\right), \\ k_2 &= h\ f\left(x_n + \frac{1}{2}h, y_n + \frac{1}{2}k_1\right), \\ k_3 &= h\ f\left(x_n + \frac{1}{2}h, y_n + \frac{1}{2}k_2\right), \\ k_4 &= h\ f\left(x_n + h, y_n + k_3\right), \end{aligned} \tag{19}$$

where *h* represents the integration step size. The size of the integration step is important for the precision of the calculation (decrease in step size increases precision and vice versa).

Figure 9 Graphical representation of the RK4 method derivation points [17]

As indicated in chapter 4.2, another GUI has been designed for displaying the calculated interring pressures over one engine cycle. The main motivation for the creation of the set of two GUIs was to aid the students in the master's study program of the Institute of Automotive Engineering in their workflow of submitting their semestral projects. Namely, the sub-routine for the blow-by calculation can be integrated into the source code of the data input GUI, which allows the running of the computation, export the results into a data file and display the course of interring pressures in another GUI, all in the frame of a standalone application. The screenshot of the data displaying GUI is shown in Figure 10.

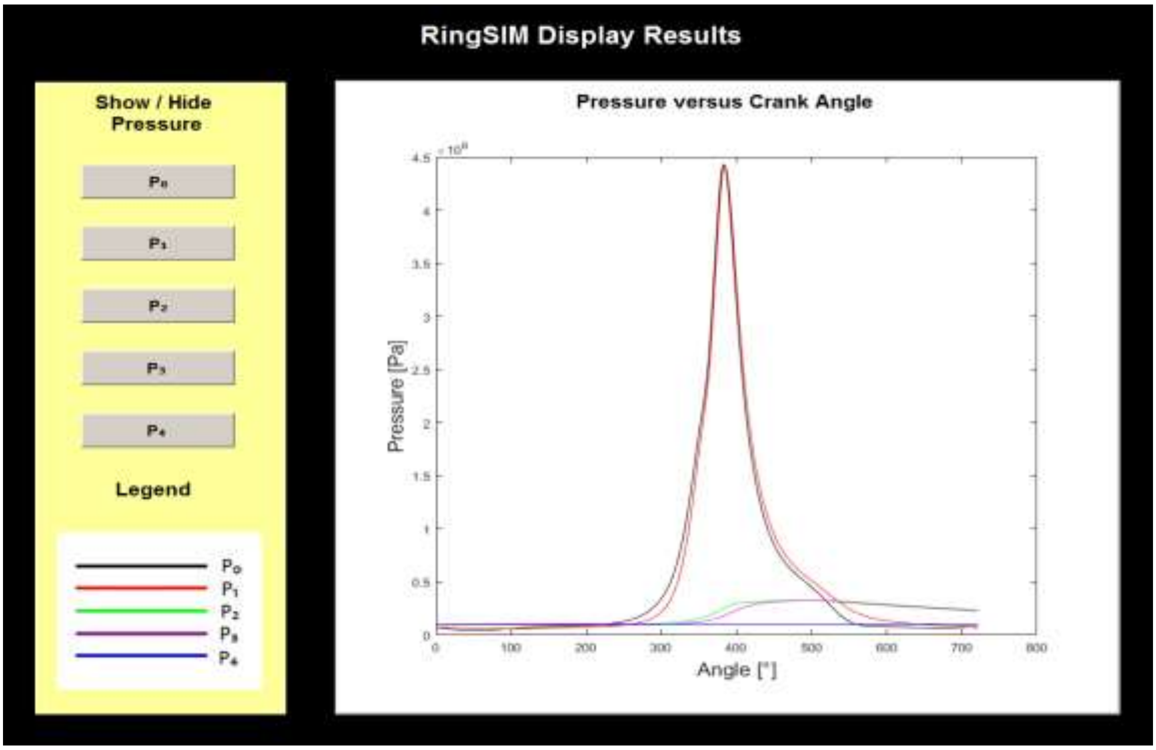

Figure 10 Screenshot of the data displaying window of RingSIM GUI

4.5 EQUILIBRIUM STATE CALCULATION

After determining the instantaneous values of ring dynamics and interring pressures the force equilibrium state calculation commences. The different force components acting on each ring are calculated separately, in distinct sub-routine functions, which are grouped and iteratively solved within the EQUILIBRIUM function.

The main outcome of the EQUILIBRIUM function is the calculation of the secondary motion of the piston rings. It is considered as the local motions of the rings inside their grooves, which result from various loads acting on the rings during their operation. Generally, the secondary motion of the rings can be divided into three main types depending on their character:

- ring axial motion,
- ring radial motion and
- ring twist.

Previous experimental [44] and theoretical [18] studies have shown that during engine operation the ring twist motion due to external loads is of order 5 minutes. This angular twist has a negligible effect on gas blow-by, and therefore on lubricating oil consumption (LOC) as well, hence can be neglected.

4.5.1 AXIAL MOTION

The axial motion of the ring in its groove is governed by the resultant force acting on the rings in the axial direction. From Figure 11 is apparent that the forces acting in the axial direction are as follows:

- gas pressure forces (acting above and below) $F_{p,a}$,
- inertia forces (resulting from piston acceleration/deceleration) $F_{i,a}$,
- friction forces (hydrodynamic and asperity in ring-liner contact) $F_{f,a}$ and
- damping forces (oil squeezing on groove flanks) $F_{s,a}$.

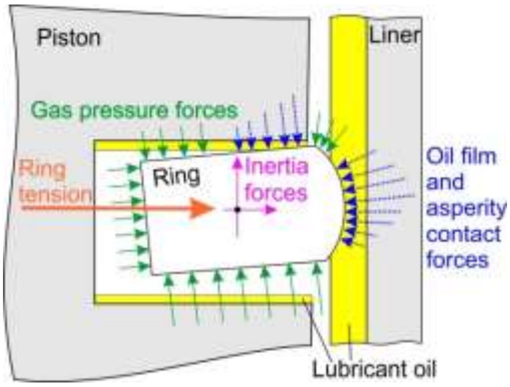

Figure 11 Forces acting on a piston ring segment

Considering the options for the resulting force, three typical positions of a piston ring in its groove can occur. Throughout most of the operation cycle, the rings are pushed either to the lower or the upper wall of the piston groove, creating a barrier for the gas flow. At the moment when the resultant force changes its direction, the ring lifts off of the surface of the groove opening a passage for the gas to flow behind the ring until it settles on the opposite surface of the groove. This phenomenon could yield in an unsteady behavior of the ring when the ring starts rapidly changing its position between the upper and lower groove flanks – also known as ring flutter. This leads to an accelerated wear of both the piston and rings, as well as to an increased gas blow-by. Since the occurrence of this phenomenon is not usual and is considered as an emergency state, the current version of RingSIM does not consider the axial motion of the rings, however, it is definitely one of the key areas of the planned future improvement.

4.5.2 RADIAL MOTION

The following forces are considered in the radial force balance:

- gas pressure forces (acting front and behind) $F_{p,r}$,
- hydrodynamic forces (between ring and liner) $F_{HD,r}$,
- asperity contact forces $F_{ct,r}$,
- inertia forces (resulting from oil film thickness change) $F_{i,r}$,
- friction forces (hydrodynamic and asperity due to ring-groove contact) $F_{f,r}$ and
- tangential ring pretension forces (from elastic deformation) $F_{t,r}$.

The situation is very similar to the case of axial ring motion, as during most of the working cycle the rings are pushed to the cylinder liner, but in some cases, mostly dependent on the ring face geometry, the gas pressure forces acting on the ring's running face can overcome the forces pushing the ring towards the cylinder liner. In these cases radial ring flutter occurs as the ring lifts off of the cylinder liner, again, opening a direct passage for the combustion gases to flow past the ring.

4.5.3 NUMERICAL SOLUTION

The force equilibrium state calculation in each time step results from the solution of a nonlinear system of equations. For this purpose a widely appreciated method has been chosen, a conventional Newton-Raphson (CNR) approach, which is favored due to its efficient convergence (quadratic) in the root-finding process.

The next iteration step value is defined by the Newton-Raphson formula [17]:

$$x_{i+1} = x_i - \frac{f(x_i)}{f'(x_i)}, \tag{20}$$

where the derivative of the function value $f'(x_i)$ can be expressed as a one-sided derivative from the right to reduce computation cost:

$$f'(x_i) = \frac{f(x_i + dx) - f(x_i)}{dx}. \tag{21}$$

The termination criteria for the iteration cycle can then be defined as:

$$\left| \frac{x_{i+1} - x_i}{x_{i+1}} \right| \le ERROR. \tag{22}$$

Despite its advantage of fast convergence, the CNR method has a few drawbacks, too. The first is its sensitivity to the close proximity of initial guess, meaning its global convergence is very poor. Fortunately in the case of piston ring secondary motion calculation, the deviation in position between the computation steps is small, therefore local convergence is successfully maintained. The other drawbacks are the unfortunate cases when the method either encounters a local extremum and the next step value approaches one of the infinities, either enters a nonconvergent recurrent iteration loop. The above mentioned disadvantages are displayed in Figure 12. The overcome the problem with local extremum the CNR method has been combined with a bisection method, while the infinite iteration loop is eliminated by applying a dampening coefficient, which is calculated in each time step of the calculation.

The following chapters are dedicated to the description of the calculation of the contributing forces to the radial force equilibrium.

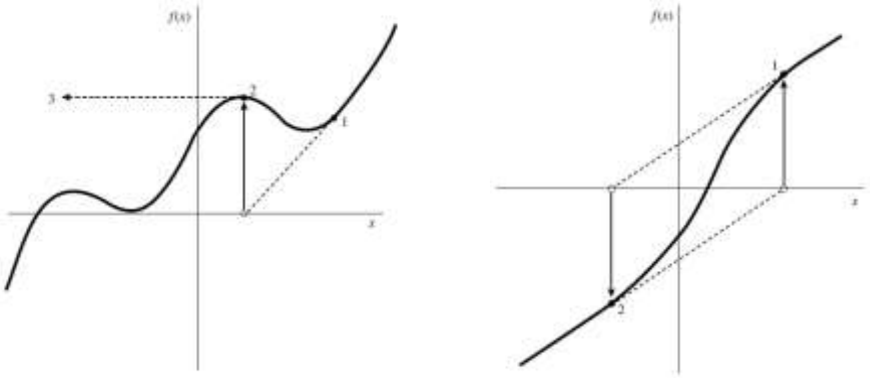

Figure 12 Drawbacks of the CNR; left: local extremum; right: nonconvergent loop [17]

4.6 RING PROFILE GENERATOR

To be able to supply the instantaneous wetted profile of each ring to the functions, a profile generating sub-routine has been created named as PROFILEGEN. As the originally designed and manufactured profile of a ring's running face runs in fast and stabilizes in a worn-in shape for the rest of its service time, RingSIM utilizes the approximate shape of a worn piston ring profile. Previous researches and experimental studies, e.g. [54],[55] and [75], have shown, that a good correlation can be achieved between the real profile and the description in the simulation model by substituting the ring's profile with an offset parabola equation (even for tapered face rings):

$$y(x)=\frac{C}{\left(\frac{b}{2}+o\right)^{2}}(x-o)^{2}. \tag{23}$$

where y is the ring profile height, x is the axial coordinate, C is the crown height, o is the offset and b is the ring height. Schematically shown in Figure 13.

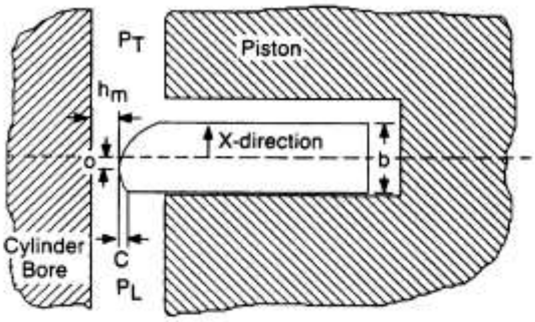

Figure 13 Graphical interpretation of the worn piston ring profile [54]

For the representation of an unworn profile, one or more than one higher order polynomials can be used if desired.

4.7 RING PRETENSION

The free shape of a piston ring is designed to ensure a desired course and magnitude of contact pressure between the ring and the liner. This results from the elastic deformation of the ring when properly mounted on the piston inside the cylinder, the corresponding nomenclature is shown in Figure 14.

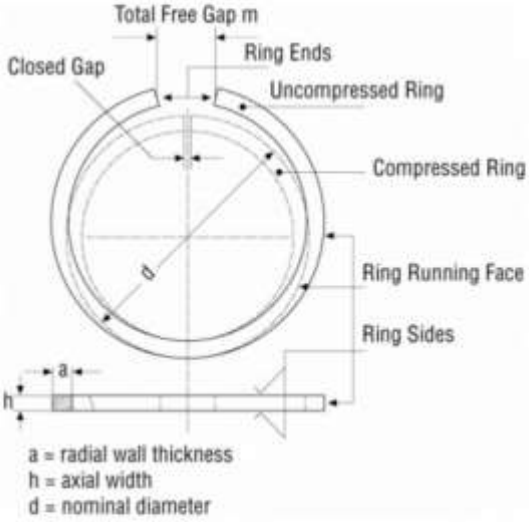

Figure 14 Piston ring design nomenclature [4]

The resultant shape of contact pressure along the ring circumference can expel a constant or variable course as shown in Figure 15.

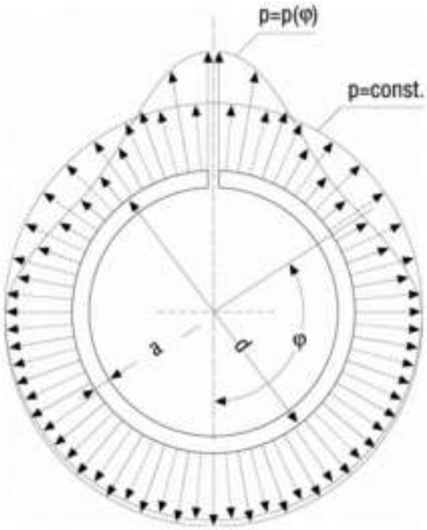

Figure 15 Different contact pressure shapes due to ring pretension [4]

The measure of contact pressure is dependent on the geometrical and material parameters of the piston ring. Its permissible value range for each ring type is stated by technical standards, e.g. in the Czech Republic by national standards of ČSN 02 7010 through 7022 and 7026.

Due to the fact that the straightforward experimental determination of the contact pressure is overly complicated and demanding, its value is mostly calculated based on the measured value of tangential force:

$$p = \frac{F_t}{r\,h}, \tag{24}$$

where p is the contact pressure due to ring pretension, F_t is the tangential force, r is the radius of the mounted ring and h is the axial height of the ring, graphically shown in Figure 16.

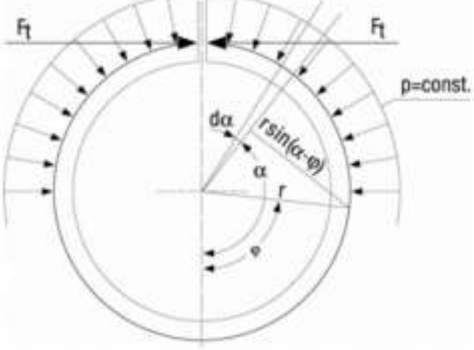

Figure 16 Nomenclature of ring pretension contact pressure and tangential force [4]

4.8 GAS PRESSURE FORCES

The interring pressures calculated in the BLOWBY function are fed to the force equilibrium computation sub-routine. In this section, the GASFORCE function transforms the pressure impacts based on the instantaneously exposed areas of the piston ring segment into radial and axial force components.

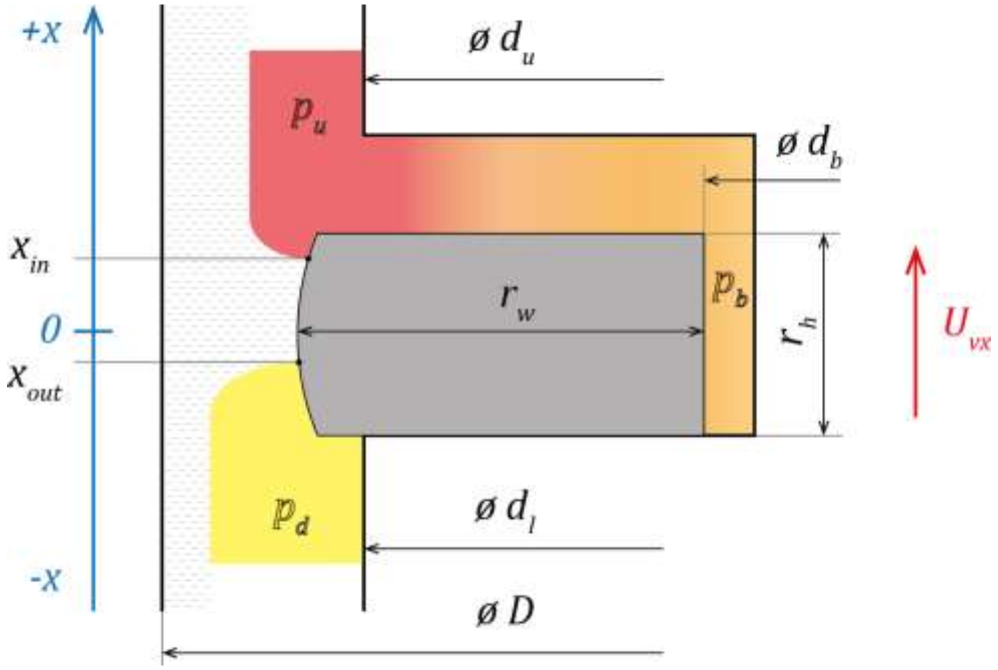

Figure 17 Interpretation of gas force calculation of a ring segment

Figure 17 shows the schematic of interring gas pressures acting on the ring surfaces. Based on this interpretation the calculation is as follows:

$$F_{GASu} = \left(\frac{r_h}{2} - x_{in} \right) \pi \; D \; p_u \, , \tag{25}$$

$$F_{GASl} = \left(\frac{r_h}{2} + x_{out} \right) \pi \; D \; p_d \, , \tag{26}$$

$$F_{GASb} = r_h \; \pi \; d_b \; p_b \, , \tag{27}$$

where

$$d_b = D - 2 \, r_w \, . \tag{28}$$

Therefore, the instantaneous resultant radial gas force component acting on a ring is:

$$F_{GAS} = F_{GASb} - F_{GASu} - F_{GASl} \, . \tag{29}$$

4.9 LUBRICATION REGIMES

Depending on the minimum oil film thickness under the ring profile, oil flooding conditions of the rings, ring pretension forces, roughness of the contact surface pair, lubricant properties, gas pressures, design parameters of the ring, temperatures of the rings, piston and liner, and the relative velocity of the sliding surfaces three lubrication regimes can be distinguished for piston rings [74]:

- hydrodynamic lubrication (incl. elasto-hydrodynamic lubrication),
- partial (mixed) lubrication and
- boundary lubrication.

Figure 18 shows a general shape of the Stribeck curve enhanced by marking the areas of the usual lubrication regimes of each piston ring type.

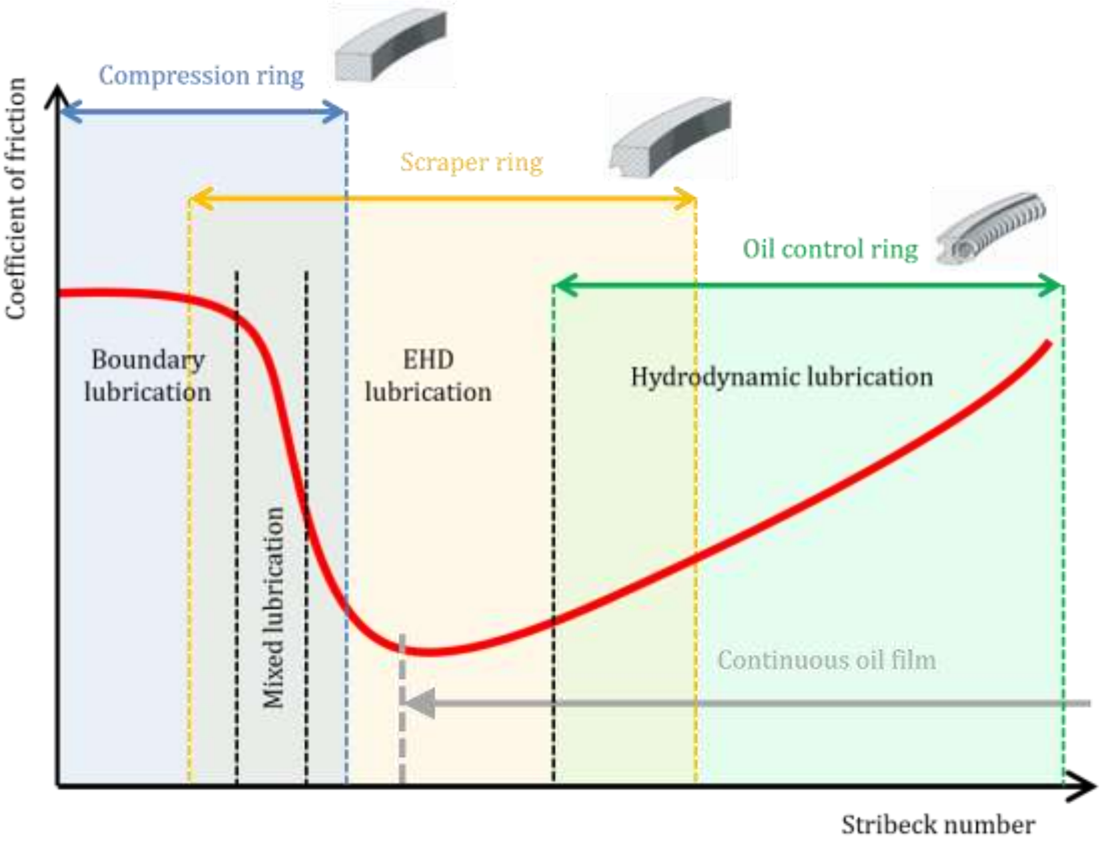

Figure 18 Lubrication regimes of piston rings – Stribeck curve

4.9.1 HYDRODYNAMIC LUBRICATION

In the case of pure hydrodynamic (HD) lubrication regime the surfaces in contact are completely separated by a viscous fluid film and no surface asperity contact occurs, therefore the external load is fully carried by forces forming in the lubrication layer, which are calculated in the HDPRESSURE function. This lubrication regime is considered when the specific film thickness – a ratio to minimum fluid film thickness to composite surface roughness is greater than or equal to 4 [48]:

$$H = \frac{h}{\sigma} \geq 4 . \tag{30}$$

The governing equation for the pressure distribution in the fluid film was named after Osborne Reynolds, who derived it [70]. The general Reynolds equation is a differential equation based on the Navier-Stokes equations and the continuity equation. Characterizing the flow of a compressible lubricant in a wedge-shaped gap of a journal bearing has a form of [77]:

$$\frac{\partial}{\partial x}\left(\frac{\rho h^3}{\eta}\frac{\partial p}{\partial x}\right)+\frac{\partial}{\partial y}\left(\frac{\rho h^3}{\eta}\frac{\partial p}{\partial y}\right)=6U\frac{\partial(\rho h)}{\partial x}+12\frac{\partial(\rho h)}{\partial t}, \tag{31}$$

where

$$U=\frac{U_1+U_2}{2}, \tag{32}$$

where ρ is the density of lubricant, h is the oil film thickness, η is the dynamic viscosity of lubricant, U_1 and U_2 are the tangential velocities of surface 1 and 2, respectively, x is the Cartesian coordinate in the tangential direction of rotation, y is the Cartesian coordinate in the axial direction, p is the hydrodynamic pressure in the lubricant film, while t stands for time.

The above equation has been derived considering the following assumptions [3]:

- Lubrication film thickness is much smaller than its other dimensions.
- Body forces (e.g. gravity) are not considered.
- Viscosity remains constant across the lubrication film thickness.
- Radius of the bearing is much larger than the lubrication film thickness.
- Lubricant is an uncompressible Newtonian fluid.
- Lubricant perfectly sticks to contact surfaces, no slip is present.
- Inertia forces in the lubrication film are neglected.

The contact pair of the piston ring and the cylinder liner represents a specific type of dynamically loaded bearing. According to the fact that in this tribological pair the oil film height is much smaller than the piston ring radius, the piston ring can be assumed to be an infinitely long slider bearing. Therefore, the average Reynolds equation for an incompressible Newtonian lubricant can be simplified to a 1-dimensional form [3]:

$$\frac{d}{dx}\left(h^3\frac{dp}{dx}\right)=6U\eta\frac{dh}{dx}+12\eta\frac{dh}{dt}. \tag{33}$$

In the procedure of hydrodynamic calculation, the dynamic viscosity of the lubricant is assumed to vary along the cylinder liner length dependent on temperature. For the determination of the local dynamic viscosity Vogel's relation is used predominantly [22]:

$$\eta(T) = a\, e^{\frac{b}{T-c}}, \tag{34}$$

where η is the dynamic viscosity of the lubricant at temperature T, a, b, c are constants.

The physical properties of liquids enable a flooded wedge-shaped surface pair to generate HD load carrying pressure in the lubricant layer in case the surfaces are in relative motion. In the converging region of the bearing, the HD pressure rises until its peak value then decreases until it reaches the ambient pressure at the trailing edge. At this point, a further decrease in pressure causes the vaporization of the lubricant and the release of dissolved gases in the liquid. In this region the lubricating layer breaks into streamers of air and liquid, which causes the loss of the load carrying ability of the fluid film. The phenomenon of this liquid rupture is called lubricant cavitation and has been widely investigated and documented by Dowson et al. [36], Elrod et al. [40] and others.

To be able to determine the exact location of the lubricating film detachment from the trailing edge of the bearing the Reynolds boundary condition has been applied. It is assumed to correlate well with experimental results [24] and could be efficiently incorporated into the numerical solution of the HD pressure profile calculation. Based on this exit condition the continuous oil film ruptures at the location where the pressure gradient in the fluid film equals to zero. Graphical interpretation of the Reynolds exit condition on a piston ring segment is shown in Figure 19.

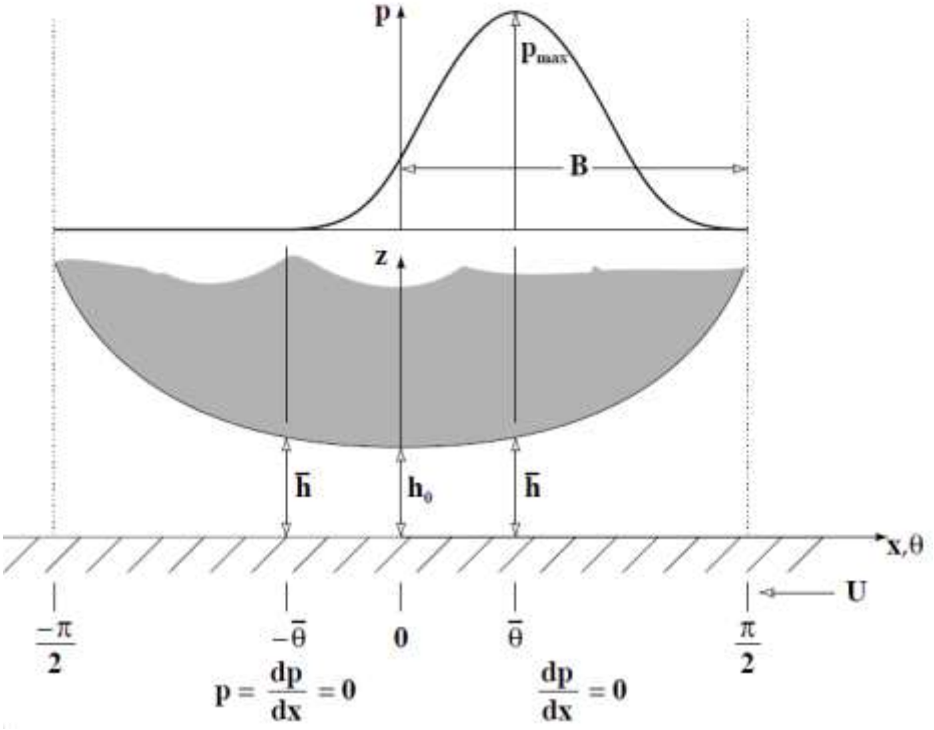

Figure 19 Hydrodynamic pressure profile with Reynolds exit condition [22]

4.9.2 PARTIAL (MIXED) LUBRICATION

The theory of the original Reynolds equation was derived with the assumption that both opposing surfaces are smooth. As real engine parts do have surface roughness resulting from the utilized machining process, and the lubricating film thickness between the ring and the liner are of similar magnitude as the surface roughness, its influence on the lubrication mechanism is significant. To include the effect of surface roughness, almost a century after the introduction of the original Reynolds equation, in 1978 researchers Patir and Cheng [64],[65] published the most widely used empirical relations applicable to any general roughness structure in their paper.

The governing parameter in their approach became the H ratio (eq. 30) again, for $H > 4$ the authors state that surface roughness effects are negligible and the original Reynolds equation for smooth surfaces is sufficiently accurate. Roughness becomes important when the H ratio falls below 4, meaning that the load on the bearing is not carried exclusively by the hydrodynamic forces exerting in the fluid film, but is partially supported by the contacts of asperity heights. This state is referred to as partial lubrication regime. This subchapter is devoted to the description of the hydrodynamic part of partial lubrication affected by the properties of surface roughness. For the description of asperity contact determination please refer to subchapter 4.9.3.

Patir and Cheng introduced parameters, which not only reflect the heights of asperities of a surface but also their directional orientation. These parameters are referred to as flow factors. Pressure flow factors ϕ_x and ϕ_y were empirically defined as the ratio of the average pressure flow in a rough bearing to the flow in a smooth bearing, while the shear flow factor ϕ_s represents the additional lubricant flow due to the sliding motion of the bearing. In this approach, the roughness heights were assumed to have a Gaussian frequency density. Deriving the average Reynolds equation on a control volume for a rough surface bearing with the local flows in x and y directions we obtain the following form of the average Reynolds equation for an isothermal, incompressible lubricant [64]:

$$\frac{\partial}{\partial x}\left(\phi_x \frac{h^3}{12\eta}\frac{\partial \overline{p}}{\partial x}\right)+\frac{\partial}{\partial y}\left(\phi_y \frac{h^3}{12\eta}\frac{\partial \overline{p}}{\partial y}\right)=\frac{U_1+U_2}{2}\frac{\partial \overline{h}_T}{\partial x}+\frac{U_1-U_2}{2}\sigma\frac{\partial \phi_s}{\partial x}+12\frac{\partial \overline{h}_T}{\partial t}, \tag{35}$$

where $\overline{p}$ is the mean pressure, σ is the standard deviation of combined surface roughness defined as:

$$\sigma=\sqrt{\sigma_1^2+\sigma_2^2}, \tag{36}$$

and h_T is the local film thickness, which based on Figure 20 can be defined as:

$$h_T = h+\delta_{R1}+\delta_{R2}. \tag{37}$$

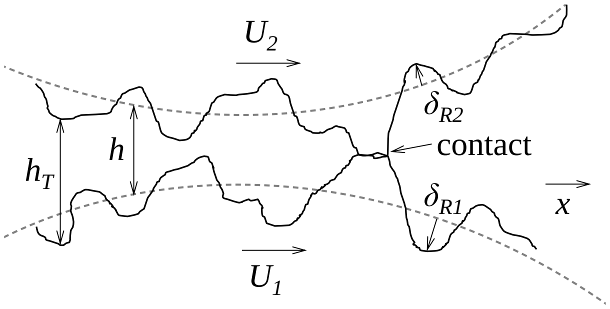

Figure 20 Rough contact interpretation [64]

Through the integration of the local film thickness for a Gaussian frequency density of roughness heights approximated by a polynomial function the mean gap separation is calculated as [65]:

$$\bar{h}_T = \begin{Bmatrix} \dfrac{3\sigma}{256}\left[35 + z\left(128 + z\left(140 + z^2\left(-70 + z^2\left(28 - 5z^2\right)\right)\right)\right)\right]; & H < 3 \\ h; & H \geq 3 \end{Bmatrix}, \tag{38}$$

where

$$z = H/3. \tag{39}$$

Due to the geometrical aspects of piston rings, namely that their diameter is much larger than their axial height, the approximation as an infinitely long slide bearing for their calculation has shown to be sufficient, as stated previously in chapter 4.9.1 [3],[22]. Therefore the 2-dimensional shape of the Reynolds equation (eq. 29) can be simplified into a 1-dimensional form by neglecting the terms in the circumferential direction:

$$\frac{\partial}{\partial x}\left(\phi_x \frac{h^3}{12\eta}\frac{\partial \bar{p}}{\partial x}\right) = \frac{U_1 + U_2}{2}\frac{\partial \bar{h}_T}{\partial x} + \frac{U_1 - U_2}{2}\sigma\frac{\partial \phi_s}{\partial x} + \frac{\partial \bar{h}_T}{\partial t}. \tag{40}$$

The resultant load bearing force acting in the lubricating layer is then determined as the integral of HD pressure developed in the wetted area of the ring profile:

$$F_{HDn} = \int_{x_1}^{x_2} p_{HD}\, dx. \tag{41}$$

To describe the directional orientation of surface roughness a surface pattern parameter (γ) was introduced by Peklenik [66], which is expressed as:

$$\gamma = \frac{\lambda_{0.5x}}{\lambda_{0.5y}}, \tag{42}$$

where $\lambda_{0.5x}$ and $\lambda_{0.5y}$ are the lengths at which the auto-correlation function of a profile reduces to half of its initial value.

Surfaces with larger correlation length in longitudinal direction $(\gamma > 1)$ enhance the lubricant flow created by the pressure difference more than smooth surfaces, therefore the pressure flow factor ϕ_x is greater than 1, Figure 21 a).

Isotropic roughness pattern $(\gamma = 1)$ restricts the pressure flow equally in both longitudinal and transverse direction, resulting in a pressure flow factor ϕ_x smaller than 1, Figure 21 b).

As the roughness pattern becomes transversely oriented $(\gamma < 1)$ the resistance against pressure flow becomes higher, which yields in a further decrease of pressure flow factor ϕ_x below 1, Figure 21 c). The relation of pressure flow factor ϕ_x to pressure flow factor ϕ_y is inversely proportional.

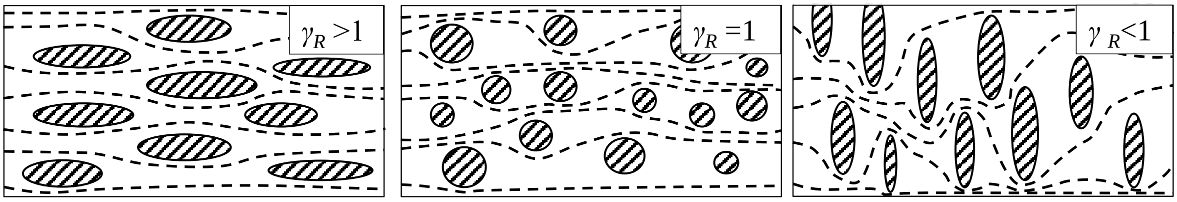

Figure 21 Surface roughness orientations [64]

For the determination of the average hydrodynamic shear stress between rough surfaces a similar approach is used, as for the previously described mean oil flow. The average shear stress after the implementation of the empirically defined shear stress factors obtains the following form [64]:

$$\bar{\tau} = \frac{\eta(U_2 - U_1)}{h}\left(\phi_f \pm \phi_{fs}\right) \pm \phi_{fp}\frac{h}{2}\frac{\partial \bar{p}}{\partial x}, \tag{43}$$

where ϕ_f is the averaged sliding velocity shear stress factor, ϕ_{fp} is the mean pressure shear stress factor and ϕ_{fs} is the shear stress factor resulting from the sliding motion of rough surfaces.

The viscous friction force acting in the oil film can be determined analogously to the normal of HD force component:

$$F_{HDf} = \int_{x_1}^{x_2} \tau_{HD}\, dx. \tag{44}$$

Empirical formulae for the calculation of flow factors are published by Patir and Cheng in [64] and [65]. Other alternative methods have been proposed, among others, by Lo [57], Tripp [76], Huang [6], and recently by Maršálek [13], [59], who presented his approach applied for both measured and generated rough surfaces.

4.9.3 BOUNDARY LUBRICATION

If the distance between the two opposing rough surfaces of a loaded bearing further decreases and the magnitude of surface roughness becomes equal to or less than the height of the lubricant film, boundary lubrication regime occurs. This lubrication regime is governed by the contact of surface roughness peaks (CT); therefore for its characterization, an asperity interaction model is needed. The most commonly used model was published by Greenwood and Tripp [48].

Their approach considers both interacting surfaces as rough, while the pairs of asperity peaks are taken as misaligned, resulting in a contact between the shoulders of the summits. According to their proposal the nominal pressure per unit area carried by the elastic deformation of the roughness contact pairs is expressed as:

$$p_{CT}(h) = \frac{8\pi}{5}(\eta\,\beta\,\sigma_s)K\,F_{5/2}(H), \tag{45}$$

where

$$K = \left(\frac{2\sqrt{2}}{3}\right)(\eta\,\beta\,\sigma_s)\,E'\left(\sqrt{\frac{\sigma_s}{\beta}}\right), \tag{46}$$

$$\frac{1}{E'} = \frac{1-\nu_1^2}{E_1} + \frac{1-\nu_2^2}{E_2}, \tag{47}$$

where σ_s is the composite summit height standard deviation, η is the surface density of asperity peaks on either surface, β is the radius of asperity summits, E' is the composite elastic modulus of the contact, while ν_1 and ν_2 are the Poisson ratios of the opposing surfaces. $F_{5/2}(H)$ is a statistical function for Gaussian distribution of the summit heights, defined by the values summarized in Table 1 [48].

Table 1 Values of the statistical function for asperity contact calculation

H	[-]	**0.0**	**0.5**	**1.0**	**1.5**	**2.0**
F5/2	[-]	0.61664	0.24040	0.08056	0.02286	0.00542

H	[-]	**2.5**	**3.0**	**3.5**	**4.0**
F5/2	[-]	0.00106	0.00017	0.00002	0.00000

For faster numerical solution it is beneficial to fit the values of Table 1 with an 8th degree polynomial. Therefore its precise value in every time step of the calculation, instead of time-consuming interpolation, can be obtained by the evaluation of polynomial equation:

$$F_{5/2}(H) = C_1 H^8 + C_2 H^7 + C_3 H^6 + C_4 H^5 + C_5 H^4 + C_6 H^3 + C_7 H^2 + C_8 H + C_9 \,, \tag{48}$$

to which Table 2 sums up the coefficients for the evaluation of the polynomial.

Table 2 Coefficients of the polynomial

Coefficient		Value
C_1	[-]	-0.000040634920635
C_2	[-]	0.000718476190479
C_3	[-]	-0.004792888888912
C_4	[-]	0.011418666666757
C_5	[-]	0.028597777777580
C_6	[-]	-0.267876333333085
C_7	[-]	0.771110746031581
C_8	[-]	-1.075215809523760
C_9	[-]	0.616639999999996

Figure 22 shows the difference between the results obtained by simple linear interpolation and the more precise polynomial approach.

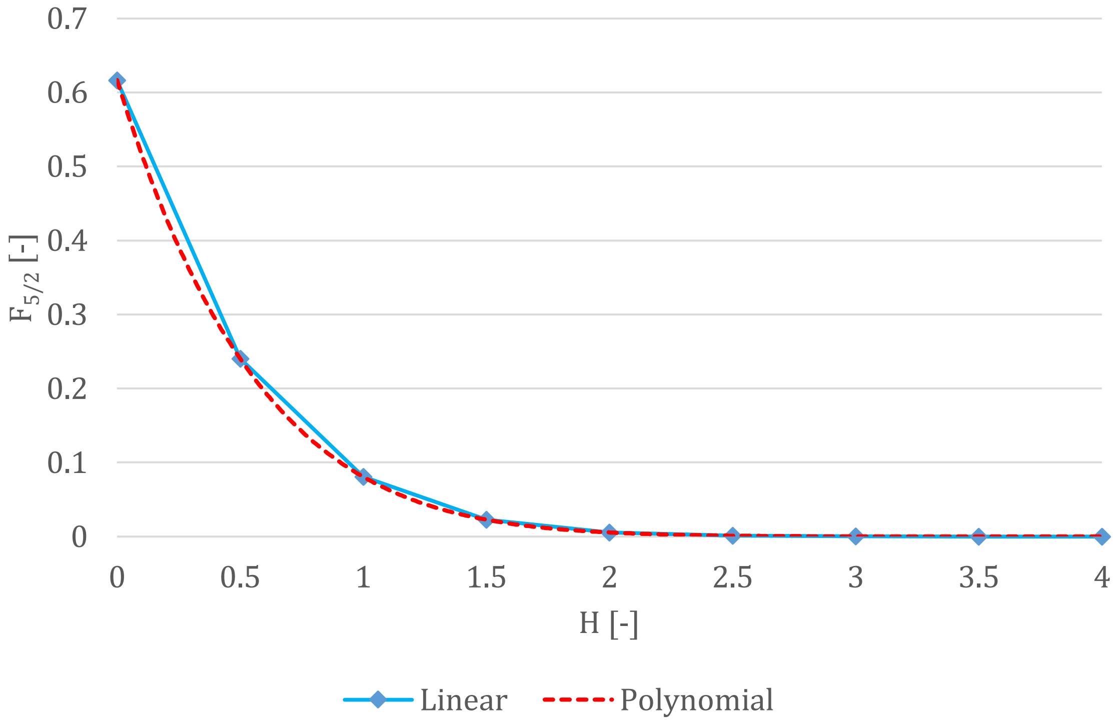

Figure 22 Comparison of linear and polynomial interpolation of the statistical function

Other, more advanced simulation approaches have been implemented in a previous work of Maršálek [13] for the determination of rough surface contact pressure at the Institute of Automotive Engineering of BUT. His simulation model is fully compatible with RingSIM, therefore the integrated CTPRESSURE function with the Greenwood and Tripp approach (G&T) can be easily substituted with one of the following contact model theories:

- contact model by Hertz [51],
- contact model by Lagemann [8] and
- contact model by Pasaribu and Schipper [63].

After the successful determination of the contact pressure between the two opposing surfaces the friction force is calculated based on Coulomb's law of friction [33]:

$$F_{CTf} = F_{CTn}\ \mu_{CT}\,, \tag{49}$$

where F_{CTn} is the normal force resulting from the contact pressure:

$$F_{CTn} = \pi\ D \int p_{CT}\ dx\,. \tag{50}$$

The coefficient of dry friction μ_{CT} for the calculation is obtained experimentally for each ring-liner contact pair separately.

4.9.4 NUMERICAL SOLUTION

For the determination of the HD pressure in the thin lubricant layer between the ring and the liner the Reynolds equation has to be solved as described in chapter 4.9.2. As it is a partial differential equation, an adequate numerical method had to be chosen for its solution. The chosen numerical method in the HDPRESSURE function became the finite difference method (FDM) with central derivative calculation, based on the following equation:

$$f'(x) \approx \frac{f(x+h) - f(x-h)}{2h}\,. \tag{51}$$

Since some of the terms of the Reynolds equation acquire very small and some again very high numerical values, it is desirable to generalize the equation by the use of a non-dimensional form. This helps to achieve a greater measure of computational stability. After introducing and substituting the following non-dimensional variables:

$$H_A = \frac{h_a}{\sigma};\ H_T = \frac{h_t}{\sigma};\ X = \frac{x}{\sigma};\ P = p\ \sigma;\ \xi = \phi_x \frac{{H_A}^3}{6\,\eta\, U_{vx}};\ \psi = \frac{U\ \Delta t}{2\,\sigma}; \tag{52}$$

equation 40 can be written in the following non-dimensional form:

$$\frac{\partial}{\partial X}\left(\xi\ \frac{\partial P}{\partial X}\right) = \frac{\partial H_A}{\partial X} + \frac{\partial \phi_s}{\partial X} + \frac{\partial H_T}{\partial \psi}\,. \tag{53}$$

After applying the above mentioned FDM, the discretized form of the Reynolds equation is as follows:

$$P_{(i)}=\frac{\xi_{\left(i+\frac{1}{2}\right)}P_{(i+1)}+\xi_{\left(i-\frac{1}{2}\right)}P_{(i-1)}}{\xi_{\left(i+\frac{1}{2}\right)}+\xi_{\left(i-\frac{1}{2}\right)}}-$$
$$\frac{\left(H_{A\left(i+\frac{1}{2}\right)}-H_{A\left(i-\frac{1}{2}\right)}+\phi_{s\left(i+\frac{1}{2}\right)}-\phi_{s\left(i-\frac{1}{2}\right)}\right)\left(\triangle X\right)}{\xi_{\left(i+\frac{1}{2}\right)}+\xi_{\left(i-\frac{1}{2}\right)}}- \tag{54}$$
$$\frac{\frac{H_t-H_{t-1}}{\partial\psi}\left(\triangle X\right)^2}{\xi_{\left(i+\frac{1}{2}\right)}+\xi_{\left(i-\frac{1}{2}\right)}}.$$

For the step-by-step derivation of equation 54, please see Appendix A.

4.10 OIL TRANSPORT MECHANISM

Analogically to the assumption that the forces acting on a ring segment at each time step of the calculation are in a quasi-static equilibrium state, the oil flow at leading and trailing edges has to meet the same balance requirement. This volumetric flow equilibrium state is calculated in the OILFLOW function. Similar mass conserving approaches were also presented by Tian [24] and Gulwadi [49].

4.10.1 FLOW BALANCE AT THE LEADING EDGE

At the leading edge of a piston ring four oil flow components have to be considered, illustrated in Figure 23:

- Oil supply from the cylinder liner.
- Oil entering the wetted area of the ring-liner contact.
- Oil flow due to the radial motion of the converging face of the piston ring.
- Oil accumulating (or depleting) at the leading edge.

In the case of oil inflow from the cylinder liner for easier understanding the liner is considered as the oil carrier moving with the instantaneous speed of the piston:

$$Q_{oil\_in}=h_{oil\_in}\,U_{vx}, \tag{55}$$

where h_{oil_in} is the oil film height on the cylinder liner and U_{vx} is the piston speed.

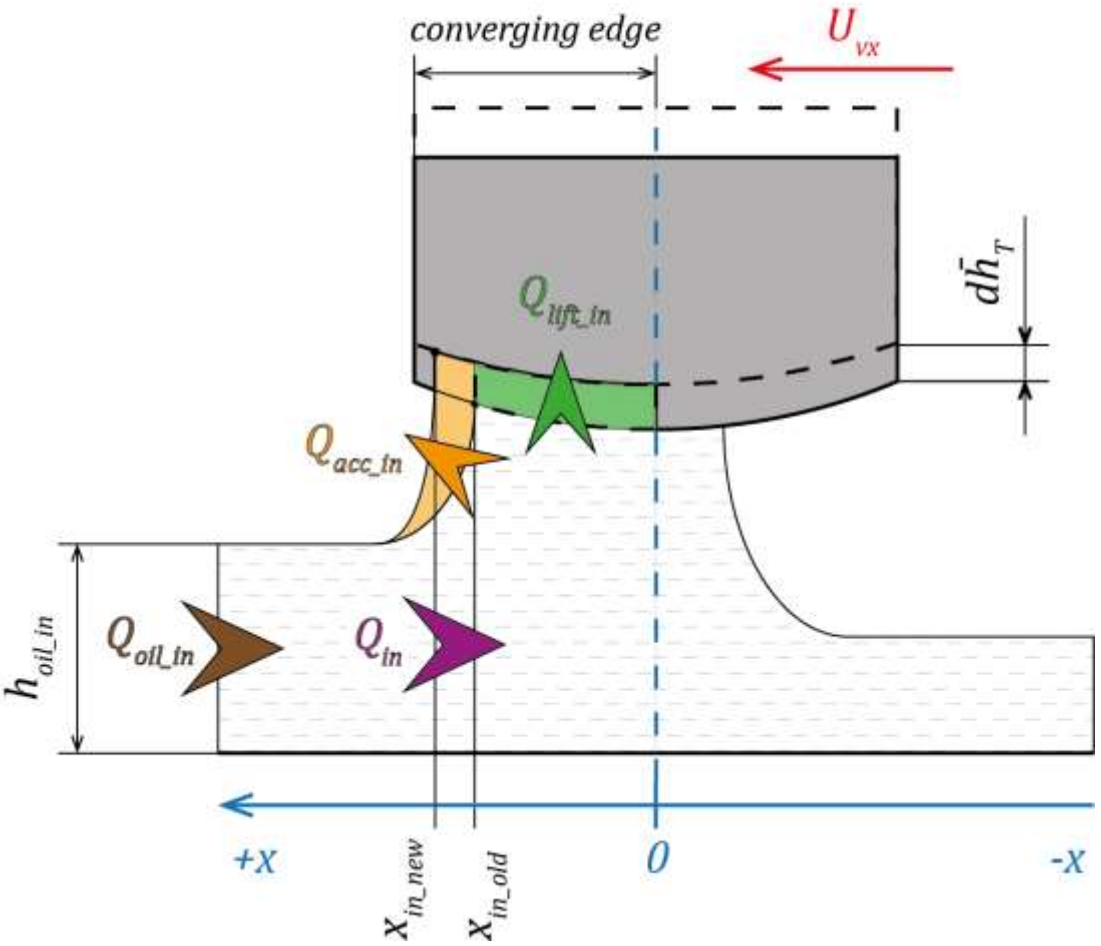

Figure 23 Oil flow components at the leading edge

In the case of oil inflow from the cylinder liner for easier understanding the liner is considered as the oil carrier moving with the instantaneous speed of the piston:

$$Q_{oil\_in} = h_{oil\_in} \, U_{vx} , \tag{56}$$

where h_{oil_in} is the oil film height on the cylinder liner and U_{vx} is the piston speed.

The oil flow entering the wetted area is determined by the relation for unit flow derived for rough surfaces by Patir and Cheng [65]:

$$Q_{in} = -\phi_x \frac{y_{in}^{\;3}}{12\,\mu} \frac{\partial \overline{p}}{\partial x} + \frac{U_{vx}}{2} y_{in} + \frac{U_{vx}}{2} \sigma \, \phi_s . \tag{57}$$

The theoretical background of this approach is described in more detail in chapter 4.9.2.

The radial motion of the piston ring is influenced by the force equilibrium state calculation. When the ring moves towards the cylinder liner it squeezes the oil out from the wetted area, serving as an inflow at the leading edge, while in other cases when the ring moves away from the liner the lubricated area draws oil into the contact area. At the leading edge flow balance however only the converging part of the wetted profile is considered, the diverging part is regarded to influence the trailing edge flow balance. This flow component can be expressed as:

$$Q_{lift\_in} = \int_{x_{in}}^{0} \frac{d\bar{h}_T}{dt}\, dx \,. \tag{58}$$

Therefore to ensure the equilibrium state of oil flows at the leading edge the accumulating oil flow has to be the difference of the two aforementioned flows:

$$Q_{acc\_in} = Q_{oil\_in} - Q_{in} \,. \tag{59}$$

This oil flow results in the change of the inlet position for the next calculation time step. Therefore the volumetric oil flow based on the current time step is transformed into accumulated volume:

$$V_{acc\_in} = Q_{acc\_in}\, dt \,. \tag{60}$$

From the obtained accumulated volume the new inlet position is calculated with the use of the Newton-Raphson iterative method described in chapter 4.5.3. Since in the present version of RingSIM the modeling approach of the rings' running face is based on the equation of an offset parabola, for the precise determination of the new inlet position due to oil accumulation at the leading edge also the parabola equation is implemented. The relation between the *x* and *y* coordinates of the new inlet position is described by equation 23. For maintaining reasonable calculation times the formula for the accumulated volume is simplified to the area of a trapezoid, which showed acceptable deviation from the area under the parabolic curve:

$$V_{acc\_in} = dx_{in} \left[\left(\frac{y_{in\_old} + y_{in\_new}}{2} \right) - h_{oil\_in} \right]. \tag{61}$$

The result could also be calculated using a built-in root finding function in Matlab, but testing has shown, that the use of the function for a cubic equation is multiple times more demanding concerning simulation time than the use of an iterative approach.

4.10.2 FLOW BALANCE AT THE TRAILING EDGE

At the trailing edge of a piston ring also four oil flow components have to be considered, shown in Figure 24:

- Oil flow in the wetted area.
- Oil flow due to the radial motion of the diverging face of the piston ring.
- Oil accumulating (or depleting) at the trailing edge.
- Oil outflow from the wetted area depositing on the cylinder liner.

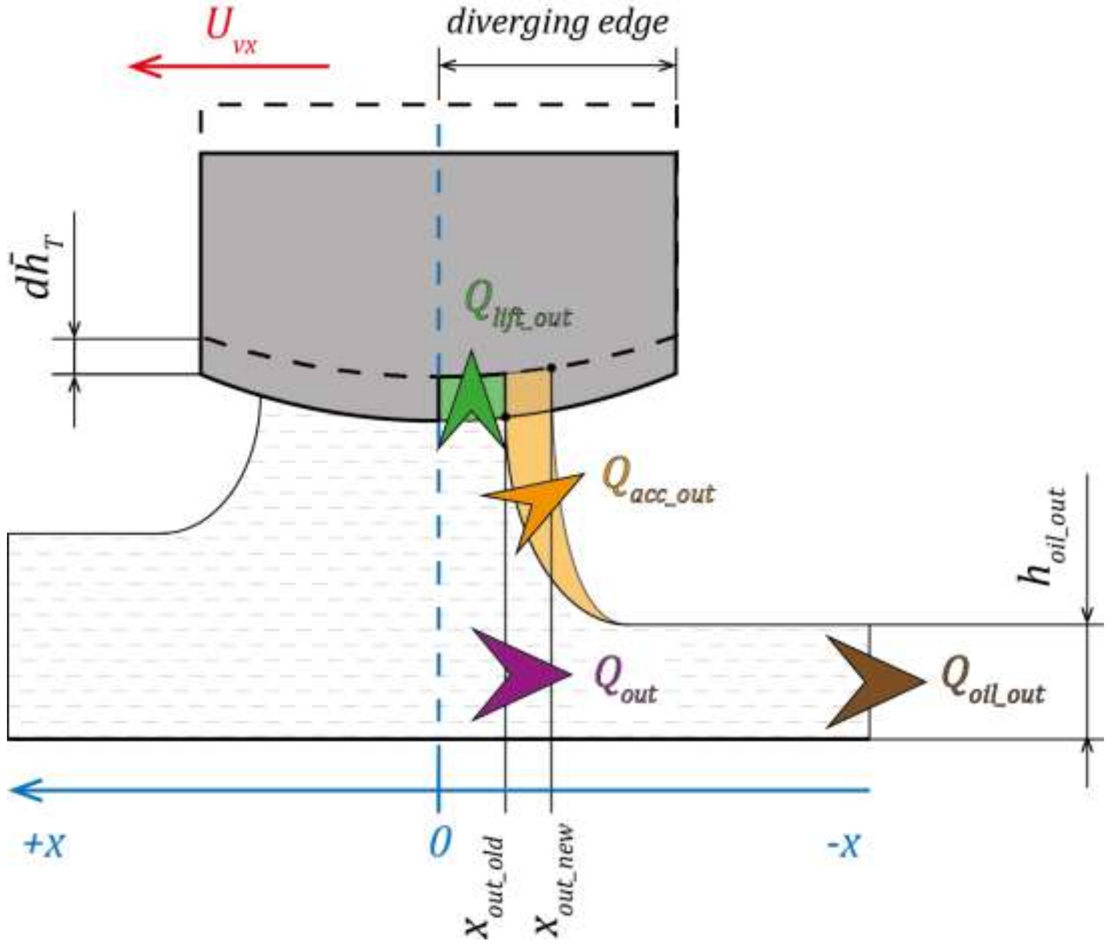

Figure 24 Oil flow components at the trailing edge

Resulting from the mass conserving assumption, the oil flowing in the wetted area is equal to the flow entering the wetted area calculated at the leading edge flow balance:

$$Q_{wet} = Q_{in} \,. \tag{62}$$

The flow induced by the ring lift is the analogy to the leading edge's lift component:

$$Q_{lift\_out} = \int_{0}^{x_{out}} \frac{d\bar{h}_T}{dt}\, dx \,. \tag{63}$$

The detachment point of the lubricant from the ring surface is determined by the HD pressure profile in the fluid layer. As described in chapter 4.9.1 in a fully developed HD lubricating regime the Reynolds exit condition is applied for the determination of the oil detachment position. This flow component is again the analogy to the change of the inlet position at the leading edge, therefore it can be written as:

$$Q_{acc\_out} = \frac{dx_{out}}{dt}\left[\left(\frac{y_{out\_old} + y_{out\_new}}{2}\right) - h_{oil\_out}\right]. \tag{64}$$

The amount of lubricant exiting the wetted area is thus the sum of the above 3 components:

$$Q_{oil\_out} = Q_{wet} + Q_{lift\_out} + Q_{acc\_out}. \tag{65}$$

The sign of each component is determined by the direction of flow, in the case of accumulation their value is negative, taking oil away from the wetted area flow, while at depletion is positive, serving as an additional oil source.

The oil height left on the cylinder liner after a ring passes can then be determined from the calculated value of oil flow exiting the lubricated area:

$$h_{oil\_out} = \frac{Q_{oil\_out}}{U_{vx} - \frac{dx_{out}}{dt}}. \tag{66}$$

With decreasing speed and/or increasing radial load from the interring gas pressures the ring is forced to move towards the cylinder liner. In these cases, the velocity driven Couette flow component of the Reynolds equation is overcome by the squeeze component resulting in an accumulation of oil at the trailing edge of the ring. The rate of the accumulation, however, is limited by the available oil supply at the trailing edge. This oil supply is composed of the flow through the wetted area and the squeeze flow from the radial motion of the ring:

$$Q_{out} = Q_{wet} + Q_{lift\_out}. \tag{67}$$

The supply, therefore, cannot be exceeded by the measure of the oil accumulation:

$$Q_{acc\_out} \leq Q_{out}. \tag{68}$$

In cases when the accumulation rate would surpass the trailing edge outflow a film non-separation exit condition replaces the Reynolds exit condition as proposed by Tian [24]:

$$Q_{acc\_out} = Q_{out}, \tag{69}$$

resulting in:

$$\begin{gathered} Q_{oil\_out} = 0, \\ h_{oil\_out} = 0. \end{gathered} \tag{70}$$

Meaning, that the whole amount of available oil at the exit accumulates in the diverging area of the ring leaving no lubricant on the cylinder liner.

When the limitation is applied to the accumulating flow a new exit position has to be calculated meeting the requirement stated by equation 69. The calculation is identical to the process described in finding a new inlet position in chapter 4.10.1. Since the change of exit condition and the variation of exit position influences the wetted profile length the HD pressure profile has to be recalculated as well. Therefore, in these cases the OILFLOW function returns the calculation with the new variables back to the beginning of the EQUILIBRIUM function. This repeats until condition written in equation 68 is met.

4.11 LUBRICATING OIL CONSUMPTION

As stated in chapter 1, lubricating oil consumption directly influences the hydrocarbon and particulate matter emissions of IC engines. Therefore precise computer simulation can help lower LOC, but simultaneously maintain sufficient oil supply for the lubrication of the piston-ring-liner tribological system.

Possible contributors to the total engine LOC, also shown in Figure 25:

- oil throw-off from the first ring and piston top land,
- oil transport to the combustion chamber in blow-back gas flow,
- oil transport to crankcase in blow-by gas flow,
- evaporation from cylinder liner wall and
- valve guide and turbocharger bearing leakage.

Valve guide leakage and oil loss from the turbochargers in case of their non-failure operation produce little contribution to the total LOC, therefore their effect can be neglected. Another aspect for their negligence is the missing source of input data for their proper computer simulation. To be able to determine the amount of oil loss from the other, major sources, correct estimation of the oil transport in the piston-rings-liner system is essential.

In RingSIM the amount of lost oil is calculated within the frame of LOC function after the equilibrium state calculation of the complete ring pack at each time step of the simulation.

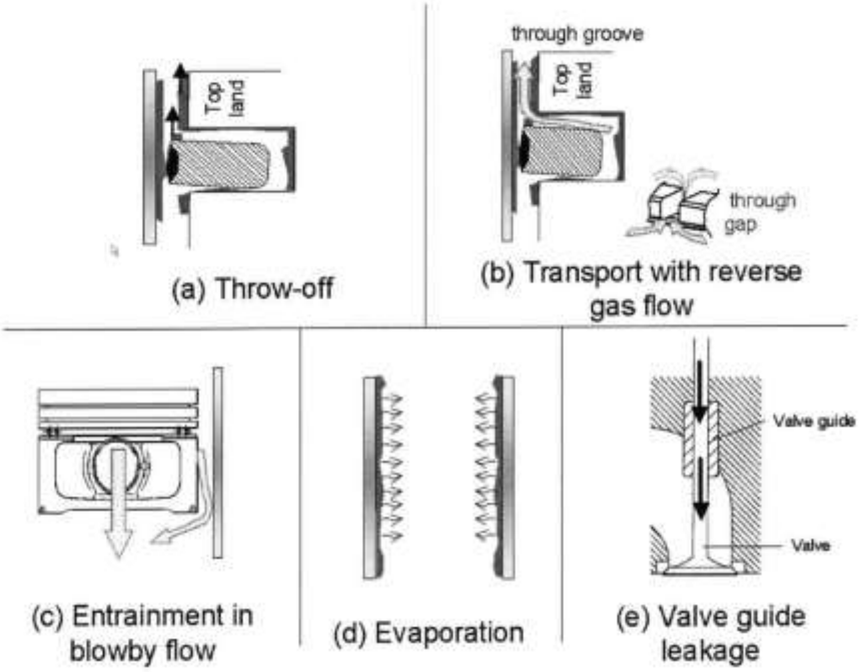

Figure 25 Oil consumption sources in an IC engine [27]

4.11.1 OIL EVAPORATION

Oil evaporation from the liner wall is assumed to be the largest contributor to total LOC at high load but low speed conditions, when during the expansion stroke the first ring sits stable on the lower ring groove flank [15]. Proven by previous experiments [78], its measure increases with loading conditions, as the liner temperature rises, and is also affected by the oil composition (volatility and viscosity).

The oil evaporation from the cylinder liner is based on the combined theory of convective mass transfer and molecular diffusion. The general turbulent flow of the cylinder charge (Flow of gas B) in close vicinity above the lubricant (Liquid A) surface creates a thin boundary layer of slowly moving oil vapor of constant thickness δ , shown in Figure 26.

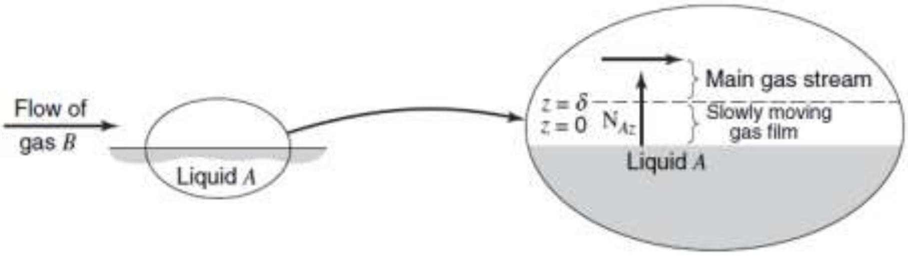

Figure 26 Character of gas flow above a liquid layer [25]

The molar mass flux at the interface between the boundary layer and the cylinder charge flow can be written in terms of convective mass transfer [25]:

$$\dot{N}_{A,z} = k_c \, \Delta c_A \, , \tag{71}$$

where k_c is the mass transfer coefficient and Δc_A is the concentration difference of lubricant vapor at the interface and in the cylinder charge stream:

$$\dot{N}_{A,z} = k_c \left(c_{A,\delta} - c_{A,\infty} \right) . \tag{72}$$

The concentration of the evaporating substance as an ideal gas can be calculated as:

$$c_A = \frac{p_A}{R_A \, T_A} \, , \tag{73}$$

where p_A is the partial pressure, R_A is the individual gas constant of the oil vapor, and T_A is the absolute temperature of the diffusing substance.

An equivalent equation to equation 74 can, therefore, be written:

$$\dot{N}_{A,z} = k_c \left(\frac{p_{A,\delta}}{R_A \, T_{A,\delta}} - \frac{p_{A,\infty}}{R_A \, T_{A,\infty}} \right) . \tag{74}$$

Since the partial pressure of the evaporating substance in the cylinder charge stream can be assumed equal to zero:

$$p_{A,\infty} = 0. \tag{75}$$

The molar flux can be simplified to:

$$\dot{N}_{A,z} = k_c \, \frac{p_{A,\delta}}{R_A \, T_{A,\delta}}. \tag{76}$$

Indexes δ denote parameter values of the oil vapor at the boundary interface, further indexed as *vapor* parameters. The equation for the calculation of the evaporated mass flow can then be written in the form:

$$\dot{m}_{evap}(t) = A_{free}(t) \frac{k_c \; p_{vapor}(s,t)}{R_{vapor} \; T_{vapor}(s,t)}, \tag{77}$$

where p_{vapor} is the partial pressure of the oil vapor at the boundary interface, R_{vapor} is the individual gas constant of the oil vapor, T_{vapor} is the temperature at the boundary interface and A_{free} is the free surface of the cylinder wall (not covered by the piston) defined as:

$$A_{free}(t) = \pi \, D \, s_{free}(t), \tag{78}$$

where D is the cylinder bore and s_{free} is the uncovered length of the oil film on the cylinder wall in the axial direction. Nomenclature is shown in Figure 27.

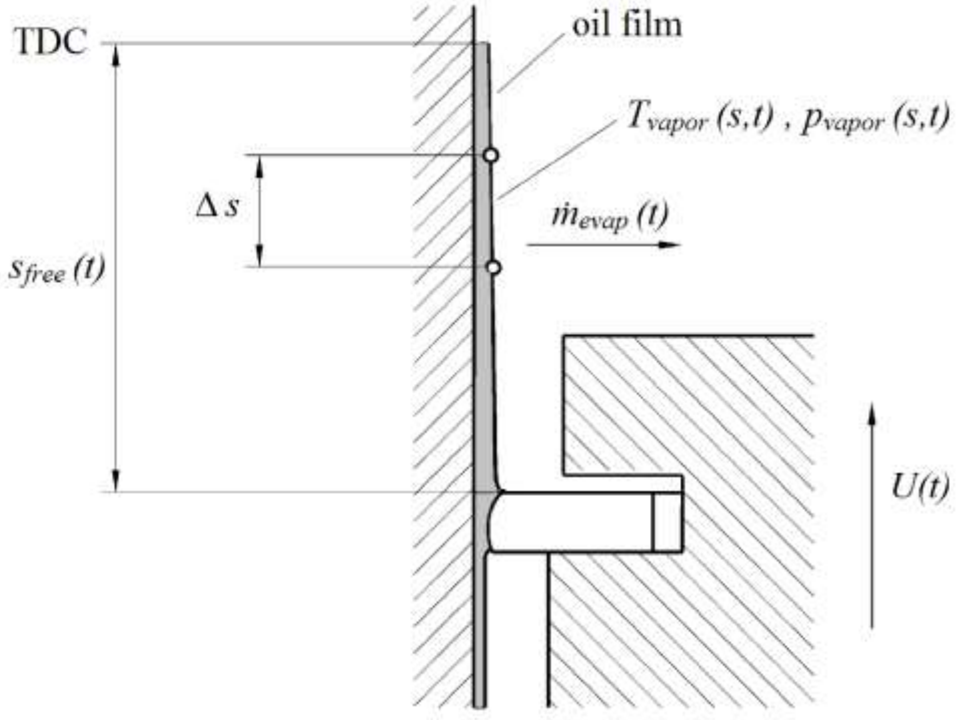

Figure 27 Nomenclature of oil evaporation mechanism from the cylinder liner [50]

Assuming the mechanism of mass transfer between the liquid lubricant and the boundary layer being pure molecular diffusion perpendicular to the surface, the molar flux can also be described by Fick's first law [21]:

$$\dot{N}_{A,z} = -D_{AB}\,\frac{dc_A}{dz}, \tag{79}$$

where D_{AB} is the mass diffusion coefficient between liquid A and gas B (mass diffusivity) and c_A is the molar concentration of the liquid vapor.

Therefore, the determination of the mass transfer coefficient can be based on the consideration that the molar flux between the lubricant and the boundary layer equals to the flux between the boundary layer and the main gas stream. In other words, the diffusive molar flux of the lubricant vapor is equal to the convective molar flux due to the flow of the cylinder charge at the boundary interface. Subsequently equating equations 74 and 81 results in:

$$k_c\left(c_{A,\delta} - c_{A,\infty}\right) = -D_{AB}\,\frac{dc_A}{dz}\,. \tag{80}$$

By rearranging and multiplying both sides by a characteristic length of L the following form arises:

$$\frac{k_c\,L}{D_{AB}} = \frac{-dc_A / dz}{\left(c_{A,\delta} - c_{A,\infty}\right)/L}, \tag{81}$$

where the right-hand side of the equation can be interpreted as a ratio of molecular mass transport resistance to convective mass transfer resistance of the lubricant. This dimensionless parameter is also referred to as the Sherwood number:

$$\mathrm{Sh} = \frac{k_c\,L}{D_{AB}} \quad \rightarrow \quad k_c = \frac{\mathrm{Sh}\,D_{AB}}{L}\,. \tag{82}$$

The Sherwood number, on the other hand, can also be expressed with empirical correlation of additional dimensionless parameters based on the flow type. Even when the main gas stream is turbulent, the flow pattern at the boundary interface is assumed to be laminar, therefore the corresponding correlation follows [25]:

$$\mathrm{Sh} = 0.664\,\mathrm{Re}^{1/2}\,\mathrm{Sc}^{1/3}\,. \tag{83}$$

Re is the Reynolds number defined as:

$$\mathrm{Re} = \frac{L\,v}{\nu}, \tag{84}$$

where ν is the kinematic viscosity and v is the flow speed of the cylinder charge, and is determined by vector superposition of the tangential (swirl) and the axial velocity of the cylinder charge flow:

$$v = \sqrt{v_{tan}^2 + v_{ax}^2}\,. \tag{85}$$

Sc is the Schmidt number defined as the ratio of kinematic viscosity to mass diffusivity:

$$\mathrm{Sc} = \frac{\nu}{D_{AB}}\,. \tag{86}$$

The mass diffusion coefficient D_{AB} is dependent e.g. on the temperature of the oil film T_{oil} and the molecular size of both the solute and the solvent. Their relation is expressed by the Stokes-Einstein equation [38]:

$$D_{AB}(s,t) = \frac{k_B\, T_{oil}(s,t)}{6\,\pi\,\nu(s,t)\,r\,f}\,, \tag{87}$$

where k_B is the Boltzmann constant, T_{oil} is the temperature of the evaporating oil, r is the hydrodynamic radius of the diffusing molecule and f is the friction factor between the diffusing molecule and the solvent fluid continuum.

The gas constant R_{vapor} is dependent on the composition of the oil:

$$R_{vapor} = \frac{R_u}{M_{oil}}\,, \tag{88}$$

where R_u is the universal gas constant and M_{oil} is the molar mass of the lubricant.

The partial pressure of the oil vapor is calculated as a function of its temperature with Antoine’s equation [28]:

$$\log_{10}\left(p_{vapor}(s,t)\right) = A - \frac{B}{T_{vapor}(s,t) + C}\,. \tag{89}$$

Parameters A, B and C can be calculated for a given type of oil by substituting known values of partial pressures at corresponding temperatures.

Characteristic values of the evaporation mechanism are mostly temperature dependent, therefore the correct determination of the temperatures of the key regions, like the liquid surface and boundary layer interface is important. The calculation is based on the theory of combined convective and conductive heat transfer, as an analogy to mass transfer. Heat from the gas stream to the lubricant is transferred by convection with the rate of:

$$\dot{q}_z = \alpha\left(T_\infty - T_{oil}\right), \tag{90}$$

where α is the heat transfer coefficient, T_∞ is the cylinder charge temperature and T_h is the temperature on the oil film surface.

The heat flux from the convective heat transfer, analogically to the mass transfer, equals to the heat flux transferred by conduction in the fluid film:

$$\dot{q}_z = -\lambda \frac{dT}{dz}, \tag{91}$$

where λ is the thermal conductivity and T is the temperature of the liquid.

By following the identical procedure as in the case of mass transfer, the heat transfer coefficient can also be expressed with the use of dimensionless parameters:

$$\alpha = \frac{\mathrm{Nu}\,\lambda}{L}. \tag{92}$$

The Nusselt number Nu is the analogy to the Sherwood number and for the laminar flow in the boundary layer can be calculated as [25]:

$$\mathrm{Nu} = 0.664\,\mathrm{Re}^{1/2}\,\mathrm{Pr}^{1/3}. \tag{93}$$

The Reynolds number Re is determined as stated previously in equation 86, while the Prandtl number is the analogy to the Schmidt number, expressed as:

$$\mathrm{Pr} = \frac{\nu}{\kappa}, \tag{94}$$

where κ is the thermal diffusion coefficient (thermal diffusivity):

$$\kappa = \frac{\lambda}{\rho\, c_p}. \tag{95}$$

Substitution of equation 97 into 96 leads to:

$$\mathrm{Pr} = \frac{\eta\, c_p}{\lambda}, \tag{96}$$

where η is the dynamic viscosity and c_p is the constant pressure heat capacity.

The thermal conductivity of hydrocarbons can be determined using the empirical formula of [32], [25]:

$$\lambda = 418.4 \times 10^{-4}\left(333 - 0.19\,T\right), \tag{97}$$

where T is a temperature in [°C].

With the use of the above assumptions and relations the temperature of the oil surface in dependence on axial height and time can be expressed as:

$$T_{oil}(s,t) = \frac{\dfrac{\lambda_{oil}(s,t)\,T_{cyl}(s,t)}{h_{oil}(s,t)} - \alpha_{gas}(s,t)\,T_{gas}(t)}{\dfrac{\lambda_{oil}(s,t)}{h_{oil}(s,t)} - \alpha_{gas}(s,t)}. \tag{98}$$

The temperature of the oil vapor at the boundary interface is considered as the arithmetic mean between the oil surface temperature and the cylinder charge temperature [25]:

$$T_{vapor}\left(s,t\right)=\frac{T_{oil}\left(s,t\right)+T_{gas}\left(t\right)}{2}\,. \tag{99}$$

Nomenclature of the mechanism is shown in Figure 28.

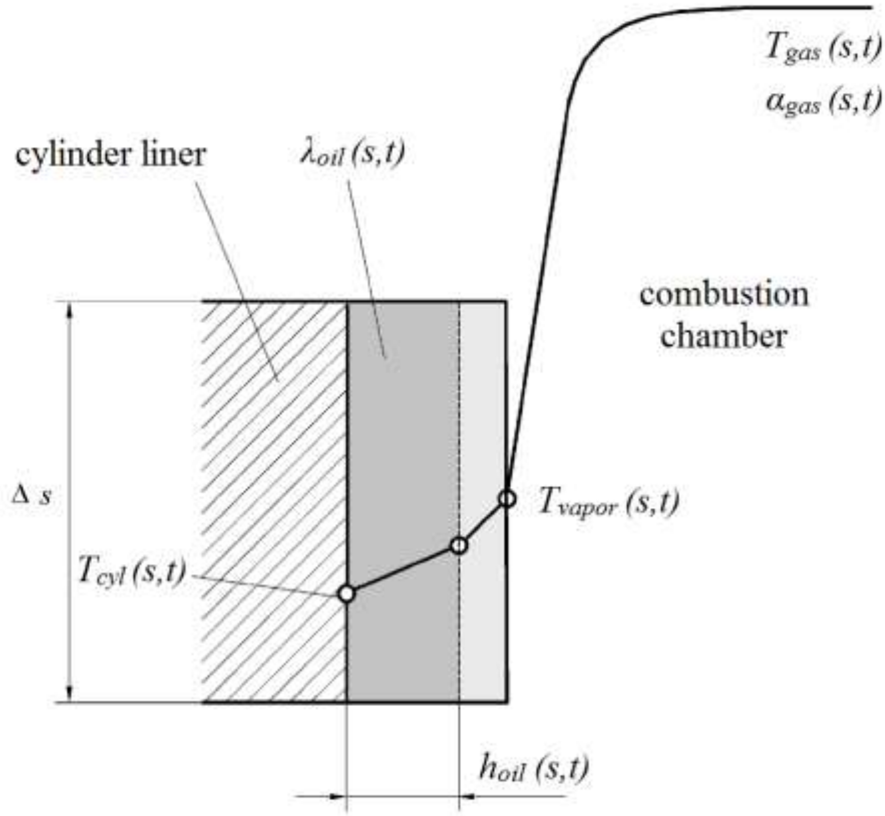

Figure 28 Nomenclature of the heat transfer mechanism [50]

4.11.2 OIL THROW-OFF

While at low speed but high load operating conditions the oil evaporation is the dominant contributor to the total oil consumption, then at low load but high speed condition the oil loss from the piston top land area and from above the first compression ring is the greatest contributor [15].

The amount of thrown-off oil into the combustion chamber can be calculated depending on the measure of inertia forces acting towards the combustion chamber resulting from the deceleration of the piston due to its reciprocating translational motion in the cylinder. The evaluated volume of oil to be potentially lost due to throw-off is the accumulated volume sitting on the leading edge of the compression ring. This volume is divided into *n* layers, considering uniform velocity and deceleration within each layer, as shown in Figure 29.

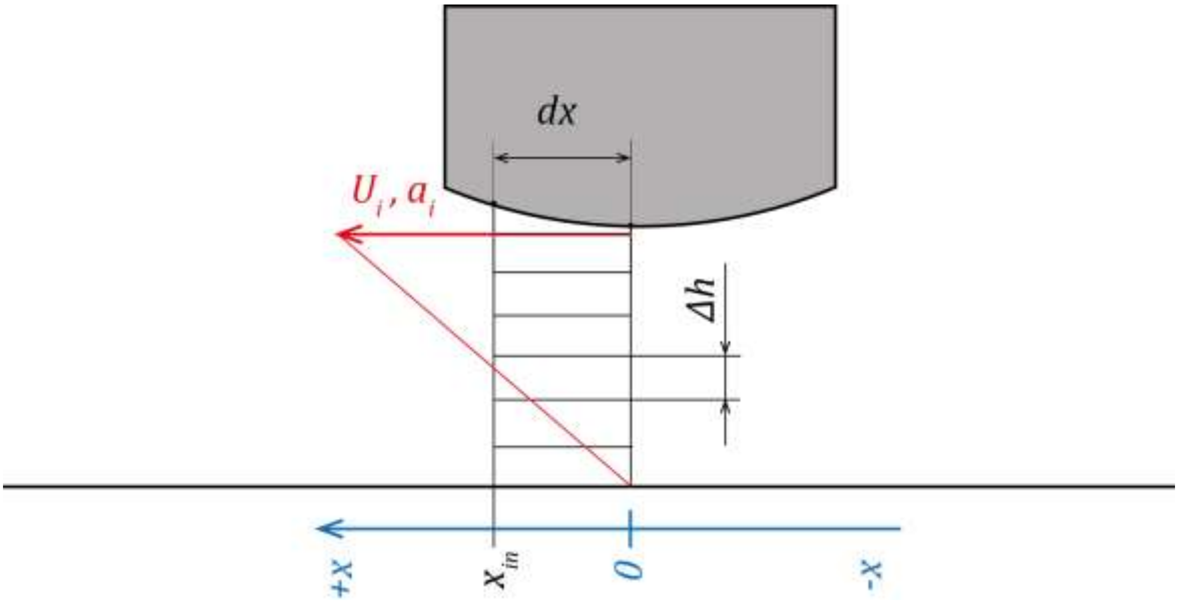

Figure 29 Nomenclature of the oil throw-off mechanism

The boundary conditions at the cylinder liner and piston ring surface due to the no-slip consideration are considered to be identical to the surfaces' conditions, with linear velocity profile in-between. During the deceleration of the piston inertia forces are acting on each liquid layer:

$$F_{inertia,i} = \int a_i \, \rho_{oil} \, \Delta h \, dx \,. \tag{100}$$

On the other hand, viscous friction force is present between the adjacent layers:

$$F_{visc,i} = \int \eta \, \frac{U_i - U_{i+1}}{\Delta h} \, dx \,. \tag{101}$$

In every time step of the calculation, the value of inertia force acting on each layer and the corresponding viscous friction force acting between adjacent layers is compared. Once the inertia force of a layer overcomes the viscous friction, oil starts flowing into the combustion chamber from the given layer with a mass flow rate of:

$$\dot{m}_{throw,i}\left(t\right) = \pi \, D \, \rho_{oil} \, \Delta h \, u_i\left(t\right). \tag{102}$$

The maximum amount of oil thrown off into the combustion chamber however cannot exceed the available volume of accumulated lubricant on the leading edge:

$$\frac{\sum_{i=1}^{n} \dot{m}_{throw,i}}{\rho_{oil}} \Delta t \le V_{acc\_in} \,. \tag{103}$$

For the accumulated oil at the leading edge of the ring, the undesired scraping ability of the first compression ring during the upward strokes could be accounted. The volume of the accumulated oil can be calculated from the oil flow balance on the leading edge described in chapter 4.10.1:

$$V_{acc\_in} = \pi\, D \int_{BDC}^{TDC} Q_{acc\_in}\, dt\,. \tag{104}$$

4.11.3 OIL FLOW DUE TO GAS BLOW-BACK

Under conditions, when the pressure in the combustion chamber is lower than in the first interring area, the direction of the gas flow changes. This flow results in an undesired transport of the lubricant into the combustion chamber. Previous investigation [58] has shown that the amount of entrained oil through the piston ring gap does not accumulate in the top land area, but is subject to immediate oil loss. For the determination of the amount of the lost lubricant due to this phenomenon the following equation is ought to be used [27]:

$$\dot{m}_{blow}\left(t\right) = \dot{m}_{gas}\left(t\right) \frac{3\,\eta_{gas}\, h_{oil}^{2}}{\eta_{oil}\, h_{gas}^{2}}\,, \tag{105}$$

where $\dot{m}_{gas}$ is the gas blow-back flow, h_{oil} is the average height of the oil film in the area between the first and second piston ring, complemented by h_{gas}, the average height of the gas layer above the oil film in the same region, graphically interpreted in Figure 30.

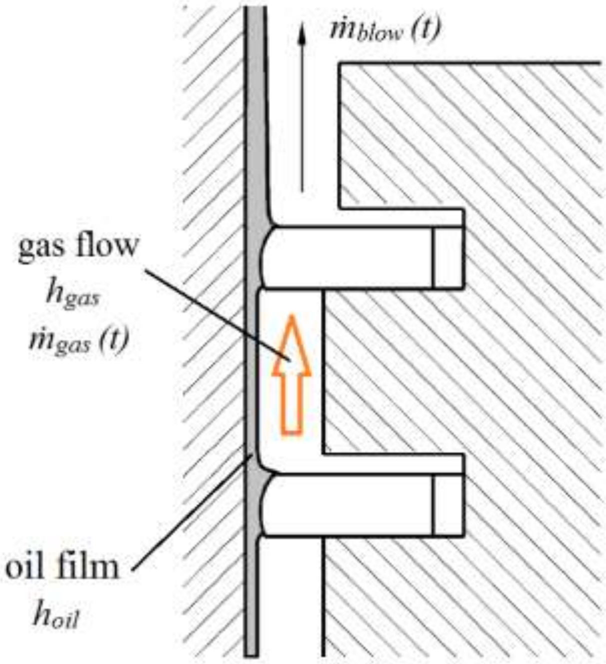

Figure 30 Nomenclature of the oil entrainment mechanism

4.12 DATA HANDLING

Resulting from the strive to develop a source code which is on the one hand compact and universal in the way of accommodating different input data, but on the other hand transparent and understandable for other users or programmers, auxiliary data handling functions have also been created. These functions are intended to load, save or evaluate selected variables to ensure proper running of the simulation tool.

The first function of this type is the PREPROCESS function, which based on the actual ring number and crank angle loads the corresponding values to the appropriate local workspace variables, which are then passed on to the EQUILIBRIUM function. As described in chapter 4.2, input data are stored in global structural variables, which would make data selection complicated and not transparent if done inside the calculation cycle, therefore, the task of a data preprocessing function is more than desirable. Besides selecting the relevant data for the corresponding ring, also incorporates and executes sub-functions e.g. for the determination of input oil film height on the cylinder liner (OILHEIGHT), or the calculation of oil viscosity (OILVISC) based on the current crank angle.

With similar intentions has been the POSTPROCESS function, which reads all the outputs of the current calculation step of the EQUILIBRIUM function, and based on the ring number and crank angle saves them into the appropriate global variables, including the ones for result evaluation and debugging purposes.

After the calculation of the complete ring pack at a single crank angle, the TERMINATE function is called, which updates the oil film height database for each ring and checks for specific crank angles, like the dead centers and work cycle ends. In case the end of a work cycle (2 revolutions for a 4 stroke engine) is detected, the termination criteria for the complete simulation is evaluated. The termination criteria for the calculation algorithm is the relative deviation of the minimum oil film height of each piston ring at the end of a work cycle (at crank angle 720°):

$$\Delta_n = \left| \frac{h_{\min n}(i) - h_{\min n}(i-1)}{h_{\min n}(i)} \right|, \tag{106}$$

where index n denotes the ring number and index i is the current computation cycle number.

Successful convergence is achieved when the relative deviation falls below the required margin for every piston ring simultaneously. After meeting this condition RingSIM steps out of the calculation cycle.

For the evaluation of the calculated data and displaying purposes, a final data handling function is run. The RESULTS function creates a new global structural variable, where only the key parameters are saved from the converged engine cycle, each ring separately. All the other local workspace variables get deleted to maintain an organized and transparent environment after the termination of the simulation.

5 EXPERIMENTAL SETUPS

One of the main goals of this dissertation thesis was the experimental validation of the simulation model. Therefore, based on the possibilities, a key parameter was chosen for validation: the amount of volumetric gas flow through the piston assembly towards the crankcase, also known as blow-by. Besides the validation process, other experiments and measurements have been conducted to obtain engine and component specific input data into the simulation tool.

5.1 FIRED ENGINE MEASUREMENT

Measurements on a fired engine had been carried out on a production inline three cylinder spark ignition engine. Basic parameters of the engine are listed in Table 3.

Table 3 Test engine parameters

Engine Type	**Škoda EA111**
Configuration	Inline 3
Valvetrain	DOHC 6V
Displacement	1198 cm^3
Bore	76.5 mm
Stroke	86.9 mm
Compression Ratio	10.3 : 1
Rated Power	44 kW @ 4750 rpm
Torque	118 Nm @ 3000 rpm

The main reason for choosing the subject engine was its success and popularity in small passenger cars of the Volkswagen concern, therefore the measured and calculated results can be considered applicable to largely used engine type.

Tests have been conducted in the laboratory of the Institute of Automotive Engineering at BUT. The engine was mounted to a Superflow SF-902S water brake power absorber engine dynamometer, complemented with a Superflow CT-700 pressurized cooling tower and an AVL Dynamic Fuel Meter. Technical specifications of the measurement devices are listed in Appendix B. The steady state test load conditions were defined on the basis of the speed-torque curve at 100% load, which was acquired with the use of the automated data acquisition system of the dynamometer, WinDyn. To cover a wide range of engine operating conditions, the engine speed was defined from 2500 rpm to 5000 rpm with 500 rpm increments. Load states were specified as 25%, 50%, 75% and 100% of the maximum power at given engine speed. Resulting load state data are shown in Table 4 and Figure *31*.

Table 4 Tested steady state engine operating conditions – values

Power	2500	3000	3500	4000	4500	5000
25%	7.25	9.25	10.00	10.75	11.00	10.25
50%	14.50	18.50	20.00	21.50	22.00	20.50
75%	21.75	27.75	30.00	32.25	33.00	30.75
100%	29.00	37.00	40.00	43.00	44.00	41.00

The complete wide-open-throttle (WOT) power curve is displayed in Appendix C.

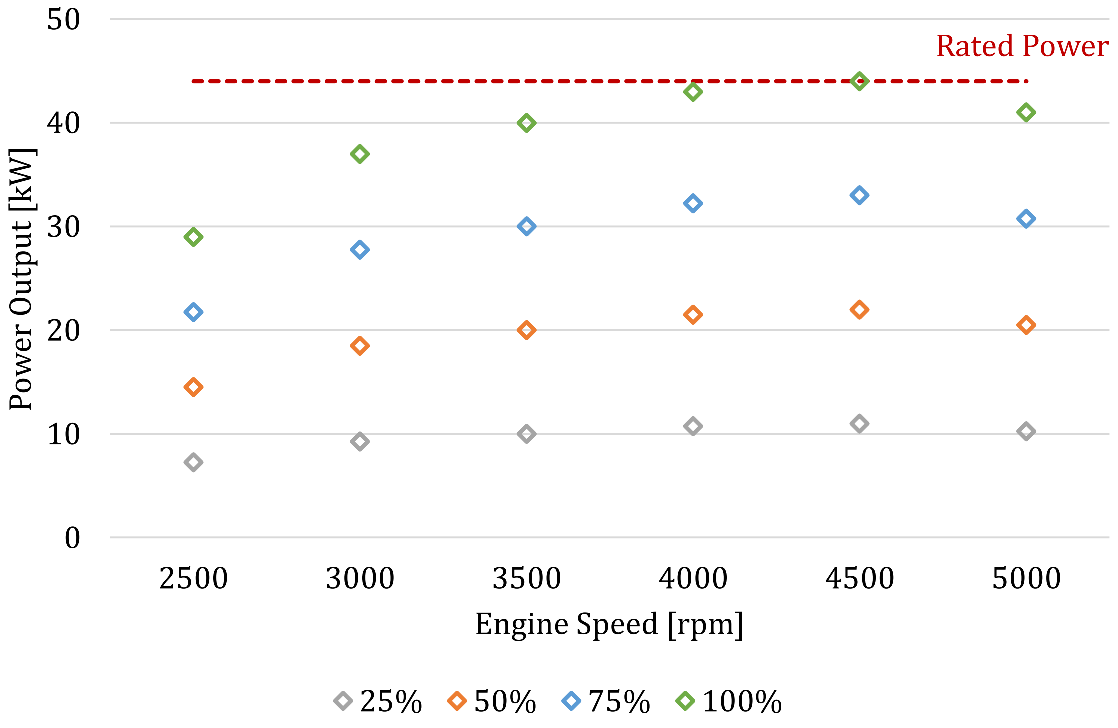

Figure 31 Tested steady state engine operating conditions – graph

For the measurement of the amount of volumetric gas flow through the piston assembly towards the crankcase, an AVL Blow By Meter has been mounted in the place of the crankcase ventilation system. This measurement device is specially designed for this application, thus is capable of measuring gas flows containing solid particles, oil droplets, and vapors. The measuring principle is based on an orifice measurement principle, where a pressure drop is measured on a neck inside the device by a differential pressure sensor, interpreted in Figure 32. Technical specifications of the measurement device are listed in Appendix B.

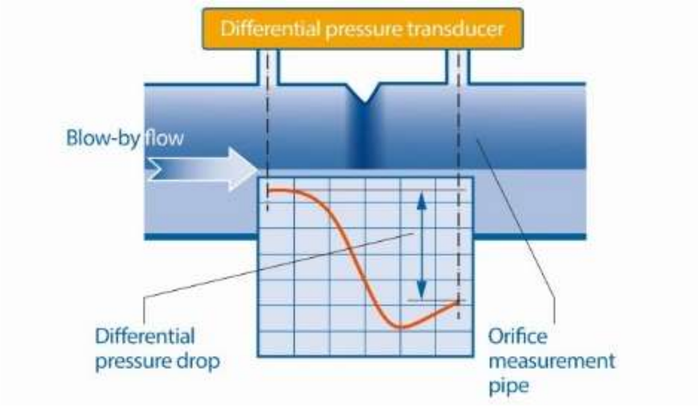

Figure 32 Measurement principle of the blow-by flow [85]

A difficulty, which could be encountered in blow-by measurement is the flow pulsation. It origins from two sources, firstly it is the pressure oscillation in the combustion chamber and secondly, it is the reciprocating motion of the piston. Although in a multi-cylinder engine, the flow pulsation is almost entirely compensated by the mutual motion of the pistons, it still has to be eliminated. To dampen the oscillations on the measuring device, an accordingly designed acoustic filter had to be integrated between the engine and measuring device. The dampener consisted of a compensation volume and connecting pipelines as shown in Figure 33.

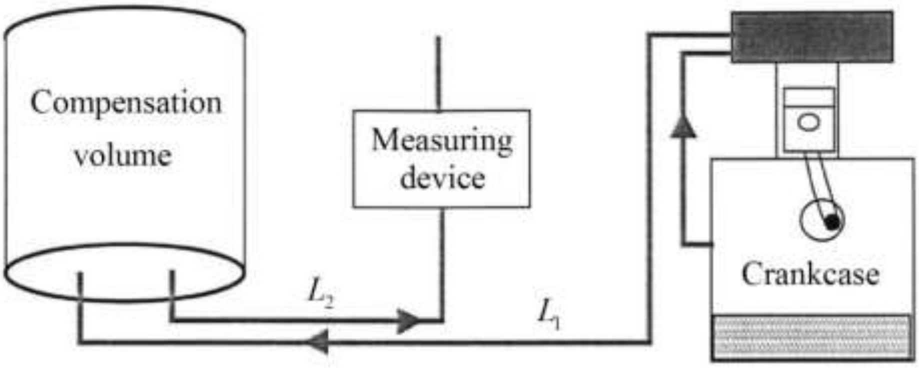

Figure 33 Blow-by measurement configuration scheme [23]

The measured values of volumetric blow-by gas flow in liters per minute are listed in Table 5.

Table 5 Measured results of volumetric gas flow through the piston assembly – values

Power	2500	3000	3500	4000	4500	5000
25%	N/A	N/A	N/A	N/A	N/A	N/A
50%	4.414	3.918	2.583	2.729	3.207	2.106
75%	8.089	6.241	6.102	5.993	5.256	3.484
100%	12.204	9.763	10.548	10.166	8.287	5.593

As can be seen from the previous table, at the lowest partial load – at 25% – the amount of gas flow did not reach the lower margin of the device's measuring range, therefore results for these running conditions were not possible to be obtained.

The accuracy of the AVL Blow By Meter is stated by its manufacturer as up to 1.5% of the full-scale output (FSO), which in this case was 150 l/min. Therefore, the systematic error for the measurements is up to ±2.25 l/min for every steady state measurement point.

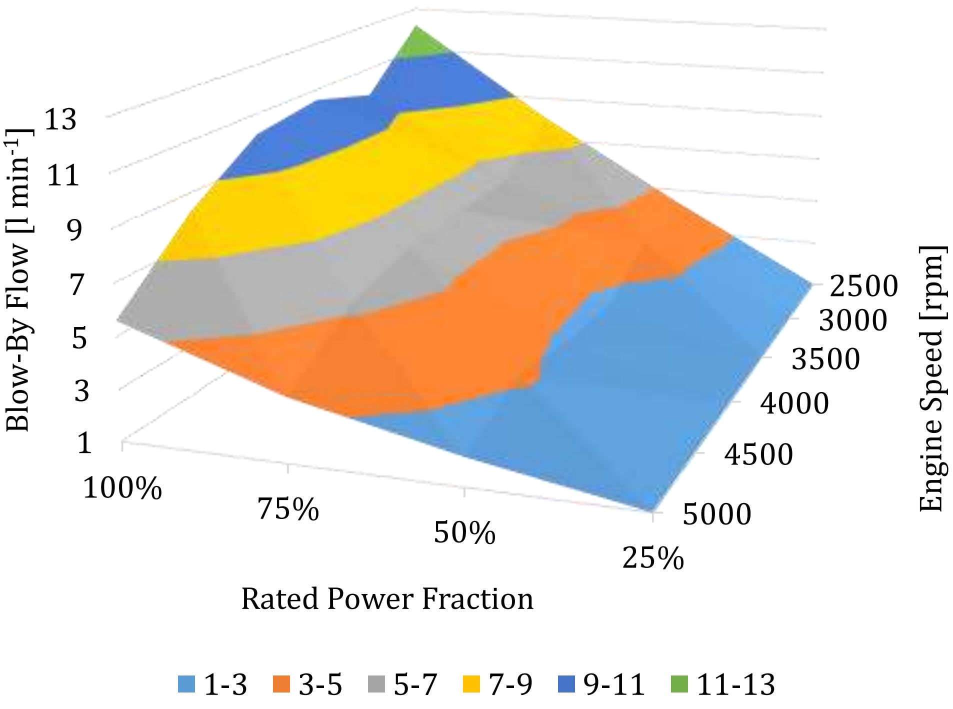

Figure 34 Measured results of volumetric gas flow through the piston assembly – graph

The course of values through the engine speed range is shown in Figure 34. It confirmed the theoretical assumptions that with increasing speed the amount of blow-by flow decreases. This could be explained by a shorter time available for the gases to make their way through the piston assembly, and also by the decreasing magnitude of combustion pressures with increasing engine speed.

Besides the experimental determination of the combustion gas flow used for the validation of the calculated results, other operating parameters of the running engine were measured, which served as input parameters of the simulation model. One of these parameters was the pressure in the combustion chamber in dependence of the crank angle, which was obtained with the use of a measuring spark plug supplemented by a crank angle encoding kit, both from Kistler. As in previous cases, their technical data are listed in Appendix B. The resultant combustion pressure profile for each steady state operating condition was created by the automated data logging system supplied for the Kistler products, by averaging 100 consecutive engine cycle data. Sample results for 2500 rpm are shown in Figure 35, while complete results for all engine speeds and loading conditions can be found in Appendix E.

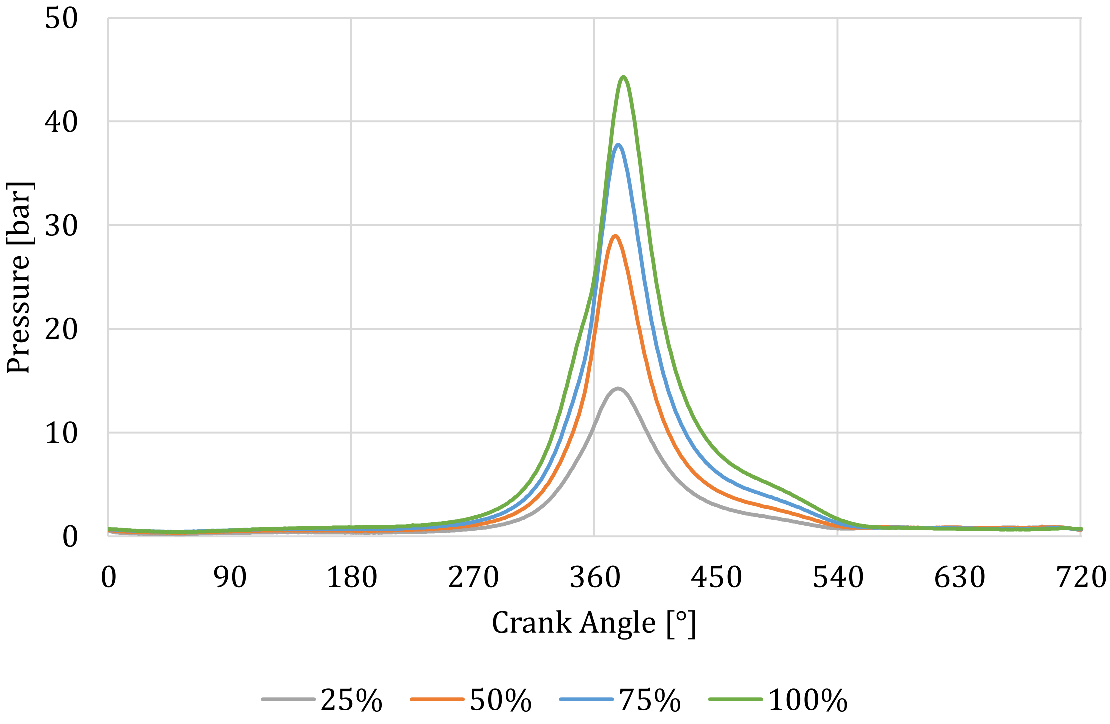

Figure 35 Measured combustion chamber pressures at 2500 rpm

Other measured operating parameters of the firing engine were the pressures in the intake manifold. The results for all running conditions are shown in Figure 36.

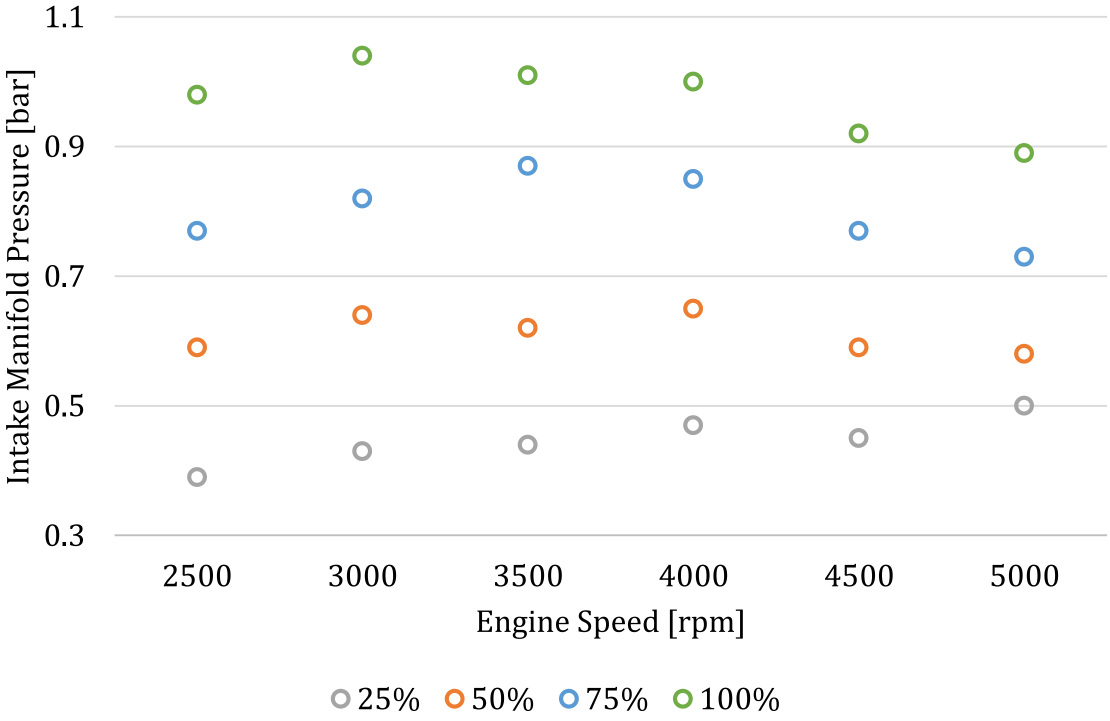

Figure 36 Intake manifold pressures at measured operating conditions

With the use of the measured parameters and a simulation tool created at the Technical University of Liberec within the frame of project Josef Božek Research Center of Engine and Automotive Engineering, the temperature distribution of the cylinder liner surface along the piston stroke was calculated for all operating conditions. Sample results for 2500 rpm are shown in Figure 37, while complete results for all engine speeds and loading conditions can be found in Appendix F.

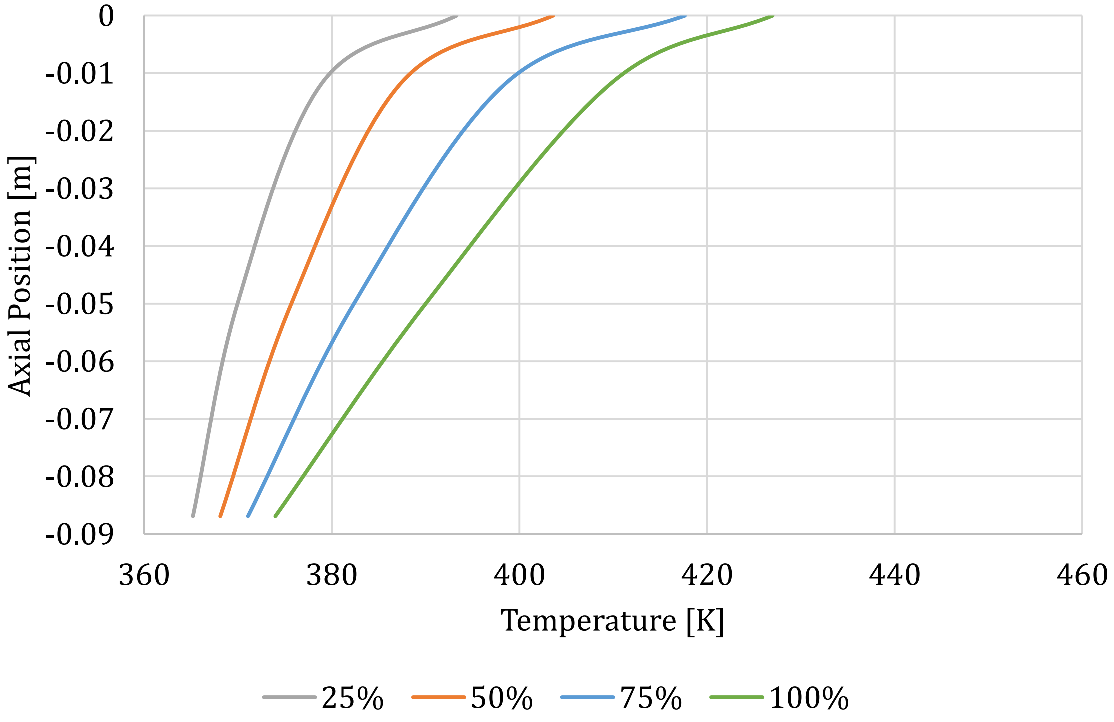

Figure 37 Calculated temperature distribution along the cylinder liner at 2500 rpm

The same simulation tool allowed the determination of the temperature variation of the cylinder charge as well. The change of temperature inside the combustion chamber shows little dependence on the engine speed, therefore the course of cylinder charge temperature is considered to vary only with different load states, not engine speed. The calculated values are shown in Figure 38.

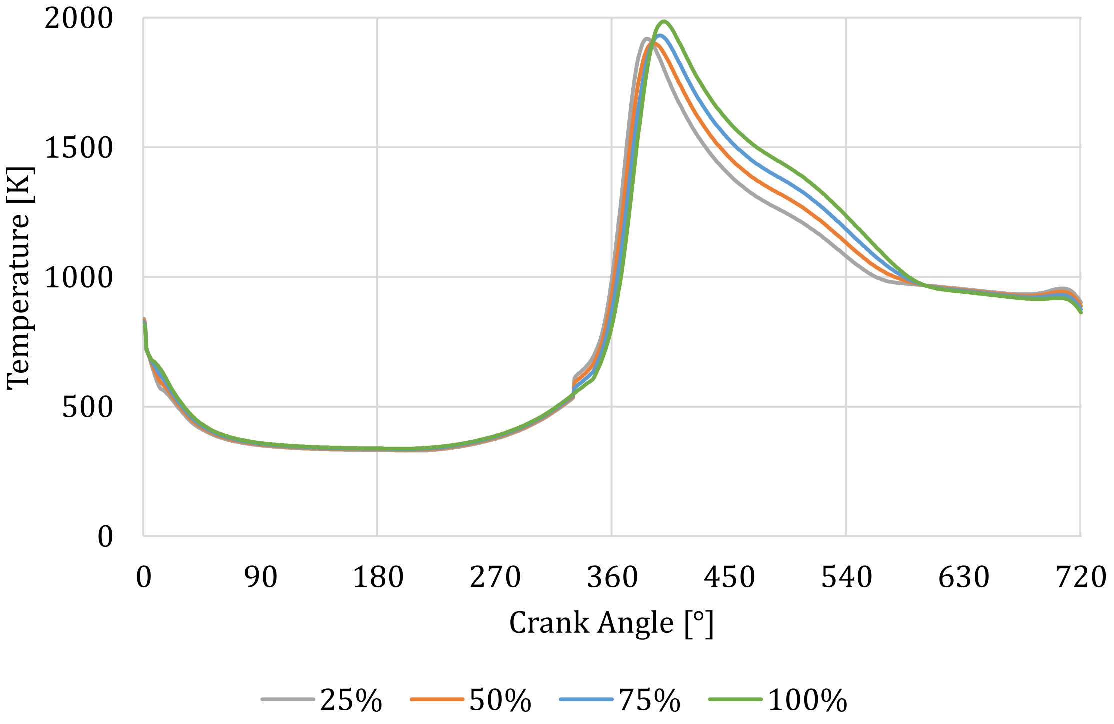

Figure 38 In-cylinder temperature variation

5.2 REAL SURFACE STRUCTURE

Every technological process of surface treatment or surface finish has its characteristic surface topography, roughness directional orientation, and descriptive parameters. Moreover, these characteristic marks significantly change during the lifecycle of an engine component, which is almost impossible to virtually simulate. Therefore the most accurate method of their inclusion in the simulation algorithm is via the experimental evaluation of their real surface structure. For this purpose, a Bruker ContourGT-X optical microscope had been utilized, which allowed the 3D inspection of the surface profile of both the cylinder liner and the piston rings as well. The measurement principle is based on a non-contact method of optical interferometry. Basic technical data of the optical profilometer are listed in Appendix B.

As for the geometry of the piston rings, worn profiles are modelled, then for the surface parameters determination worn piston rings and the corresponding worn cylinder liner were used, however, the exact number of their previous running hours were not known.

For the surface inspection lens type IX20 was used, which gave an effective sampling area of 0.3137 × 0.2352 mm at a resolution of 640 × 480 pixels and pixel size of 4.9×10^{-7} m. Each component had been measured five times at five different spots, the resultant values are the averaged values of the five measurements. Besides the matrix of asperity heights, other descriptive parameters of surface roughness were chosen to be obtained from the measurement, based on the input parameters entering the Greenwood and Tripp contact pressure calculation module. These parameters include:

a) The root mean square of asperity heights [13]:

$$Sq = \sqrt{\frac{1}{A}\iint_A z^2(x,y)\,dx\,dy}\,. \tag{107}$$

The corresponding G&T parameter is the composite summit height standard deviation:

$$\sigma_s = \sqrt{Sq_1^2 + Sq_2^2}\,. \tag{108}$$

b) The density of surface summits:

$$Sds = \frac{Number\ of\ summits}{Area}\,. \tag{109}$$

c) The mean summit curvature [13]:

$$Ssc = -\frac{1}{2n}\iint_A \left(\frac{\partial^2 z(x,y)}{\partial x^2} + \frac{\partial^2 z(x,y)}{\partial y^2}\right) dx\,dy\,. \tag{110}$$

The corresponding G&T parameter is the radius of asperity summits:

$$\beta = \frac{1}{Ssc}\,. \tag{111}$$

Besides the statistical descriptive surface parameters entering the G&T calculation another element to consider for surface roughness characterization is the directional orientation of surface texture. This feature affects the flow of lubricating oil in the contact area, as the directional orientation directly impacts the flow factors. The best way to describe the directional dependence of surface roughness is through the analysis of its areal autocorrelation function (*AACF*). The key descriptive parameter is the Peklenik number – γ, introduced in chapter 4.9.2. As the calculation of the *AACF* and the determination of the Peklenik number of a rough surface was one of the main goals of the dissertation thesis of Maršálek [13], his source code was utilized for the detection of these parameters.

Further, to allow the investigation of the influence of wear on the lubrication and asperity contact between the ring pack and the liner, unworn ring and liner surfaces had also been scanned. Test specimens of cylinder liners were supplied by the engine manufacturer, Škoda Auto, while the ring pack by the piston ring manufacturer, Buzuluk. Their support is greatly appreciated.

Sample images of a 3D scanned worn and unworn cylinder liner topography are shown in Figure 39 and Figure 40, respectively. Images have been cropped to 480 × 480 gridpoints.

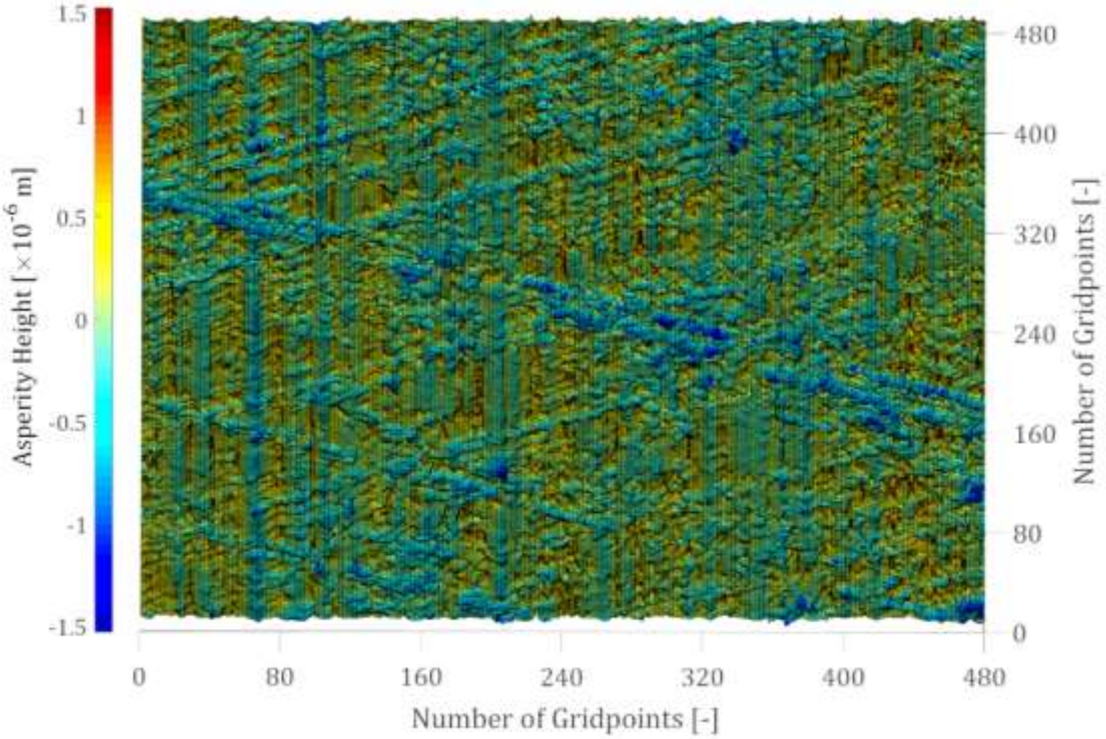

Figure 39 Surface topography of a worn cylinder liner

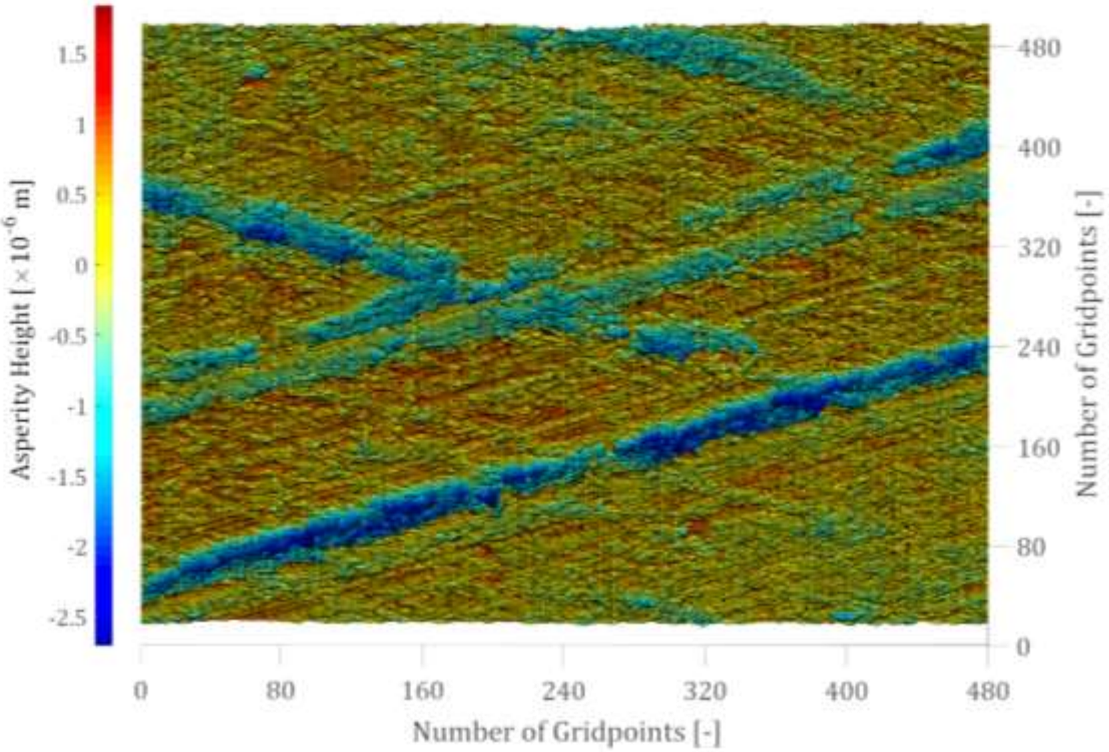

Figure 40 Surface topography of an unworn cylinder liner

From the surface topographies is visible, that the honing grooves are more noticeable on the unworn surface, while the worn surface is smoothed out from the marks of this technological operation, but already carries signs of abrasive wear in the form of low-amplitude and dense axial (vertical) grooving.

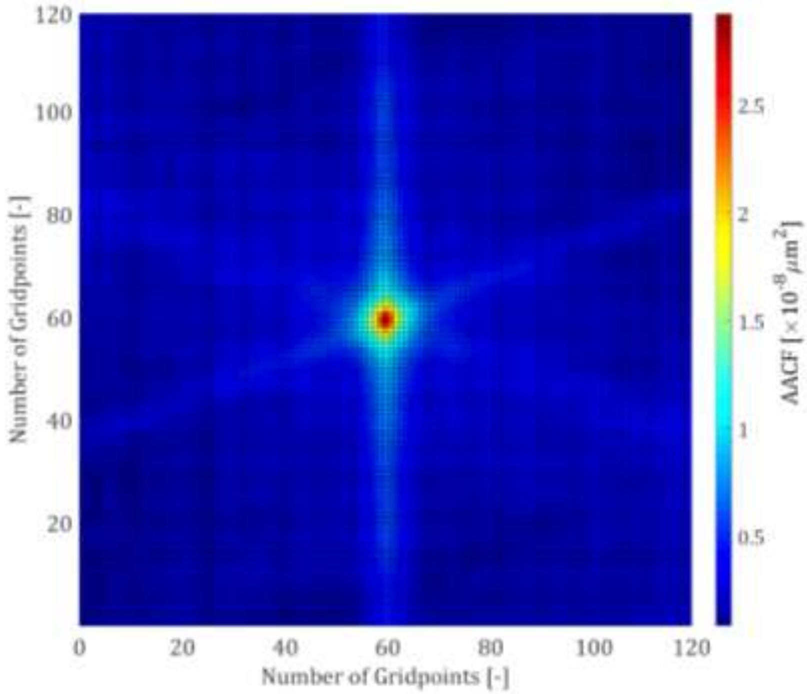

Figure 41 Areal autocorrelation function of the worn cylinder liner surface

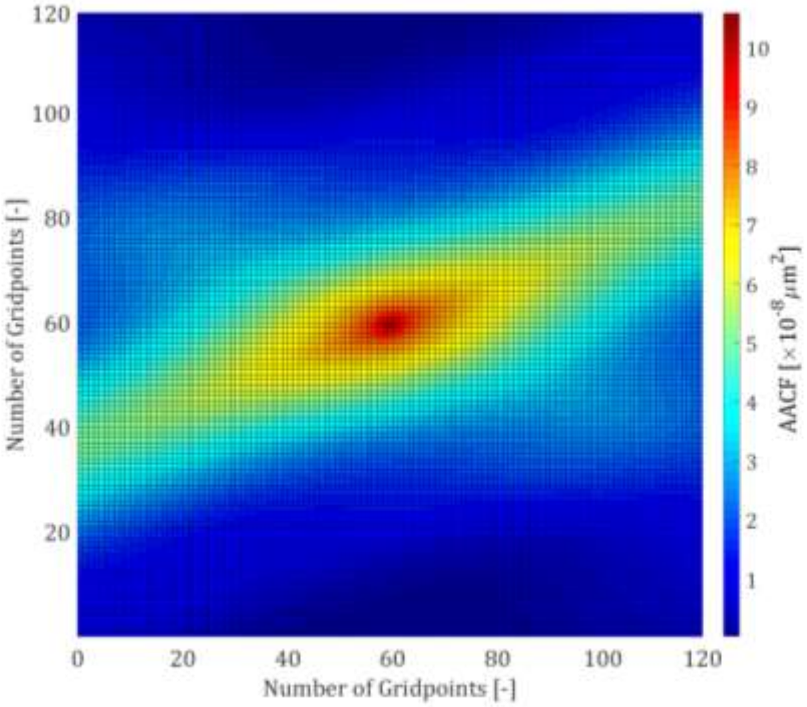

Figure 42 Areal autocorrelation function of the unworn cylinder liner surface

The hypotheses about the directional orientations are proven by the courses of both *AACF*, shown in Figure 41 and Figure 42. In the case of worn cylinder liner the function shows slight (almost isotropic) longitudinal orientation in the direction of piston motion and oil flow, while in the case of unworn cylinder liner a strong transversal orientation is present, resulting from the honing process. This “flow restricting” surface pattern is created intentionally, as the grooving inhibits the lubricant to efflux from the liner surface due to gravitation and other external impacts, and the so created valleys serve as a reservoir of oil during the engine cycle.

The significant difference between the two surfaces is also notable by comparing the rest of the averaged statistical descriptive data, summarized in Table 6 and Table 7.

Table 6 Worn cylinder liner surface parameters

Measurement	***Sq*** [μm]	***Sds*** [μm^{-2}]	***Ssc*** [nm^{-1}]	***γ*** [-]
1	0.3350559	0.0344129	0.0010767	1.67
2	0.2257830	0.0232590	0.0006523	0.80
3	0.3065896	0.0418144	0.0017256	1.25
4	0.3207685	0.0378124	0.0015130	1.33
5	0.3357574	0.0426160	0.0018532	1.00
Average	0.3047909	0.0359830	0.0013642	1.21

Table 7 Unworn cylinder liner surface parameters

Measurement	***Sq*** [μm]	***Sds*** [μm^{-2}]	***Ssc*** [nm^{-1}]	***γ*** [-]
1	0.4121475	0.0489519	0.0013277	0.83
2	0.4217994	0.0524114	0.0026768	0.63
3	0.4678134	0.0476538	0.0023634	0.67
4	0.4951858	0.0383030	0.0016911	0.73
5	0.4986521	0.0482607	0.0024281	0.53
Average	0.4591196	0.0471162	0.0020974	0.68

The experimental acquisition of surface parameters of the worn complete piston ring pack brought identical results for all three rings, therefore their numerical expressions are only displayed for the compression ring profile.

Sample image of a 3D scanned worn compression ring topography is shown in Figure 43 (the image has been cropped to 480 × 480 gridpoints), while the *AACF* is in Figure 44.

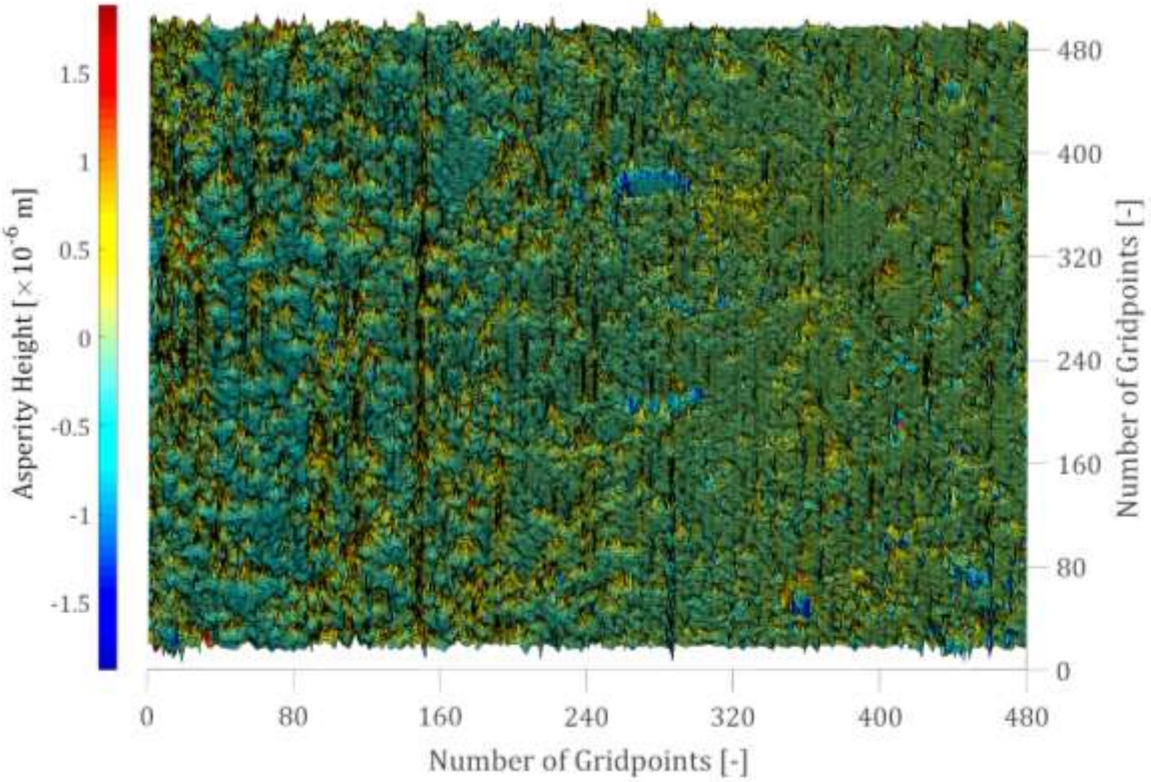

Figure 43 Surface topography of the worn compression ring

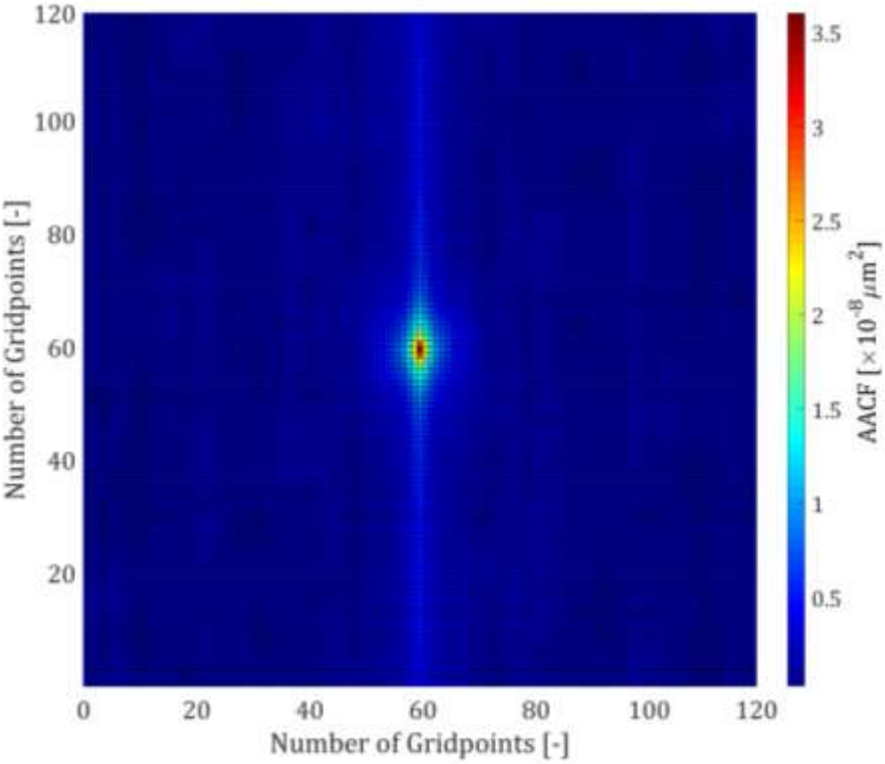

Figure 44 Areal autocorrelation function of the worn compression ring surface

Note that to be able to assess the directional orientation of surfaces, their inspection and the resultant surface matrix of asperity peaks require precise orientation of all the specimens underneath the microscope lens. Exact orientation had been ensured by the use of the electronically positionable base in both x and y directions, which was appropriately equipped for the accurate alignment of the specimens.

Similarly to the worn cylinder liner, the profile of the worn compression piston ring (together with the others) also displays, though more substantial, signs of abrasive wear and the resulting complete loss of honed grooving. Therefore, the obtained parameters confirmed the expectations of reflecting a worn-out surface with significant longitudinal roughness orientation. Values are listed in Table 8.

Table 8 Worn compression ring surface parameters

Measurement	***Sq*** [μm]	***Sds*** [μm^{-2}]	***Ssc*** [nm^{-1}]	***γ*** [-]
1	0. 5010326	0.0399524	0.0030449	3.50
2	0.5077264	0.0459686	0.0034817	2.50
3	0.3983524	0.0469145	0.0032909	2.00
4	0.4200752	0.0316793	0.0023930	3.50
5	0.3769385	0.0305646	0.0022466	2.00
Average	0.4408250	0.0390159	0.0028914	2.70

Modern trends of enhancing the mechanical properties of commercial piston ring surfaces include, besides others, the surface treatment process of nitridation (N) and plasma vapor deposition (PVD) of chromium nitride (CrN) coating and diamond-like carbon (DLC) coating. Due to the fact that the most strain is put on the compression ring, which therefore mostly operates in mixed or boundary lubrication regime, different surface treatments and coating options were only inspected on the compression ring profile.

Resultant values of the Peklenik number are mostly affected by the technological process of surface treatment. In case when the coating operation creates a sufficiently thick layer of deposition, perfectly isotropic texture is built (CrN), but in cases when the deposition layer is very thin, the resultant topography copies the honed base (DLC), also when the honing is carried out after the coating process (N). The orientation always copies the direction of motion of the honing tool. This motion for piston rings is more transversal (axial), while for the cylinder liner more rotational (tangential). That is the reason why the Peklenik number for the unworn cylinder liner is well below 1, while for the unworn piston rings well above 1.

Table 9 through Table 11 sums up the averaged parameters of the different unworn compression ring profile surfaces, while sample 3D topographies and their correspondent *AACF* are shown in Figure 45 through Figure 50.

Table 9 Surface parameters of the nitrided compression ring

Surface Treatment	***Sq*** [μm]	***Sds*** [μm^{-2}]	***Ssc*** [nm^{-1}]	***γ*** [-]
N	0.2350745	0.0389072	0.0009428	2.53

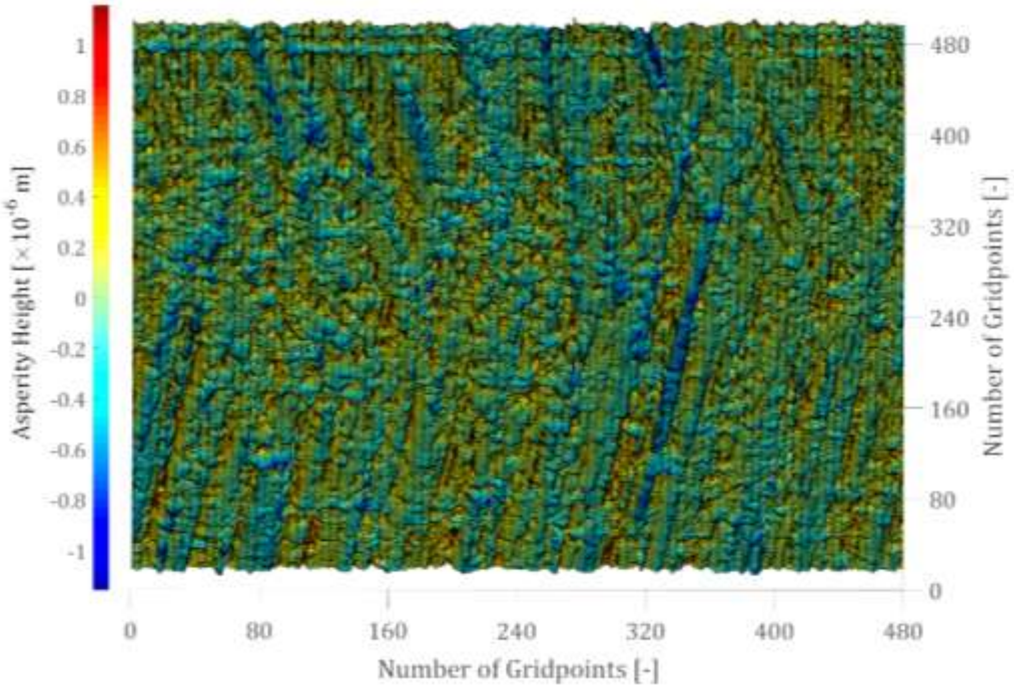

Figure 45 Surface topography of the nitrided compression ring

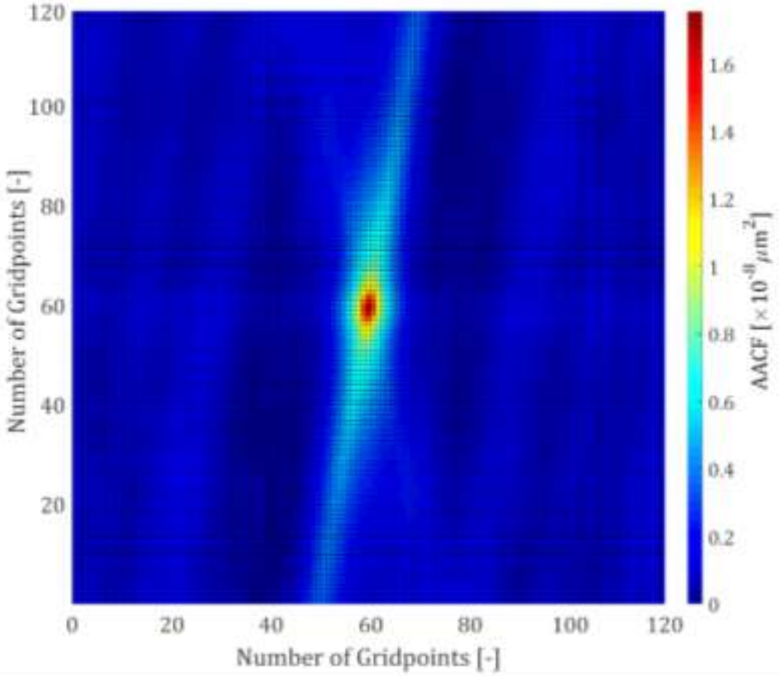

Figure 46 Areal autocorrelation function of the nitrided compression ring surface

Table 10 Surface parameters of the PVD CrN coated compression ring

Surface Treatment	***Sq*** [μm]	***Sds*** [μm^{-2}]	***Ssc*** [nm^{-1}]	***γ*** [-]
CrN	0.3129625	0.0357389	0.0016709	1.00

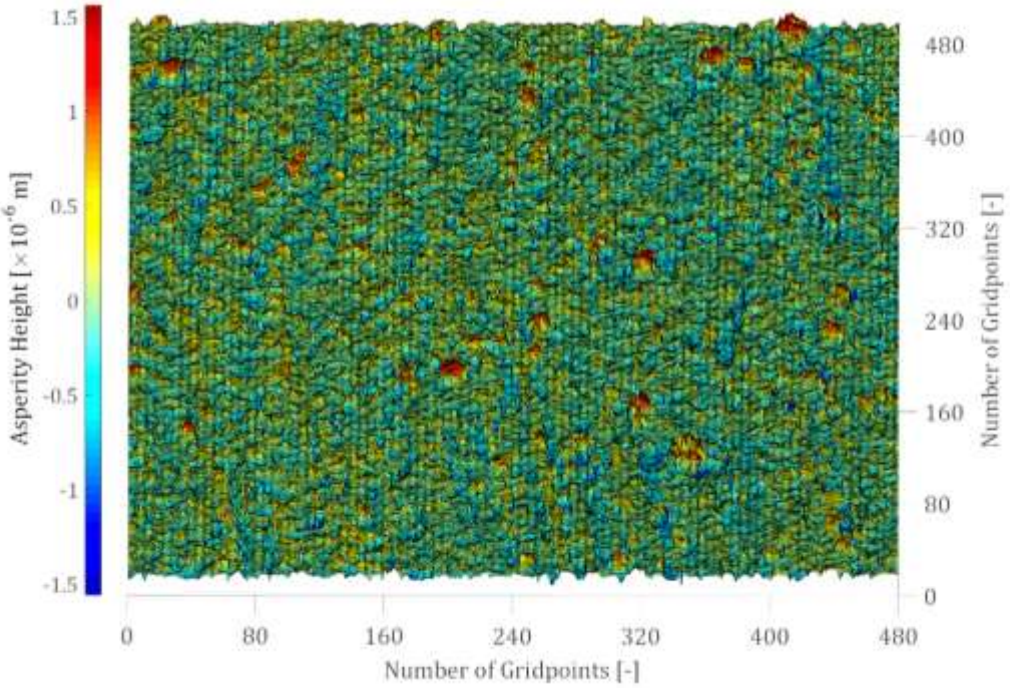

Figure 47 Surface topography of the PVD CrN coated compression ring

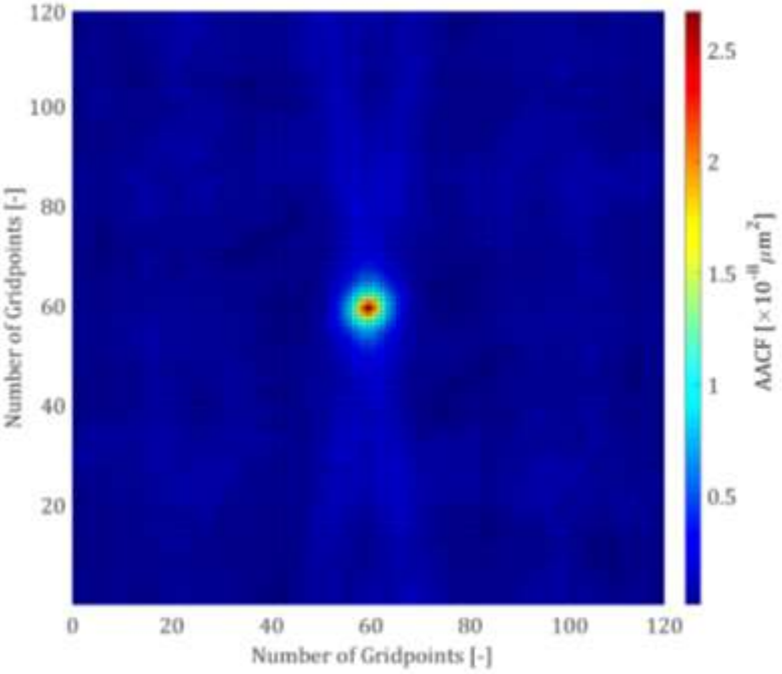

Figure 48 Areal autocorrelation function of the PVD CrN coated compression ring

Table 11 Surface parameters of the PVD DLC coated compression ring

Surface Treatment	***Sq*** [μm]	***Sds*** [μm^{-2}]	***Ssc*** [nm^{-1}]	***γ*** [-]
DLC	0.2529555	0.0378224	0.0015513	3.67

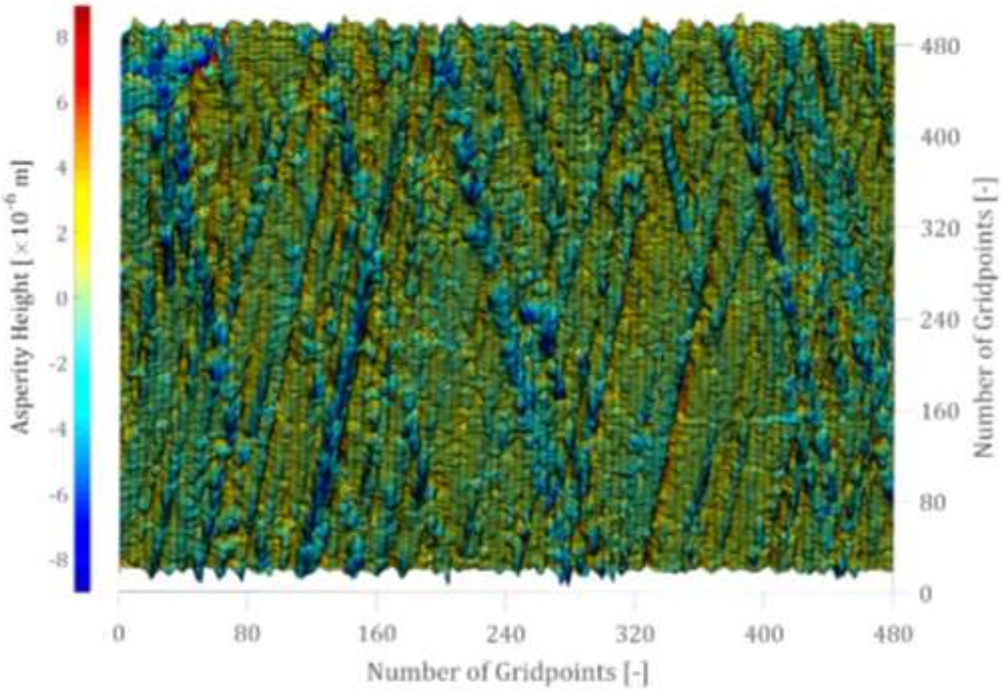

Figure 49 Surface topography of the PVD DLC coated compression ring

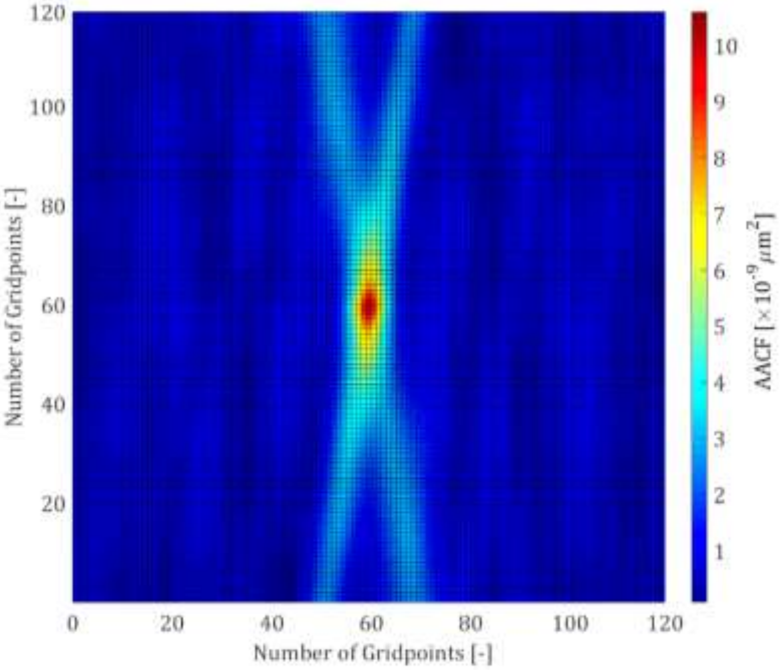

Figure 50 Areal autocorrelation function of the PVD DLC coated compression ring

6 SAMPLE RESULTS AND DISCUSSION

The utilized engine in the experimental part of the work determines all the baseline input parameters for the simulation to ensure the applicability of the measured values for the validation of the model. Calculations were performed for all operation conditions stated in Table 4 and Figure 31, although sample results at some places are only shown for the lowest and highest measured engine speed at wide open throttle running condition – 2500 and 5000 rpm – in order to maintain transparency of the displayed data.

6.1 PISTON RINGS PRIMARY MOTION

Key parameters for the calculation of the piston rings primary motion are listed in Table 3. The resultant accelerations and their derivatives are shown in Figure 51.

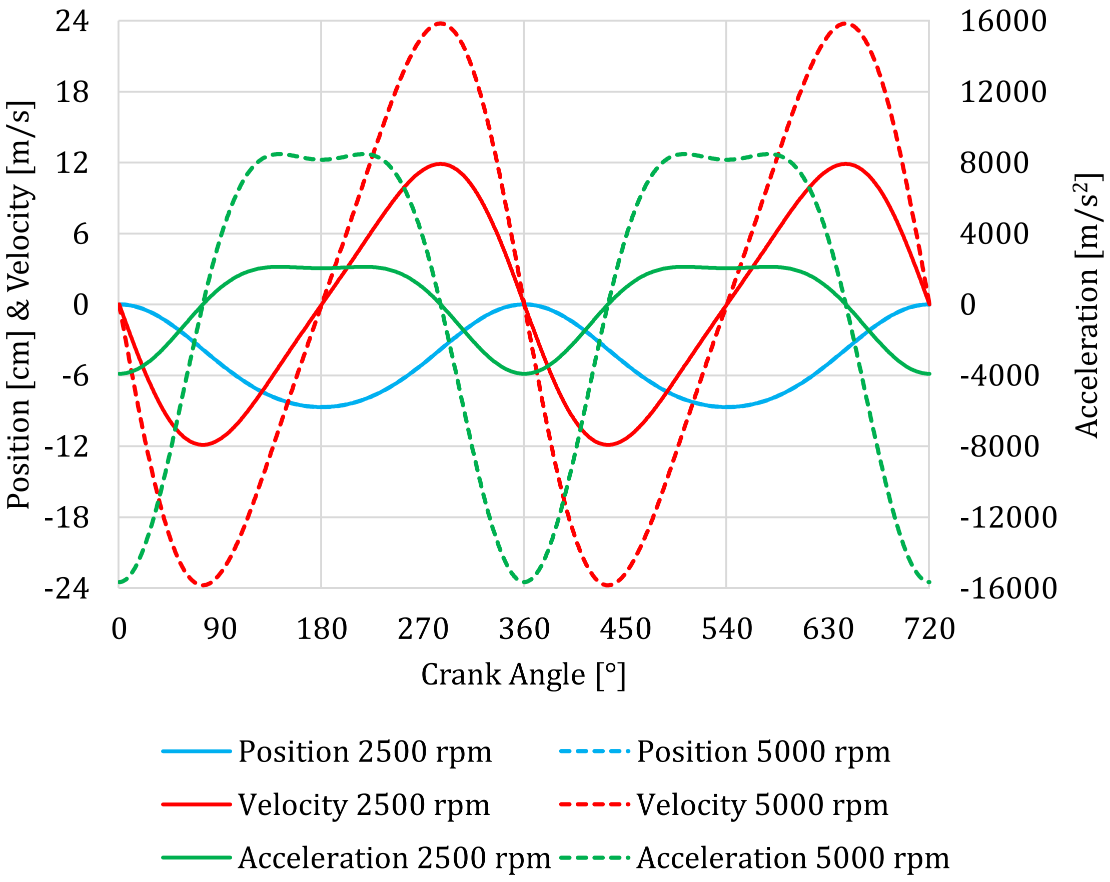

Figure 51 Axial position, velocity and acceleration of the piston at 2500 and 5000 rpm

6.2 INTERRING GAS PRESSURES

Based on the geometry of the production piston and ring pack of the Škoda EA111 1.2 HTP engine and the measured combustion chamber pressure, the instantaneous pressures in the interring volumes were calculated for each crank angle of the engine cycle. The calculation requires approx. 3-5 cycles (depending on engine speed) to stabilize and achieve a periodic course of flow and pressure values in each crevice volume of the piston assembly throughout the whole power cycle of the engine. This is due to the initial values of the volumes other than the combustion chamber and crankcase since the calculation considers atmospheric pressure in each volume from 2 to 5, depicted in Figure 52.

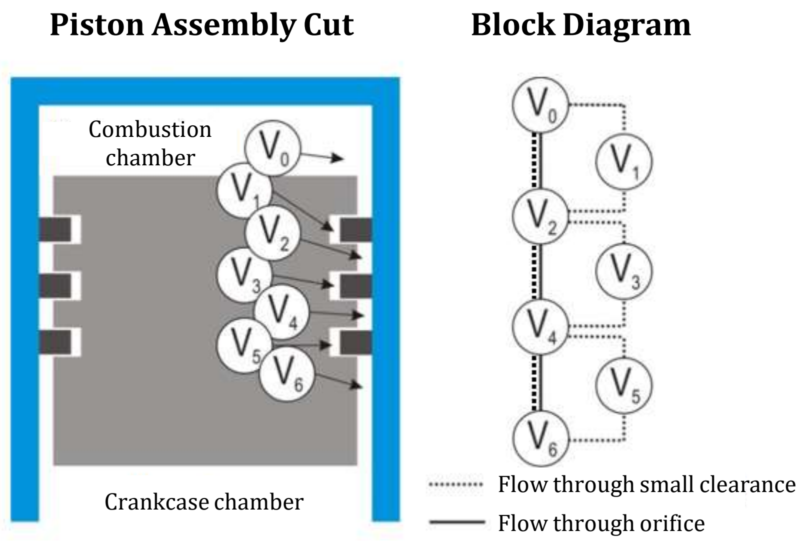

Figure 52 Interring volume and flow type nomenclature

Another aspect had to be taken into consideration is the thermal expansion of the piston due to the resulting heat from the combustion process. The deviation of the piston land diameters from their manufacturing dimensions had already been calculated by Novotný within the frame of a project with an industrial partner. The determination of the piston "growth" was based on a FEM model of the piston, loaded with corresponding heat and pressure boundary conditions, which were experimentally obtained. Other information, like material characteristics, were supplied by the engine manufacturer. Figure 53 shows the workflow of the piston radial deformation determination.

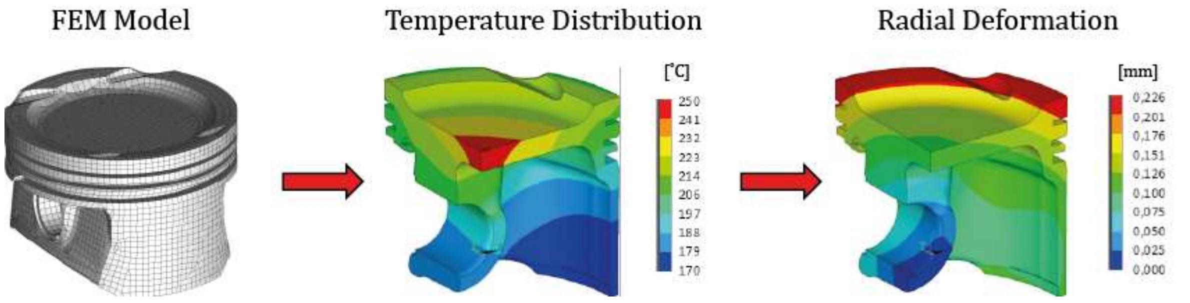

Figure 53 Temperature distribution and deformation of the piston at 2500 rpm WOT

Based on the calculation of the FEM model the determined values of radially deformed first and second piston land diameters are summarized in Table 12. The displayed values are calculated for WOT running conditions.

Table 12 Piston land diameters of the thermally loaded piston

Position	**Cold** [mm]	**2500** [mm]	**3000** [mm]	**3500** [mm]	**4000** [mm]	**4500** [mm]	**5000** [mm]
1. Land	75.85	76.37	76.38	76.39	76.40	76.41	76.41
2. Land	75.30	75.86	75.88	75.88	75.89	75.90	75.91

Sample results of the stabilized pressure curves in the interring volumes for 2500 rpm WOT running condition are shown in Figure 54.

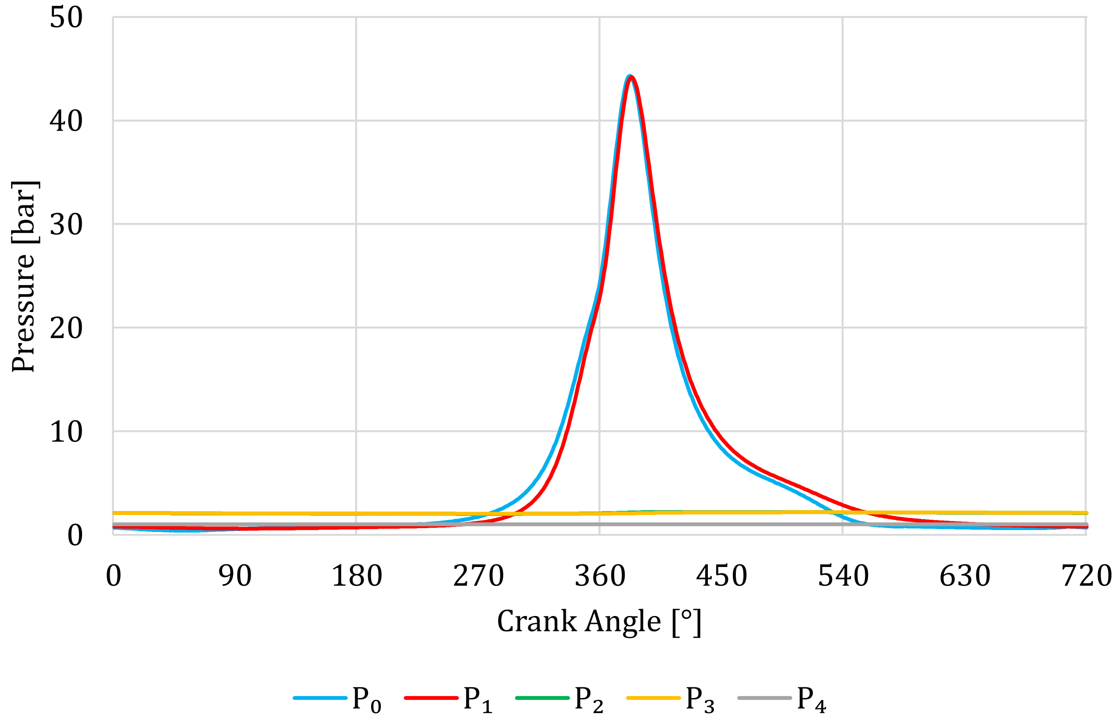

Figure 54 Interring gas pressures at 2500 rpm WOT

As can be seen from the results, the pressure in volumes V_2 and V_3 are always higher than the assumed crankcase pressure in volume V_4 and below. This results in an unchanged direction of flow towards the crankcase throughout the whole engine cycle and is referred to as blow-by flow. The other undesired phenomenon of flow through the piston assembly is the flow into the combustion chamber, which is referred to as blow-back flow. The magnitude of this phenomenon is composed of the motion of gases from volume V_2 to V_0 through the ring gap of the first piston ring. This component negatively affects the oil consumption, as the gas stream entrain molecules of the lubricant. While the amount of oil in the blow-back stream is considered instantaneously lost into the exhaust gases, the volume of entrained oil in the blow-by stream depends on the performance of the oil separator of the crankcase ventilation system. Figure 55 and Figure 56 show the courses of blow-back and blow-by mass flows, respectively. Note that negative values of blow-back gas flow represent the direction towards the combustion chamber.

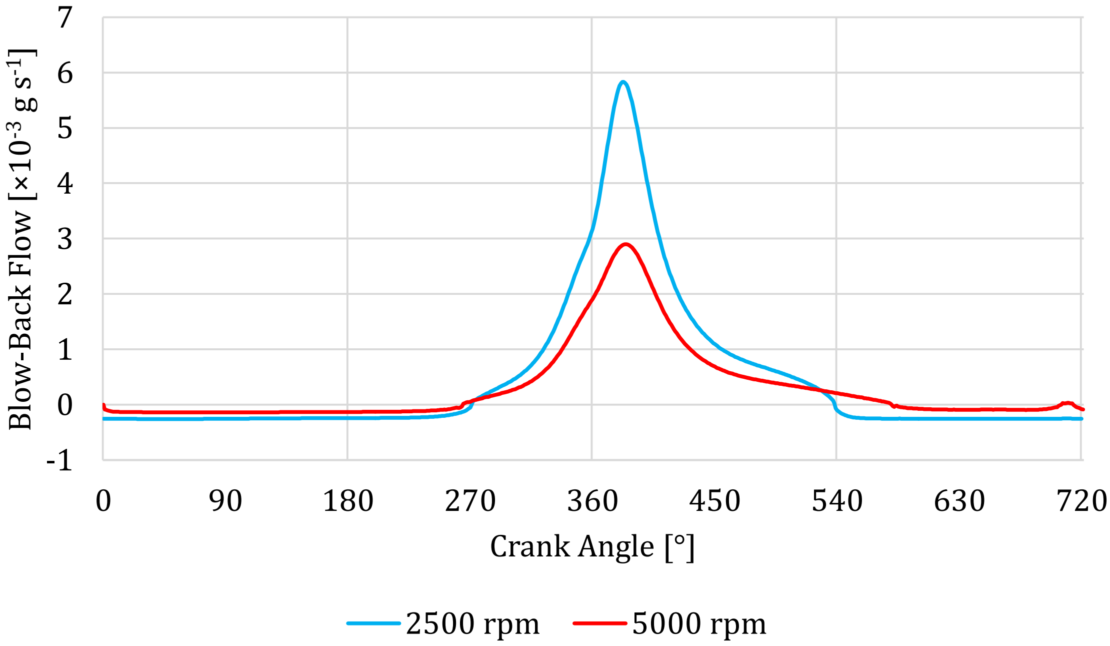

Figure 55 Blow-back mass flow at 2500 and 5000 rpm WOT

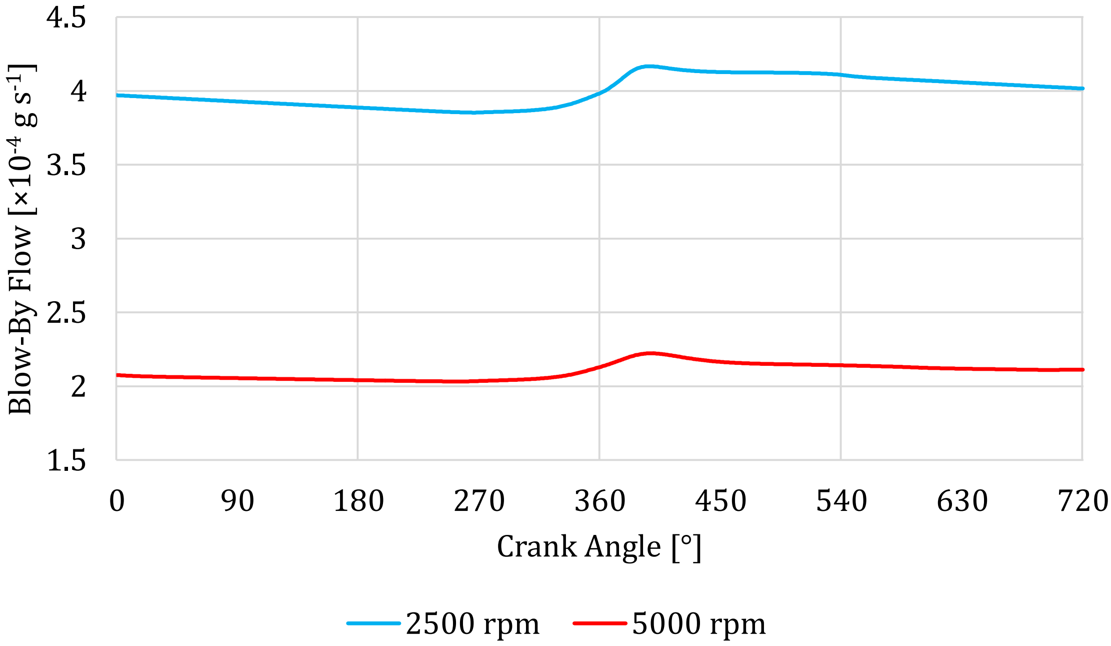

Figure 56 Blow-by mass flow at 2500 and 5000 rpm WOT

To be able to compare the measured and calculated results of blow-by gas flow, the values of the calculated gas mass flow rate of [g s^{-1}] into volume V_4 have to be converted to the volumetric flow rate unit of [l min^{-1}], matching the AVL Blow By Meter's output format. The conversion utilizes the equation of state of ideal gas, equation 8, written in the form:

$$p\,\dot{V} = \frac{\dot{m}}{M} R_u\, T\,, \tag{112}$$

Since the measuring orifice in the blow-by meter caused a negligible pressure change in the gas stream, and the experiment was set up as an open system, meaning that the leaking gas freely exited the measurement device without recirculation into the intake manifold, the pressure in equation 112 could be considered atmospheric:

$$p_{ATM} = 101325\ \mathrm{Pa}\,. \tag{113}$$

The universal gas constant equals to:

$$R_u = 8.3144598\ \mathrm{J\ mol^{-1}\ K^{-1}}\,. \tag{114}$$

The absolute temperature of the exhaust gas stream in the compensation volume and tubing decreased to ambient, which for the experiment exerted to:

$$T_{amb} = 293.73\ \mathrm{K}\,. \tag{115}$$

Another parameter to be determined is the molar mass of exhaust gases. Since the fuel to air ratio was kept stoichiometric at all loading conditions throughout the experiment, we can assume complete burning of the gasoline in the combustion chamber. Therefore, for the perfect combustion of octane in air (assuming the ratio of 79% nitrogen and 21% oxygen) the following reaction equation can be written:

$$C_8H_{18} + 12.5\left(O_2 + 3.76\ N_2\right) \rightarrow 8\ CO_2 + 9\ H_2O + 47\ N_2\,. \tag{116}$$

Number of moles of the combustion product:

$$8\ \mathrm{mol}\left(CO_2\right) + 9\ \mathrm{mol}\left(H_2O\right) + 47\ \mathrm{mol}\left(N_2\right) = 64\ \mathrm{mol}\,. \tag{117}$$

Mass of the combustion product:

$$\begin{gathered} 8\ \mathrm{mol}\cdot 44.009\ \mathrm{g\ mol^{-1}}\left(CO_2\right) + 9\ \mathrm{mol}\cdot 18.015\ \mathrm{g\ mol^{-1}}\left(H_2O\right) + \\ 47\ \mathrm{mol}\cdot 28.013\ \mathrm{g\ mol^{-1}}\left(N_2\right) = 1830.818\ \mathrm{g}\,. \end{gathered} \tag{118}$$

Molar mass of the combustion product:

$$\frac{1830.818\ \mathrm{g}}{64\ \mathrm{mol}} = 28.607\ \mathrm{g\ mol^{-1}}\,. \tag{119}$$

Comparison of the measured and calculated results of volumetric blow-by gas flow for WOT running conditions are shown in Figure 57. Error bars represent the accuracy of the measuring device stated in Appendix B. Comparisons for the other partial loading conditions are to be found in Appendix G.

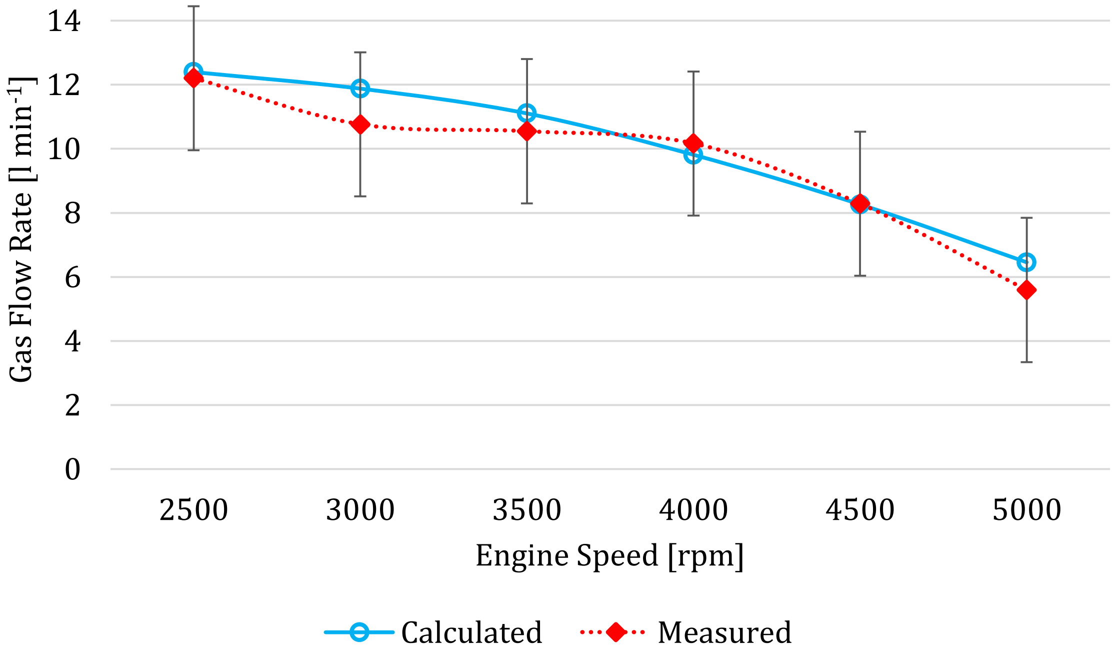

Figure 57 Measured and calculated blow-by flows at WOT

For the statistical comparison of the calculated and measured data, the t-test for paired data samples was utilized. This test was intended to evaluate the statistically significant difference between the two data sets. Two-tailed tests were carried out with a confidence level of 95%, for 6 sample sets. Table 13 summarizes the calculated parameters of the t-test for WOT, 75% and 50% rated power running conditions.

Table 13 Parameters of the t-tests

Parameter		WOT	75%	50%
α	[-]	0.05	0.05	0.05
DOF	[-]	5	5	5
t	[-]	1.729398277	2.500070575	2.244275237
t_α	[-]	2.570581836	2.570581836	2.570581836
p	[-]	0.144303316	0.054485396	0.074812208

where α is the statistical significance, *DOF* are the degrees of freedom, t is the calculated test statistic value, t_α is the critical value of test statistic for α and *DOF* and p is the probability of observing the calculated test statistic under the null hypothesis.

In all three cases, the calculated test statistic values are below the critical values for the given statistical significance and degrees of freedom, and the calculated probabilities are also higher than the statistical significances. Therefore, we can state that the difference between the calculated and measured data was not found statistically significant.

6.3 RING PROFILES

The piston ring pack of the Škoda EA111 1.2 HTP engine follows the conventional configuration of small size spark ignition combustion engines, with a barrel-face compression ring (CR), a trapezoid scraper ring (SR) and a three-piece oil control ring (OCR). As the experimental engine was a run-in engine, therefore the profiles of the rings were also simulated as worn with the use of the equation of an offset parabola, as described in chapter 4.6. Key design parameters of the baseline ring pack geometry are summarized in Table 14.

Table 14 Design parameters of the baseline ring pack

Parameter		**CR**	**SR**	**OCR**
Ring Height	[m]	1.2×10^{-3}	1.5×10^{-3}	2.5×10^{-3}
Ring Width	[m]	3.0×10^{-3}	3.2×10^{-3}	2.6×10^{-3}
Blade Height	[m]	N/A	N/A	2.5×10^{-4}
Crown Height	[m]	1.8×10^{-6}	1.0×10^{-6}	0.5×10^{-6}
Offset	[m]	0.0	-5.0×10^{-4}	0.0
Tangential Force	[N]	11.2	9.5	37.5

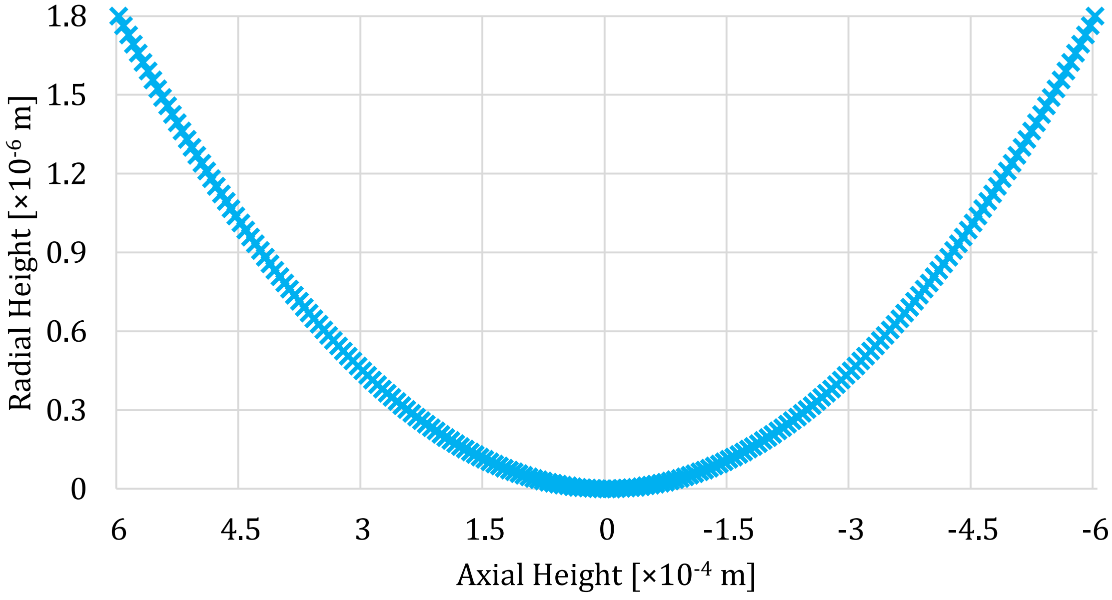

Figure 58 Compression ring profile

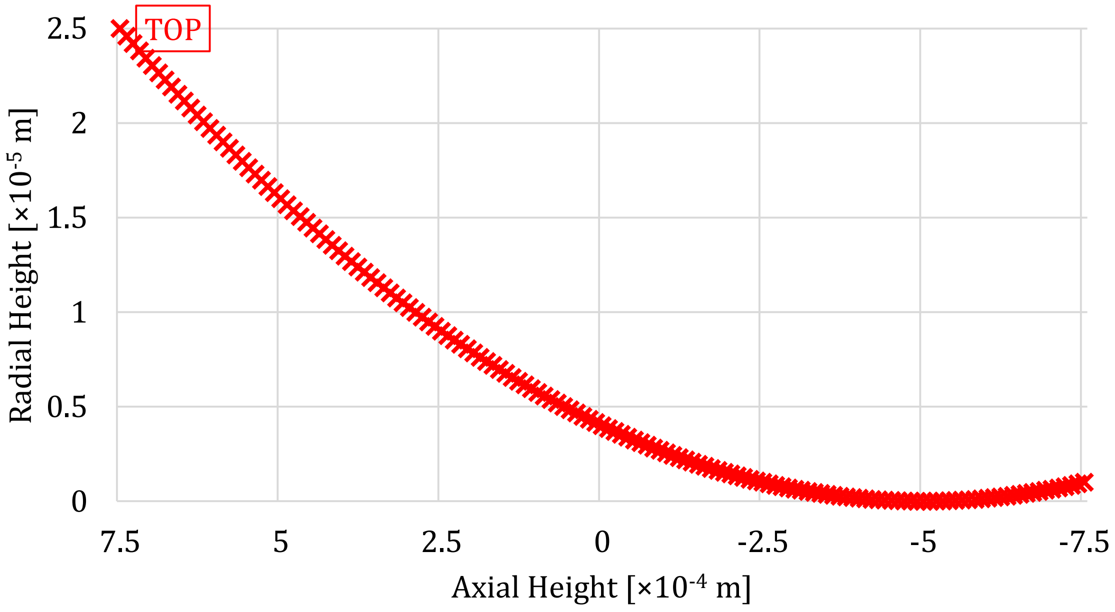

Figure 59 Scraper ring profile

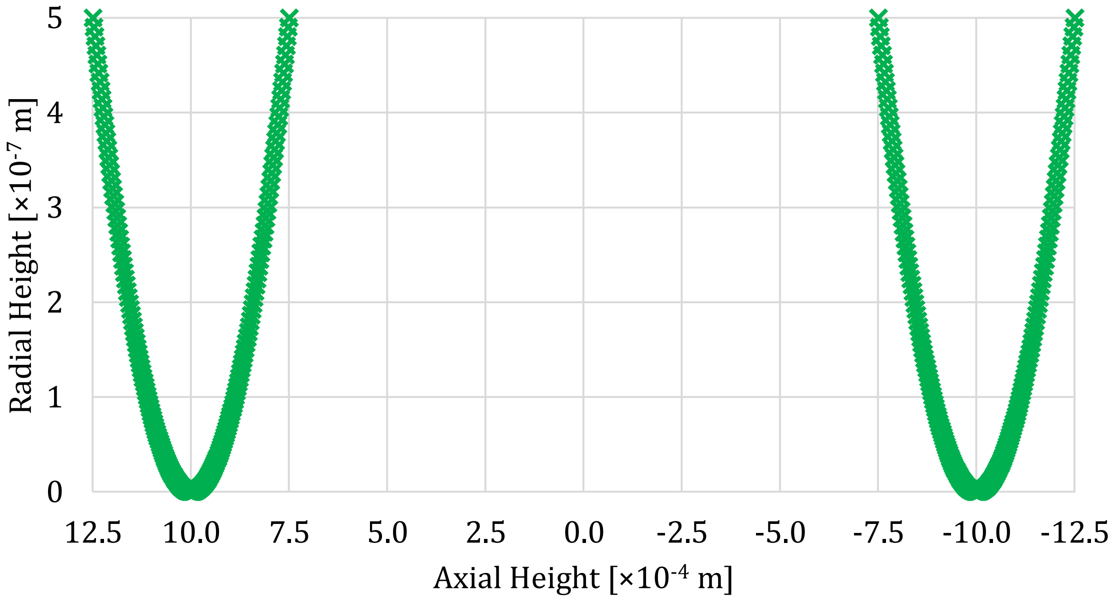

Figure 60 Oil control ring profile

The ring profile generator subroutine – based on the oil attachment and detachment point – computes the instantaneous wetted profile of the ring, which is then handed over to the following calculation modules as a user-defined number of discrete points, which results in reducing the computation time. Modeled are only those parts of the profile, which are capable of establishing a load carrying HD lubricating layer. Sample results in this thesis are set to 201 points over the wetted profile. The fully flooded discrete profile of the baseline worn CR is shown in Figure 58, SR in Figure 59 and OCR in Figure 60.

6.4 FORCE EQUILIBRIUM

The calculation of an engine cycle is divided into a user-defined number of steps. Each step is characterized by a corresponding crank angle value, which governs the boundary parameters entering the simulation, while other initial values are taken from the equilibrium state results of the previous step. The force equilibrium is therefore determined for every calculation step separately, assuming a quasi-static state. A calculation step reaches an equilibrium state, when the external forces acting on a ring segment balance out, meaning that their sum falls below the value of the termination criteria. This subchapter is dedicated to the demonstration and comparison of the calculated equilibrium state forces of the complete piston ring pack.

6.4.1 MINIMUM OIL FILM THICKNESS

Each equilibrium state of a ring segment is greatly influenced by the wetting parameters: the oil attachment and detachment point, which determine the wetted area of a ring profile and minimum oil film thickness (MOFT) between the profile and the liner, which dictates the actual lubrication regime. Stabilized courses of the MOFT for the complete ring pack are shown in Figure 61 to Figure 63.

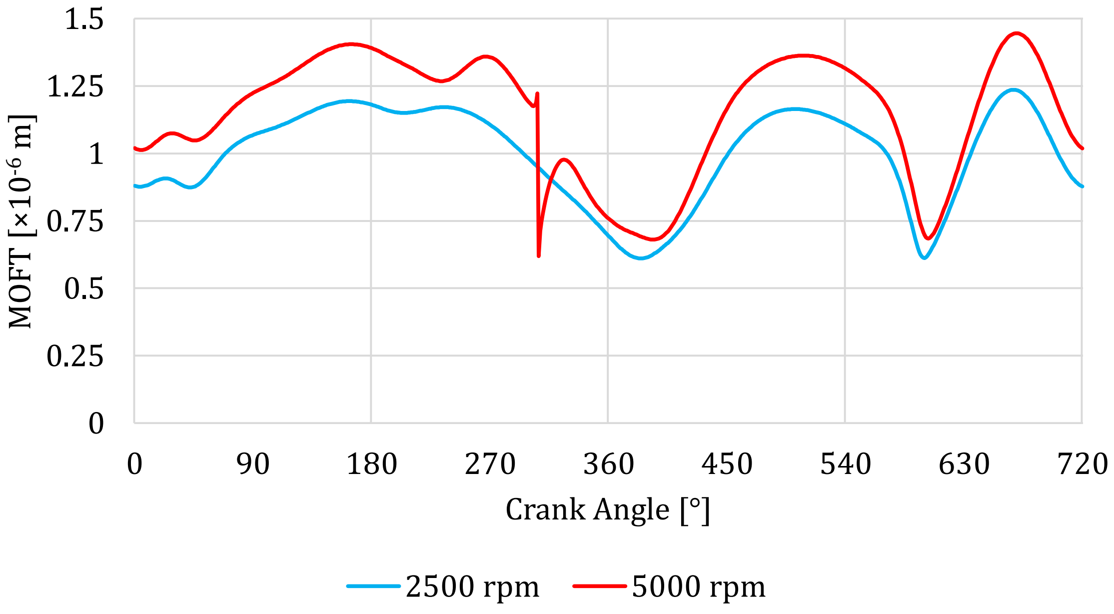

Figure 61 Minimum oil film thickness of the compression ring at 2500 and 5000 rpm WOT

Note the sudden drop at 304° of the higher engine speed. This occurrence is caused by the radial ring flutter phenomenon, whereas the ring due to its higher axial speed generates a stronger hydrodynamic load bearing force. On the one hand, the increased measure of this force component is not compensated by the pretension, nor the gas forces due to the absence of sufficient back pressure behind the ring at this phase of the engine cycle. Nevertheless, as the ring emerges from the lubricating film, enough area is exposed to the upstream pressure to act on, which causes the ring to loose contact with the cylinder liner.

With the complete loss of the accumulated lubricant volume from the ring area the support of the HD pressure disappears, too. The impact of gas pressures on the ring profile in the next calculation step is overcome by the opposing forces again, which causes the incidence of the ring back into the lubricating layer. For this particular ring configuration and operating conditions, the phenomenon of radial ring flutter cannot be observed based on the simulation results.

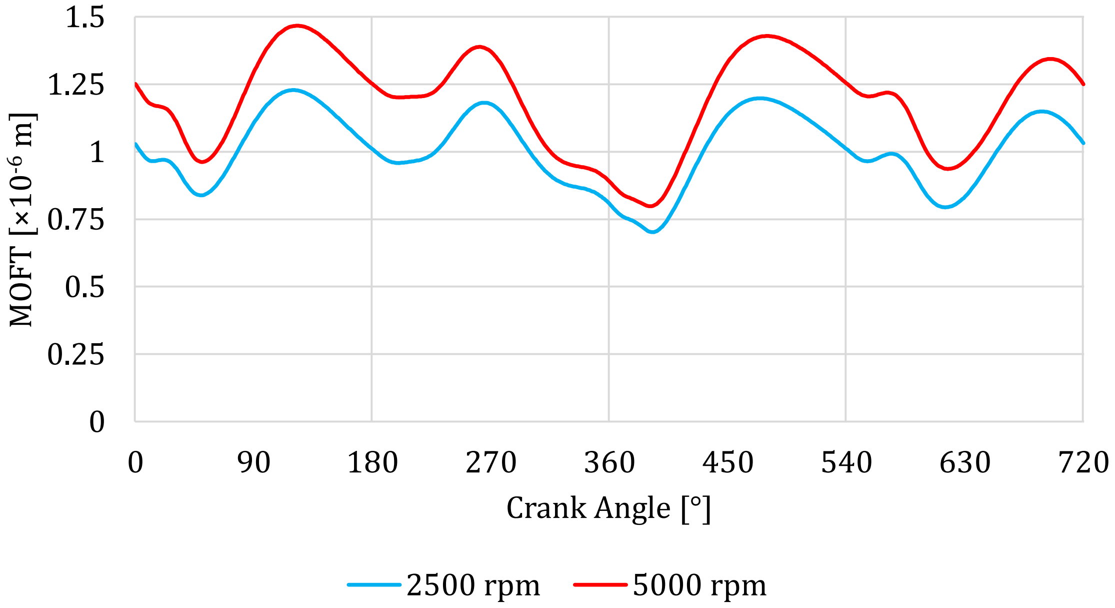

Figure 62 Minimum oil film thickness of the scraper ring at 2500 and 5000 rpm WOT

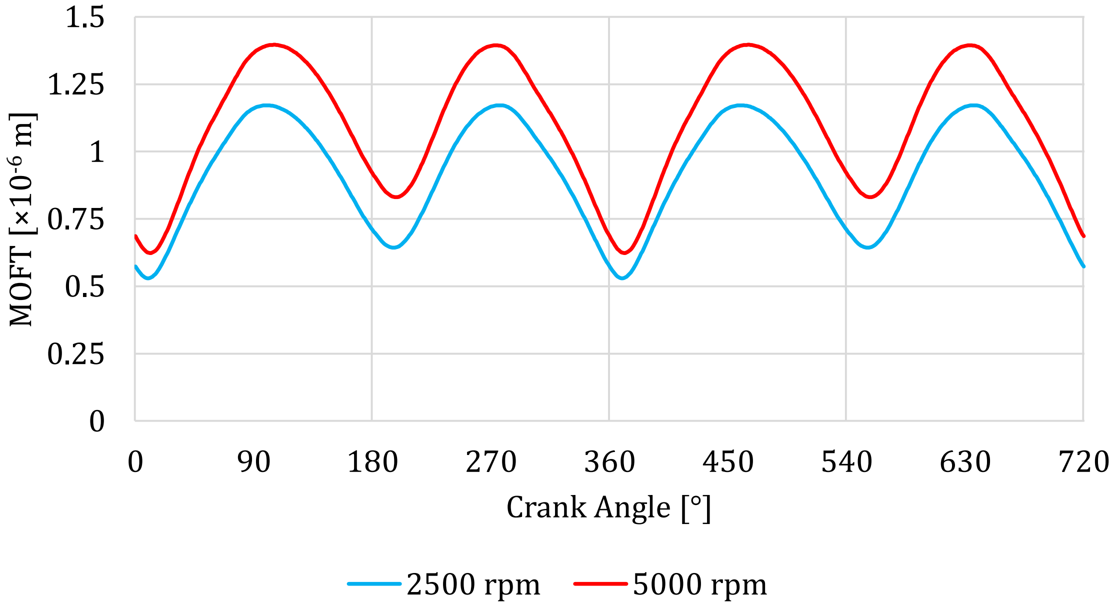

Figure 63 Minimum oil film thickness of the oil control ring at 2500 and 5000 rpm WOT

6.4.2 WETTED AREA

The other general descriptive parameter, besides the MOFT, is the instantaneous wetted area of the piston ring profile. As described at the oil flow mechanism in chapter 4.10, the oil attachment point is influenced by the positive or negative accumulation due to the scraping effect, while the detachment point depends on the fulfillment of the Reynolds exit condition, further complemented with the consideration of the available oil flux at the trailing edge. The calculated wetted profile of the compression ring for 2500 and 5000 rpm WOT is shown in Figure 64 and Figure 65, respectively.

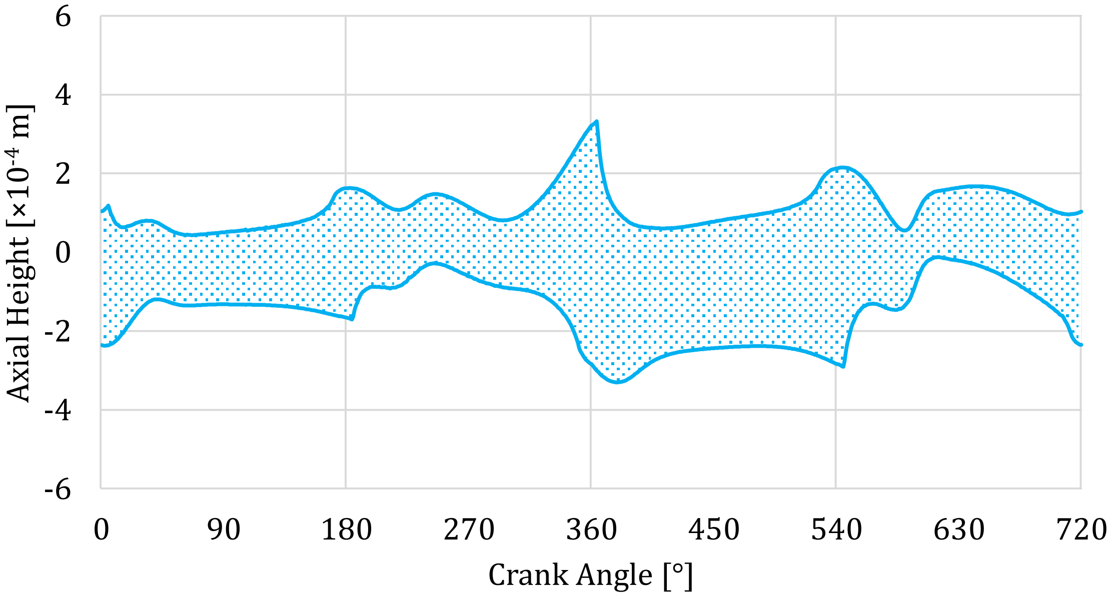

Figure 64 Wetted profile of the compression ring at 2500 rpm WOT

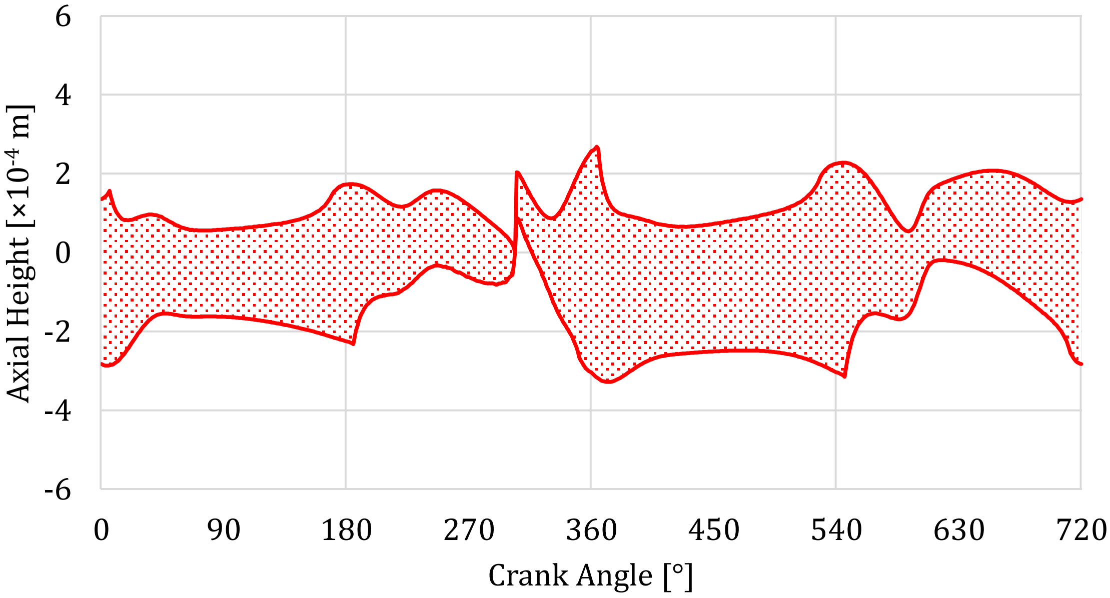

Figure 65 Wetted profile of the compression ring at 5000 rpm WOT

The wetted profiles of the scraper and oil control ring show very little deviation throughout the various running conditions, for 2500 and 5000 rpm WOT are almost identical, therefore their courses are only shown for 2500 rpm WOT condition in Figure *66* for the scraper, and Figure 67 for the oil control ring.

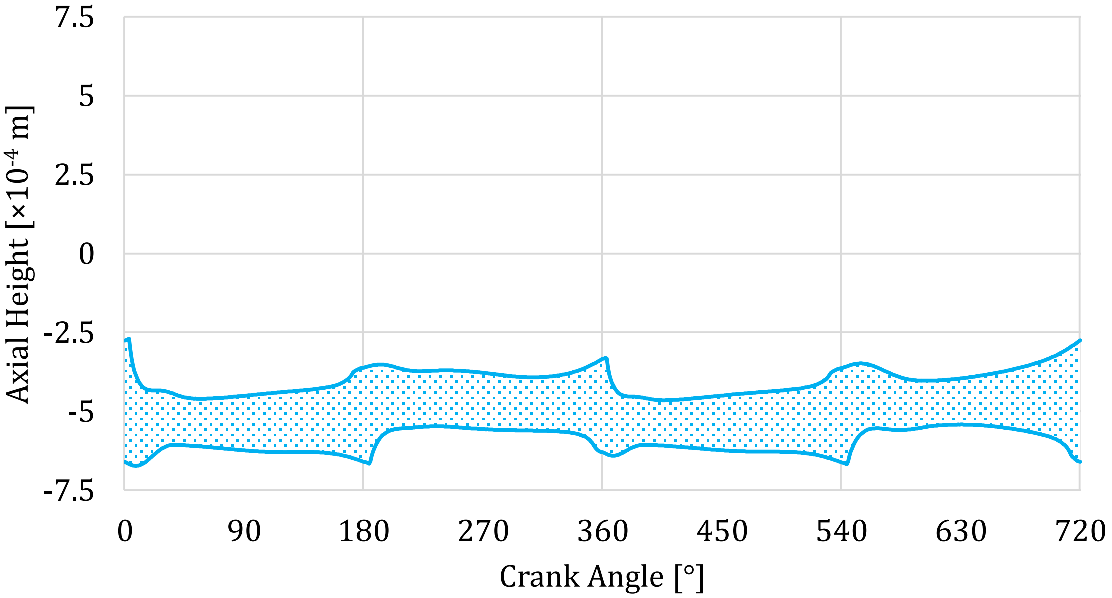

Figure 66 Wetted profile of the scraper ring at 2500 rpm WOT

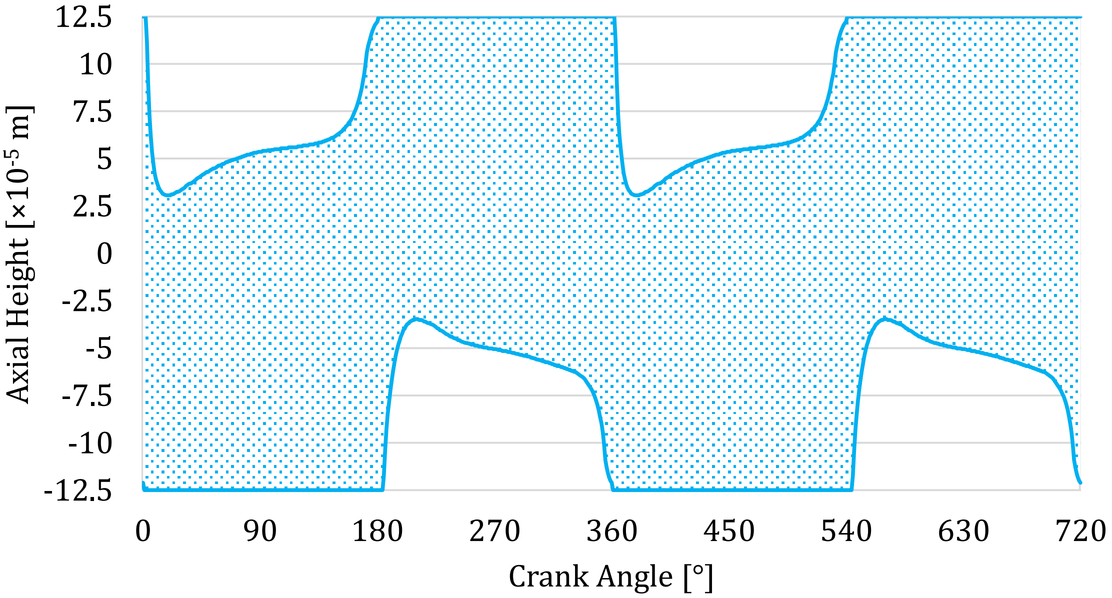

Figure 67 Wetted profile of the oil control ring blade at 2500 rpm WOT

6.4.3 GAS FORCE

Besides the ring pretension force, the gas force is the other radial force component pushing the ring towards the cylinder liner. The only difference between these two components is that while the ring pretension force is considered constant throughout the computation (variations caused by the change of the MOFT are neglected), than the gas forces are ought to be calculated at each time step of the simulation, because their measure is dependent on the instantaneous wetted area of the ring profiles and the actual interring gas pressures surrounding the rings. Stabilized courses of the resultant gas forces are shown in Figure 68 through Figure 70.

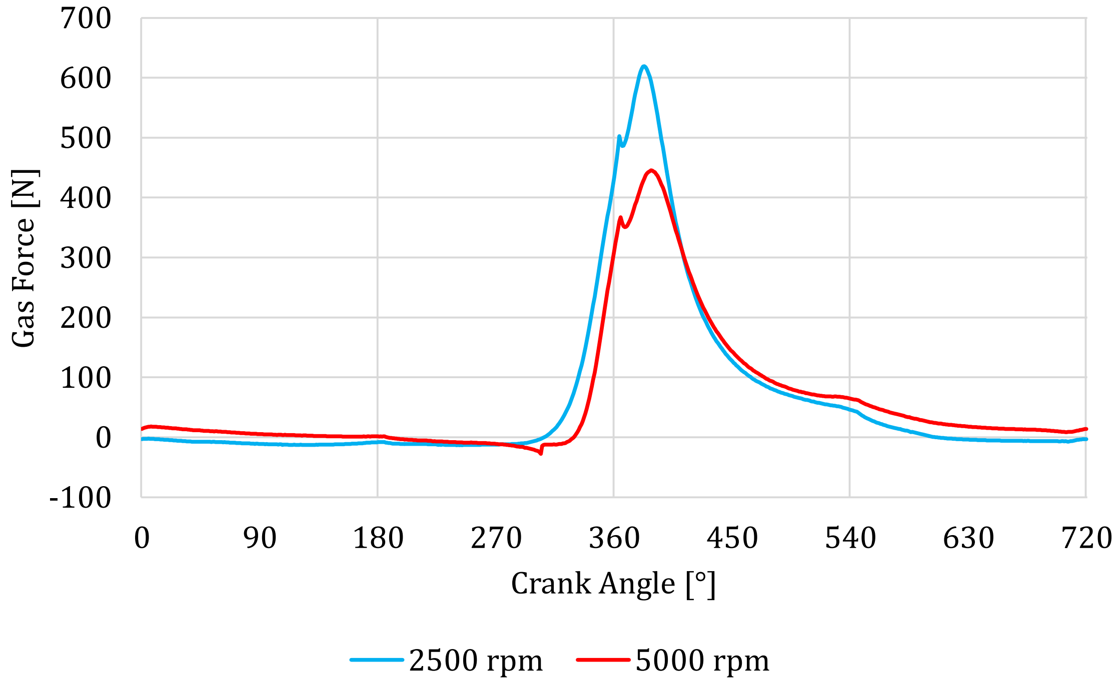

Figure 68 Gas pressure forces acting on the compression ring

Note the indication of ring flutter at crank angle 304° in the course of gas force at 5000 rpm. The negative value of total gas force overcame the value of ring pretension force, meaning that the ring pretension could not further compensate the fallout of the lifting effect of the upstream gas pressure, which resulted in the unwanted phenomenon of radial ring flutter.

Another phenomenon to be noticed is the switch between the exit conditions at 364° and 365° for 2500 and 5000 rpm, respectively. These are the crank angles when the Couette term of the Reynolds equation of the accelerating piston ring regains its dominance, therefore the oil detachment point becomes determined by the position of the fulfillment of the Reynolds exit condition instead of the film non-separation exit condition.

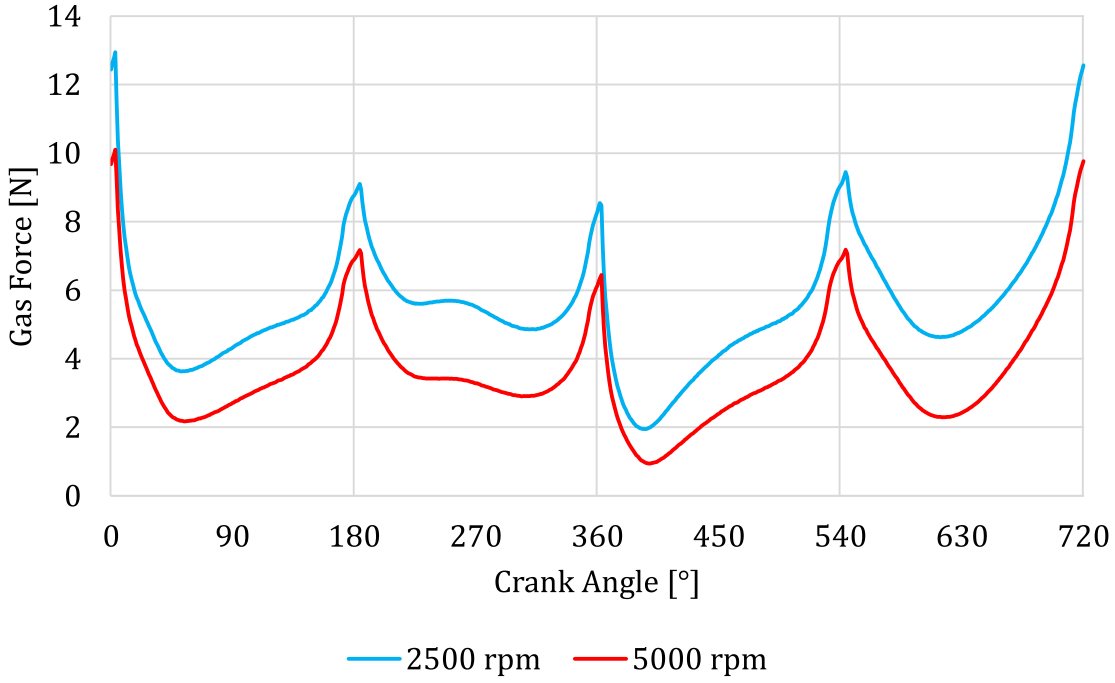

Figure 69 Gas pressure forces acting on the scraper ring

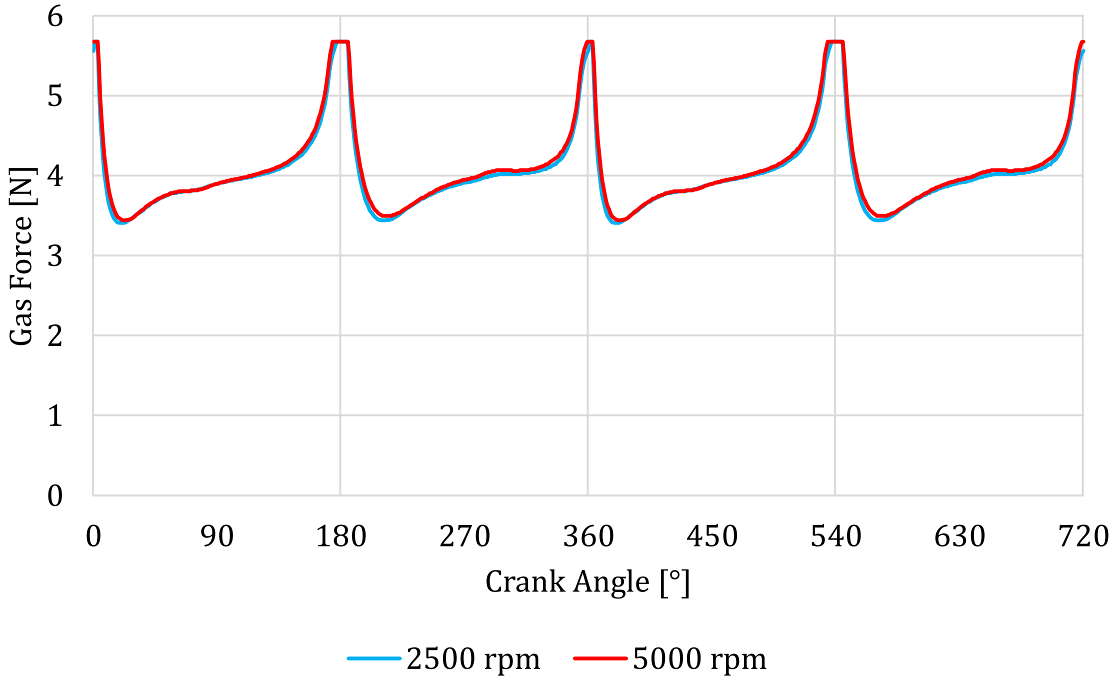

Figure 70 Gas pressure forces acting on the oil control ring

6.4.4 HYDRODYNAMIC FORCE

The mechanism of lubrication of contact pairs in relative motion is intended to separate the two rough surfaces with a thin layer of lubricant to prevent or decrease the measure of asperity contact. Thus, hydrodynamic forces developing in dynamically loaded slide bearings, like piston rings, are supposed to carry the vast majority of radial load.

In order to be able to determine the normal forces acting in the HD lubricating layer, first, the HD pressure profiles have to be calculated. Important input parameter for this sub module is the instantaneous value of dynamic viscosity of the lubricant underneath the ring profile. The baseline oil recommended by the engine manufacturer is of viscosity grade 5W40, specification VW502.00. The corresponding Vogel parameters describing the temperature (in °C) dependence of dynamic viscosity are listed in Table 15.

Table 15 Parameters of the Vogel equation for engine oil viscosity grade 5W40

Viscosity Grade	***a*** [N s m^{-2}]	***b*** [-]	***c*** [-]
5W40	2.703×10^{-4}	723.9	-90.08

Based on the axial temperature distribution of the cylinder liner and the instantaneous position of the piston rings the dynamic viscosity is calculated in each simulation step. Computed values of the baseline 5W40 viscosity grade oil are plotted in Figure 71.

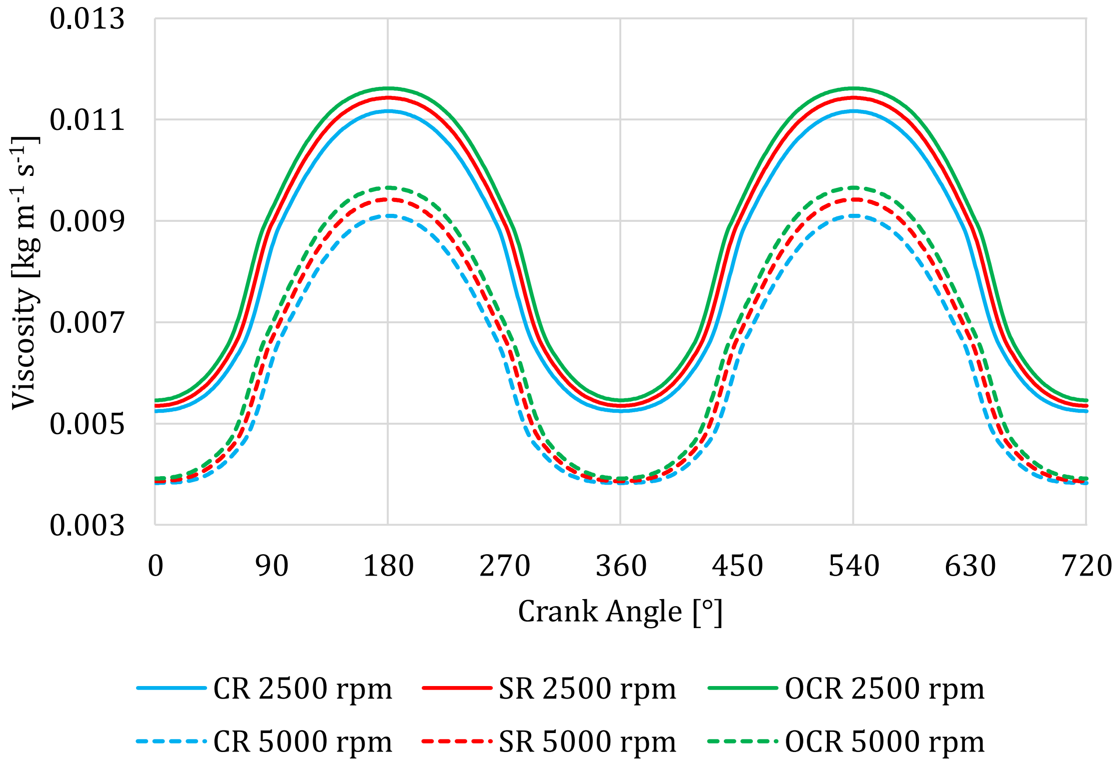

Figure 71 Values of dynamic viscosity under the ring profiles at 2500 and 5000 rpm WOT

The surface roughness orientation affects the values of flow factors, which also are input parameters into the modified Reynolds equation. Their numerical expressions for each piston ring – cylinder liner junction were determined with the use of F-CALC, the computation tool developed by Maršálek [13].

Baseline pairing of the piston ring – cylinder liner was made with both worn surfaces, matching the experimental conditions. Values of flow factors were calculated in dependence of the *H* parameter (eq. 30), and are shown in Figure 72.

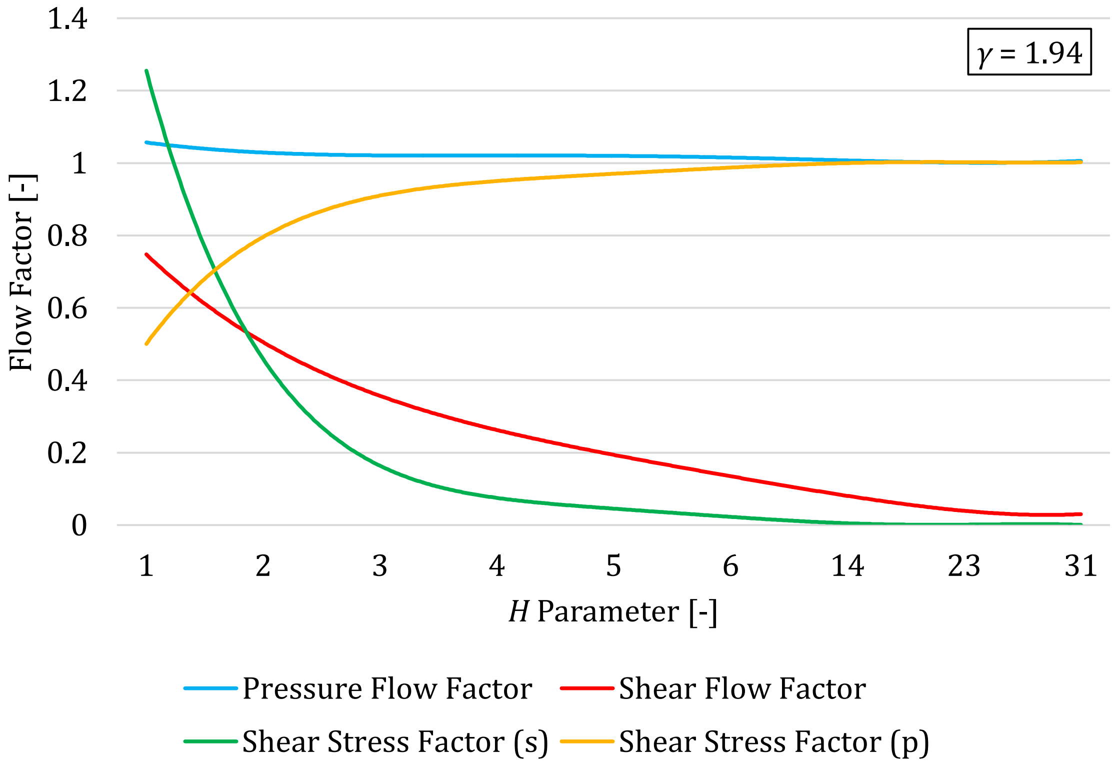

Figure 72 Flow factors of the worn cylinder liner and worn piston ring surface pair

For the calculation of HD pressure and the HD shear stress a total of five flow factors are required, but as can be seen the F-CALC calculates only four of them: the value of the pressure flow factor ϕ_x, the shear flow factor ϕ_s, the pressure shear stress factor ϕ_{fp} and the shear stress factor resulting from the sliding motion ϕ_{fs}. The last one, the averaged sliding velocity shear stress factor ϕ_f is calculated in RingSIM, within the HDPRESSURE function with the use of empirical formulae [65]:

For $H \le 3$:

$$\phi_f = \frac{35}{32} z \left\{ \left(1-z^2\right)^3 \ln\frac{z+1}{e} + \frac{1}{60}\left[-55 + z\left(132 + z\left(345 + z\left(-160 + z\left(-405 + z\left(60 + 147z\right)\right)\right)\right)\right)\right]\right\} \qquad (120)$$

For $H > 3$:

$$\phi_f = \frac{35}{32} z \left\{ \left(1 - z^2\right)^3 \ln \frac{z+1}{z-1} + \frac{z}{15} \left[66 + z^2 \left(30z^2 - 80 \right) \right] \right\}. \tag{121}$$

Based on the input parameters sample shapes of the built up HD pressure profile in the wetted area of the CR, SR and OCR over one engine cycle at 2500 rpm WOT running condition are shown in Figure 73, Figure 74 and Figure 75, respectively.

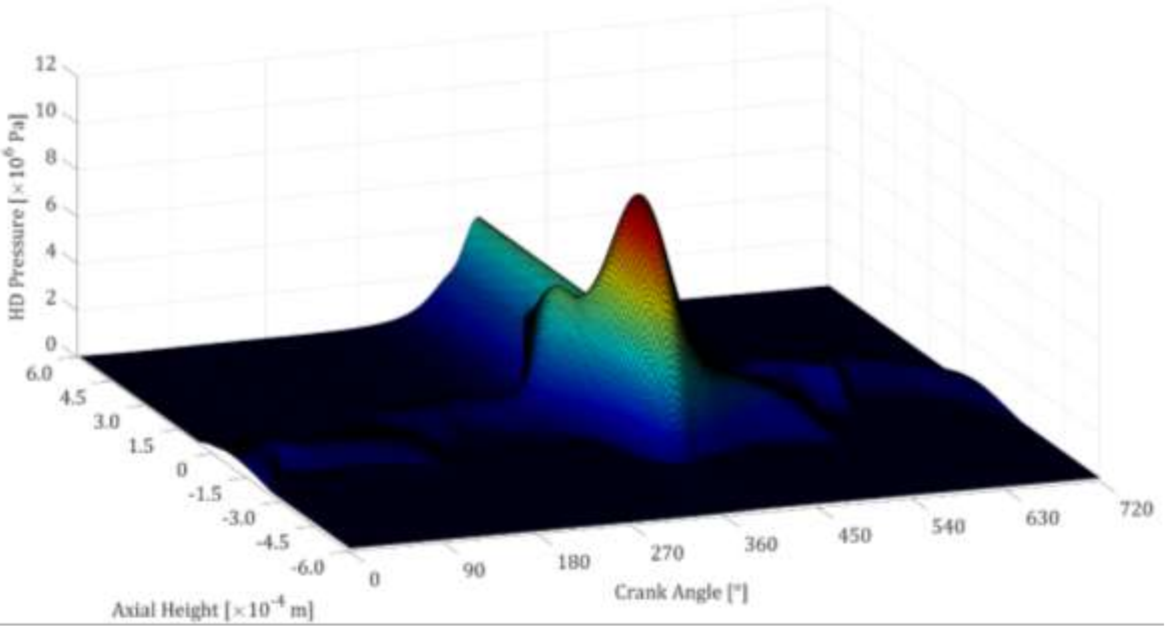

Figure 73 Hydrodynamic pressure profile of the compression ring

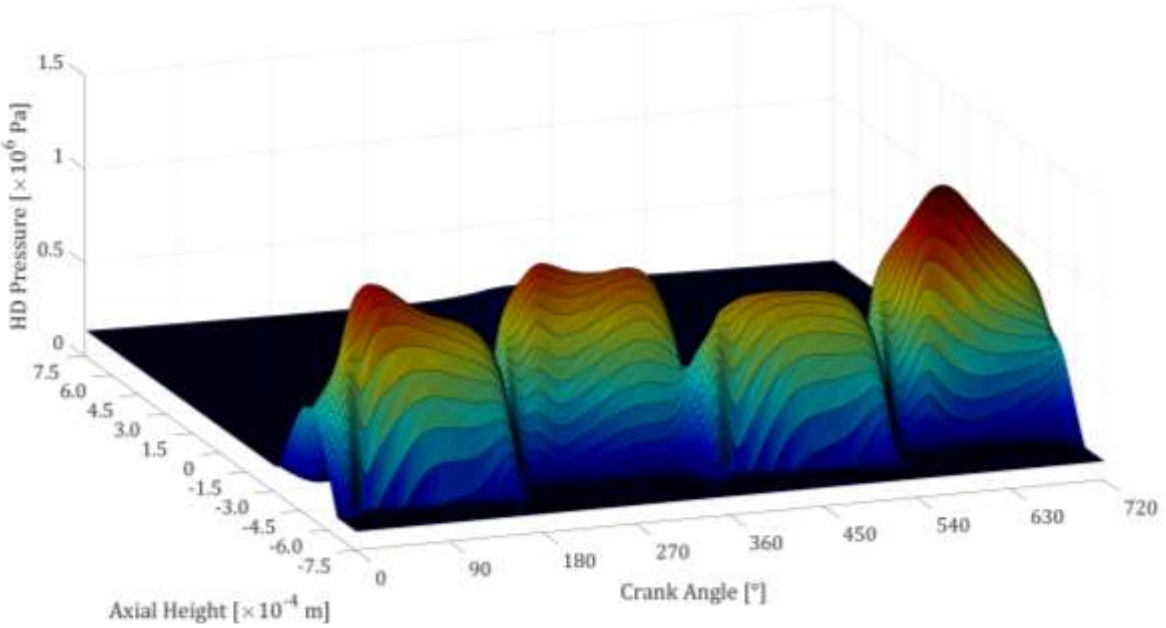

Figure 74 Hydrodynamic pressure profile of the scraper ring

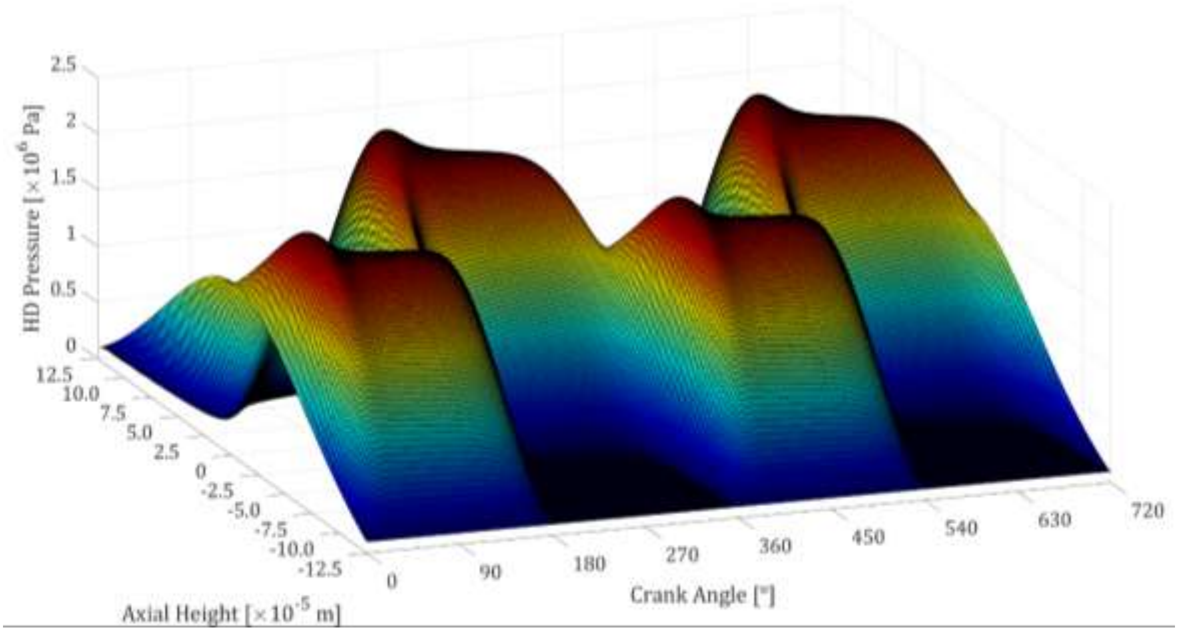

Figure 75 Hydrodynamic pressure profile of the oil control ring

The resultant HD forces acting in the radial and axial directions are calculated with the use of the pressure integrals over the wetted area. Corresponding forces to the presented pressure profiles for 2500 rpm, as well as for 5000 rpm are shown in Figure 76 through Figure 78.

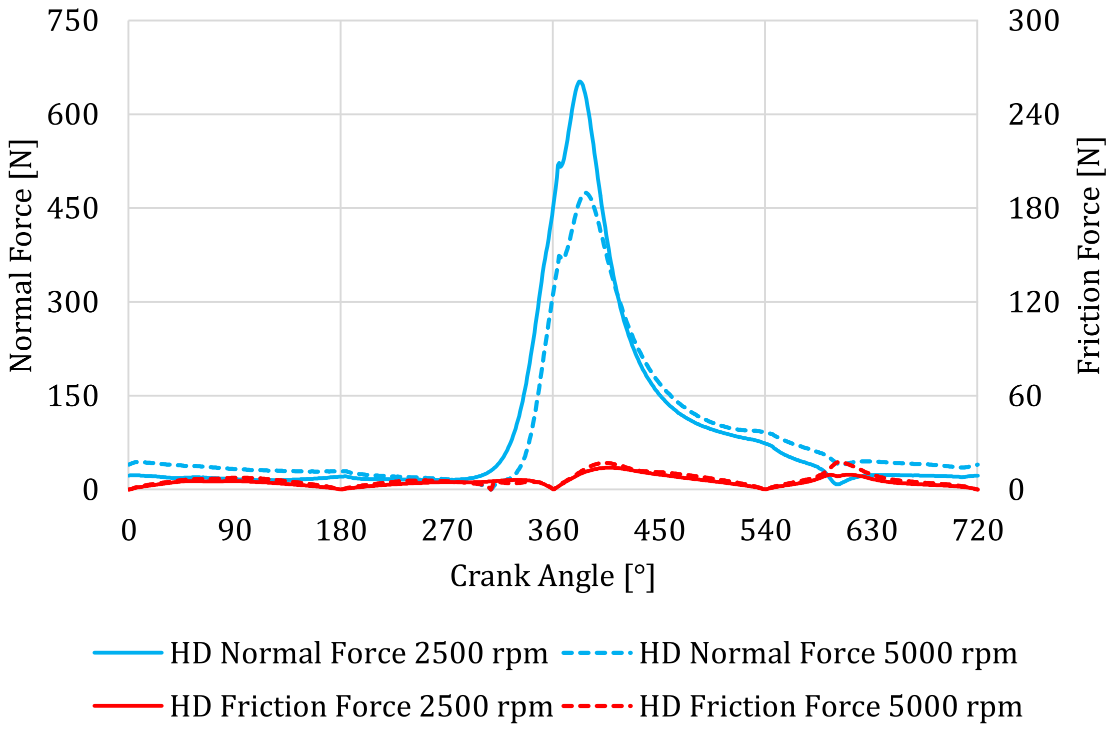

Figure 76 Hydrodynamic forces acting on the compression ring profile

Note that the values of the viscous friction forces in the axial direction are displayed in an absolute measure, the directional change of their acting resulting from the reciprocal motion of the piston is omitted.

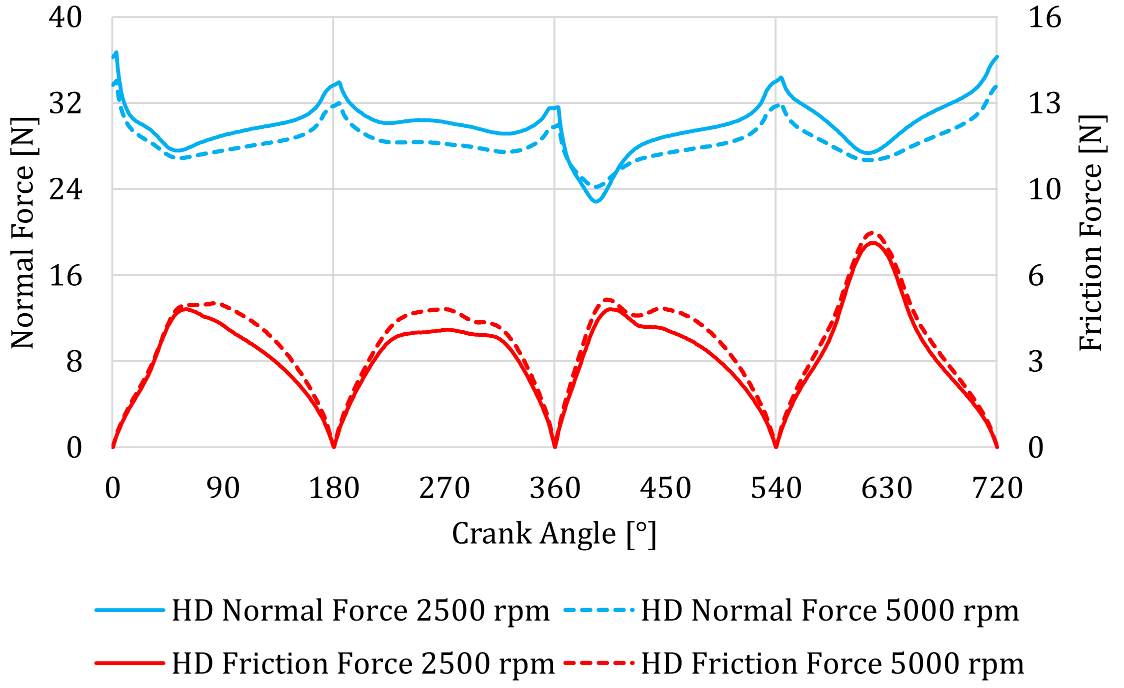

Figure 77 Hydrodynamic forces acting on the scraper ring profile

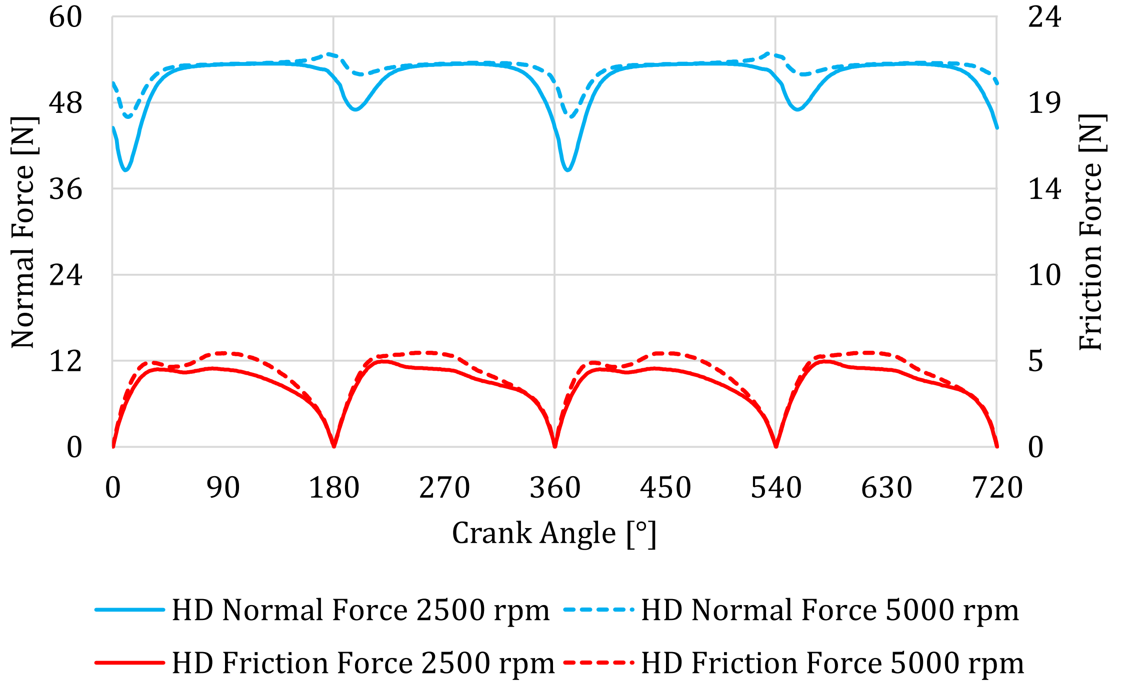

Figure 78 Hydrodynamic forces acting on the oil control ring profile

6.4.5 CONTACT FORCE

In cases when the conditions for the development of a complete load bearing HD pressure profile are not ideal – the radial load is higher than the capability of the oil film with a given viscosity in combination with the geometry and relative velocity of the surfaces to compensate the load – the relative distance between the bearing surfaces decrease, creating an additional, hydrodynamic (squeeze) pressure component. If the total hydrodynamic force component is still insufficient and the relative surface distance further decreases, the radial load becomes partially carried by the contact pressure resulting from the elastic or elasto-plastic deformation of surface asperity peaks getting in contact with each other.

The built-in approach for the determination of asperity contact pressure is the theory of Greenwood and Tripp [48], for which the input parameters (based on the description in chapter 4.9.3) are partially obtained from the real surface scanning process, partially result from the material properties. Their values for the worn cylinder liner and worn piston ring pack are listed in Table 16.

Table 16 Surface parameters of the worn cylinder liner and ring pack

Parameter		Liner	CR	SR	OCR
Material		Grey Cast Iron	Chromium Steel	Grey Cast Iron	Chromium Steel
E	[GPa]	110	200	100	200
ν	[-]	0.26	0.30	0.21	0.30
β	[m]	7.33×10^{-7}	3.46×10^{-7}	3.46×10^{-7}	3.46×10^{-7}
η	[m^{-2}]	35.98×10^{-9}	39.02×10^{-9}	39.02×10^{-9}	39.02×10^{-9}
σ	[m]	0.31×10^{-6}	0.44×10^{-6}	0.44×10^{-6}	0.44×10^{-6}

Table 17 sums up the combined surface parameters entering the G&T calculation.

Table 17 Combined input parameters for the G&T calculation

Parameter		Liner + CR	Liner + SR	Liner + OCR
E'	[GPa]	77	55	77
β	[m]	5.38×10^{-7}	5.38×10^{-7}	5.38×10^{-7}
η	[m^{-2}]	37.50×10^{-9}	37.50×10^{-9}	37.50×10^{-9}
σ_s	[m]	0.54×10^{-6}	0.54×10^{-6}	0.54×10^{-6}
c_f	[-]	0.2	0.2	0.2

Since the experimental determination of the dry friction coefficient c_f of each real piston ring against a real cylinder liner will be part of the resuming future work on this topic, the current calculation of friction force was carried out with an averaged tabular value of friction coefficient between a piston ring pack and cylinder liner [7].

The resultant CT forces acting in the radial and axial directions for 2500 and 5000 rpm are shown in Figure 79 through Figure 81.

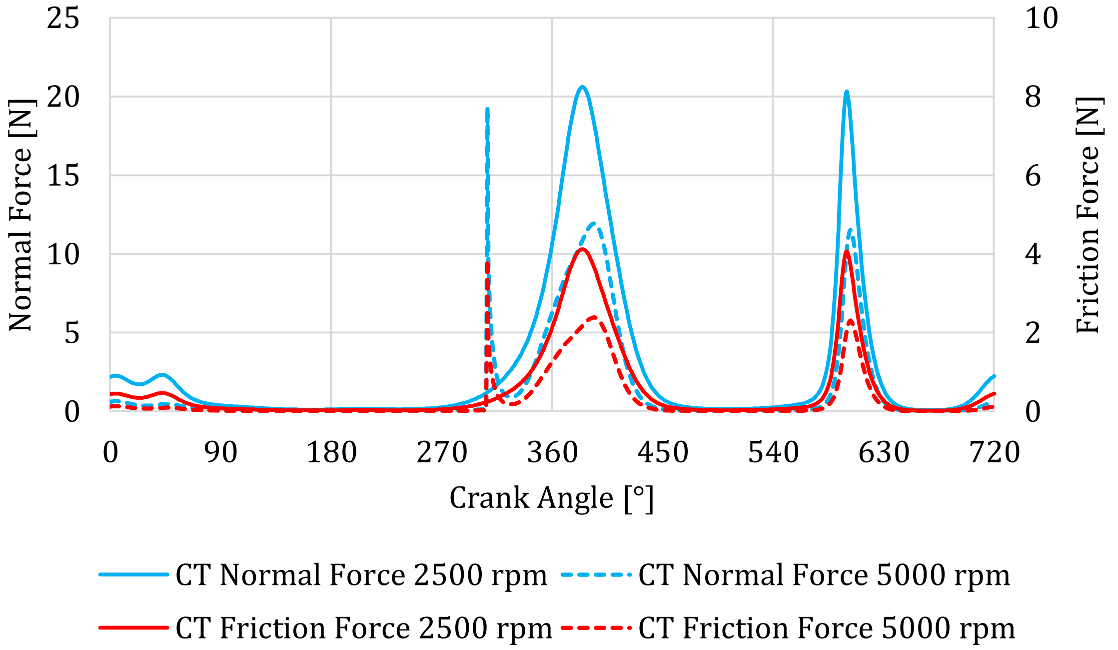

Figure 79 Asperity contact forces acting on the compression ring profile

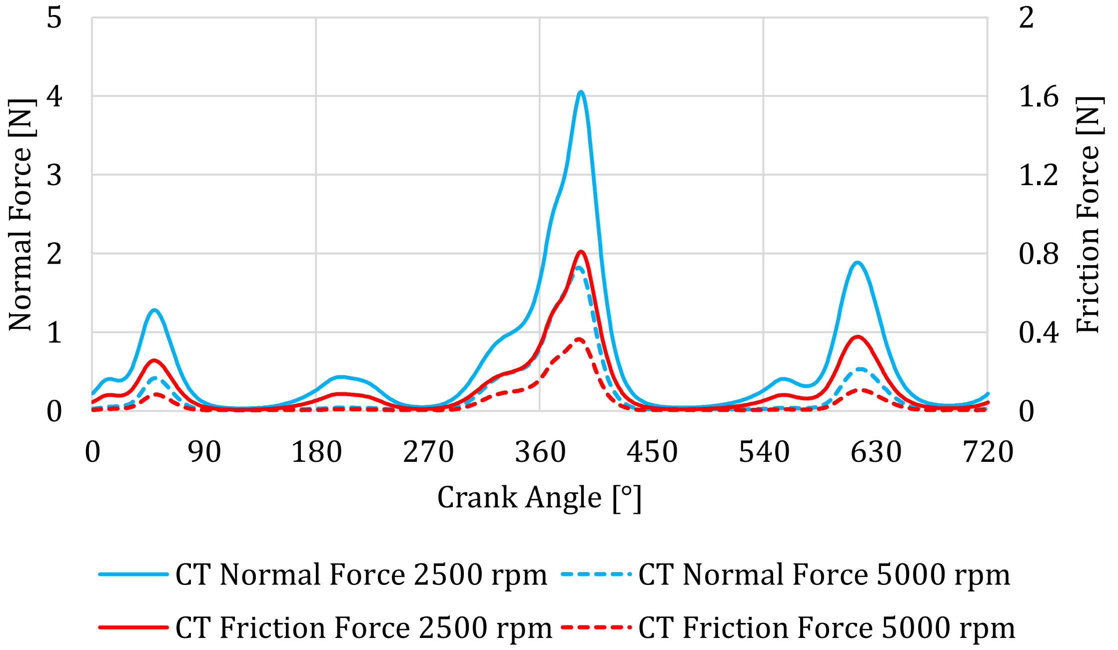

Figure 80 Asperity contact forces acting on the scraper ring profile

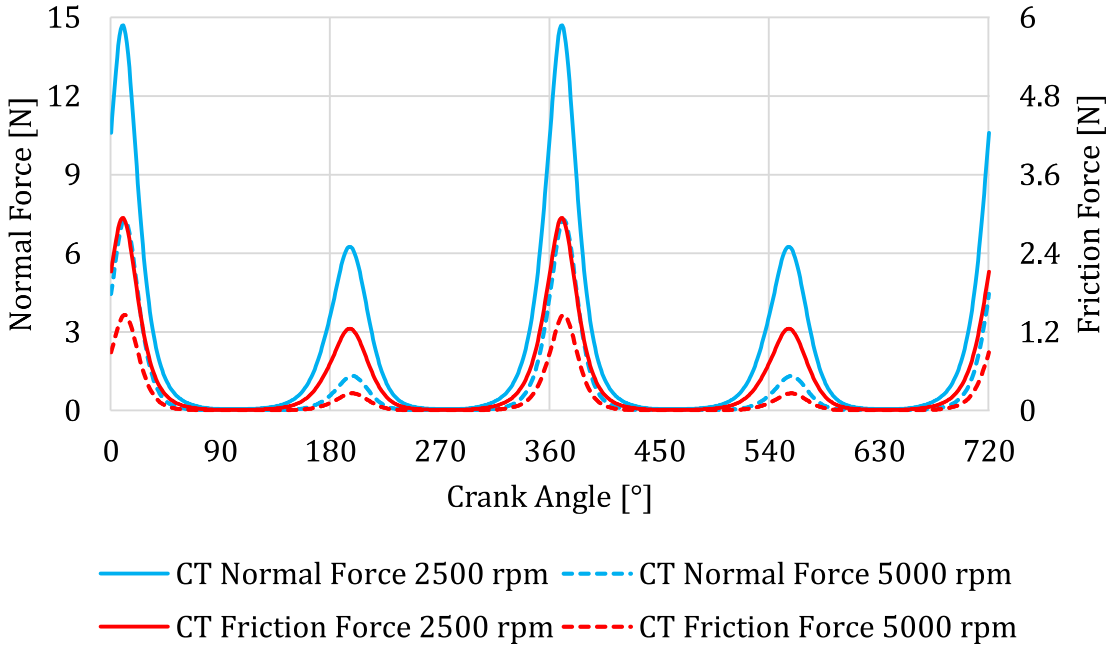

Figure 81 Asperity contact forces acting on the oil control ring profile

6.5 OIL FILM THICKNESS ON THE CYLINDER LINER

The flow balance calculation at the leading and trailing edge of each ring ensures, besides others, the correct determination of the oil film height left on the cylinder liner after the passage of a ring. The approach utilized in RingSIM considers the influence of the leading ring on the trailing one, as the oil height entering the control volume of the wetted area of the trailing ring equals to the height exiting the control volume of the leading ring's wetted area. This mutual interaction ensures the precise determination of the oil film thickness (OFT) left on the cylinder liner after the passing of the complete ring pack in both directions of piston motion.

While the thickness left on the cylinder liner above the piston – by the compression ring – influences the measure of lubricating oil consumption and the subsequent lubricant supply of the compression ring during the upward piston stroke, then the oil film height left below the piston – by the oil control ring – influences the lubrication of the piston skirt.

When the piston reaches its TDC position, the simulation algorithm refills the oil layer height on the cylinder liner wall, which ensures a constant oil supply of the oil control ring during the downward stroke of the piston. This consideration conforms real life running condition of the engine.

Figure 82 shows the OFT left on the liner by the compression ring after the downward piston strokes, both the intake and expansion strokes.

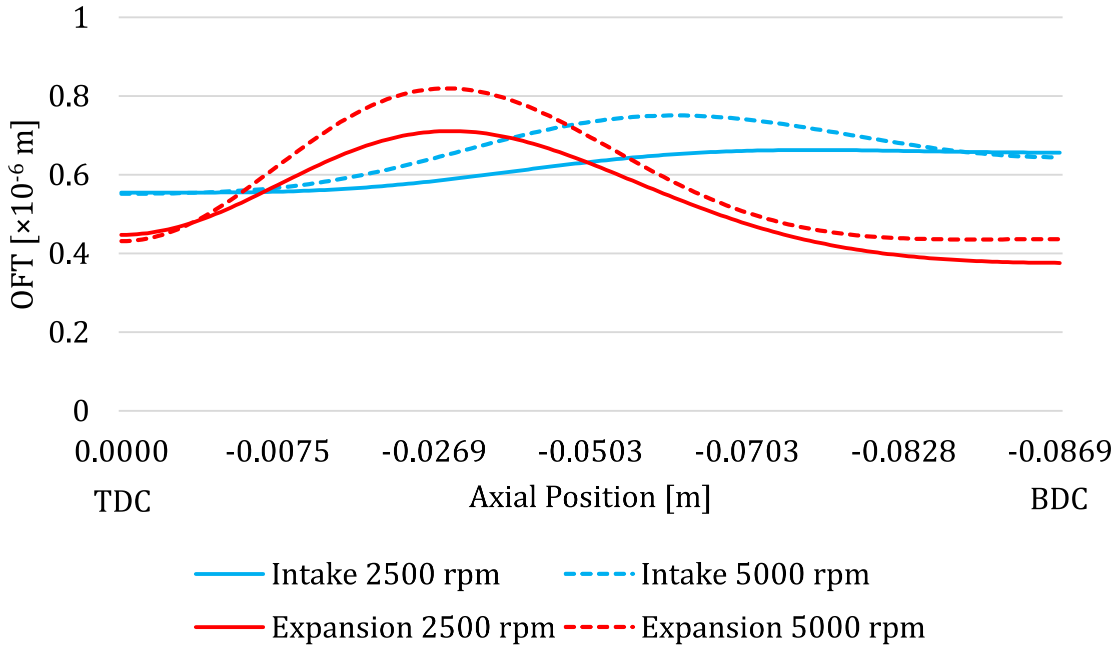

Figure 82 Oil film thickness left on the cylinder liner after the downward piston strokes

Figure 83 shows the OFT left on the liner by the oil control ring after the upward piston strokes, both the compression and exhaust strokes. As the oil control ring is not affected by the gas pressure variation, the course of OFT after the compression and exhaust strokes are identical for a given engine speed.

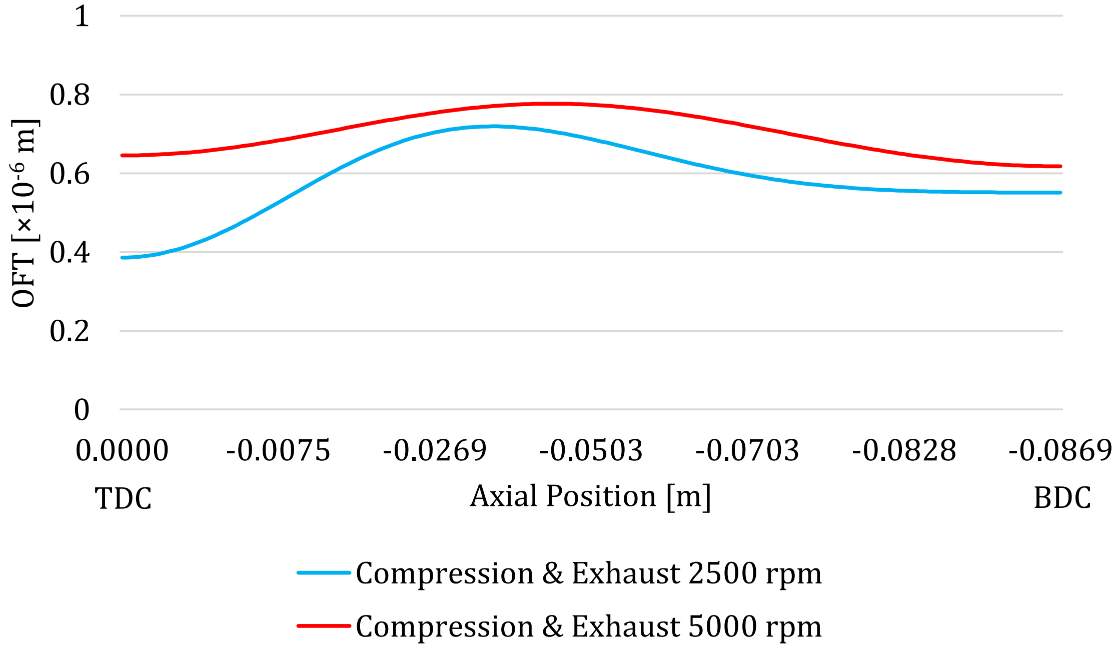

Figure 83 Oil film thickness left on the cylinder liner after the upward piston strokes

6.6 OIL CONSUMPTION

The amount of lubricating oil consumed over an engine cycle is calculated on the basis of the theory presented in detail in chapter 4.11. Operating parameters of the engine which influence the LOC were either experimentally determined or calculated. Other parameters impacting the measure of evaporated or thrown-off oil amount result from the physical and chemical properties of the specific lubricant. The investigation and experimental obtainment of these lubricant specific parameters were outside the scope of this thesis. The variables used for the generation of sample results for demonstration purposes of the developed oil consumption model within the frame of this dissertation were taken from other scientific publications with a proper quotation of their source.

6.6.1 EVAPORATION INDUCED LOC

The numerical expression and their method of the determination of input parameters fed into equation 79 follows.

The base stock of an engine oil consists of a broad range of aromatic and aliphatic hydrocarbons. A typical distribution of these compounds in a new motor oil sample by their weight percentage (wt %) is summarized in Table 18 [34].

Table 18 Lubricating oil base stock composition

Component	**Formula**	**Molar Weight** [g mol^{-1}]	**wt %** [%]
n-Octadecane	$C_{18}H_{38}$	254.50	3.69
n-Nonadecane	$C_{19}H_{40}$	268.52	4.03
n-Eicosane	$C_{20}H_{42}$	282.55	4.76
n-Heneicosane	$C_{21}H_{44}$	296.57	6.71
n-Docosane	$C_{22}H_{46}$	310.60	8.65
n-Tricosane	$C_{23}H_{48}$	324.63	10.06
n-Tetracosane	$C_{24}H_{50}$	338.65	9.96
n-Pentacosane	$C_{25}H_{52}$	352.68	9.60
n-Hexacosane	$C_{26}H_{54}$	366.71	8.59
n-Heptacosane	$C_{27}H_{56}$	380.73	8.25
n-Octacosane	$C_{28}H_{58}$	394.78	8.14
n-Nonacosane	$C_{29}H_{60}$	408.79	7.25
n-Triacontane	$C_{30}H_{62}$	422.83	5.91
n-Dotriacontane	$C_{32}H_{66}$	450.87	4.40
Weighted Average		350.18	

a) Specific Gas Constant

The specific gas constant of the lubricating oil vapor can be calculated from the weighted average of the base stock molar weight:

$$R_{vapor} = \frac{R_u}{MW_{oil}} = \frac{8.314\ \mathrm{J\ mol^{-1}\ K^{-1}}}{350.18\ \mathrm{g\ mol^{-1}}} = 23.75\times10^{-3}\ \mathrm{J\ g^{-1}\ K^{-1}}. \tag{122}$$

b) Diffusion Coefficient

For the calculation of the diffusion coefficient of the oil vapor, a refined, more precise form of the original Stokes-Einstein equation is used, which eliminates inaccuracies caused by e.g. the initial assumption of perfectly sphere shape of the molecules. The modified version of the relation incorporates the molar weights of the compounds, which is very suitable for the current solution. The utilized equation has a form of [41]:

$$D_{AB} = \frac{k_B\, T_{oil} \left(\frac{3\alpha}{2} + \frac{1}{1+\alpha} \right)}{6\,\pi\,\nu_{gas} \sqrt[3]{\frac{3\,MW_{oil}}{4\,\pi\,\rho_{eff}\,N_A}}}, \tag{123}$$

where

$$\alpha = \sqrt[3]{\frac{MW_{gas}}{MW_{oil}}}. \tag{124}$$

As the solvent of the diffusion process – the cylinder charge – air is considered, while the influence of cylinder pressure and temperature is incorporated in the value of instantaneous kinematic viscosity ν_{gas} of the cylinder charge. Constants fed into equations 123 and 124 are listed in Table 19.

Table 19 Variables of the diffusion coefficient calculation

Parameter	Symbol	Value	Units
Boltzmann constant	k_B	1.38×10^{-23}	[$\mathrm{m^2\ kg\ s^{-2}\ K^{-1}}$]
Avogadro number	N_A	6.02×10^{23}	[$\mathrm{mol^{-1}}$]
Effective density	ρ_{eff}	619.00	[$\mathrm{kg\ m^{-3}}$]
Molar weight (solute)	MW_{oil}	350.18	[$\mathrm{g\ mol^{-1}}$]
Molar weight (solvent)	MW_{gas}	28.96	[$\mathrm{g\ mol^{-1}}$]

c) Kinematic and Dynamic Viscosity

The kinematic viscosity of air for the actual pressure and temperature is calculated from its dynamic viscosity and density.

$$\nu_{gas} = \frac{\eta_{gas}}{\rho_{gas}}. \tag{125}$$

Since the dynamic viscosity of fluids is only dependent on their temperature, it can be calculated with the Sutherland viscosity law [73] from a reference temperature and viscosity:

$$\eta_{gas} = \eta_0 \sqrt{\left(\frac{T_{gas}}{T_0}\right)^3} \frac{T_0 + S}{T_{gas} + S}, \tag{126}$$

where S is an effective temperature. Coefficients for air are listed in Table 20 [26].

Table 20 Sutherland constants for air viscosity

Gas	η_0 [kg m^{-1} s^{-1}]	T_0 [K]	S [K]
Air	1.716×10^{-5}	273	111

The matching density is determined with the use of the equation of state of ideal gas:

$$\rho_{gas} = \frac{p_{gas}\, MW_{gas}}{R_u\, T_{gas}}. \tag{127}$$

d) Characteristic Length

The cylinder charge flow over the lubricant surface in the boundary layer is considered as a laminar flow over a flat plate, therefore the characteristic length of the flow is the circumference of the cylinder bore:

$$L = \pi\, D = \pi\, 0.0765\,\mathrm{m} \approx 0.2403\,\mathrm{m}. \tag{128}$$

e) Cylinder Charge Flow Speed

The flow speed of the cylinder charge is determined by the vector superposition of the tangential (swirl) and the axial component of the velocity according to equation 87. The axial component of flow is considered to be equal to the instantaneous axial velocity of the piston, while the tangential component is proportional to the engine speed [5]:

$$v_s = \frac{R_s\, \pi\, D\, n}{60}, \tag{129}$$

where R_s is a swirl ratio, D is the cylinder bore and n is the engine speed in [min^{-1}]. The swirl ratio is dependent on the geometry of the cylinder head, camshaft, valves, piston, etc., its precise determination for the simulated engine was outside the scope of this thesis. Therefore, a common value for production engines was used [12]:

$$R_s = 2.0\,. \tag{130}$$

f) Partial Pressure of Oil Vapor

The partial pressure of the evaporating oil vapor is the pressure at a given temperature at which the liquid and vapor phases are in equilibrium with each other. Since the base stock of the engine oil consists of a variety of hydrocarbon compounds, for the calculation of the partial pressure of the oil vapor the n-Pentacosane component has been chosen. The selection has been made based on the molecular weight, as the n-Pentacosane's molecular weight (352.68 g mol^{-1}) is almost identical to the weight averaged molecular weight of the complete base stock. Parameters of Antoine's equation (eq. 131) characterizing the n-Pentacosane for p_{vapor} [bar] and T_{vapor} [K] are listed in Table 21 [72].

$$\log_{10}\left(p_{vapor}\right) = A - \frac{B}{T_{vapor} + C}\,. \tag{131}$$

Table 21 Antoine equation parameters for n-Pentacosane

Hydrocarbon	***A*** [-]	***B*** [-]	***C*** [-]
n-Pentacosane	6.65073	4317.287	-14.252

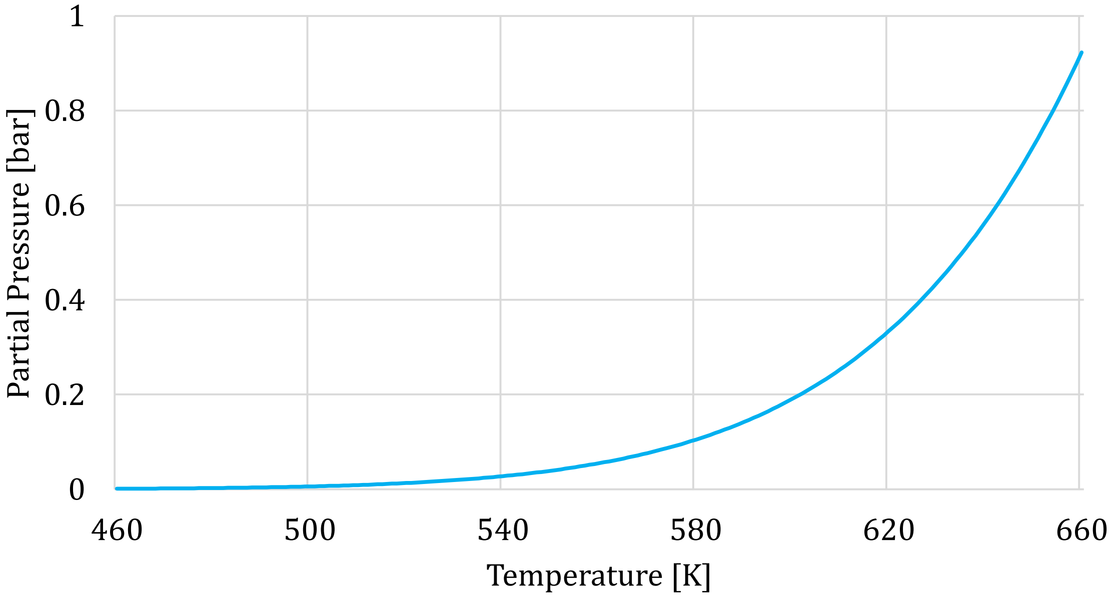

Figure 84 Partial pressure of the n-Pentacosane vapor

g) Oil Film Temperature

A significant influence on the measure of evaporated oil mass has also the temperature of the oil film surface. Its determination is governed by boundary conditions like the cylinder liner temperature, cylinder charge temperature above the oil film surface and other thermo-chemical parameters of the lubricant. For the complete definition of the necessary input parameters the constant pressure specific heat capacity of the cylinder charge is also required for the calculation of the dimensionless Prandtl number:

$$\mathrm{Pr} = \frac{\eta \, c_p}{\lambda}. \tag{132}$$

Its value is listed in Table 22 [10].

Table 22 Isobaric specific heat capacity

Substance	**c_p** [J kg^{-1} K^{-1}]
Air	1121

h) Evaporated Oil Mass Flow

Based on the calculation algorithm described in chapter 4.11.1 and the numerical expression of the input parameters, sample results of the oil evaporation are shown in Figure 85.

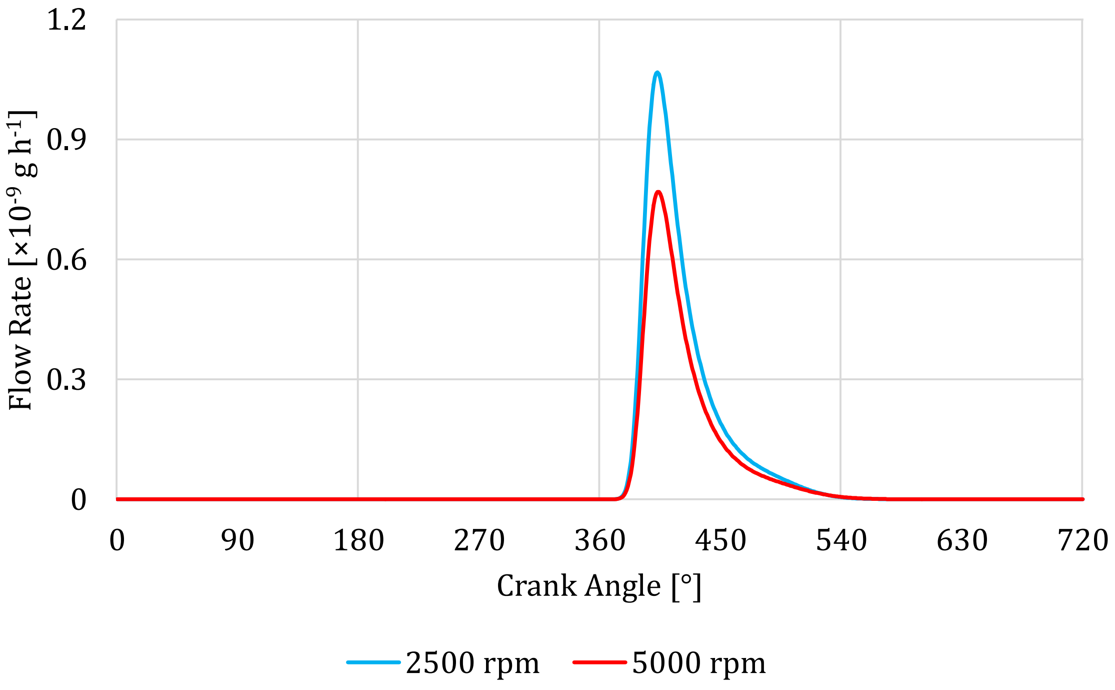

Figure 85 Oil evaporation rate from cylinder liner surface

6.6.2 BLOW-BACK INDUCED LOC

The measure of lost oil from this source is mainly governed by the gas mass flow from the first piston land volume towards the combustion chamber, but also by the ratio of the oil film height deposited on the piston surface to the height of flowing gas above this lubricant layer. Since the average value of oil film height between the first and second ring left on the cylinder liner is approximately 1 μm, the same value had been chosen for the thickness on the piston surface. However this value is only approximate, its precise determination is outside the scope of the current thesis. The gas flow height is the residual gap between the oil film surface on the piston and the cylinder liner, including the consideration of the thermal expansion of the piston for the given loading condition. Sample results of the consumption rate due to gas blow-back is shown in Figure 86.

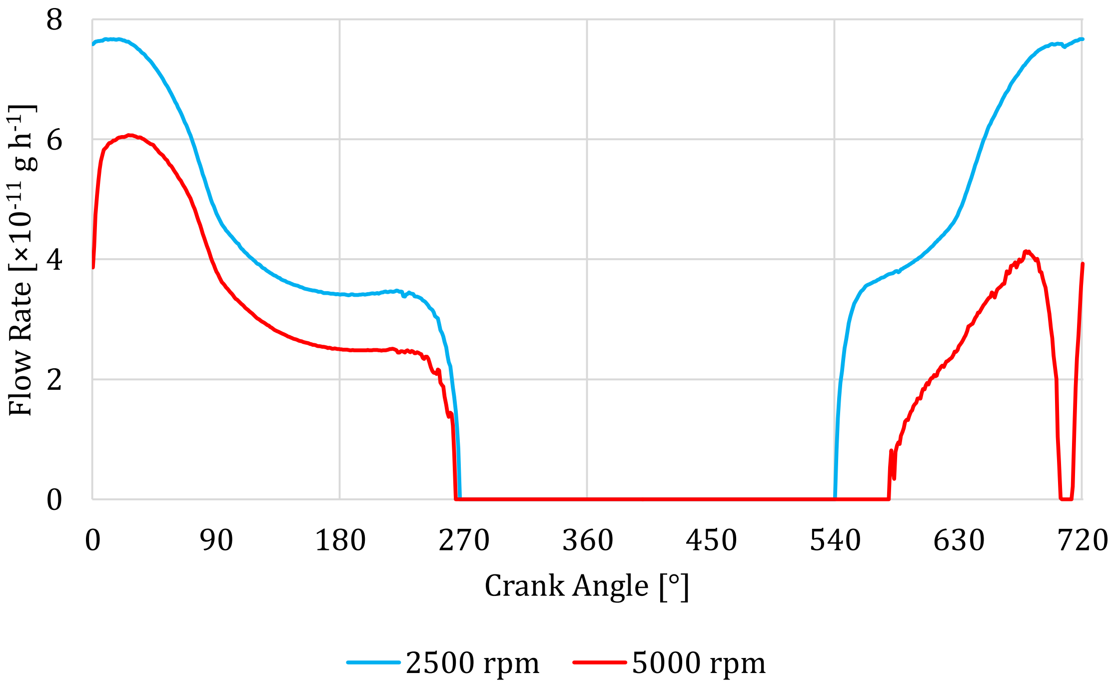

Figure 86 Oil consumption rate due to gas blow-back

6.6.3 THROW-OFF INDUCED LOC

The amount of thrown-off oil into the combustion chamber from the top ring's leading edge is the smallest contributor to the total oil consumption. This is due to the wetting conditions of the ring during the deceleration of its upward stroke. From Figure 64 and Figure 65 is visible, that the top ring's leading edge is never completely flooded, therefore only a tiny volume of oil underneath the converging edge is potentially exposed to be lost due to this phenomenon. The key parameter is the measure of deceleration of the piston, therefore the amount of thrown-off oil rises with increasing engine speed.

Another area of the piston assembly with oil scraping ability is the piston top land edge. In comparison with the top ring the amount of the scrapped and accumulated oil volume by the piston top land is more significant, therefore the quantity of oil thrown off from the piston top land area is also of higher measure [1], [15], [50]. This mechanism requires the detailed study and calculation of the piston dynamics, namely its secondary tilt motion and force decomposition. This area of interest is outside the scope of this thesis.

Sample results of the consumption rate due to oil throw-off is shown in Figure 87.

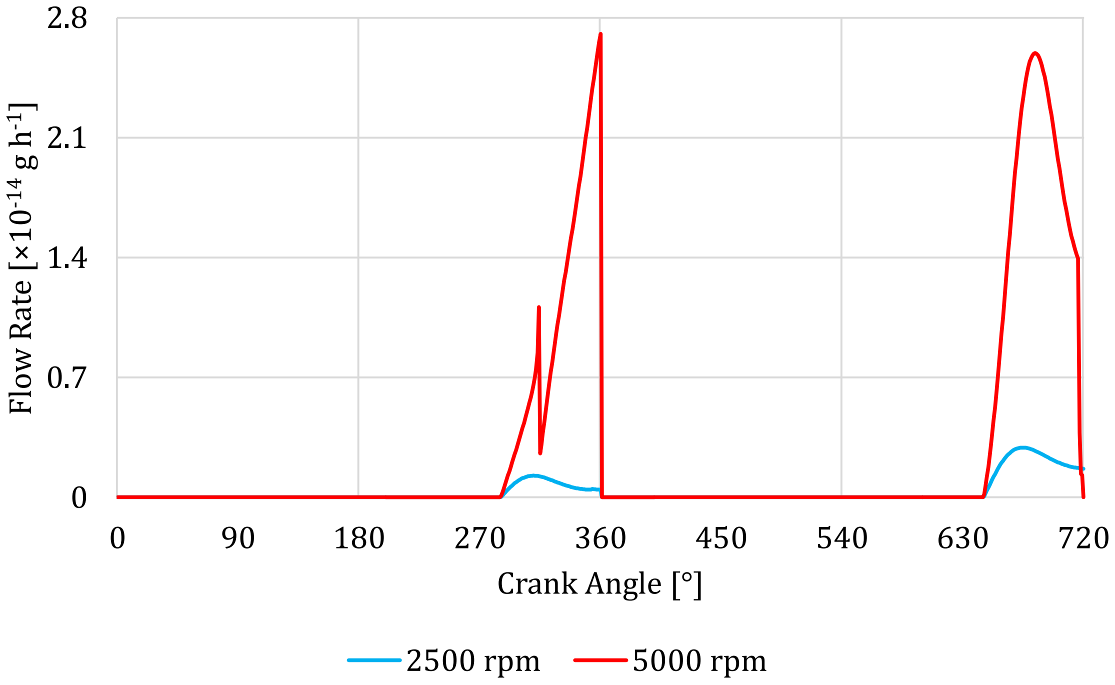

Figure 87 Oil consumption rate due to throw-off

6.6.4 TOTAL LUBRICANT OIL CONSUMPTION

The amount of total lubricant oil consumption influenced by the piston ring pack is the sum of the three partial sources. The numerical expression of their results for the complete engine speed range WOT running condition is summarized in Table 23 and graphically shown in Figure 88.

Table 23 Total lubricant oil consumption for WOT running condition

LOC		2500	3000	3500	4000	4500	5000
Evaporation	[g h^{-1}]	10.056	12.349	13.066	13.621	14.387	14.839
Blow-Back	[g h^{-1}]	2.937	4.053	4.694	5.611	6.083	6.150
Throw-Off	[×10^{-4} g h^{-1}]	0.511	1.474	2.414	4.668	7.787	9.341
Total	[g h^{-1}]	12.993	16.402	17.760	19.232	20.471	20.990

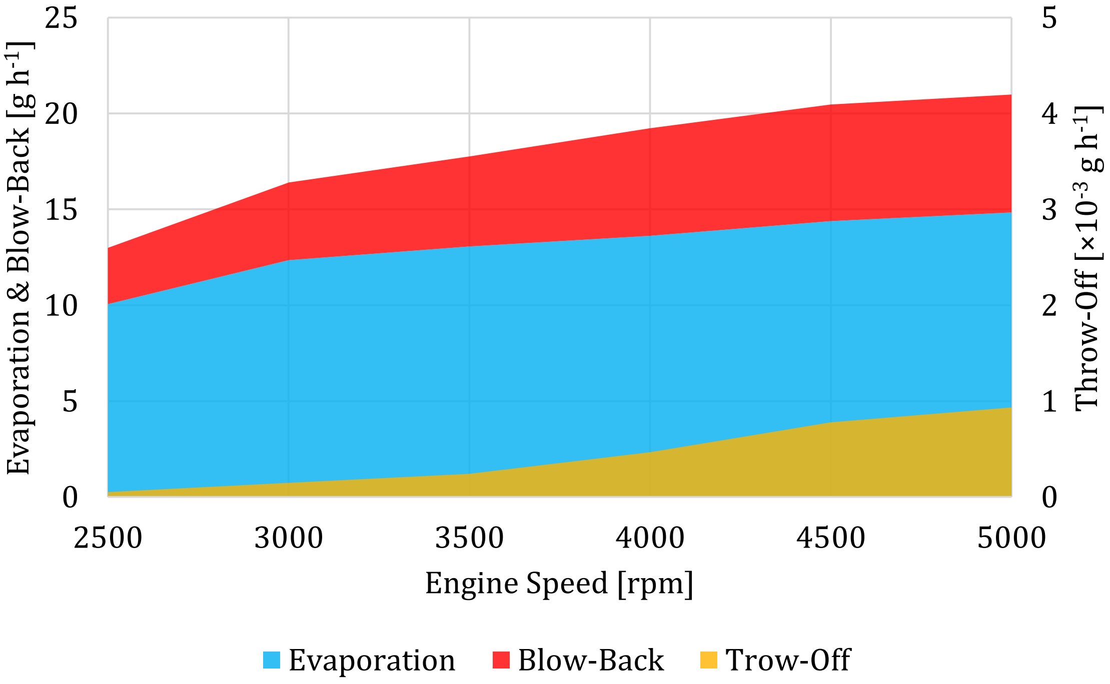

Figure 88 Total amount of lubricant oil consumption at WOT condition

7 PARAMETER STUDIES

Convenient industrial application of the developed simulation tool provides the option of parameter study execution, which could indicate the influence of key design parameters or material properties on the resulting performance. These studies can either be used for the optimization process of newly designed parts or the performance evaluation of existing components under different conditions. For demonstration, the effect of different oil properties and surface structure on the friction losses have been chosen.

7.1 VISCOSITY INFLUENCE ON FRICTION

A modern trend of lowering the global friction losses of an ICE is to reduce the viscous friction forces in the lubricant layer. This could be achieved by lowering the viscosity grade of the specified oil for the given engine. The potential influence of this approach on the investigated engine's performance is shown by comparing the simulated results for oils of viscosity grades 0W30 and 0W20 with the baseline 5W40. The values of dynamic viscosity under the CR profile for 2500 rpm WOT running condition are compared in Figure 89.

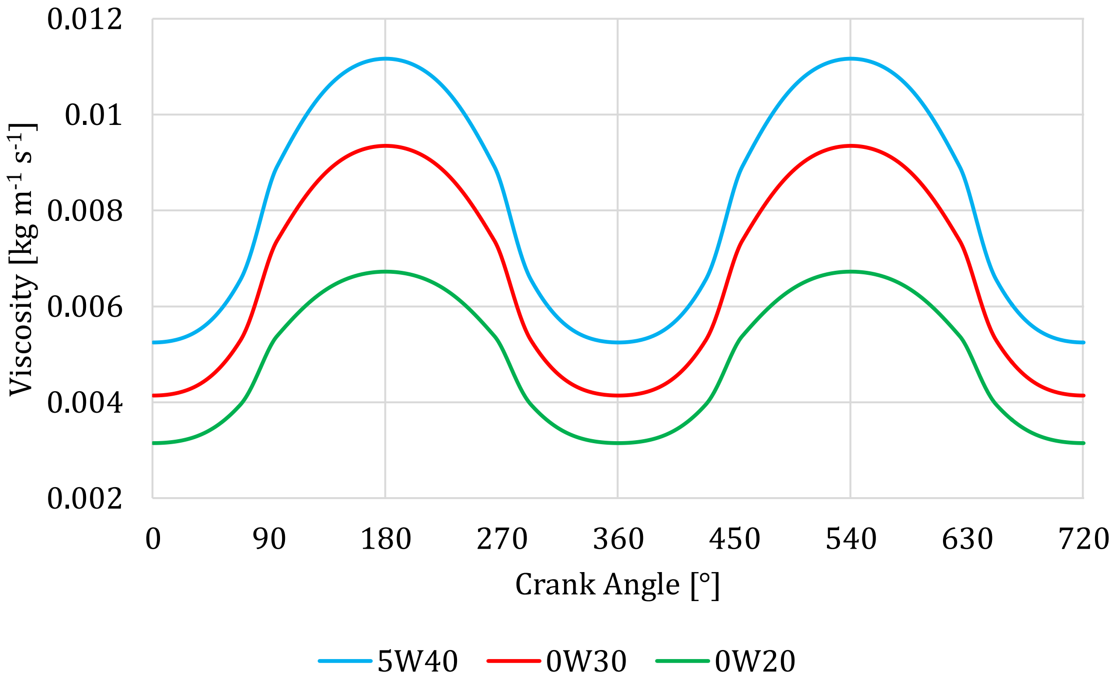

Figure 89 Comparison of dynamic viscosities under the CR profile at 2500 rpm WOT

Viscosity parameters for the Vogel equation are listed in Table 24.

$$\eta(T) = a\, e^{\frac{b}{T-c}}. \tag{133}$$

Table 24 Vogel parameters of the compared engine oils

Viscosity Grade	*a* [N s m^{-2}]	*b* [-]	*c* [-]
5W40	2.703×10^{-4}	723.9	-90.08
0W30	9.735×10^{-5}	1041	-123.6
0W20	1.125×10^{-4}	889.1	-112.9

Different viscosity values mostly influence the HD load bearing ability of the built up pressure in the lubricant layer under the rings' profiles. The best way to show this difference is throughout the comparison of MOFT, values of the CR for 2500 rpm WOT condition are shown in Figure 90.

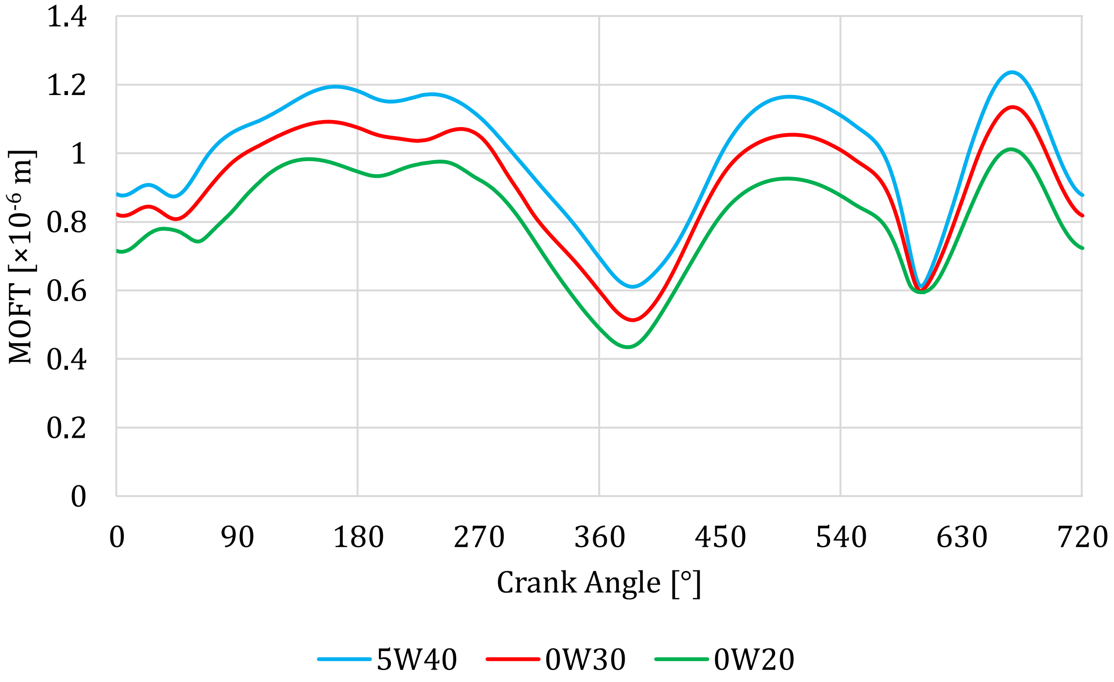

Figure 90 Comparison of the CR MOFT for different viscosities at 2500 rpm WOT

Besides affecting the oil film thickness distinct viscosity values also influence the viscous shear stress in the fluid film. Both parameters have a direct influence on the frictional losses. To be able to numerically express the deviations between the alternate versions throughout the whole engine speed, friction losses are ought to be expressed as friction mean effective pressures (fmep). Global fmep of the investigated engine is determined from the experimental results as a difference between the indicated mean effective pressure (imep) and brake mean effective pressure (bmep). The bmep can be calculated according to relation [5]:

$$\text{bmep} = \frac{60\, P_e}{V_d\; n\, \tau\, i}, \tag{134}$$

where P_e is the measured effective engine power, V_d is the displacement of one cylinder, n is the engine speed in [min^{-1}], i is the number of cylinders and τ is the tact coefficient of an engine. For four-stroke engines:

$$\tau = 0.5. \tag{135}$$

The value of *imep* is calculated as the ratio of indicated work per engine cycle to the volumetric displacement of the engine [5]:

$$\text{imep} = \frac{W_i}{V_d}. \tag{136}$$

The indicated work per engine cycle equals to the sum of works in each partial engine stroke, which can be determined from the *p*-*V* diagram for every engine speed individually. Sample *p*-*V* diagram for 2500 rpm WOT is shown in Figure 91.

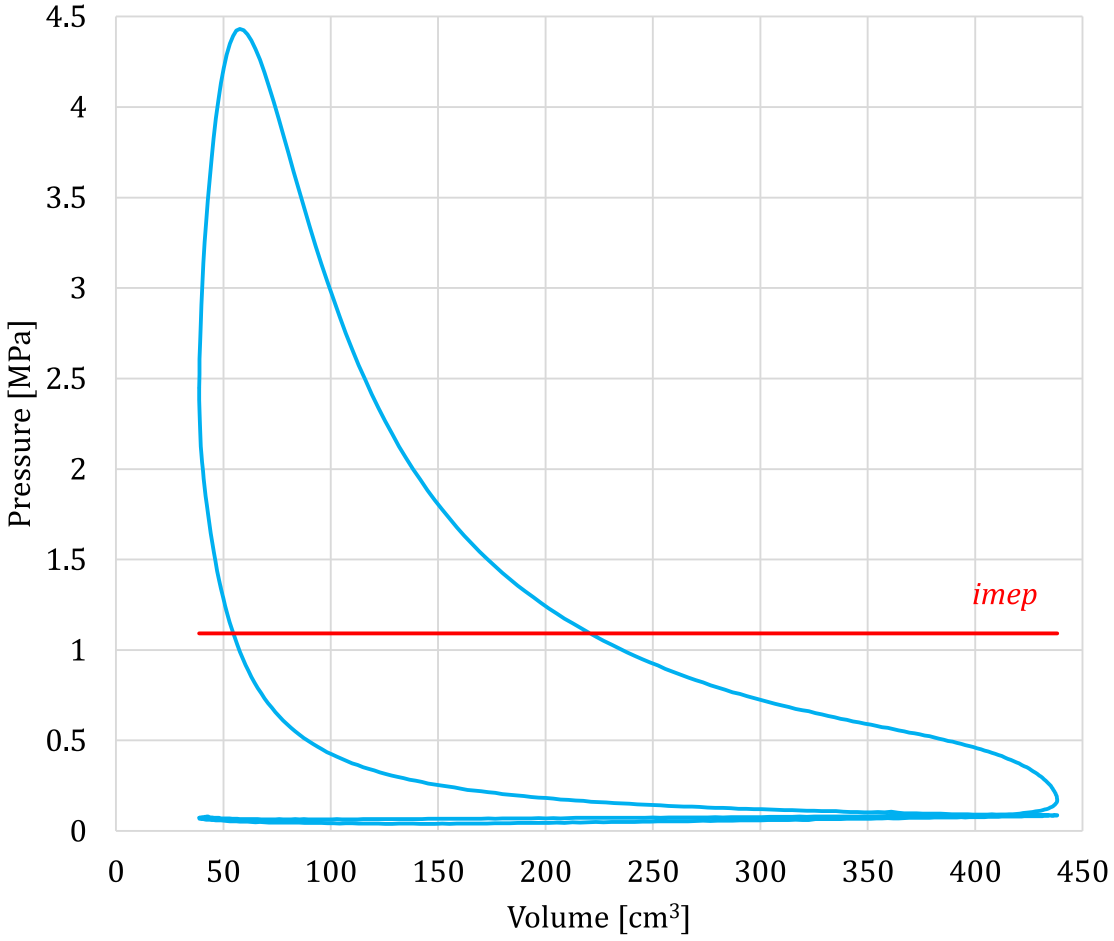

Figure 91 p-V diagram of the Škoda EA111 engine for 2500 rpm WOT

The friction mean effective pressure then equals to the difference between the indicated and brake mean effective pressure:

$$\mathrm{fmep} = \mathrm{imep} - \mathrm{bmep}\,. \tag{137}$$

Resultant values of mean effective pressures and mechanical efficiency of the Škoda EA111 engine for WOT running conditions are summarized in Table 25 and Figure 92.

Table 25 Mean effective pressures and mechanical efficiency at WOT

Parameter		**2500**	**3000**	**3500**	**4000**	**4500**	**5000**
imep	[kPa]	1092.09	1152.31	1079.34	1030.09	920.37	824.71
bmep	[kPa]	1017.47	1065.54	983.99	921.08	812.06	716.63
fmep	[kPa]	74.62	86.77	95.34	109.02	108.31	108.08
$\boldsymbol{\eta}$	[%]	93.17	92.47	91.17	89.42	88.23	86.90

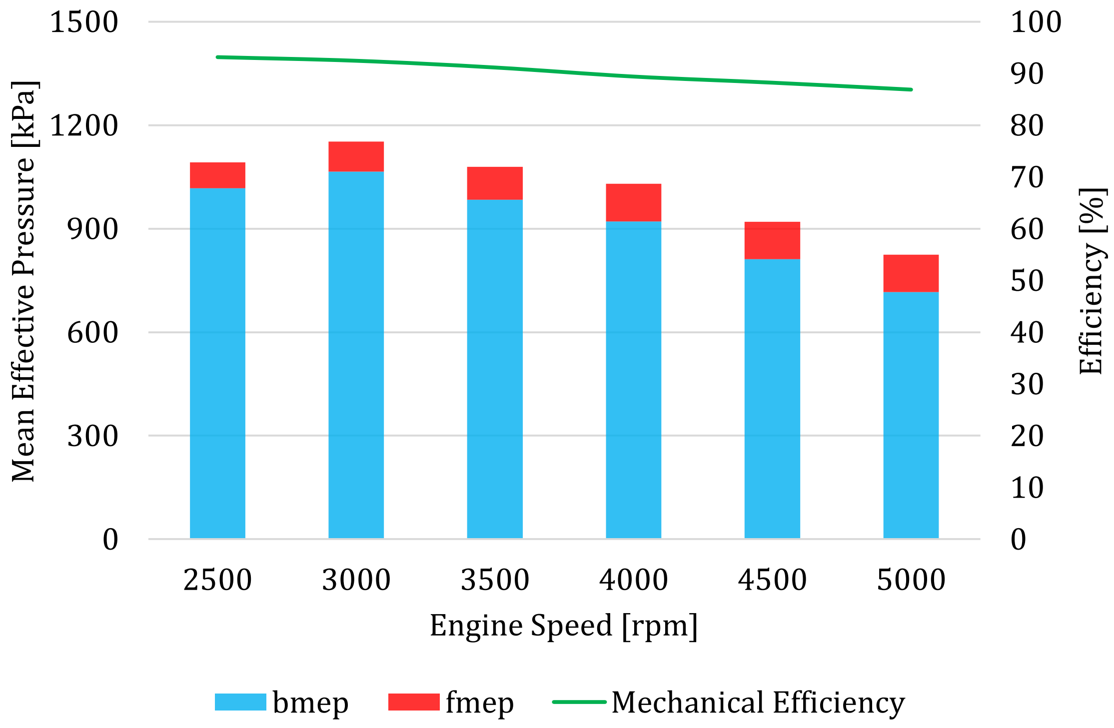

Figure 92 Mean effective pressures and mechanical efficiency at WOT

The friction mean effective pressures of the complete ring pack with the three different viscosity grade oils are listed in Table 26 through Table 28. Values of the HD and CT fmep represent the cumulative friction losses due to hydrodynamic and asperity contact friction, respectively. The complete results of ring friction power loss are included in Appendix H.

Table 26 Friction mean effective pressures of the ring pack with 5W40 oil at WOT

fmep		**2500**	**3000**	**3500**	**4000**	**4500**	**5000**
CR	[kPa]	6.09	6.29	6.60	6.80	6.65	6.78
SR	[kPa]	3.72	3.80	3.83	3.99	4.00	4.05
OCR	[kPa]	7.24	7.35	7.53	7.77	7.88	8.01
Total	[kPa]	17.05	17.44	17.90	18.55	18.53	18.84

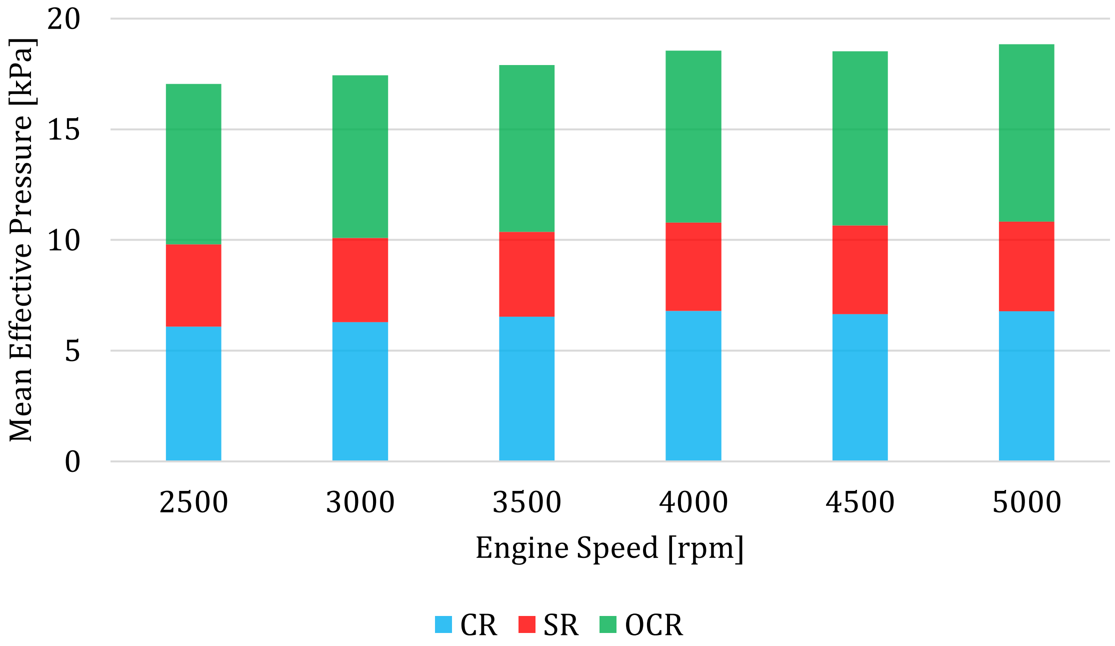

Figure 93 Friction mean effective pressure share of the rings with 5W40 oil at WOT

The comparison of the performance of the other two viscosities is made by the determination of the deviation of the total fmep of the piston ring pack from the values obtained with the baseline 5W40 viscosity grade oil.

Table 27 Friction mean effective pressures of the ring pack with 0W30 oil at WOT

fmep		**2500**	**3000**	**3500**	**4000**	**4500**	**5000**
CR	[kPa]	5.92	5.80	6.27	6.47	6.13	6.36
SR	[kPa]	3.64	3.59	3.77	3.78	3.95	3.80
OCR	[kPa]	7.14	7.18	7.27	7.41	7.47	7.55
Total	[kPa]	16.71	16.58	17.30	17.66	17.55	17.70
Deviation	[%]	-2.00	-4.94	-3.35	-4.82	-5.26	-6.03

Table 28 Friction mean effective pressures of the ring pack with 0W20 oil at WOT

fmep		**2500**	**3000**	**3500**	**4000**	**4500**	**5000**
CR	[kPa]	6.06	6.34	6.49	6.35	5.95	5.99
SR	[kPa]	3.64	3.66	3.66	3.62	3.60	3.57
OCR	[kPa]	7.27	7.21	7.16	7.16	7.17	7.18
Total	[kPa]	16.97	17.21	17.31	17.13	16.71	16.74
Deviation	[%]	-0.44	-1.33	-3.29	-7.68	-9.81	-11.17

Comparison of the total fmep of the complete piston ring pack for all three evaluated oils is shown in Figure 94.

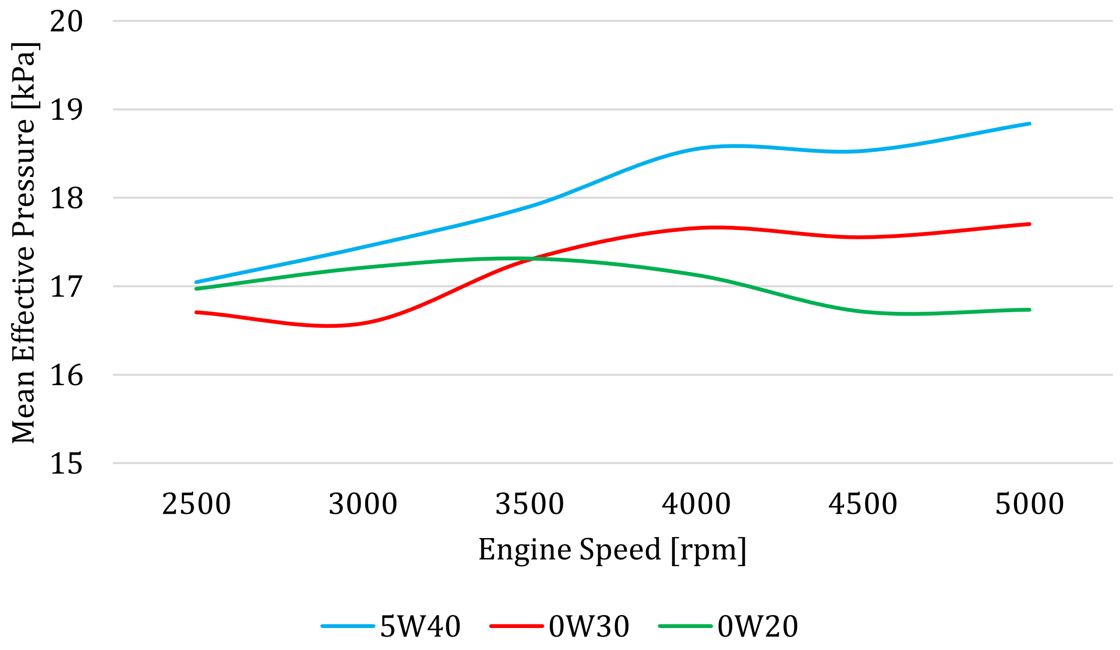

Figure 94 Total friction mean effective pressures of the piston ring pack at WOT

From the numerical results is visible, that the tested oils of lower viscosities expel reduced frictional losses, just as expected. On the other hand, notice the course of fmep for viscosity grade 0W20. In comparison with 0W30, which shows an almost constant deviation from the baseline values, these results are almost identical to the baseline values at low engine speeds, while with increasing engine speed their deviation progressively rises. To understand and justify this behavior we must look at the share of hydrodynamic and asperity contact friction to the total fmep.

The numerical expressions of hydrodynamic fmep are summarized in Table 29 and Figure 95.

Table 29 Hydrodynamic friction mean effective pressures at WOT

HD fmep		2500	3000	3500	4000	4500	5000
5W40	[kPa]	15.74	16.45	17.19	17.89	17.96	18.42
0W30	[kPa]	15.07	15.22	16.02	16.62	16.59	16.99
0W20	[kPa]	13.86	14.41	14.78	15.26	15.11	15.50

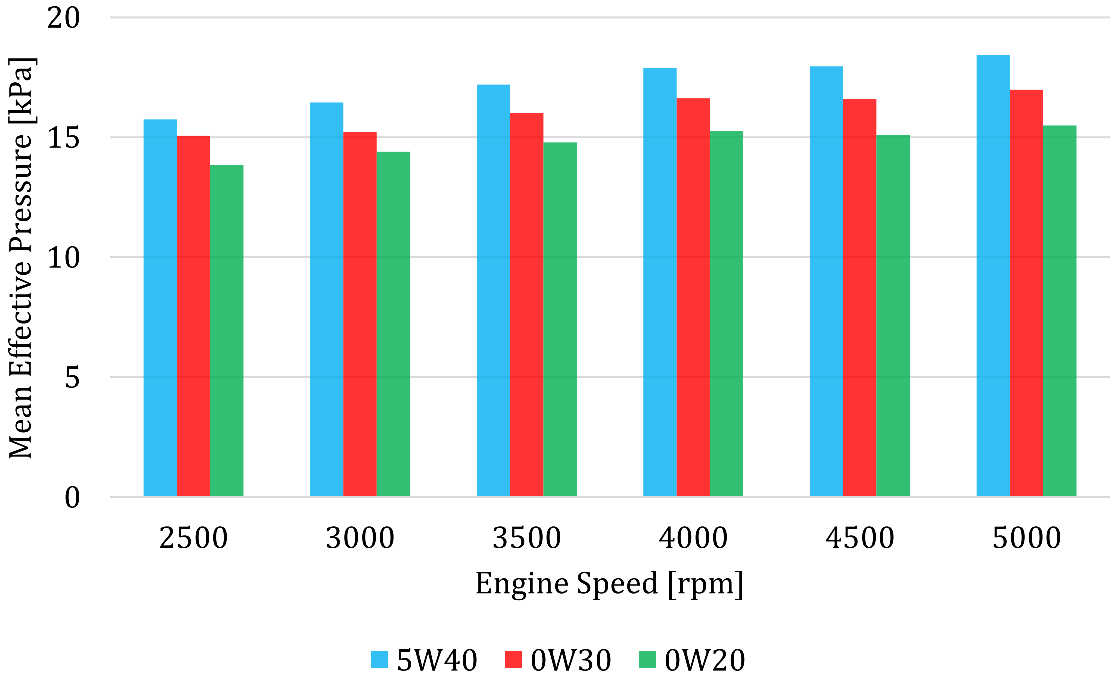

Figure 95 Friction mean effective pressures due to viscous friction at WOT

The numerical expressions of asperity contact fmep are summarized in Table 30 and Figure 96.

Table 30 Asperity contact friction mean effective pressures at WOT

CT fmep		2500	3000	3500	4000	4500	5000
5W40	[kPa]	1.30	0.99	0.77	0.66	0.58	0.42
0W30	[kPa]	1.64	1.36	1.28	1.03	0.97	0.71
0W20	[kPa]	3.12	2.80	2.53	1.86	1.60	1.24

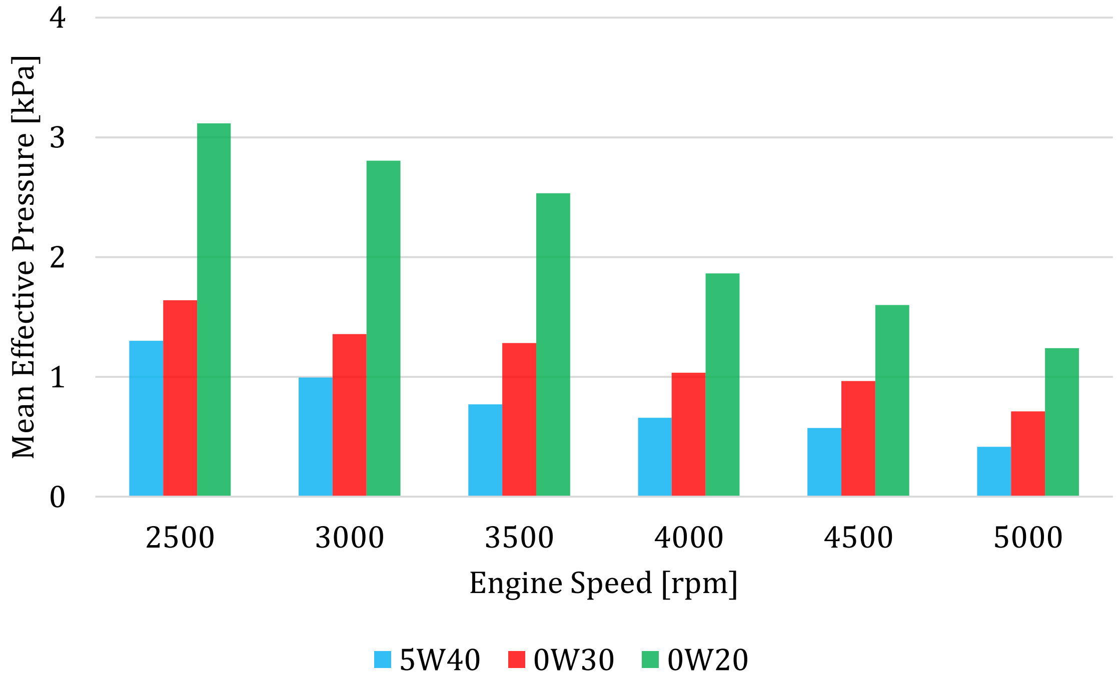

Figure 96 Friction mean effective pressures due to asperity contact friction at WOT

The individual interpretation of the viscous and asperity contact friction mean effective pressures reveals the cause of behavior of each fmep course. That lower viscosities result in the decrease of load bearing capacity of the hydrodynamic lubrication layer. This circumstance induces lower minimum oil film thicknesses under the rings' profiles, which result in higher overall friction losses due to asperity contact. On the other hand, lower viscosity values decrease the friction losses induced by the viscous shear stress in the lubricant. The resultant difference induced by the change in viscosity then equals to the superposition of the individual variations of friction loss.

In the case of viscosity grade 0W30, the decrease of minimum oil film thickness is small enough to keep the effect of viscous friction loss reduction prevailing against the increased asperity contact friction loss throughout the whole engine speed range. The results of viscosity grade 0W20, however, showed that the loss of load bearing capacity and the resulting asperity contact friction increase already overpowered the positive outcome of viscous friction decrease in lower engine speed range. On the other hand at higher engine speeds, when the hydrodynamic lubrication regime regains dominance, the advantage of lower viscosity lubricant becomes significant.

Based on the results one can conclude, that the current geometrical and mechanical properties of the piston ring pack can profit from the change of the baseline 5W40 viscosity grade oil to 0W30 throughout the calculated engine speed range, while results of viscosity grade 0W20 have shown that the current ring pack configuration is not able to take the full advantage of its utilization. Also keeping in mind that an increased measure of asperity contact friction results in raised wear rate of the components.

7.2 SURFACE STRUCTURE INFLUENCE ON FRICTION AND LOC

Surface parameters of a lubricated contact pair influence both the hydrodynamic and asperity contact friction properties. The HD pressure development in the wetted area of the bearing is affected by the magnitude of flow factors, which are dependent on the directional orientation of the coupled rough surface pair. The asperity contact pressure, on the other hand, is proportional to the descriptive parameters of surface roughness and the mechanical properties of the materials in contact.

Within the frame of this thesis, different surface structures were experimentally obtained only for the compression ring. Therefore, the influence of this attribute is only evaluated on this type of ring.

7.2.1 IMPACT ON HYDRODYNAMIC LUBRICATION

The baseline pairing of the piston ring – cylinder liner was made with both worn surfaces, as presented in chapter 6.4.4. To evaluate the influence of different surface coatings, three different unworn piston rings and the unworn surface of a matching cylinder liner were observed with the use of a 3D optical microscope. Surface coatings of the rings included gas nitridation (N) and physical vapor deposition of chromium nitride (CrN) and diamond-like carbon (DLC). The individual surfaces and their properties are shown in chapter 5.2. However, more important from the hydrodynamic point of view are the resultant flow factors arising from their pairing.

Flow factors of the unworn cylinder liner and nitrided piston ring coupling are shown in Figure 97.

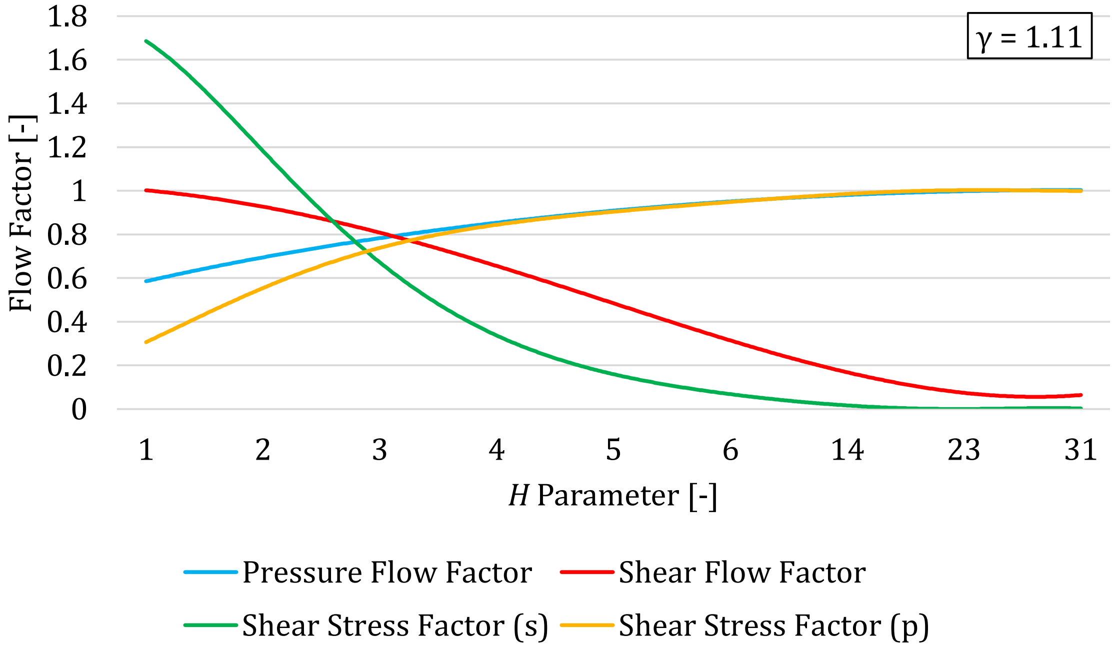

Figure 97 Flow factors of the unworn cylinder liner – nitrided piston ring

Flow factors of the unworn cylinder liner and chromium nitrided piston ring coupling are shown in Figure 98.

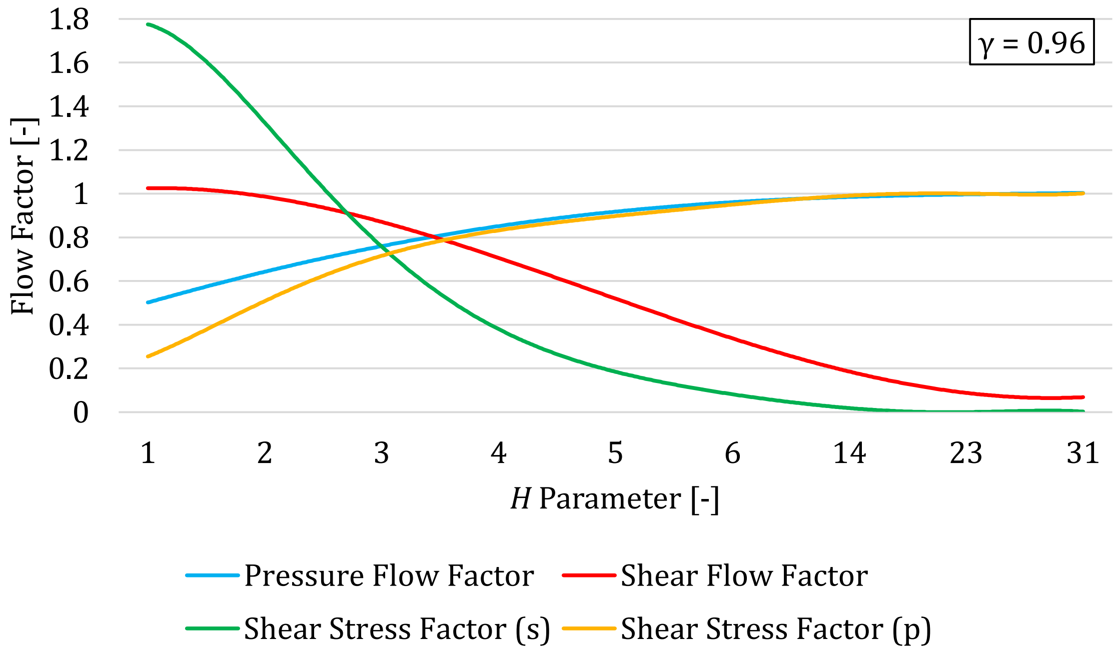

Figure 98 Flow factors of the unworn cylinder liner – chromium nitrided piston ring

Flow factors of the unworn cylinder liner and diamond-like carbon piston ring coupling are shown in Figure 99.

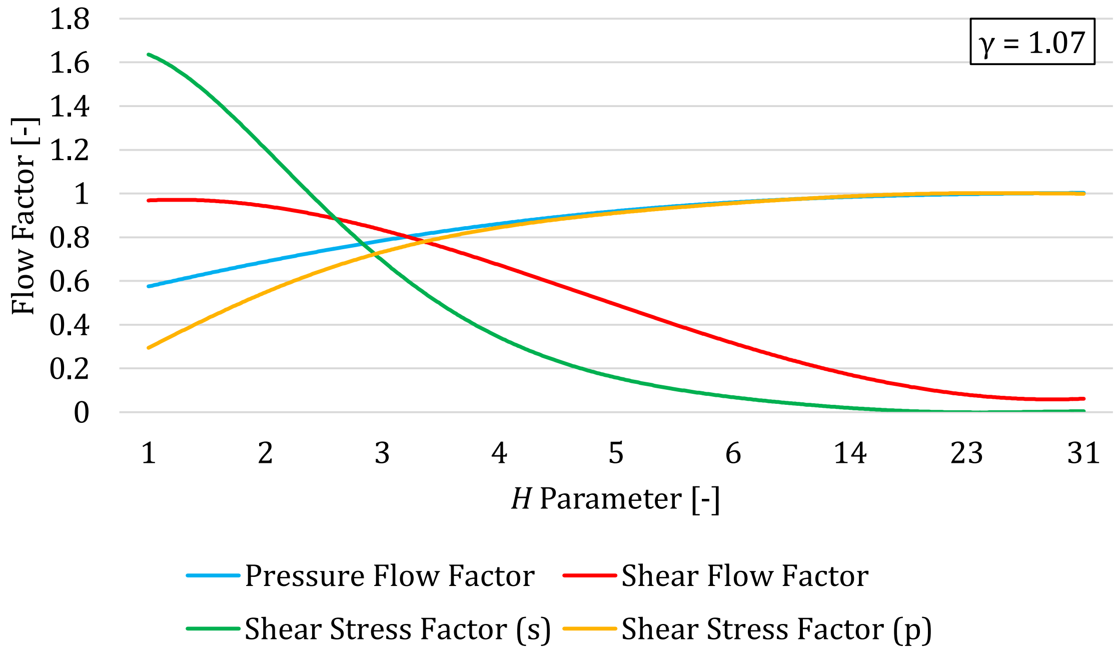

Figure 99 Flow factors of the unworn cylinder liner – diamond-like carbon piston ring

Though the technological process of surface finish results in strong directional dependence of the individual unworn surfaces, the coupling of all three types of unworn ring structures with the unworn cylinder liner brought results close to isotropic surface topography with corresponding flow factor courses, as can be seen from the results

7.2.2 IMPACT ON ASPERITY CONTACT

Both statistical descriptive parameters of a surface structure and properties of the base material affect the development of asperity contact pressure and therefore the measure of resulting friction losses.

Surface and material parameters of the unworn components are summarized in Table 31.

Table 31 Surface parameters of the unworn cylinder liner and compression rings

Parameter		**Liner**	**N**	**CrN**	**DLC**
Material		Grey Cast Iron	Chromium Steel	Chromium Steel	Chromium Steel
E	[GPa]	110	200	200	200
ν	[-]	0.26	0.30	0.30	0.30
β	[m]	4.77×10^{-7}	10.61×10^{-7}	5.98×10^{-7}	6.45×10^{-7}
η	[m^{-2}]	47.12×10^{-9}	38.91×10^{-9}	35.74×10^{-9}	37.82×10^{-9}
σ	[m]	0.46×10^{-6}	0.24×10^{-6}	0.31×10^{-6}	0.25×10^{-6}

Combined surface parameters entering the asperity contact calculation based on the Greenwood & Tripp approach are summarized in Table 32.

Table 32 Combined surface parameters for the G&T calculation

Parameter		**Liner + N**	**Liner + CrN**	**Liner + DLC**
E'	[GPa]	77	77	77
β	[m]	7.69×10^{-7}	5.38×10^{-7}	5.61×10^{-7}
η	[m^{-2}]	43.02×10^{-9}	41.43×10^{-9}	42.47×10^{-9}
σ_s	[m]	0.36×10^{-6}	0.39×10^{-6}	0.37×10^{-6}
c_f	[-]	0.2	0.2	0.2

7.2.3 TOTAL IMPACT ON FRICTION

The simulations were conducted with the use of baseline (5W40) oil parameters. The obtained results of friction losses of the unworn compression rings were compared to the values of the baseline worn components presented in chapter 7.1.

Results are listed in Table 33 through Table 35.

Table 33 Friction mean effective pressures of the nitrided ring at WOT

fmep		**2500**	**3000**	**3500**	**4000**	**4500**	**5000**
HD	[kPa]	5.58	5.88	6.29	6.68	6.71	7.04
CT	[kPa]	0.40	0.36	0.34	0.30	0.21	0.17
Total	[kPa]	5.98	6.24	6.63	6.98	6.92	7.21
Deviation	[%]	-1.82	-0.80	0.52	2.75	4.05	6.35

Table 34 Friction mean effective pressures of the chromium nitrided ring at WOT

fmep		**2500**	**3000**	**3500**	**4000**	**4500**	**5000**
HD	[kPa]	6.17	6.50	6.94	7.34	7.30	7.40
CT	[kPa]	0.46	0.39	0.38	0.34	0.26	0.18
Total	[kPa]	6.63	6.89	7.32	7.68	7.56	7.59
Deviation	[%]	8.83	9.53	10.98	12.95	13.66	11.93

Table 35 Friction mean effective pressures of the diamond-like carbon ring at WOT

fmep		**2500**	**3000**	**3500**	**4000**	**4500**	**5000**
HD	[kPa]	5.81	6.07	6.48	6.90	6.88	7.22
CT	[kPa]	0.30	0.25	0.24	0.16	0.16	0.12
Total	[kPa]	6.11	6.32	6.72	7.06	7.04	7.34
Deviation	[%]	0.42	0.53	1.83	3.94	5.80	8.31

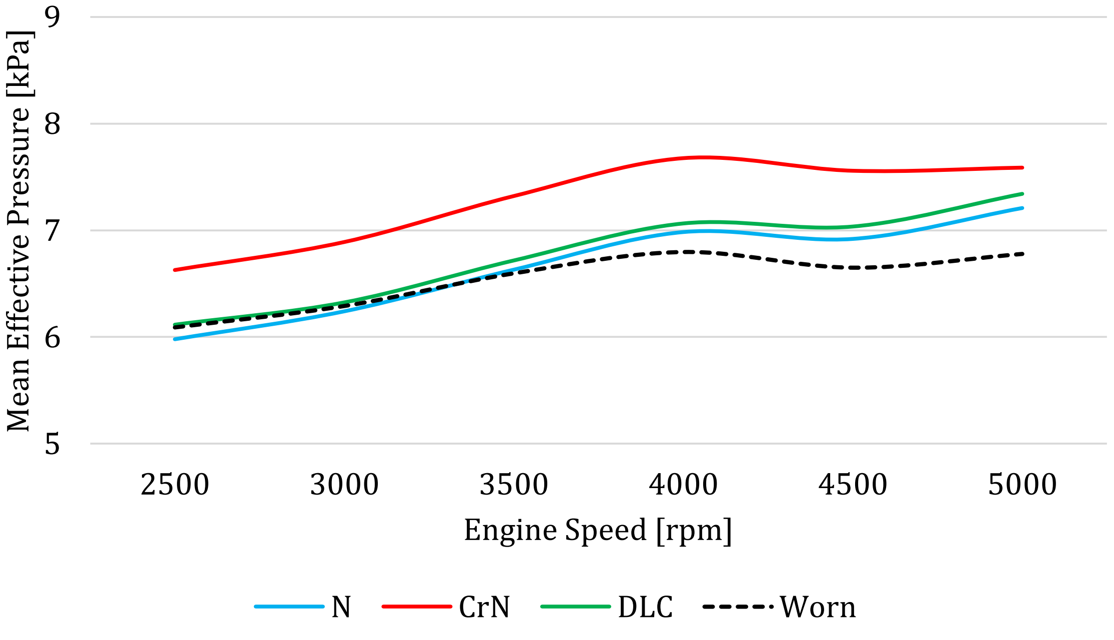

Figure 100 Comparison of fmep of compression rings with different coatings at WOT

For a comprehensive analysis of the final results of the total fmep shown in Figure 100, the best way is to take a look at the individual HD and CT components again. Values of the calculated friction power losses are shown in Appendix I.

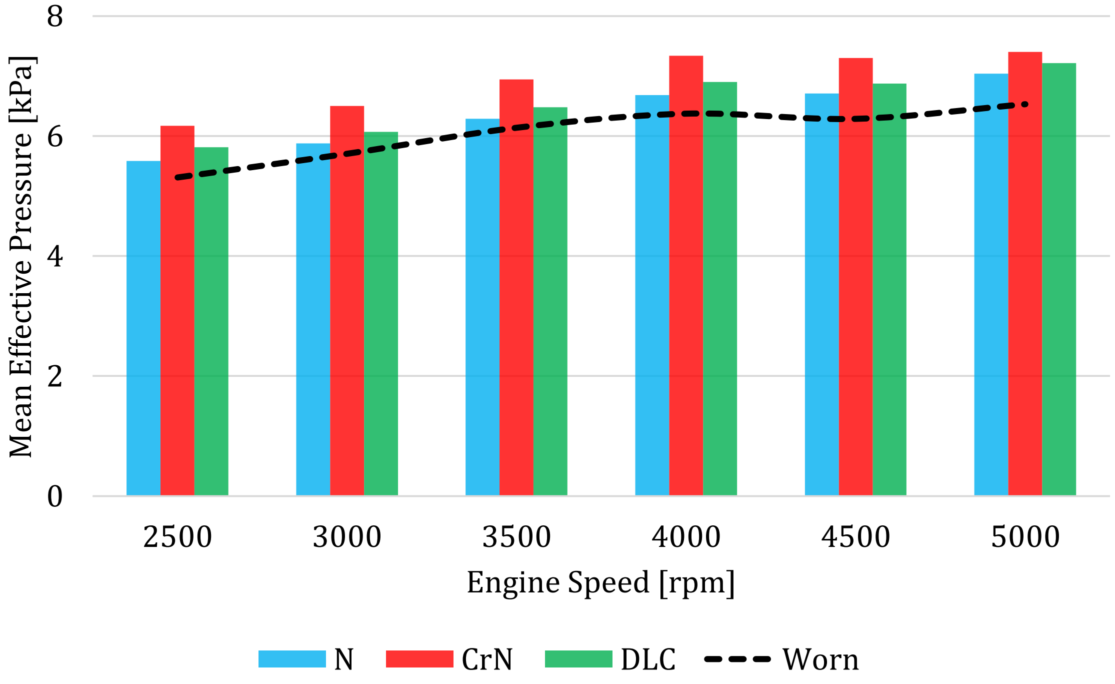

Figure 101 Viscous friction mean effective pressures at WOT

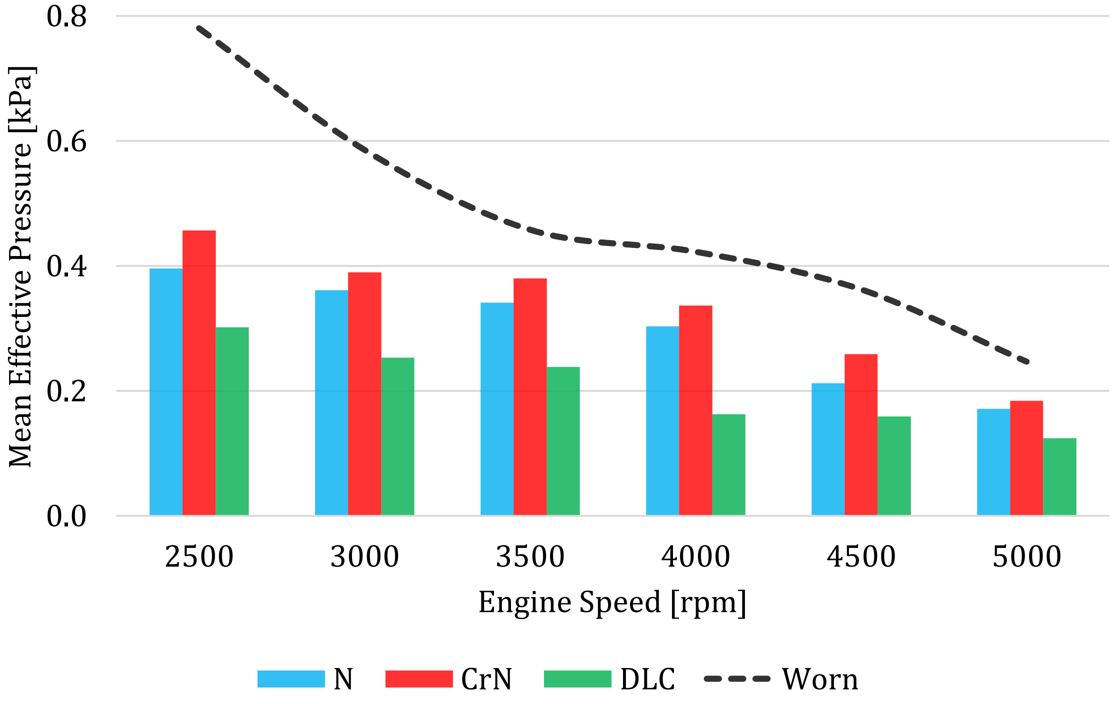

Figure 102 Asperity contact friction mean effective pressures at WOT

The HD fmep results in Figure 101 show that the viscous friction losses of the unworn rings are higher than in the case of the worn ring. This is caused by the different directional orientation of the surface roughness. The pairing of the worn ring and worn cylinder liner results in a strong longitudinal orientation in the axial direction along the piston stroke, which supports the flow of the oil in the direction of motion, producing less resistance, therefore lower hydrodynamic pressures and lower resulting viscous friction loss. From the three unworn compression rings the lowest Peklenik number, for that reason the most transversally oriented roughness topography belongs to the combination of the unworn cylinder liner and CrN ring. The assumption that this contact pair generates the highest hydrodynamic resistance during their relative motion is also proven by the results, as the total fmep values of this coupling are visibly the highest during the entire engine speed range.

The more longitudinal the roughness orientation is, the lower hydrodynamic load bearing force is generated, so the minimum oil film thickness under the ring profile becomes smaller to compensate this deficit. Further, the smaller the minimum oil film thickness is, the higher asperity contact pressure and friction develops, as seen in Figure 102. This is why the worn ring – liner contact pair has higher values of asperity contact fmep, then all unworn ring – liner couples. Slight differences between the results of the unworn rings are caused by the variation in the statistical descriptive surface data, most importantly the combined aerial root mean square height of roughness asperity heights.

Another substantial parameter influencing the final results of asperity contact friction is the dry contact coefficient. The experimental determination of this parameter, which is characteristic for every contact pair individually and cannot be determined by computer simulation, is another possible area of future work in this field. The present state can only be completed by the assumption that the more advanced surface coating technologies probably result in a reduced dry friction coefficient, which allows the expectation, that the evaluated unworn rings would show an even lower level of asperity friction losses.

7.2.4 IMPACT ON LOC

Numerical expressions of the consumed oil from all three sources for the case of the nitrided ring is summarized in Table 36. Values are compared to the worn surface pair.

Table 36 Lubricant oil consumption with the nitrided ring at WOT

LOC		**2500**	**3000**	**3500**	**4000**	**4500**	**5000**
Evaporation	[g h^{-1}]	10.004	12.345	13.082	13.663	14.447	14.897
Blow-Back	[g h^{-1}]	2.812	4.053	5.108	5.894	5.976	5.894
Throw-Off	[×10^{-4} g h^{-1}]	1.319	2.051	3.637	4.756	7.179	9.947
Total	[g h^{-1}]	12.816	16.398	18.190	19.557	20.424	20.792
Deviation	[%]	-1.362	-0.024	2.422	1.690	-0.230	-0.943

Numerical expressions of the consumed oil from all three sources for the case of the chromium nitrided ring is summarized in Table 37.

Table 37 Lubricant oil consumption with the chromium nitrided ring at WOT

LOC		2500	3000	3500	4000	4500	5000
Evaporation	[g h^{-1}]	10.005	12.345	13.088	13.662	14.490	14.889
Blow-Back	[g h^{-1}]	3.005	4.117	4.694	5.710	5.976	6.026
Throw-Off	[×10^{-4} g h^{-1}]	1.118	2.096	3.135	4.463	7.078	12.130
Total	[g h^{-1}]	13.010	16.462	17.782	19.372	20.467	20.916
Deviation	[%]	0.131	0.366	0.124	0.728	-0.020	-0.351

Numerical expression of the consumed oil from all three sources for the case of the diamond-like carbon ring is summarized in Table 38.

Table 38 Lubricant oil consumption with the diamond-like carbon ring at WOT

LOC		2500	3000	3500	4000	4500	5000
Evaporation	[g h^{-1}]	10.009	12.343	13.086	13.659	14.489	14.897
Blow-Back	[g h^{-1}]	3.005	3.837	4.787	5.508	5.976	5.893
Throw-Off	[×10^{-4} g h^{-1}]	0.112	0.223	0.341	0.473	0.740	1.557
Total	[g h^{-1}]	12.993	16.402	17.760	19.232	20.471	20.990
Deviation	[%]	0.000	0.000	0.000	0.000	0.000	0.000

Each source of oil consumption is governed by different influences, therefore not all of them are significantly influenced by the difference in the compression ring surface structure. The most affected source is clearly the throw-off, which is highly affected by the scraping ability of the ring, which is, on the other hand, dependent on the hydrodynamic and asperity contact performance of the surface pair. Slightly affected by the surface structure is the oil loss in the blow-back gas stream. Its measure is only influenced by the variation of oil film thickness in the upstream crevice left by the compression ring. Almost unaffected is the measure of evaporated oil mass, due to the fact that the current simulation only considered the change of the oil film height left on the liner, which shows to have very little influence on the oil evaporation. Other key parameters, like the temperature of the cylinder liner wall and the combustion chamber, or even more importantly the chemical properties of the lubricant, remained identical to those used in the calculation of the worn surface pair. The deviation of total lubricant oil consumption in all cases is less than one percent, which indicates that the difference in surface topography of the compression has a negligible effect on the LOC.

8 FUTURE WORK

Based on the character of work that has been carried out within the frame of this dissertation, the proposals of future work to augment the current state can be divided into two main areas: enhancing the simulation model and executing measurements. This chapter is devoted to the specification of some thoughts and ideas, which are believed to add further value to the present state.

8.1 IMPROVEMENTS OF THE SIMULATION MODEL

The simulation tool presented in this doctoral thesis has been developed from scratch, with the intention to create a comprehensive solution of the piston ring pack. The structure of the software was intentionally comprised of sub-models to allow the individual improvement of separate areas of calculation, without affecting the functionality of the rest of the algorithm. This modularity could very much aid the process of future development.

The greatest potential influence on the simulation results, and therefore the next planned addition to the simulation model is the inclusion of the currently neglected components of ring secondary motions: the consideration of the translational motion in the axial direction and the ring twist. These extra influences could alter mainly the geometry of passages for the gas flow calculations, as well as allow the determination of the axial ring flutter phenomenon. Another aspect considered including is the modeling of lubricant viscosity. The current model utilizes Newtonian fluid behavior, while modern multigrade engine oils doped with a wide variety of additives support their non-Newtonian behavior when it comes to shear rate – viscosity dependence.

8.2 INPUT PARAMETER OBTAINMENT AND EXPERIMENTAL VALIDATION

Every chain is only as strong as its weakest link, which is also valid for the case of computer simulation. Namely, the results cannot be expected to overcome the precision of the input parameters. This is what makes the task of input parameters obtainment so important. Based on the available possibilities to experimentally acquire input parameters for the calculations, the courses of in-cylinder pressure variations and some key operative conditions of the fired engine have been measured. Some future calculations could take serious benefit from the experimentally collected temperature distribution of the cylinder liner and the piston, and from the necessary physical and chemical properties of the lubricant, but also from the correct dry friction coefficient for each individual ring – liner junction. The first steps towards this last goal have already been taken, as parts of an experimental setup capable of measuring the friction force generated by a set of five rings are already designed and manufactured. The system consists of an experimental piston reciprocally moved in an experimental cylinder with honed surface finish. The motion is to be induced by the linear electromotor of the measurement device, which incorporates the force transducers as well. The exact value of the friction coefficient is then calculated from the known tangential and friction forces.

Besides the accurate experimental obtainment of the input parameters another important aspect of carrying out measurements on a fired engine is the validation process of the computed results. The experimental determination of the volumetric gas flow towards the crankcase showed good correlation with their calculated counterparts. However, the most important goal for the future would be the validation of the oil consumption module. For this purpose, the most suitable system would be a measurement device capable of real-time consumption monitoring, like the one presented by Froelund [42], [43]. The Da Vinci Lubricant Oil Consumption (DALOC™) measurement system is based on a sulfur tracing method, which ensures a high level of resolution and repeatability, but more importantly, allows the use of conventional lubricants for the testing procedure.

9 SUMMARY

Concerning their size, piston rings belong to the smallest components of modern internal combustion engines, however, their contribution to friction losses, exhaust gas composition and general proper function of the engine is significant. The detailed study of their behavior ensures a better understanding of the various mechanisms taking place during their operation. This understanding then allows the support of the design and optimization process of new piston rings throughout computer simulation.

The main goal of this doctoral dissertation was the development of a complex simulation tool dealing with all key mechanisms occurring during standard piston ring operation in a piston – ring – liner assembly. The created algorithm addresses i.a. ring dynamics, ring – liner interactions, gas flows, lubrication regimes and oil transports to predict:

- gas blow-by and blow-back flows,
- interring gas pressures and forces,
- oil film thicknesses on the cylinder liner,
- hydrodynamic and asperity contact friction losses and
- oil consumption rates from evaporation, gas blow-back and throw-off.

Each sub-module of the software tool is built on strong physical and chemical foundations supplemented with appropriate mathematical approaches. The resulting theoretical background is embedded into an effective and user-friendly programming language to form the expected final outcome. The outputs of the complete simulation cycle are designed in accordance to industrial interest and ease of use. The presented numerical values are applicable for the investigated inline spark ignition engine of a small passenger car.

The experimental part is focused on the obtainment of appropriate input parameters and the partial validation of the developed source code and its results. For the determination of the correlation between the measured and calculated blow-by results suitable statistical comparison method is utilized, which shows that the achieved deviation is statistically insignificant.

Finally, the practical use of the simulation tool is shown by the execution of parameter studies, which are all based on real contemporary trends in the field of engine research.

The work carried out within the frame of this doctoral dissertation is intended to fill the gap in the research area of piston rings yet not widely discussed, nor published. Namely a combined simulation tool able to support the needs of piston ring manufacturers and engine research centers of car companies to calculate the impact of design parameter changes on friction losses and lubricant oil consumption simultaneously.

10 REFERENCES

[1] AFFENZELLER, Josef. *Schmierspalthöhen und Ölverbrauch bei der Kolbenringschmierung von Verbrennungskraftmaschinen*. Dissertation. Graz (Austria), 1973.

[2] BAELDEN, Camille. *A Multi-Scale Model for Piston Ring Dynamics, Lubrication and Oil Transport in Internal Combustion Engines.* Cambridge, MA (USA), 2014.

[3] BOOSER, Richard. *CRC Handbook of Lubrication: Theory and Practice of Tribology*. Boca Raton: CRC Press, 1983. ISBN 08493390303.

[4] FEDERAL-MOGUL. *Kolbenring-Handbuch.* Burscheid: FEDERAL-MOGUL Burscheid, 2003.

[5] HEYWOOD, John B. *Internal Combustion Engine Fundamentals*. New York: McGraw-Hill, 1988. ISBN 0-07-028637-X.

[6] HUANG, Xiubao. *Hydrodynamic Lubrication under Severe Conditions*. Dissertation. Evanston, IL (USA), 1990.

[7] KRAGELSKY, Igor Viktorovich and ALISIN, Valery Vasilevich. *Friction, Wear, Lubrication: Tribology Handbook.* New York: Pergamon Press, 1982. ISBN 978-008-0275-918.

[8] LAGEMANN, Volker. *Numerische Verfahren zur tribologischen Charakterisierung bearbeitungsbedingter rauher Oberflächen bei Mikrohydrodynamik und Mischreibung.* Dissertation. Kassel (Germany), 2000.

[9] LIAO, Kai. *Factors Affecting Piston Ring Friction.* Dissertation. Cambridge, MA (USA), 2013.

[10] LIDE, David R. *CRC Handbook of Chemistry and Physics*. 88th ed. Boca Raton: CRC Press, 2008. ISBN 978-084-9304-880.

[11] LIU, Liang. *Modeling the Performance of the Piston Ring-Pack with Consideration of Non-Axisymmetric Characteristics of the Power Cylinder System in Internal Combustion Engines.* Dissertation. Cambridge, MA (USA), 2005.

[12] LUMLEY, John L. *Engines: An Introduction*. New York: Cambridge University Press, 1999. ISBN 978-052-1644-891.

[13] MARŠÁLEK, Ondřej. *Advanced Methods for the Solution of Journal Bearing Dynamics.* Dissertation. Brno (Czech Republic), 2015.

[14] NIKOLOV, Slavcho. *Parameterstudie der typischen Kenngrößen zur Bewertung der Kolbenringfunktion an einem MKS-Kolbensystem*. Master's thesis. Aachen (Germany), 2012.

[15] ORTHABER, Gerhard. *Berechnungsverfahren für Ölverbrauch und Blow-By zwischen Kolben, Kolbenringen und Zylinderlaufbuchse*. Dissertation. Graz (Austria), 1992.

[16] PERRY, Robert H., GREEN, Don W. and MALONEY, James O. *Perry's Chemical Engineers' Handbook*. 7th ed. New York: McGraw-Hill, 1997. ISBN 0-07-049841-5.

[17] PRESS, William H., TEUKOLSKY, Saul A., VETTELING, William T. and FLANNERY, Brian P. *Numerical Recipes: The Art of Scientific Computing.* 3rd ed. Cambridge: Cambridge University Press, 2007. ISBN 978-0-521-88068-8.

[18] RANGERT, Bo. *Hydrodynamic Piston Ring Lubrication with Reference to Lubricating Oil Consumption*. Dissertation. Göteborg (Sweden), 1974.

[19] SHAPIRO, Ascher. *The Dynamics and Thermodynamics of Compressible Fluid Flow*. New York: The Ronald Press Company, 1953. ISBN 978-047-1066-910.

[20] SIGLOCH, Herbert. *Technische Fluidmechanik*. 8. Auflage. Berlin: Springer, 2011. ISBN 978-364-2228-445.

[21] ŠNITA, Dalimil. *Chemické inženýrství I.* Praha: Vysoká škola chemicko-technická v Praze, 2006. ISBN 80-708-0589-7.

[22] STACHOWIAK, Gwidon and BATCHELOR, Andrew. *Engineering Tribology*. 3rd ed. Amsterdam: Elsevier Butterworth-Heinemann, 2005. ISBN 07-506-7836-4.

[23] THIROUARD, Benoist. *Characterization and Modeling of the Fundamental Aspects of Oil Transport in the Piston Ring Pack of Internal Combustion Engines*. Dissertation. Cambridge, MA (USA), 2001.

[24] TIAN, Tian. *Modeling the Performance of the Piston Ring-Pack in Internal Combustion Engines*. Dissertation. Cambridge, MA (USA), 1997.

[25] WELTY, J.R., WICKS, C.E., WILSON, R.E. and RORRER, G.L. *Fundamentals of Momentum, Heat, and Mass Transfer.* 5th ed. Danvers: John Wiley & Sons, Inc., 2008. ISBN 978-047-0128-688.

[26] WHITE, Frank M. *Viscous Fluid Flow*. 2nd ed. New York: McGraw-Hill, 1991. ISBN 00-706-9712-4.

[27] YILMAZ, Ertan. *Sources and Characteristics of Oil Consumption in a Spark-Ignition Engine*. Dissertation. Cambridge, MA (USA), 2003.

[28] ANTOINE, Charles. Tensions des vapeurs; nouvelle relation entre les tensions et les températures. *Comptes Rendus des Séances de l'Académie des Sciences*. 1888. vol. 107, p. 836–850.

[29] ARCOUMANIS, Constantine, OSTOVAR, Pendar and MORTIER, Roy. Mixed Lubrication Modelling of Newtonian and Shear Thinning Liquids in a Piston-Ring Configuration. *SAE Technical Paper 972924*. 1997. DOI 10.4271/972924.

[30] ARIGA, Susumu, SUI, Ping, BAILEY, Brent, KUMAKIRI, Tonami, OSUMI, Yasuyuki and SAKAMOTO, Akihiro. On-Line Oil Consumption Measurement and Characterization of an Automotive Gasoline Engine by SO2 Method. *SAE Technical Paper 920652*. 1992. DOI 10.4271/920652.

[31] ARTMANN, Christina and RABL, Hans-Peter. Continuous Online Oil Consumption Measurement with the SO2 Tracer Method. *SAE Technical Paper 2011-01-2404*. 2011. DOI 10.4271/2011-01-2404.

[32] BRIGGS, D. K. H. Thermal Conductivity of Liquids. *Industrial and Engineering Chemistry*. 1957. vol. 49, no. 3, p. 418-421. DOI 10.1021/ie51392a039.

[33] COULOMB, C. A. Essai sur une application des règles de maximis & minimis à quelques problèmes de statique, relatifs à l'architecture. De L'Imprimerie Royale. 1776. vol. 7, p. 343–382.

[34] DOMINGUEZ-ROSADO, Elena and PICHTEL, John. Chemical characterization of fresh, used and weathered motor oil via GC/MS, NMR and FTIR techniques. *Proceedings of the Indiana Academy of Science*. 2003. vol. 112, no. 2, p. 109-116.

[35] DOWSON, D., RUDDY, B. L. and ECONOMOU, P. N. The Elastohydrodynamic Lubrication of Piston Rings. *Proceedings of the Royal Society A: Mathematical, Physical and Engineering Sciences*. 1983. vol. 386, no. 1791, p. 409-430. DOI 10.1098/rspa.1983.0043.

[36] DOWSON, D. and TAYLOR, C. M. Cavitation in Bearings. Annual Review of Fluid Mechanics. 1979. vol. 11, no. 1, p. 35-65. DOI 10.1146/annurev.fl.11.010179.000343.

[37] DUNAEVSKY, Val. Analysis of Distortions of Cylinders and Conformability of Piston Rings. *Tribology Transactions*. 1990. vol. 33, no. 1, p. 33-40. DOI 10.1080/10402009008981927.

[38] EINSTEIN, Albert. Über die von der molekularkinetischen Theorie der Wärme geforderte Bewegung von in ruhenden Flüssigkeiten suspendierten Teilchen. Annalen der Physik. 1905. vol. 322, no. 8, p. 549-560. DOI 10.1002/andp.19053220806.

[39] EJAKOV, Mikhail, DIAZ, Alejandro and SCHOCK, Harold. Numerical Optimization of Ring-Pack Behavior. *SAE Technical Paper 1999-01-1521*. 1999. DOI 10.4271/1999-01-1521.

[40] ELROD, H. G. A Cavitation Algorithm. *Journal of Lubrication Technology*. 1981. vol. 103, no. 3, p. 350-354. DOI 10.1115/1.3251669.

[41] EVANS, Robert, DENG, Zhaoxia, ROGERSON, Alexandria K., MCLACHLAN, Andy S., RICHARDS, Jeff J., NILSSON, Mathias and MORRIS, Gareth A. Quantitative Interpretation of Diffusion-Ordered NMR Spectra: Can We Rationalize Small Molecule Diffusion Coefficients? *Angewandte Chemie*. 2013. vol. 125, no. 11, p. 3281-3284. DOI 10.1002/ange.201207403.

[42] FROELUND, Kent. Real-Time Steady-State Oil Consumption Measurement on Commercial SI-Engine. *SAE Technical Paper 1999-01-3461*. 1999. DOI 10.4271/1999-01-3461.

[43] FROELUND, Kent, MENEZES, Leandro A., JOHNSON, Hal R. and REIN, Wolfgang O. Real-Time Transient and Steady-State Measurement of Oil Consumption for Several Production SI-Engines. *SAE Technical Paper 2001-01-1902*. 2001. DOI 10.4271/2001-01-1902.

[44] FURUHAMA, Shouichi and HIRUMA, Masaru. The Relationship Between Piston Ring Scuffing and the Formation of Surface Profile. In: *Piston Ring Scuffing*. London: Institution of Mechanical Engineers Conference, 1976. p. 35-43. ISBN 0852983352.

[45] FURUHAMA, Shouichi, OYA, Yositane and NAKAMURA, Tomikazu. A Study of the Oil Loss through the Piston. *Bulletin of Japan Society of Mechanical Engineers*. 1963. Vol. 6, no. 22p. 378-387. DOI 10.1299/jsme1958.6.378.

[46] FURUHAMA, Shouichi and TADA, Tosio. On the Flow of Gas Through the Piston-Rings: 1st Report, The Discharge Coefficient and Temperature of Leakage Gas. *Transactions of the Japan Society of Mechanical Engineers*. 1961. vol. 27, no. 174, p. 240-247. DOI 10.1299/kikai1938.27.240.

[47] FURUHAMA, Shouichi and TADA, Tosio. On the Flow of Gas Through the Piston-Rings: 2nd Report, The Character of Gas Leakage. *Transactions of the Japan Society of Mechanical Engineers*. 1961. vol. 27, no. 174, p. 247-255. DOI 10.1299/kikai1938.27.247.

[48] GREENWOOD, J. A. and TRIPP, J. H. The Contact of Two Nominally Flat Rough Surfaces. *Proceedings of the Institution of Mechanical Engineers*. 1970. vol. 185, no. 1, p. 625-634. DOI 10.1243/PIME_PROC_1970_185_069_02.

[49] GULWADI, Sanjay D. Analysis of Tribological Performance of a Piston Ring Pack. *Tribology Transactions*. 2000. vol. 43, no. 2, p. 151-162. DOI 10.1080/10402000008982325.

[50] HERBST, Hubert M. and PRIEBSCH, Hans H. Simulation of Piston Ring Dynamics and Their Effect on Oil Consumption. *SAE Technical Paper 2000-01-0919*. 2000. DOI 10.4271/2000-01-0919.

[51] HERTZ, Heinrich. Ueber die Berührung fester elastischer Körper. Journal für die reine und angewandte Mathematik. 1882. vol. 92, no. 1, p. 156-171.

[52] HU, Yuanzhong, CHENG, Herbert S., ARAI, Takayuki, KOBAYASHI, Yoichi and AOYAMA, Shunichi. Numerical Simulation of Piston Ring in Mixed Lubrication—A Nonaxisymmetrical Analysis. *Journal of Tribology*. 1994. vol. 116, no. 3, p. 470-478. DOI 10.1115/1.2928867.

[53] HWU, Chu-Jung and WENG, Cheng-I. Elastohydrodynamic Lubrication of Piston Rings. *Wear*. 1991. vol. 150, no. 12, p. 203-215. DOI 10.1016/0043-1648(91)90317-N.

[54] JENG, Yeau-Ren. Theoretical Analysis of Piston-Ring Lubrication Part I—Fully Flooded Lubrication. *Tribology Transactions.* 1992. vol. 35, no. 4, p. 696-706.

[55] JENG, Yeau-Ren. Theoretical Analysis of Piston-Ring Lubrication Part II—Starved Lubrication and Its Application to a Complete Ring Pack. *Tribology Transactions.* 1992. vol. 35, no. 4, p. 707-714.

[56] KUO, Tang-Wei, SELLNAU, Mark, THEOBALD, Mark and JONES, John. Calculation of Flow in the Piston-Cylinder-Ring Crevices of a Homogeneous-Charge Engine and

Comparison with Experiment. *SAE Technical Paper 890838*. 1989. DOI 10.4271/890838.

[57] LO, Sy-Wei. On the Effects of Roughness Orientation—A Mapping and Double Scale Analysis of Flow Factors. *Journal of Tribology*. 1992. vol. 114, no. 4, p. 747-754. DOI 10.1115/1.2920944.

[58] MAEKAWA, Kazuhiko, MITSUTAKE, Shoji and MOROHOSHI, Shozo. A Study on Engine Lubricating Oil Consumption by Computer Simulation. *SAE Technical Paper 860546*. 1986. DOI 10.4271/860546.

[59] MARSALEK, Ondrej, NOVOTNY, Pavel and RAFFAI, Peter. Micro-lubrication of Directionally Oriented Contact Surfaces. *Tribology in Industry*. 2014. vol. 36, no. 4, p. 451-464.

[60] NAMAZIAN, Mehdi and HEYWOOD, John. Flow in the Piston-Cylinder-Ring Crevices of a Spark-Ignition Engine: Effect on Hydrocarbon Emissions, Efficiency and Power. *SAE Technical Paper 820088*. 1982. DOI 10.4271/820088.

[61] NOVOTNY, Pavel, PISTEK, Vaclav, DRAPAL, Lubomir, SVIDA, David and DEVERA, Tomas. Efficient Approach for Solution of the Mechanical Losses of the Piston Ring Pack. *Proceedings of the Institution of Mechanical Engineers, Part D: Journal of Automobile Engineering*. 2013. vol. 227, no. 10, p. 1377-1388. DOI 10.1177/0954407013495187.

[62] ORTJOHANN, Timo, VONCKEN, Antonius and PISCHINGER, Stefan. Simulation der Kolbenring dynamik mittels FEM-Software. *MTZ - Motortechnische Zeitschrift*. 2008. vol. 69, no. 12, p. 1050-1055. DOI 10.1007/BF03227511.

[63] PASARIBU, H. R. and SCHIPPER, D. J. Application of a Deterministic Contact Model to Analyze the Contact of a Rough Surface Against a Flat Layered Surface. *Journal of Tribology*. 2005. vol. 127, no. 2, p. 451-455. DOI 10.1115/1.1866163.

[64] PATIR, Nadir and CHENG, H. S. An Average Flow Model for Determining Effects of Three-Dimensional Roughness on Partial Hydrodynamic Lubrication. *Journal of Lubrication Technology*. 1978. vol. 100, no. 1, p. 12-17. DOI 10.1115/1.3453103.

[65] PATIR, Nadir and CHENG, H. S. Application of Average Flow Model to Lubrication between Rough Sliding Surfaces. *Journal of Lubrication Technology*. 1979. Vol. 101, no. 2, p. 220-229. DOI 10.1115/1.3453329.

[66] PEKLENIK, Janez. New Developments in Surface Characterization and Measurements by Means of Random Process Analysis. *Proceedings of the Institution of Mechanical Engineers*. 1967. vol. 182, no. 11, p. 108-126. DOI 10.1243/PIME_CONF_1967_182_309_02.

[67] RAFFAI, Peter, NOVOTNY, Pavel and MARSALEK, Ondrej. Numerical Calculation of Mechanical Losses of the Piston Ring Pack of Internal Combustion Engines. *BALKANTRIB '14 - 8th International Conference on Tribology*. 2014. p. 734-747.

[68] RAGOT, Patrick and REBBERT, Martin. Investigations of Crank Offset and It's Influence on Piston and Piston Ring Friction Behavior Based on Simulation and Testing. *SAE Technical Paper 2007-01-1248*. 2007. DOI 10.4271/2007-01-1248.

[69] REIPERT, Peter and VOIGT, Marco. Simulation of the Piston / Cylinder Behavior for Diesel Engines. *SAE Technical Paper 2001-01-0563*. 2001. DOI 10.4271/2001-01-0563.

[70] REYNOLDS, Osborne. On the Theory of Lubrication and Its Application to Mr. Beauchamp Tower's Experiments, Including an Experimental Determination of the Viscosity of Olive Oil. *Proceedings of the Royal Society of London*. 1886. vol. 40, no. 242-245, p. 191-203. DOI 10.1098/rspl.1886.0021.

[71] RICHARDSON, Dan. Review of Power Cylinder Friction for Diesel Engines. *Journal of Engineering for Gas Turbines and Power*. 2000. vol. 122, no. 4, p. 506-519. DOI 10.1115/1.1290592.

[72] STULL, Daniel R. Vapor Pressure of Pure Substances. Organic and Inorganic Compounds. *Industrial & Engineering Chemistry*. 1947. vol. 39, no. 4, p. 517-540. DOI 10.1021/ie50448a022.

[73] SUTHERLAND, William. The viscosity of gases and molecular force. *Philosophical Magazine Series 5*. 1893. vol. 36, no. 223, p. 507-531. DOI 10.1080/14786449308620508.

[74] TIAN, Tian, WONG, Victor and HEYWOOD, John. A Piston Ring-Pack Film Thickness and Friction Model for Multigrade Oils and Rough Surfaces. *SAE Technical Paper 962032*. 1996. DOI 10.4271/962032.

[75] TING, L. L. and MAYER, J. E. Piston Ring Lubrication and Cylinder Bore Wear Analysis, Part I—Theory. *Journal of Lubrication Technology*. 1974. vol. 96, no. 3, p. 305-314. DOI 10.1115/1.3451948.

[76] TRIPP, John. Surface Roughness Effects in Hydrodynamic Lubrication: The Flow Factor Method. *Journal of Lubrication Technology*. 1983. vol. 105, no. 3, p. 458-463. DOI 10.1115/1.3254641.

[77] WANNATONG, Krisada. Simulation Algorithm for Piston Ring Dynamics. *Simulation Modelling Practice and Theory*. 2008. vol. 16, no. 1, p. 127-146. DOI 10.4271/2001-01-3368.

[78] YILMAZ, Ertan, TIAN, Tian, WONG, Victor and HEYWOOD, John. An Experimental and Theoretical Study of the Contribution of Oil Evaporation to Oil Consumption. *SAE Technical Paper 2002-01-2684*. 2002. DOI 10.4271/2002-01-2684.

[79] COUNCIL DIRECTIVE of 20 March 1970 on the approximation of the laws of the Member States relating to measures to be taken against air pollution by gases from positive-ignition engines of motor vehicles (70/220/EEC). In: *Official Journal L 076*. 1970.

[80] COUNCIL DIRECTIVE of 26 June 1991 amending Directive 70/220/EEC on the approximation of the laws of the Member States relating to measures to be taken

against air pollution by emissions from motor vehicles (91/441/EEC). In: *Official Journal L 242*. 1991.

[81] COUNCIL DIRECTIVE 93/59/EEC of 28 June 1993 amending Directive 70/220/EEC on the approximation of the laws of the Member States relating to measures to be taken against air pollution by emissions from motor vehicles. In: *Official Journal L 186*. 1993.

[82] DIRECTIVE 94/12/EC OF THE EUROPEAN PARLIAMENT AND THE COUNCIL of 23 March 1994 relating to measures to be taken against air pollution by emissions from motor vehicles and amending Directive 70/220/EEC. In: *Official Journal L 100*. 1994.

[83] DIRECTIVE 98/69/EC OF THE EUROPEAN PARLIAMENT AND OF THE COUNCIL of 13 October 1998 relating to measures to be taken against air pollution by emissions from motor vehicles and amending Council Directive 70/220/EEC. In: *Official Journal L 350*. 1998.

[84] REGULATION (EC) No 715/2007 OF THE EUROPEAN PARLIAMENT AND OF THE COUNCIL of 20 June 2007 on type approval of motor vehicles with respect to emissions from light passenger and commercial vehicles (Euro 5 and Euro 6) and on access to vehicle repair and maintenance information. In: *Official Journal of the European Union*. 2007.

[85] AVL Blow By Meter. *AVL LIST GmbH* [online]. 2017. [Accessed 01 February 2017]. Retrieved from: http://www.avl.com

[86] AVL Fuel Balance and Fuel Temperature Control. *AVL LIST GmbH* [online]. 2017. [Accessed 02 February 2017]. Retrieved from: http://www.avl.com

[87] Bruker ContourGT-X. *Bruker* [online]. 2017. [Accessed 16 March 2017]. Retrieved from: https://www.bruker.com

[88] Commission plans legislative framework to ensure the EU meets its target for cutting CO2 emissions from cars. *European Commission* [online]. 2007. [Accessed 22 April 2015]. Retrieved from: http://europa.eu

[89] MOCK, Peter. EU car manufacturers likely to meet 2015 CO2 target early. *International Council on Clean Transportation* [online]. 2012. [Accessed 21 April 2015]. Retrieved from: http://www.theicct.org

[90] Kistler Measuring Spark Plug. *Kistler measure. analyze. innovate.* [online]. 2010. [Accessed 03 February 2017]. Retrieved from: http://www.kistler.com

[91] Kistler Crank Angle Encoder. *Kistler measure. analyze. innovate*. [online]. 2011. [Accessed 03 February 2017]. Retrieved from: http://www.kistler.com

[92] Outdoor air pollution a leading environmental cause of cancer deaths. *World Health Organization* [online]. 2013. [Accessed 21 April 2015]. Retrieved from: http://www.euro.who.int

[93] SF-902S ENGINE DYNAMOMETER. *SuperFlow Dynamometers & Flowbenches* [online]. 2017. [Accessed 01 February 2017]. Retrieved from: http://www.superflow.com

11 LIST OF ABBREVIATIONS

1D, 3D	1-dimensional, 3-dimensional
BDC	Bottom dead center
CO	Carbon oxide compounds
CO_2	Carbon dioxide
COS	Carbonyl sulfide
CR	Compression ring
CT	Asperity contact
DLC	Diamond-like carbon
EHD	Elastohydrodynamic
EU	European union
FEM	Finite element method
HC	Hydrocarbon compounds
HD	Hydrodynamic
ICE	Internal combustion engine(s)
LOC	Lubricating oil consumption
MBS	Multi-body system
NOx	Nitrogen oxide compounds
OCR	Oil control ring
PM	Particulate matter
PVD	Physical vapor deposition
R&D	Research and development
SO	Sulfur monoxide
SO_2	Sulfur dioxide
SR	Scraper ring
TDC	Top dead center
WHO	World Health Organization

12 LIST OF SYMBOLS

a	[N s m^{-2}]	Parameter for dynamic viscosity calculation
A	[m]	Amplitude of the cylinder bore profile
A', B'	[-]	Parameters for partial oil pressure calculation
A_{free}	[m^2]	Free surface of the cylinder wall
A_g	[m^2]	Ring gap area
b	[m]	Ring axial height
b, c	[-]	Parameters for dynamic viscosity calculation
b_{fl}	[m]	Ring flank and ring groove overlap
C_∞	[kg m^{-3}]	Concentration of the diffusing in the combustion chamber
C_d	[-]	Discharge coefficient
c_p	[J kg^{-1} K^{-1}]	Isobaric heat capacity
c_v	[J kg^{-1} K^{-1}]	Isochoric heat capacity
C_{oil}	[kg m^{-3}]	Concentration of the diffusing oil on the film surface
d	[m]	Middle diameter of the ring groove
D	[m]	Cylinder bore diameter
D_C	[m^2 s^{-1}]	Diffusion coefficient related to concentration C
D_{C0}	[m^2 s^{-1}]	Diffusion coefficient at reference pressure p_0
d_{film}	[m]	Oil film diameter of the accumulated oil volume
E'	[Pa]	Composite elastic modulus
$F_{5/2}$	[-]	Statistical function for Gaussian distr. of the summit heights
$F_{ct,r}$	[N]	Asperity contact force in radial direction
$F_{f,a}$, $F_{f,r}$	[N]	Friction forces in axial and radial direction
$F_{HD,r}$	[N]	Hydrodynamic force in radial direction
$F_{i,a}$, $F_{i,r}$	[N]	Inertia forces in axial and radial direction
f_m	[-]	Compressibility factor

$F_{p,a}$, $F_{p,r}$	[N]	Gas pressure forces in axial and radial direction
$F_{s,a}$	[N]	Damping force due to oil squeezing in axial direction
$F_{t,r}$	[N]	Ring pretension force in radial direction
h	[m]	Oil film thickness
h_{film}	[m]	Oil film thickness of the accumulated oil volume
h_{fl}	[m]	Distance between the ring flank and ring groove
$\bar{h}_T$	[m]	Local oil film thickness
h_{vapor}	[m]	Oil vapor thickness
H	[-]	Specific height ratio, $H = \frac{h}{\sigma}$
l	[m]	Conrod length
L	[m]	Characteristic length for oil evaporation calculation
m_{0_i}	[kg]	Initial mass of volume *i*
$M_{C_m H_n}$	[kg mol^{-1}]	Molar mass of hydrocarbon $C_m H_n$
$\dot{m}_{clea}$	[kg s^{-1}]	Mass flow through the ring-groove clearance
$\dot{m}_{evap}$	[kg s^{-1}]	Mass flow due to oil evaporation
$\dot{m}_{gap}$	[kg s^{-1}]	Mass flow through the piston ring gap
$\dot{m}_{ij}$	[kg s^{-1}]	Mass flow between volumes *i* and *j*
N	[-]	Number of rings on the piston
Nu	[-]	Nusselt number
p	[Pa]	Hydrodynamic pressure
$\bar{p}$	[Pa]	Mean pressure
p_0	[Pa]	Reference pressure for diffusion coefficient calculation
P_{0_i}	[Pa]	Initial pressure of volume *i*
p_∞	[Pa]	Partial pressure of the oil film in the combustion chamber
p_c	[Pa]	Asperity contact pressure

p_d	[Pa]	Downstream pressure
p_{oil}	[Pa]	Partial pressure of the oil film on the film surface
p_u	[Pa]	Upstream pressure
r	[m]	Crankshaft radius
R	[J kg^{-1} K^{-1}]	Gas constant
r_0	[m]	Radius of the middle circle of the cylinder bore profile
$R_{C_mH_n}$	[J kg^{-1} K^{-1}]	Specific gas constant of hydrocarbon C_mH_n
Re	[-]	Reynolds number
R_m	[J mol^{-1} K^{-1}]	Universal gas constant
s	[m]	Piston axial position
Δs	[m]	Axial length increment
Sc	[-]	Schmidt number
Sh	[-]	Sherwood number
s_{free}	[m]	Free length of the cylinder wall
t	[s]	Time
T	[°C]	Temperature for dynamic viscosity calculation
Δt	[s]	Time increment
T_{cyl}	[K]	Temperature of the cylinder wall
T_{gas}	[K]	Temperature of the cylinder charge
T_{oil}	[K]	Temperature of the evaporating oil
T_{vapor}	[K]	Temperature of the oil vapor
$\Delta\bar{u}$	[m s^{-1}]	Mean oil velocity difference
U_1, U_2	[m s^{-1}]	Tangential velocity of surface 1 and 2
U_{ax}	[m s^{-1}]	Axial ring velocity
u_i	[m s^{-1}]	Velocity of *i*-th layer
u_{inst}	[m s^{-1}]	Instationary velocity

$\bar{u}_{inst}$	[m s^{-1}]	Mean instationary velocity
U_{piston}	[m s^{-1}]	Axial piston velocity
u_{st}	[m s^{-1}]	Stationary velocity
$\bar{u}_{st}$	[m s^{-1}]	Mean stationary velocity
$x,\ y$		Cartesian coordinates along *x* and *y* axis
v	[m s^{-1}]	Flow speed of the cylinder charge
V_{acc}	[m^3]	Accumulated oil volume above the first piston ring
v_{axial}	[m s^{-1}]	Axial flow speed of the cylinder charge
V_{blow}	[m^3]	Accumulated oil volume due to gas blow-by
v_{circ}	[m s^{-1}]	Circular flow speed of the cylinder charge
V_{pump}	[m^3]	Accumulated oil volume due to ring secondary motion
V_{scr}	[m^3]	Accumulated oil volume due to scraping effect
V_{throw}	[m^3]	Thrown-off oil volume
v_u	[m^3 kg^{-1}]	Specific volume of upstream gas
α_{gas}	[W m^{-2} K^{-1}]	Convective heat transfer coefficient between gas and vapor
β	[m]	Radius of asperity summits
γ	[-]	Surface pattern parameter
$\delta_1,\ \delta_2$	[m]	Roughness amplitudes of surface 1 and 2
η	[kg m^{-1} s^{-1}]	Lubricant dynamic viscosity
η	[m^{-2}]	Surface density of asperity peaks
η_{gas}	[kg m^{-1} s^{-1}]	Gas dynamic viscosity
κ	[-]	Specific heat ratio
λ	[-]	Conrod ratio, $\lambda = \frac{r}{l}$
$\lambda_{0.5x}$, $\lambda_{0.5y}$	[-]	0.5 correlation lengths of a profile in *x* and *y* direction

λ_{oil}	[W K^{-1}]	Thermal conductivity of the oil
ν	[m^2 s^{-1}]	Kinematic viscosity of the cylinder charge
ν_1, ν_2	[-]	Poisson ratios of surface 1 and 2
ρ	[kg m^{-3}]	Lubricant density
σ	[m]	Standard deviation of combined surface roughness
σ_s	[m]	Composite summit height standard deviation
τ	[Pa]	Shear stress
$\bar{\tau}$	[Pa]	Average shear stress in lubricant film
φ	[rad]	Crank angle
φ	[rad]	Polar angle of cylinder bore
ϕ_f	[-]	Averaged sliding velocity shear stress factor
ϕ_{fp}	[-]	Mean pressure shear stress factor
ϕ_{fs}	[-]	Shear stress factor resulting from the sliding motion
ϕ_s	[-]	Shear flow factor
ϕ_x, ϕ_y	[-]	Pressure flow factors in *x* and *y* direction
ω	[rad s^{-1}]	Angular velocity

APPENDIX A

DISCRETIZATION OF THE REYNOLDS EQUATION WITH NON-DIMENSIONAL VARIABLES

$$\frac{\partial}{\partial x}\left(\phi_x \frac{h_a^{\,3}}{12\,\eta}\frac{\partial p}{\partial x}\right)=\frac{U}{2}\left(\frac{\partial h_a}{\partial x}+\frac{\sigma\,\partial \phi_s}{\partial x}\right)+\frac{\partial h_t}{\partial t}.$$
$$\frac{\partial}{\partial x}\left(\phi_x \frac{h_a^{\,3}}{6\,\eta\,U}\frac{\partial p}{\partial x}\right)=\frac{\partial h_a}{\partial x}+\frac{\sigma\,\partial \phi_s}{\partial x}+\frac{2\,\partial h_t}{U\,\partial t}. \tag{A-1}$$

Non-dimensional variables:

$$H_A=\frac{h_a}{\sigma};\,H_T=\frac{h_t}{\sigma};\,X=\frac{x}{\sigma};\,P=p\,\sigma;\,\xi=\phi_x\frac{H_A^{\,3}}{6\,\eta\,U};\psi=\frac{U\,\Delta t}{2\,\sigma}. \tag{A-2}$$

Non-dimensional form of the 1D Reynolds equation:

$$\frac{\partial}{\partial X}\left(\xi\,\frac{\partial P}{\partial X}\right)=\frac{\partial H_A}{\partial X}+\frac{\partial \phi_s}{\partial X}+\frac{\partial H_T}{\partial \psi}. \tag{A-3}$$

Poiseuille component discretization using FDM:

$$\frac{\partial}{\partial X}\left(\xi\,\frac{\partial P}{\partial X}\right)_{(i)}\cong\frac{\left(\xi\,\frac{\partial P}{\partial X}\right)_{\left(i+\frac{1}{2}\right)}-\left(\xi\,\frac{\partial P}{\partial X}\right)_{\left(i-\frac{1}{2}\right)}}{\vartriangle X}. \tag{A-4}$$

Internal derivations:

$$\left(\xi\,\frac{\partial P}{\partial X}\right)_{\left(i+\frac{1}{2}\right)}=\xi_{\left(i+\frac{1}{2}\right)}\frac{P_{(i+1)}-P_{(i)}}{\vartriangle X}.$$
$$\left(\xi\,\frac{\partial P}{\partial X}\right)_{\left(i-\frac{1}{2}\right)}=\xi_{\left(i-\frac{1}{2}\right)}\frac{P_{(i)}-P_{(i-1)}}{\vartriangle X}. \tag{A-5}$$

Step-by-step substitution and derivation:

$$\frac{\partial}{\partial X}\left(\xi\frac{\partial P}{\partial X}\right)_{(i)} \cong \frac{\xi_{\left(i+\frac{1}{2}\right)}\frac{P_{(i+1)}-P_{(i)}}{\triangle X}-\xi_{\left(i-\frac{1}{2}\right)}\frac{P_{(i)}-P_{(i-1)}}{\triangle X}}{\triangle X}=$$

$$=\frac{\frac{1}{\triangle X}\left(\xi_{\left(i+\frac{1}{2}\right)}\left(P_{(i+1)}-P_{(i)}\right)-\xi_{\left(i-\frac{1}{2}\right)}\left(P_{(i)}-P_{(i-1)}\right)\right)}{\triangle X}=$$

$$=\frac{\xi_{\left(i+\frac{1}{2}\right)}\left(P_{(i+1)}-P_{(i)}\right)-\xi_{\left(i-\frac{1}{2}\right)}\left(P_{(i)}-P_{(i-1)}\right)}{\left(\triangle X\right)^2}. \tag{A-6}$$

$$\frac{\partial}{\partial X}\left(\xi\frac{\partial P}{\partial X}\right)_{(i)} \cong \frac{\xi_{\left(i+\frac{1}{2}\right)}P_{(i+1)}-\xi_{\left(i+\frac{1}{2}\right)}P_{(i)}-\xi_{\left(i-\frac{1}{2}\right)}P_{(i)}+\xi_{\left(i-\frac{1}{2}\right)}P_{(i-1)}}{\left(\triangle X\right)^2}.$$

$$\frac{\partial}{\partial X}\left(\xi\frac{\partial P}{\partial X}\right)_{(i)} \cong \frac{-\xi_{\left(i+\frac{1}{2}\right)}P_{(i)}-\xi_{\left(i-\frac{1}{2}\right)}P_{(i)}+\xi_{\left(i+\frac{1}{2}\right)}P_{(i+1)}+\xi_{\left(i-\frac{1}{2}\right)}P_{(i-1)}}{\left(\triangle X\right)^2}.$$

$$\frac{\partial}{\partial X}\left(\xi\frac{\partial P}{\partial X}\right)_{(i)} \cong \frac{-\xi_{\left(i+\frac{1}{2}\right)}P_{(i)}-\xi_{\left(i-\frac{1}{2}\right)}P_{(i)}}{\left(\triangle X\right)^2}+\frac{\xi_{\left(i+\frac{1}{2}\right)}P_{(i+1)}+\xi_{\left(i-\frac{1}{2}\right)}P_{(i-1)}}{\left(\triangle X\right)^2}.$$

$$\frac{\partial}{\partial X}\left(\xi\frac{\partial P}{\partial X}\right)_{(i)} \cong \frac{P_{(i)}\left(-\xi_{\left(i+\frac{1}{2}\right)}-\xi_{\left(i-\frac{1}{2}\right)}\right)}{\left(\triangle X\right)^2}+\frac{\xi_{\left(i+\frac{1}{2}\right)}P_{(i+1)}+\xi_{\left(i-\frac{1}{2}\right)}P_{(i-1)}}{\left(\triangle X\right)^2}.$$

$$\frac{\partial}{\partial X}\left(\xi\frac{\partial P}{\partial X}\right)_{(i)} \cong P_{(i)}\frac{\left(-\xi_{\left(i+\frac{1}{2}\right)}-\xi_{\left(i-\frac{1}{2}\right)}\right)}{\left(\triangle X\right)^2}+\frac{\xi_{\left(i+\frac{1}{2}\right)}P_{(i+1)}+\xi_{\left(i-\frac{1}{2}\right)}P_{(i-1)}}{\left(\triangle X\right)^2}. \tag{A-7}$$

Couette component discretization using FDM:

$$\frac{\partial H_A}{\partial X}_{(i)}=\frac{H_{A\left(i+\frac{1}{2}\right)}-H_{A\left(i-\frac{1}{2}\right)}}{\triangle X}. \tag{A-8}$$

Shear flow factor component discretization using FDM:

$$\frac{\partial \phi_s}{\partial X}_{(i)} = \frac{\phi_{s\left(i+\frac{1}{2}\right)} - \phi_{s\left(i-\frac{1}{2}\right)}}{\triangle X}. \tag{A-9}$$

Transient component discretization using FDM:

$$\frac{\partial H_T}{\partial \psi}_{(i)} = \frac{H_t - H_{t-1}}{\partial \psi}. \tag{A-10}$$

(A-7) $\wedge$ (A-8) $\wedge$ (A-9) $\wedge$ (A-10) $\rightarrow$ (A-3)

$$P_{(i)} \frac{\left(-\xi_{\left(i+\frac{1}{2}\right)} - \xi_{\left(i-\frac{1}{2}\right)}\right)}{\left(\triangle X\right)^2} + \frac{\xi_{\left(i+\frac{1}{2}\right)} P_{(i+1)} + \xi_{\left(i-\frac{1}{2}\right)} P_{(i-1)}}{\left(\triangle X\right)^2} =$$

$$= \frac{H_{A\left(i+\frac{1}{2}\right)} - H_{A\left(i-\frac{1}{2}\right)}}{\triangle X} + \frac{\phi_{s\left(i+\frac{1}{2}\right)} - \phi_{s\left(i-\frac{1}{2}\right)}}{\triangle X} + \frac{H_t - H_{t-1}}{\partial \psi}.$$

$$P_{(i)} \left(-\xi_{\left(i+\frac{1}{2}\right)} - \xi_{\left(i-\frac{1}{2}\right)}\right) + \xi_{\left(i+\frac{1}{2}\right)} P_{(i+1)} + \xi_{\left(i-\frac{1}{2}\right)} P_{(i-1)} =$$

$$= \left(H_{A\left(i+\frac{1}{2}\right)} - H_{A\left(i-\frac{1}{2}\right)} + \phi_{s\left(i+\frac{1}{2}\right)} - \phi_{s\left(i-\frac{1}{2}\right)}\right)\left(\triangle X\right) + \frac{H_t - H_{t-1}}{\partial \psi}\left(\triangle X\right)^2.$$

$$P_{(i)} \left(-\xi_{\left(i+\frac{1}{2}\right)} - \xi_{\left(i-\frac{1}{2}\right)}\right) = \left(H_{A\left(i+\frac{1}{2}\right)} - H_{A\left(i-\frac{1}{2}\right)} + \phi_{s\left(i+\frac{1}{2}\right)} - \phi_{s\left(i-\frac{1}{2}\right)}\right)\left(\triangle X\right) +$$

$$+ \frac{H_t - H_{t-1}}{\partial \psi}\left(\triangle X\right)^2 - \xi_{\left(i+\frac{1}{2}\right)} P_{(i+1)} - \xi_{\left(i-\frac{1}{2}\right)} P_{(i-1)}.$$

Calculation of the non-dimensional HD pressure at node *i*:

$$P_{(i)} = \frac{\xi_{\left(i+\frac{1}{2}\right)} P_{(i+1)} + \xi_{\left(i-\frac{1}{2}\right)} P_{(i-1)}}{\xi_{\left(i+\frac{1}{2}\right)} + \xi_{\left(i-\frac{1}{2}\right)}} - \frac{\left(H_{A\left(i+\frac{1}{2}\right)} - H_{A\left(i-\frac{1}{2}\right)} + \phi_{s\left(i+\frac{1}{2}\right)} - \phi_{s\left(i-\frac{1}{2}\right)} \right)\left(\vartriangle X\right)}{\xi_{\left(i+\frac{1}{2}\right)} + \xi_{\left(i-\frac{1}{2}\right)}} - \frac{\frac{H_t - H_{t-1}}{\partial \psi}\left(\vartriangle X\right)^2}{\xi_{\left(i+\frac{1}{2}\right)} + \xi_{\left(i-\frac{1}{2}\right)}}. \tag{A-11}$$

APPENDIX B

TECHNICAL SPECIFICATIONS OF THE SUPERFLOW SF-902S ENGINE DYNAMOMETER [93]

Absorber Type	Water brake power absorber with Teflon water seals, high speed bearings, stainless trunnion and backing plate and aluminum bronze rotor – low inertia design for precise control.
Maximum Speed	15 000 rpm
Power Capacity	1 119 kW
Torque Capacity	1 627 Nm
Temperature	16-channel thermocouple panel with 12 transducers
Pressure	10-channel pressure panel with 3 sensors
Air / Fuel	2 pre-configured analog inputs
Fuel Flow	2 fuel flow measurement turbines
Air Flow	1 air flow measurement turbine

TECHNICAL SPECIFICATIONS OF THE AVL DYNAMIC FUEL METER [86]

Type	AVL 733S
Measurement Principle	Gravimetric
Measurement Range	0 – 150 kg/h
Measurement Accuracy	≤ 0.12 %
Interfaces / Output	RS232, analog I/O, 0 – +10 V, digital I/O
Measurement Frequency	10 Hz (max.)
Response Time	< 440 ms
Fuel Types	Standard and 100% bio fuels
Fuel Circulation	240 / 450 / 540 l/h
Control Range	10 – 80 ˚C
Stability	≤ 0.02 ˚C
Power Supply	230 V, 50-60 Hz; 100V, 50-60 Hz
Power Consumption	400 W
Ambient Temperature	5 – 50 °C
Dimensions (W×H×D)	770 × 1 350 × 345 mm

Technical Specifications of the AVL Blow By Meter [85]

Type	AVL 442
Measurement Principle	Differential pressure
Measurement Range	3 – 150 l/min
Measurement Accuracy	≤ 1.5 % FSO standard linearization
Interfaces / Output	RS232 (AK-compliant), analog I/O, -10 – +10 V
Power Supply	24 V DC
Power Consumption	35 W
Ambient Temperature	-10 – 55 °C
Dimensions (W×H×D)	330 × 350 × 75 mm

Technical Specifications of the Kistler Measuring Spark Plug [90]

Type	6118BFD16
Pressure Range	0 – 200 bar
Overload Capacity	250 bar
Sensitivity at 200 °C	≈ -10 pC/bar
Natural Frequency	≈ 65 kHz
Operating Temperature	-20 – 350 °C
Weight	50 g

Technical Specifications of the Kistler Crank Angle Encoder Set [91]

Type	2613A
Signal Resolution	0.1 – 0.6 °
Dynamic Accuracy	+0.02 °
Trigger Signal Resolution	0.1 – 6 °
Speed Range	1 – 20 000 rpm
Temperature Range	-30 – 60 °C
Power Supply	5±0.25 V DC
Mounting Diameter	69 mm (encoder)
Weight	460 g (encoder); 300 g (amplifier)
Dimensions	98 × 64 × 37 mm (amplifier)

TECHNICAL SPECIFICATIONS OF THE BRUKER CONTOURGT-X OPTICAL MICROSCOPE [87]

Max. Scan Range	Up to 10 mm
Vertical Resolution	0.05 nm (motor); 0.01 nm (PZT)
RMS Repeatability	0.01 nm (motor); 0.004 nm (PZT)
Lateral Resolution	Max. 0.01 µm (with NanoLens™)
Step Height Accuracy	< 0.75% (for step heights of 8 µm and greater)
Step Height Repeatability	< 0.1%
Max. Scan	114 µm / sec
Sample Reflectivity	0.05% – 100%
Max. Sample Slope	Up to 87° (for rough surfaces)
Sample Height	Up to 100 mm
Sample Weight	Up to 23 kg
XY Sample Stage	200 mm automated
Z Focusing	100 automated
Optical Metrology Module	Patented dual-LED illumination; Single-objective adapter; Optional automated or manual turret
Objectives	Parfocal: 2.5x, 5x, 10x, 20x, 50x, 115x; LWD: 1x, 1.5x, 2x, 5x,10x; TTM: 2x, 5x, 10x, 20x; Bright field: 2.5x, 5x, 10x, 50x
Camera	Standard monochrome: 640x480; High-resolution monochrome (option): 1392x1040; Color (option): 640x480
Dimensions	852mm (W) × 793mm (D) × 1608mm (H)
Weight	493 kg

APPENDIX C

MEASURED WIDE-OPEN-THROTTLE POWER CURVE OF THE ŠKODA EA111 1.2 HTP ENGINE

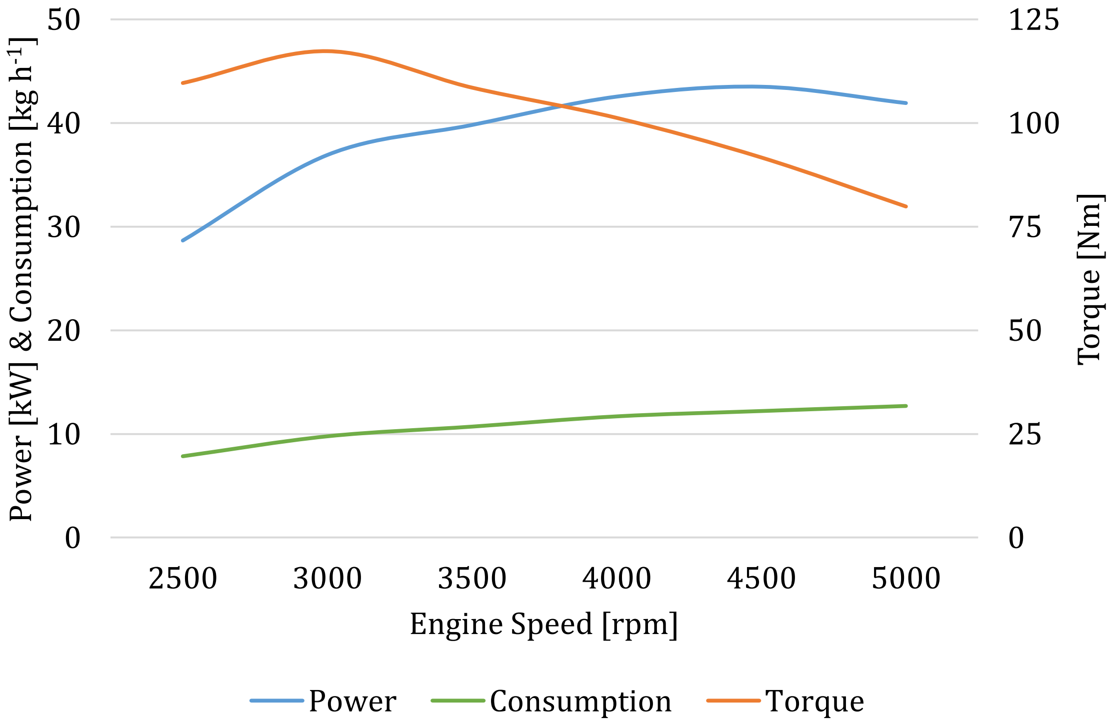

Figure C.1 WOT power curve of the Škoda EA111 engine

Table C.1 Values of WOT power curve

Parameter		**2500**	**3000**	**3500**	**4000**	**4500**	**5000**
Power	[kW]	28.66	36.93	39.82	42.55	43.51	41.93
Torque	[Nm]	109.6	117.3	108.5	101.2	91.7	79.8
Consumption	[kg h^{-1}]	7.84	9.77	10.70	11.69	12.21	12.70

APPENDIX D

PHOTO DOCUMENTATION OF THE EXPERIMENT

Figure D.1 Engine test cell control room

Figure D.2 Instrumented engine in the test cell

APPENDIX E

COMBUSTION CHAMBER PRESSURES OF THE ŠKODA EA111 1.2 HTP ENGINE

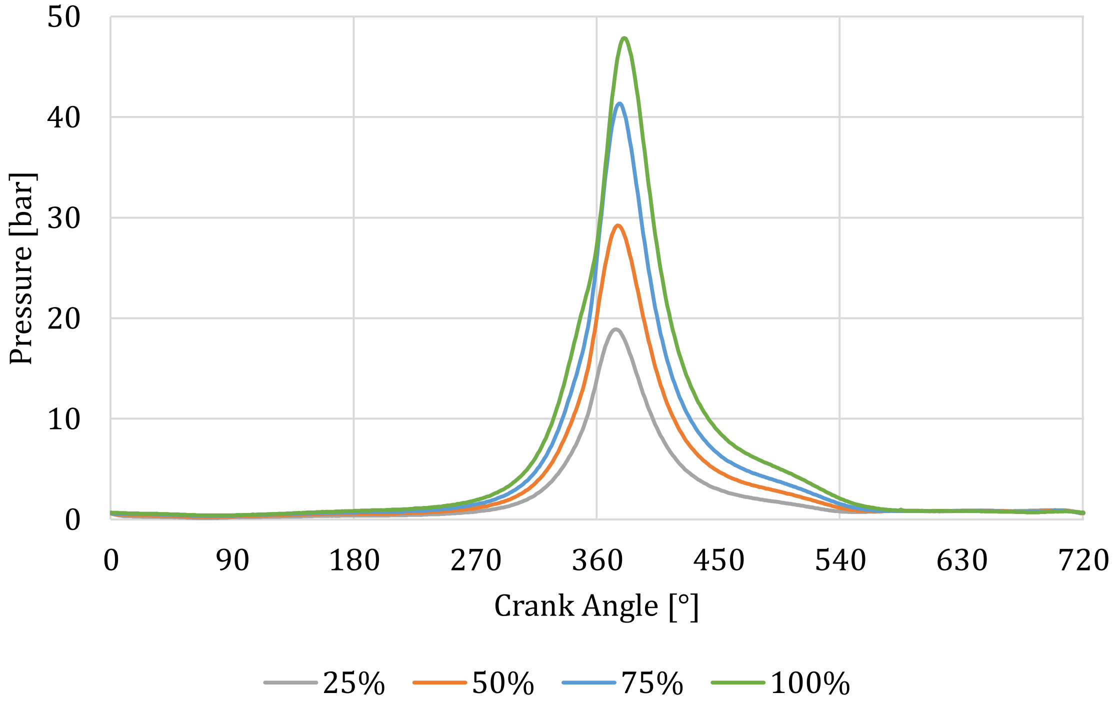

Figure E.1 Combustion chamber pressures at 3000 rpm

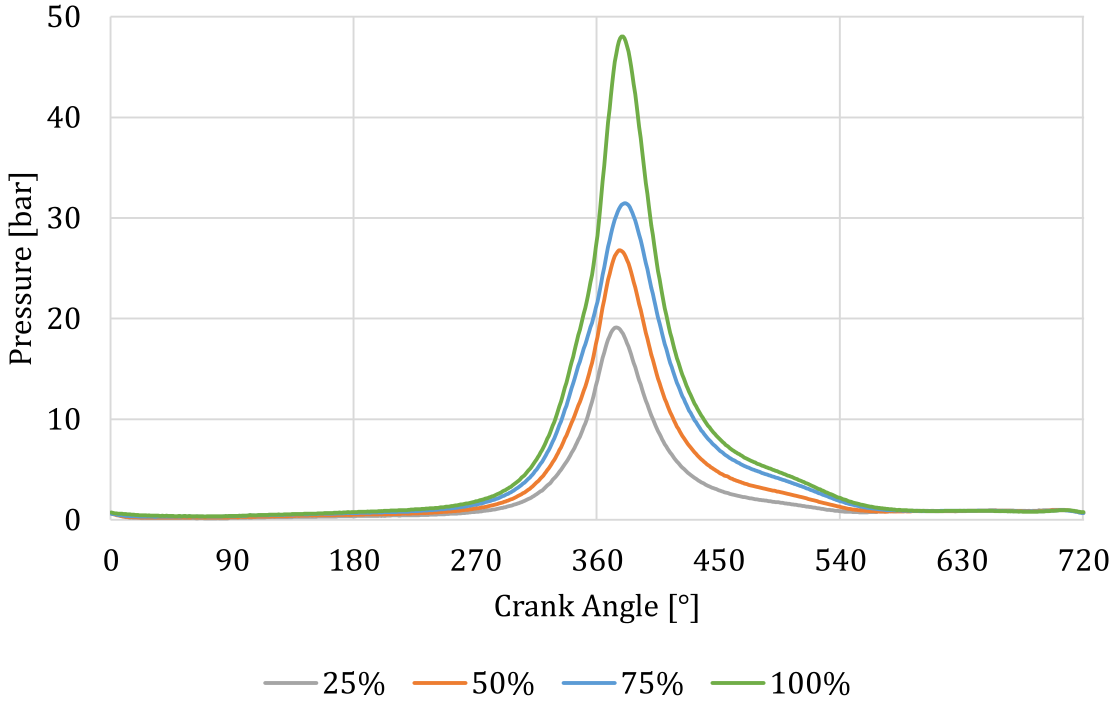

Figure E.2 Combustion chamber pressures at 3500 rpm

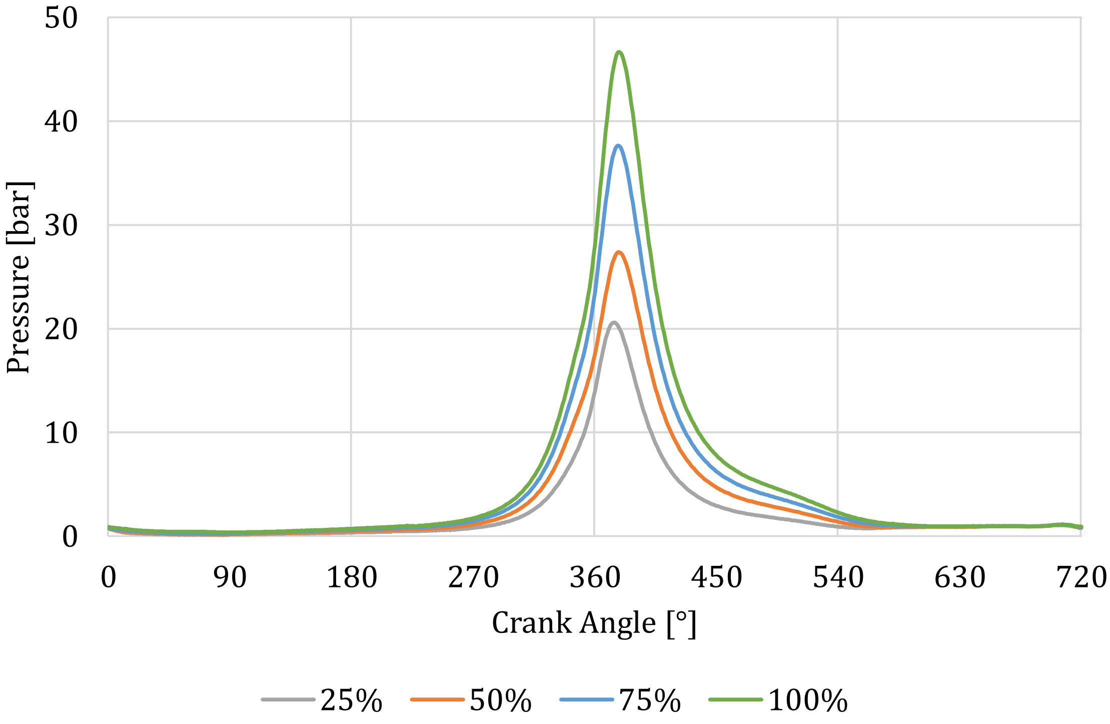

Figure E.3 Combustion chamber pressures at 4000 rpm

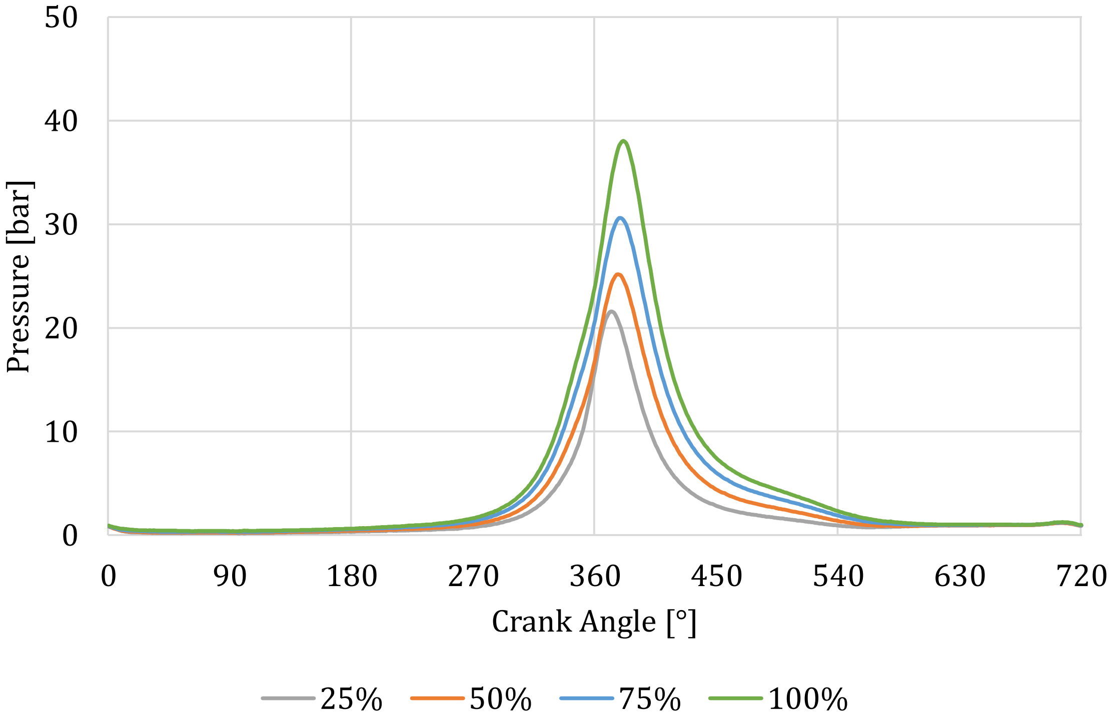

Figure E.4 Combustion chamber pressures at 4500 rpm

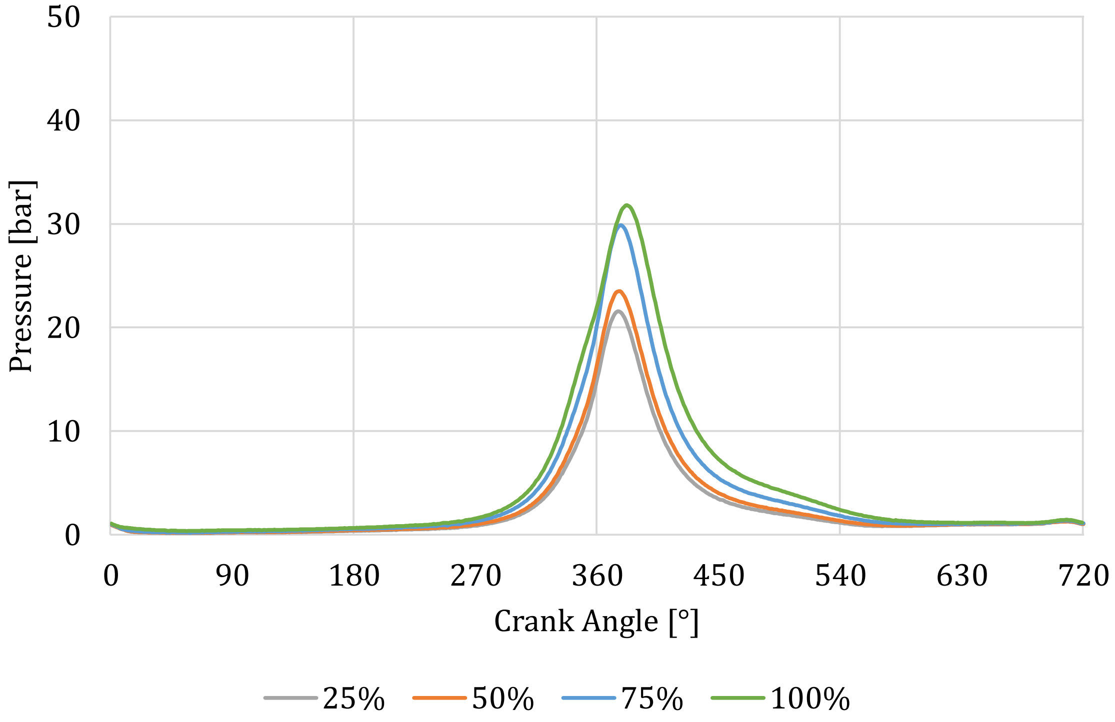

Figure E.5 Combustion chamber pressures at 5000 rpm

APPENDIX F

CYLINDER LINER TEMPERATURES OF THE ŠKODA EA111 1.2 HTP ENGINE

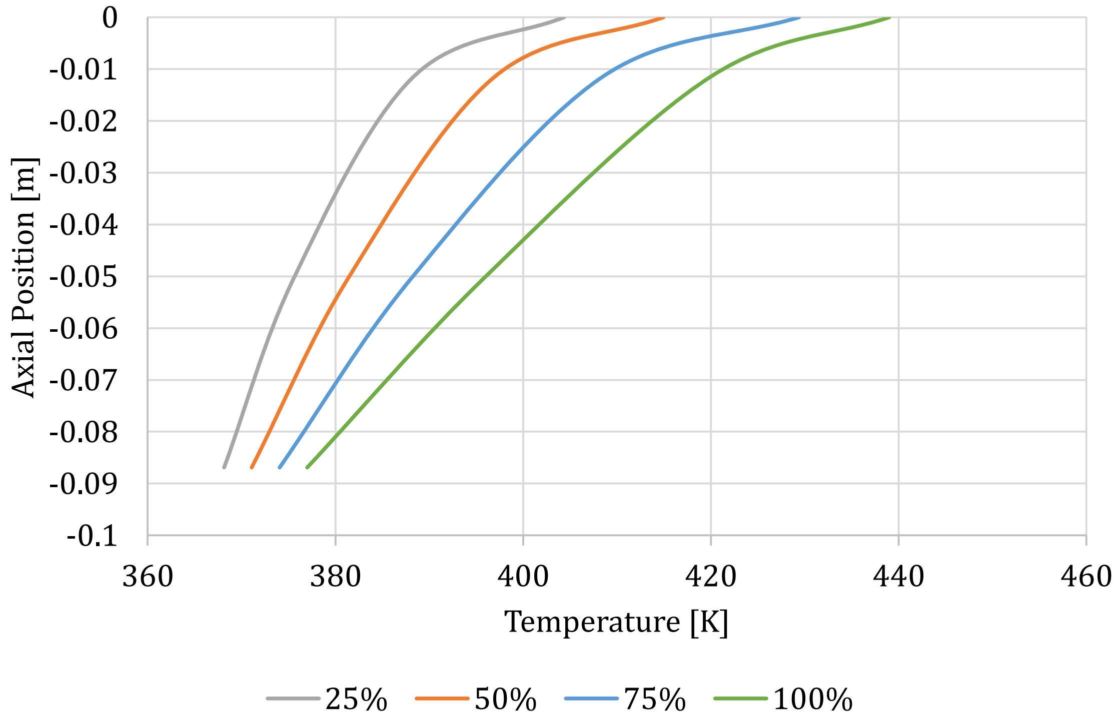

Figure F.1 Cylinder liner temperature distribution at 3000 rpm

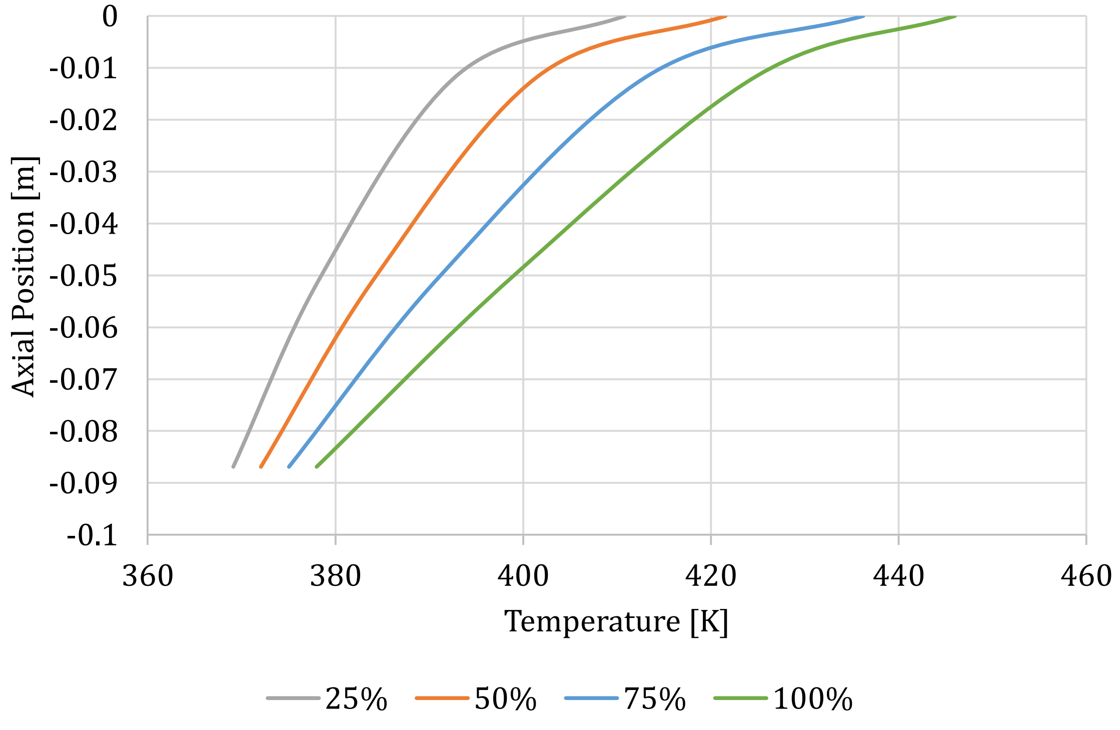

Figure F.2 Cylinder liner temperature distribution at 3500 rpm

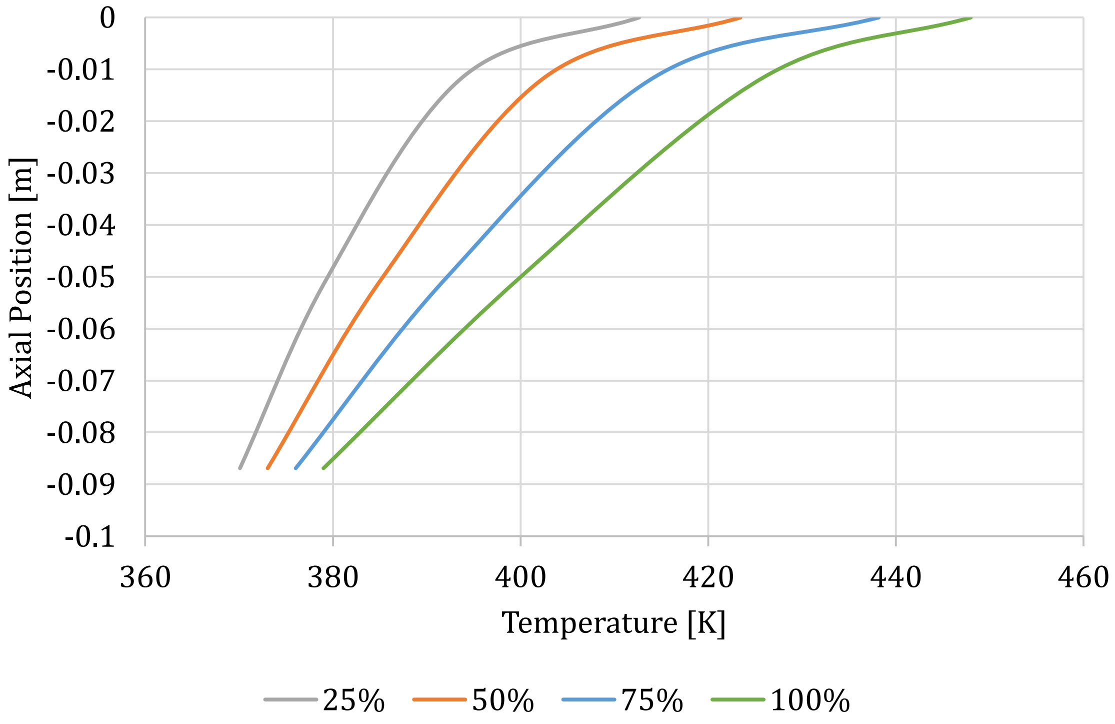

Figure F.3 Cylinder liner temperature distribution at 4000 rpm

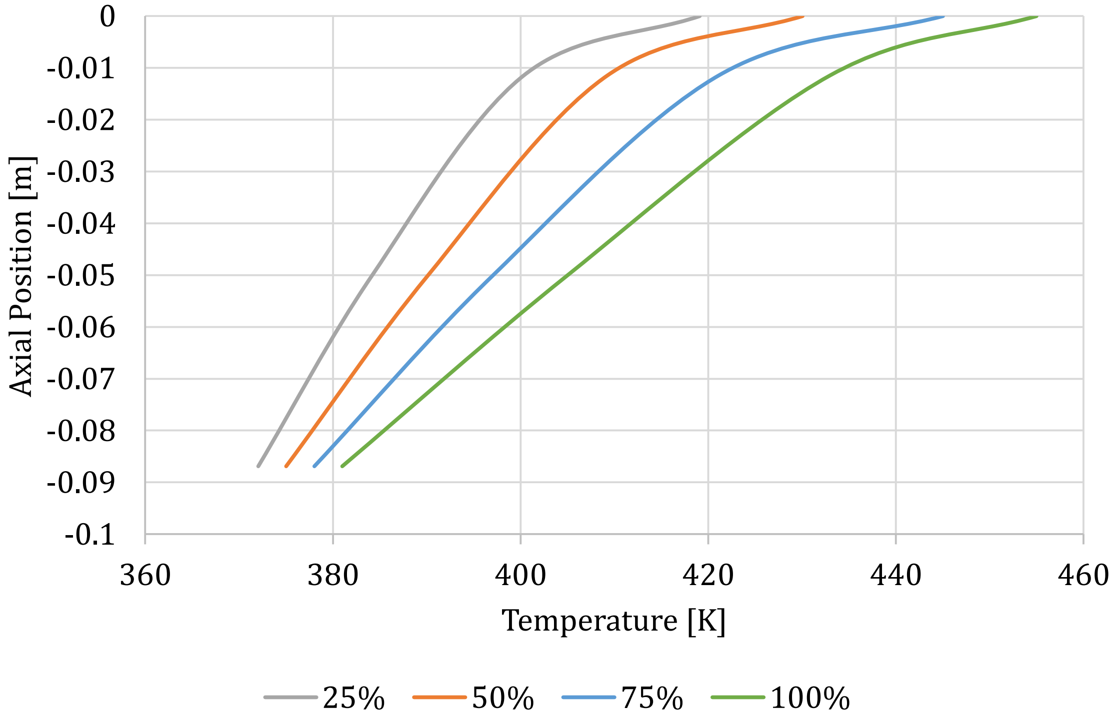

Figure F.4 Cylinder liner temperature distribution at 4500 rpm

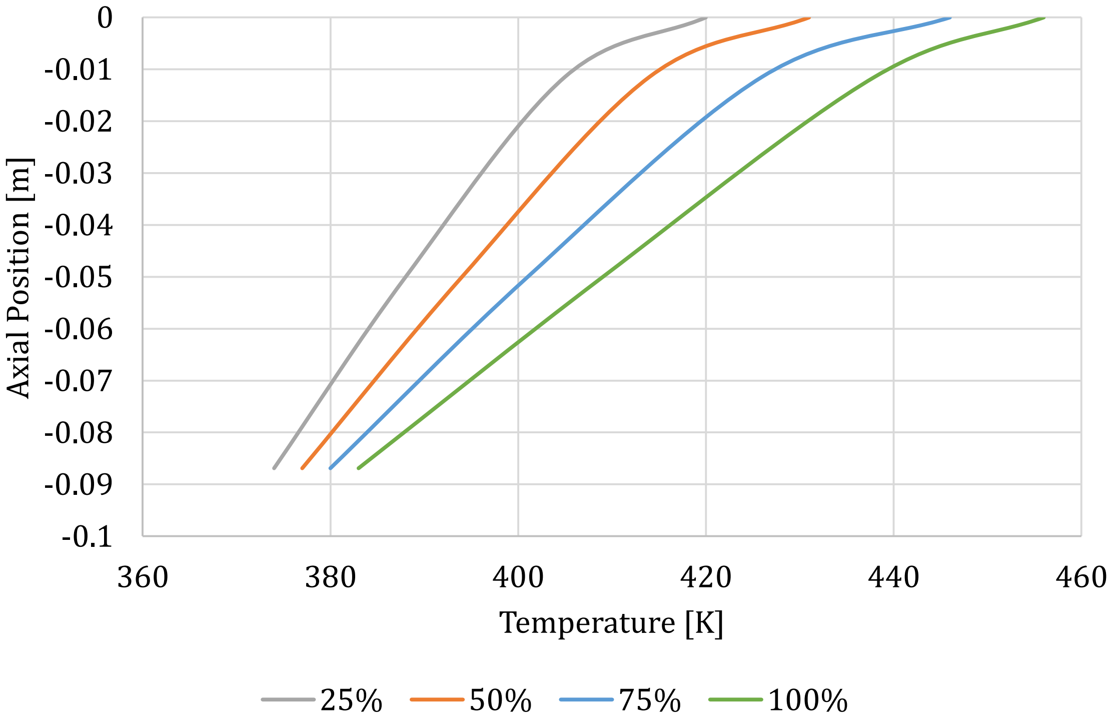

Figure F.5 Cylinder liner temperature distribution at 5000 rpm

APPENDIX G

COMPARISON OF MEASURED AND CALCULATED VOLUMETRIC BLOW-BY GAS FLOW

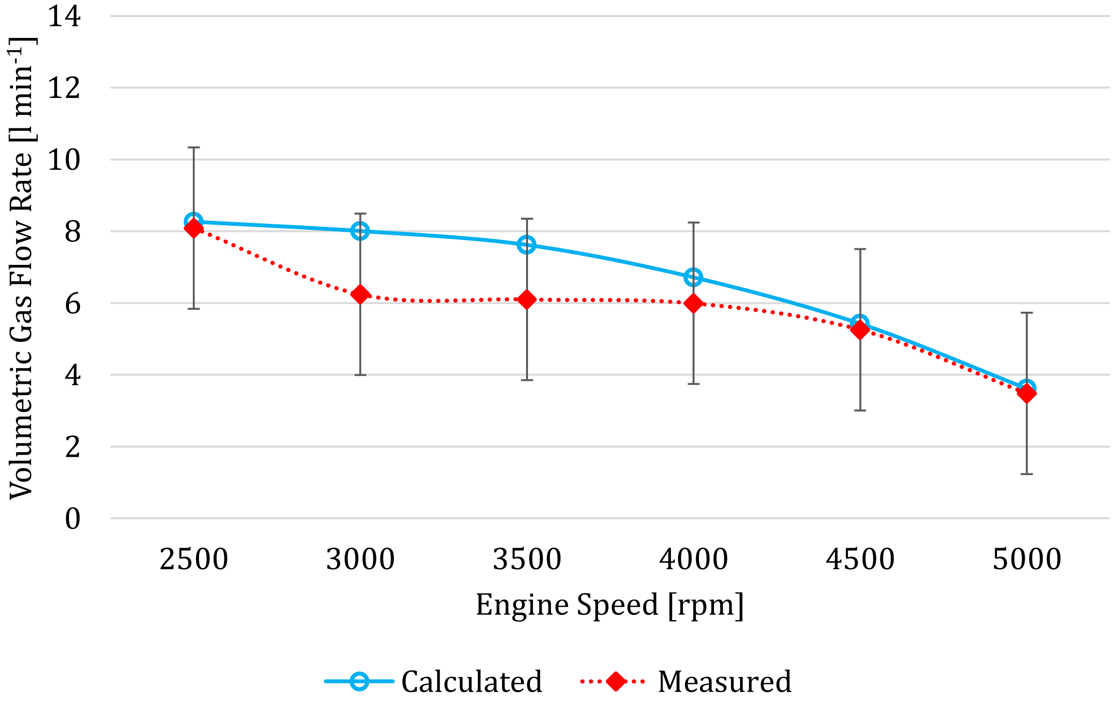

Figure G.1 Volumetric blow-by gas flow at 75% partial load running condition

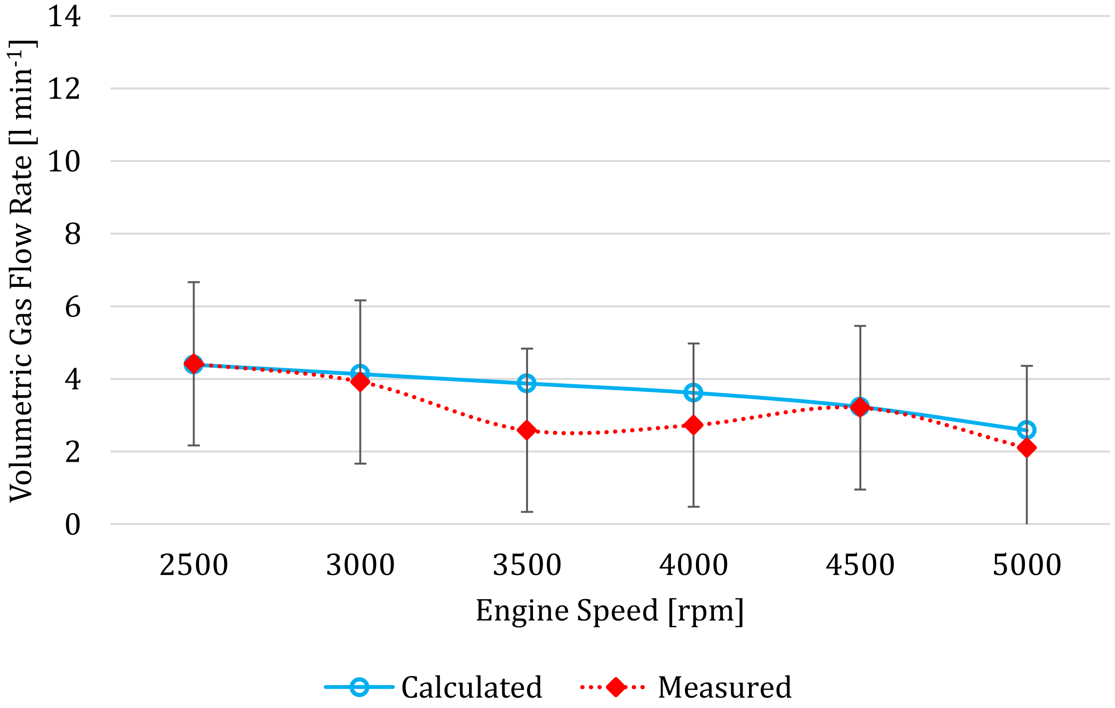

Figure G.2 Volumetric blow-by gas flow at 50% partial load running condition

APPENDIX H

FRICTION POWER LOSS ON THE COMPLETE RING PACK WITH DIFFERENT VISCOSITY OILS

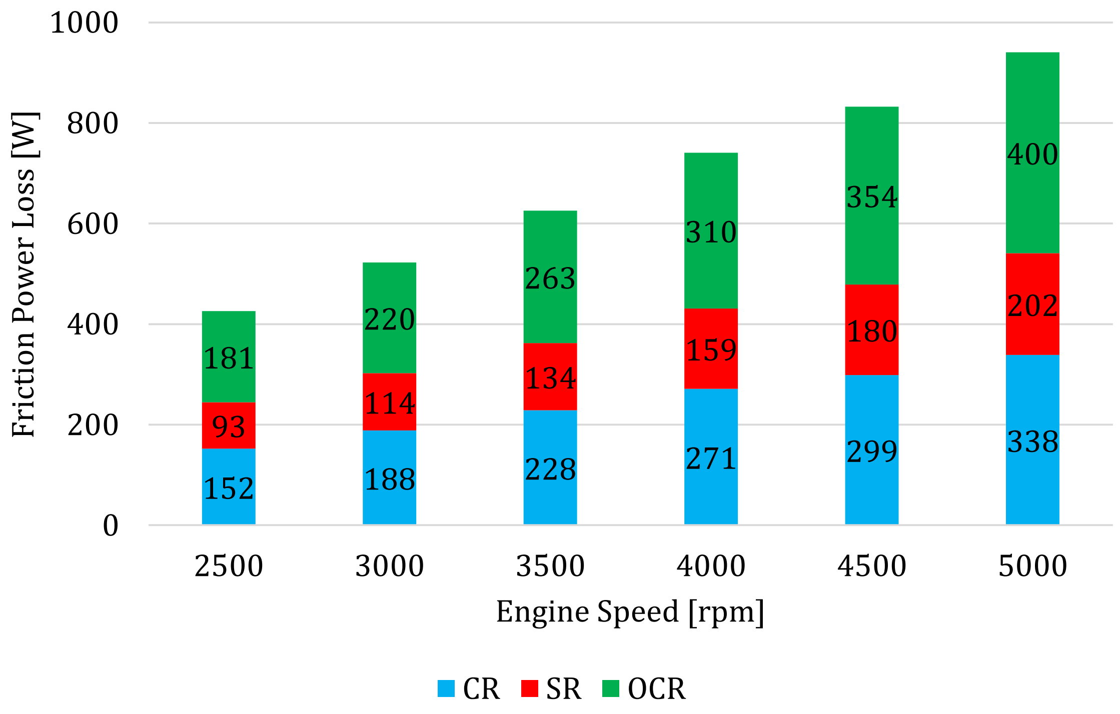

Figure H.1 Friction power loss on the ring pack with the baseline 5W40 viscosity oil

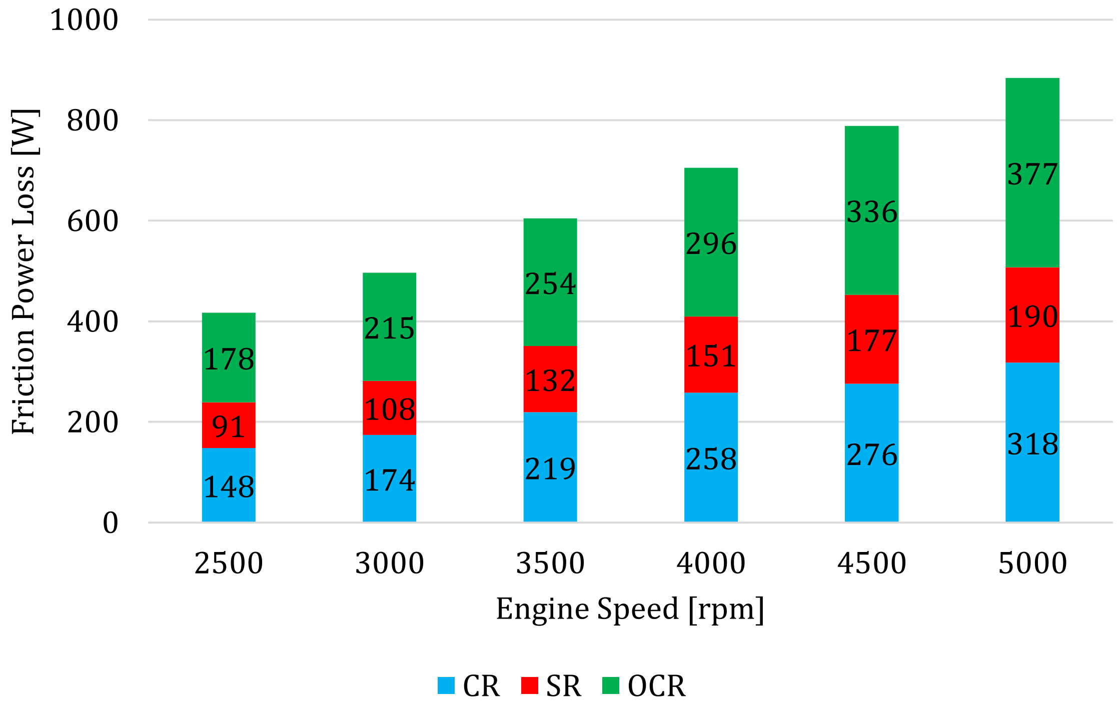

Figure H.2 Friction power loss on the ring pack with the 0W30 viscosity oil

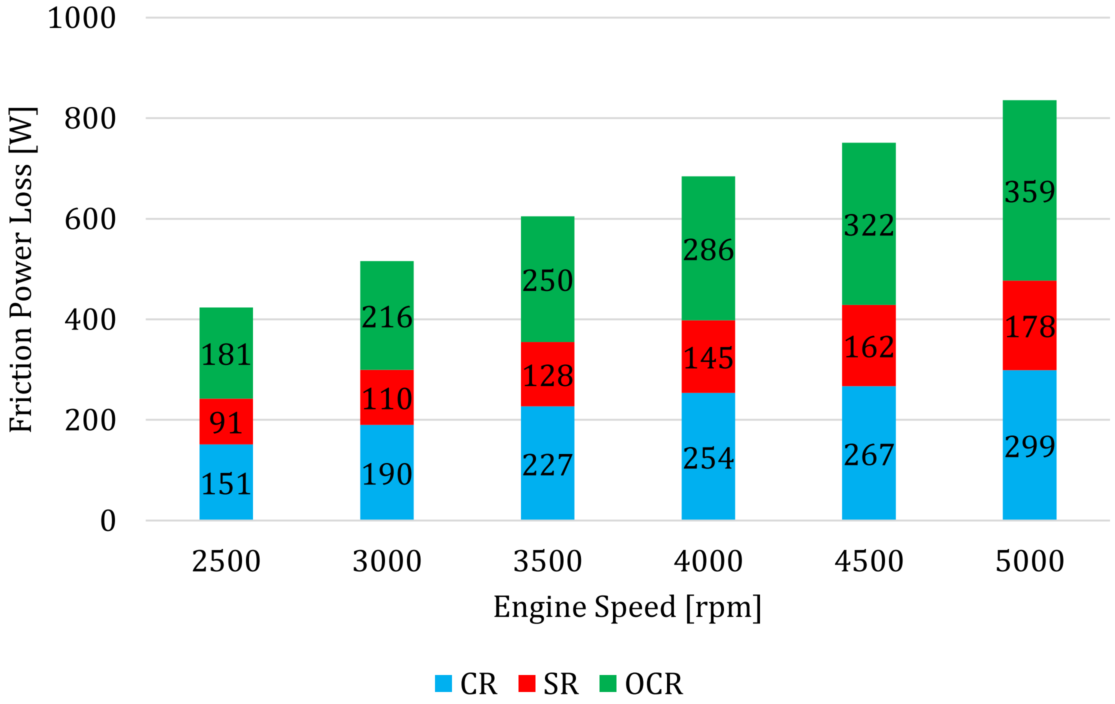

Figure H.3 Friction power loss on the ring pack with the 0W20 viscosity oil

APPENDIX I

FRICTION POWER LOSS ON THE COMPRESSION RING WITH DIFFERENT SURFACE STRUCTURES

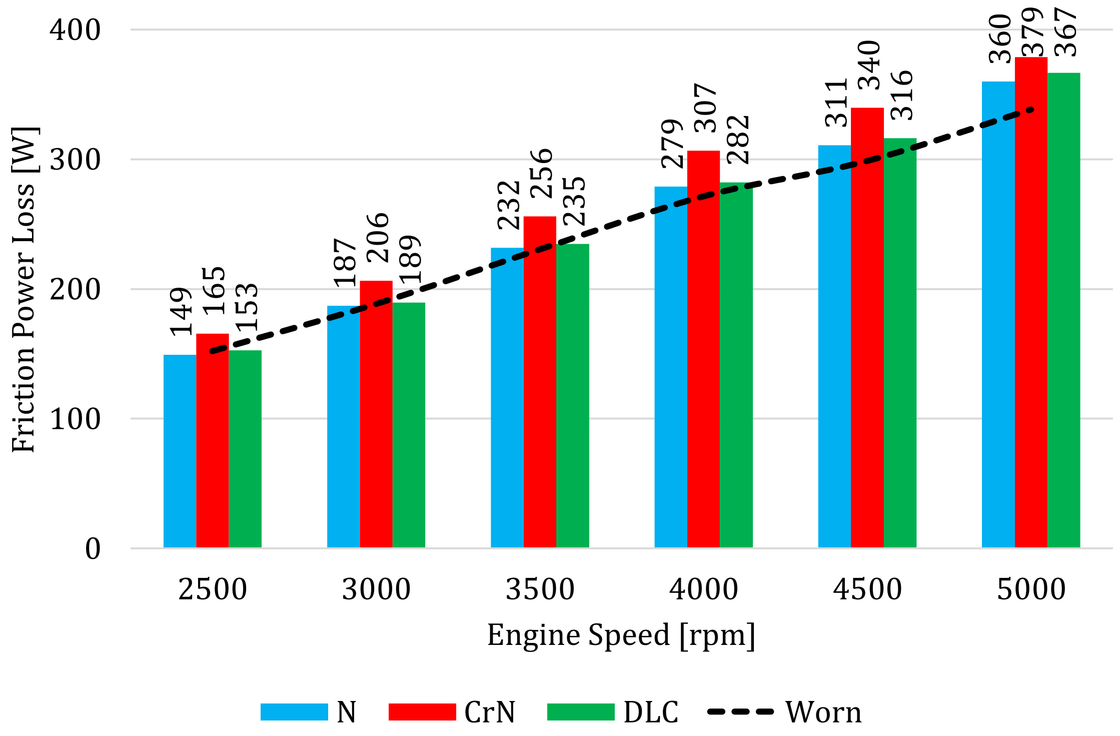

Figure I.1 Friction power loss on the compression ring with different surface structures